Programa de Doctorado en Ingeniería Matemática, Estadística e Investigación Operativa

por la

Universidad Complutense de Madrid

y la

Universidad Politécnica de Madrid





A mathematical and computational approach to the study of transport in ocean flows

---

Doctoral Candidate

Guillermo García Sánchez

Supervisor

Ana María Mancho Sánchez

Year

2023

Tribunal nombrado por el Magnífico Rector de la Universidad Politécnica de Madrid el día _____ de _____ de _____.

Presidente: _____

Vocal: _____

Vocal: _____

Vocal: _____

Secretario: _____

Suplente: _____

Suplente: _____

Realizado el acto de defensa y lectura de la Tesis el día _____ de _____ de _____ en Madrid, habiendo obtenido la calificación de _____

El presidente, El secetario, Los vocales,

Declaration

I hereby declare that except where specific reference is made to the work of others, the contents of this dissertation are original and have not been submitted in whole or in part for consideration for any other degree or qualification in this, or any other University. This dissertation is my own work and contains nothing which is the outcome of work done in collaboration with others.

Guillermo García Sánchez
November 2023

Acknowledgements

First and foremost, I would like to express my deepest gratitude to my supervisor, Ana María Mancho. Her guidance, patience, and unwavering support throughout this journey have been invaluable. She has been a mentor in both professional and personal domains, a person I greatly admire. Without her expertise and encouragement, this work would not have been possible.

I owe a debt of gratitude to my family: my mother, father, and brother Rodrigo. My deepest thanks also go to my girlfriend Camila. Their love, understanding, and constant encouragement have been the pillars of my strength. Their unwavering support during all moments, especially when doubts surfaced, has been invaluable.

I was privileged to spend valuable time at the Joint Research Centre (JRC) in Ispra, which was truly transformative for me. I owe a huge thanks to Michalis Vousdoukas, Lorenzo Mentaschi and Luc Feyen. Their insights were eye-opening, and I am truly grateful for their patience, the support and the guidance they provided throughout my time there. I also want to extend my gratitude to the entire community at JRC, particularly Virginia Bernardi. Her introduction to SciArt initiated many enlightening discussions on science and philosophy. I wish to acknowledge Caterina Benincasa and Adriaan Eeckles for integrating me into the SciArt program, paving the way for a stimulating collaboration with Kristin Bergaust and Evangelos Voukouvalas on the Oslo Fjord project. My sincere thanks to Kristin Bergaust for our transformative discussions during our residencies.

My research stay at MIT, under the expert supervision of Prof. Pierre Lermusiaux, was a period of great growth. Also, the camaraderie of friends I made during this time added immense value to my experience.

I am grateful to Antonio G. Ramos and Josep Coca for providing the satellite images and ocean knowledge to complete the results of this thesis. My heartfelt gratitude goes to Antonio G. Ramos for our invaluable discussions and for welcoming me to the Canary Islands, as well as his lab and home. His enthusiasm and passion is an inspiration. Special thanks to Steven Wiggins, Makrina Agaoglou, Ángel Rodríguez Santana, Jerome Daquin, Jezabel Curbelo. Their insights, feedback, and encouragement have been pivotal to this work. Also I want to

thank all my friends but special mention to Rodrigo de Medrano and Juan Roos that have been a rock and important part of this journey.

I extend my thanks to my tutor from UPM, Francisco Navarro, and program coordinator, Salvador Jimenez, for navigating me through the complexities of university protocols.

Additionally, I want to express my profound thanks to my co-founders of Digital Earth Solutions, Juan Roos and Maria Jose Mancho. With them and once again, Ana M. Mancho, I am fortunate to further my research passion in an inventive setting, aiming for tangible societal impacts. Heartfelt thanks to our investors, Michael Tzannes and Jose Manuel Aisa.

It is important to acknowledge the financial backing from IMPRESSIVE, courtesy of the European Union's Horizon 2020 research and innovation programme (grant agreement No 821922), from BEWATS funded by the Programa Pleamar of the Biodiversity Foundation (Fundación Biodiversidad) of Spain's Ministry for the Ecological Transition and Demographic Challenge (Ministerio para la Transición Ecológica y el Reto Demográfico), CSIC PIE project Ref. 202250E001, and grant PID2021-123348OB-I00 funded by MCIN AEI 10.13039501100011033 and by FEDER A way for making Europe. I also appreciate the assistance with the publication fee provided by the CSIC Open Access Publication agreement and the support from PTI Teledetect.

In our pursuit of knowledge, we are often uplifted by countless others. To all those who have contributed in so many ways to my academic journey and this work, I offer my heartfelt thanks.

Resumen

El océano es un sistema circulatorio complejo que sostiene una diversa vida marina y es esencial para regular el clima de la Tierra. Predecir con precisión las corrientes oceánicas y su transporte es esencial para comprender la distribución global del calor, la conservación de los ecosistemas marinos y la solución a la contaminación marina, entre otros. Esta tesis aborda diversas técnicas matemáticas y computacionales capaces de caracterizar los fenómenos de transporte en el océano y sus aplicaciones.

Nuestro objetivo es estudiar la monitorización de accidentes por derrames de petróleo utilizando herramientas de sistemas dinámicos y técnicas de teledetección tanto a escala costera como a gran escala. Esto introduce en nuestra discusión la necesidad de evaluar el rendimiento o la calidad de diferentes conjuntos de datos y productos oceánicos disponibles, y el uso de las observaciones remotas para este fin.

Nuestra primera discusión a nivel costero se centra en el accidente del ferry Volcán Tamasite. Este es un evento bien documentado de derrame de diésel. Se utilizan tanto modelos hidrodinámicos de alta resolución específicamente preparados para el área de interés, como datos más genéricos. El uso de estos datos proporcionan salidas que se validan con productos de teledetección y observaciones complementarias in situ. Para comparar el rendimiento de los datos utilizados, se introduce un nuevo cuantificador para la incertidumbre hacia adelante en el tiempo para trayectorias derivadas de conjuntos de datos. Esta métrica de incertidumbre revela un patrón intrínsecamente vinculado a las estructuras dinámicas invariantes (variedades estables de trayectorias hiperbólicas) asociadas al conjunto de datos oceánico subyacente. Es destacable el hecho de que este marco facilita una comparación cuantitativa de métricas de transporte de diferentes conjuntos de datos oceánicos, permitiendo una evaluación objetiva de estos datos en diversos contextos.

El evento de gran escala analizado es un incidente que afectó a la costa mediterránea de varios países de Oriente Medio a principios de 2021. Las estructuras coherentes lagrangianas (LCS) permiten entrever patrones caóticos de tales eventos. Combinando observaciones satelitales y modelado computacional, se determinan los orígenes y cronologías de estos derrames. La naturaleza de este evento, donde la fuente del derrame es desconocida, permite introducir una nueva métrica de incertidumbre diseñada para evaluar la capacidad de trans-

porte de los modelos oceánicos para identificar cual es el origen de observaciones a posteriori. El análisis de la métrica en el nuevo escenario completa las conexiones con estructuras dinámicas invariantes, encontrando en este caso un vínculo con las variedades inestables de trayectorias hiperbólicas.

Finalmente, proponemos una metodología para construir y validar modelos oceánicos de alta resolución utilizando imágenes satelitales. Este enfoque correlaciona observaciones satelitales con resultados de corrientes obtenidos de la ejecución del modelo con diferentes selecciones de parámetros. Se presenta un índice de rendimiento que evalúa la consistencia entre las salidas del modelo y los datos observacionales.

En resumen, esta tesis enfatiza la importancia y aplicabilidad de las metodologías matemáticas y computacionales en estudios oceánicos. Las perspectivas derivadas tienen importantes implicaciones en la toma de decisiones informadas en crisis relacionadas con el mar.

Abstract

The ocean is a complex circulatory system that sustains a wide variety of marine life and is essential for regulating Earth's climate. Accurately predicting oceanic currents and their transport is essential for understanding global heat distribution, marine ecosystem conservation and addressing marine pollution among others. This thesis examines the mathematical and computational techniques necessary to characterize transport phenomena in the ocean and their practical applications.

We address the monitoring of oil spill accidents using dynamical systems tools and remote sensing observations both at local coastal scale and at large scale. This brings into our discussion the need to evaluate the performance of different available datasets and oceanic products and the use and role of remote observations to this end.

Our first discussion at coastal level is focused on the 'Volcan Tamasite' ferry accident. This is a well-documented diesel fuel spill event. We used both high-resolution hydrodynamic models specifically prepared for the area and coarser data from more generic sources. The outputs of the analysis of these data are validated with remote sensing products and complementary in situ observations. For comparing the performance of the used data, a novel quantifier for forward time uncertainty for trajectories derived from datasets is introduced. This uncertainty metric reveals a pattern intrinsically tied to the invariant dynamical structures (stable manifolds of hyperbolic trajectories) associated to the underlying dataset. Importantly, this framework facilitates a quantitative comparison of transport metrics from disparate ocean datasets, allowing for an objective evaluation of these data sources in various contexts.

The large-scale event that we have analyzed is an incident involving the Mediterranean coast of several Middle Eastern countries at the beginning of 2021. Lagrangian Coherent Structures (LCS) allow to foreseen chaotic patterns of such events. Through the integration of satellite observations and computational modeling, the origins and timelines of these spills are determined. The nature of this event, where the source of the spill is unknown, allows to introduce a new uncertainty metric designed to assess the transport capacity of oceanic models when identifying the origin of specific observations. The analysis of the metric in the new setting completes the connections to invariant dynamical structures, finding in this case a link with unstable manifolds of hyperbolic trajectories.

Finally, we outline a methodology to build and validate high-resolution ocean models using satellite imagery. This approach correlates satellite observations with current results obtained from running the model with different parameter selections. A performance index is presented that evaluates the consistency between the model outputs and observational data.

In summary, this thesis emphasizes the significance and applicability of mathematical and computational methodologies in oceanic studies. The insights derived are crucial for informed decision-making in marine-related crises.

Contents

List of Figures XV

List of Tables XVII

List of acronyms XIX

1. Introduction **1**
1.1. Motivation 1
1.2. State of the art 2
1.2.1. Ocean Modelling 2
1.2.2. Oil Spill and Particle Drift Models 5
1.2.3. Dynamical Systems 6
1.2.4. Uncertainty Quantification 8
1.3. Objectives 9
1.4. Thesis organization 9

2. Methodology **11**
2.1. Ocean Modelling 11
2.2. Dynamical Systems 12

3. Volcán de Tamasite Oil Spill Accident **17**
3.1. Data and Methodology 20
3.1.1. Satellite imagery and remote sensing 20
3.1.2. Ocean Models 21
3.1.3. The transport problem 28
3.2. Results and discussion 31
3.2.1. The dynamical system perspective 33
3.2.2. Uncertainty quantification 36
3.3. Conclusions 39

4. Forward Time Lagrangian Uncertainty Quantification **41**
4.1. Transport uncertainty quantification in ocean models 45
4.2. Formal results 51
4.2.1. The autonomous saddle point 52
4.2.2. The autonomous rotated saddle point 57
4.2.3. Discrete maps 60
4.3. The Duffing equation 63
4.4. Discussion 66
4.5. Conclusions 69

5. Eastern Mediterranean Oil Spill Accident **71**
5.1. Satellite Data 73
5.2. Satellite Results 75
5.3. The transport problem 77
5.4. Ocean Data 79
5.5. The Dynamical Systems Perspective 79
5.6. Transport Results 80
5.7. Discussion and Conclusions 82

6. Backward Time Lagrangian Uncertainty Quantification **87**
6.1. Uncertainty Quantification in Backward Time 91
6.2. A proof for singularites in L_{BUQ} 95
6.3. Results 97
6.4. Conclusions 104

7. Dynamical Systems and Satellite Imagery for Hydrodynamic Models **107**
7.1. The hydrodynamic model 109
7.1.1. The oceanic regional model 109
7.1.2. The geographical domain 113
7.1.3. Discretization and numerical algorithms 114
7.1.4. Boundary Conditions 116
7.2. Remote sensing 121
7.3. Transport and dynamical systems 122
7.4. Numerical experiment setups and performance quantification 126
7.5. Results 129
7.6. Conclusions 132

8. Conclusions and Outlook **135**
8.1. Research conclusions 135
8.2. Outlook 136

Bibliography **139**

List of Figures

2.1. Sketch of a hyperbolic trajectory 14
2.2. Sketch representation of M function for two different τ. 15

3.1. A map of the N-NE Gran Canaria Coast 18
3.2. SAR Sentinel images 22
3.3. Spatial domain of IBI, Coast and Port models 24
3.4. Sketch of the IBI and CST grids 29
3.5. Currents IBI, CST and PRT ocean models 31
3.6. Evolution of the spill in the Volcan de Tamasite accident location 32
3.7. Sketch of a hyperbolic trajectory in a detachment configuration 34
3.8. The Lagrangian skeleton of the Coast model 35
3.9. The Lagrangian skeleton IBI, Coastal and Port models 36
3.10. Quantitative measure of the uncertainty of the IBI and Coast models 38

4.1. Representation of two sequential observations and their evolution according to a mathematical model 43
4.2. Representation of the uncertainty quantification in a neighbourhood of the accident location 44
4.3. Quantitative measure of uncertainty for the Puertos del Estado model 46
4.4. Evaluation of the Lagrangian uncertainty quantifier 47
4.5. The Lagrangian skeleton of the ocean model on the accident day 48
4.6. The Lagrangian skeleton of the ocean model on the 23rd April 2017 49
4.7. Successive observations of the spill 52
4.8. A representation of L_{UQ} for $p > 1$ and $p < 1$ for the continuous saddle case 56
4.9. A representation of L_{UQ} for $p > 1$ and $p < 1$ for the continuous saddle rotated case. 60
4.10. Representation for the autonomous saddle L_{UQ} for $p = 2$ 62

4.11. Representation for the rotated saddle L_{UQ} for $p = 1/\delta = 2$ in the discrete saddle rotated case 63
4.12. Evaluation of L_{UQ} for the Duffing equation 64
4.13. Evaluation of the M function backwards integration on the Duffing equation 65
4.14. Evaluation of L_{UQ} for $p > 1$ on the Duffing equation 66
4.15. Evaluation of L_{UQ} $p < 1$ on the Duffing equation 67

5.1. Scenario of affected areas in Eastern Mediterranean accident 74
5.2. Satellite radar images 76
5.3. Spreading on the sea and the arrival of the oil to the coast 84
5.4. Simulations that connect successive oil spill observations. 85

6.1. Graphical representation of two sequential observations and their forward time evolution 90
6.2. A representation in the plane of L_{BUQ} for the saddle point 92
6.3. Evolution of L_{UQ} versus τ on the fixed point of saddle point system 94
6.4. Representation of the spills observed along the coastline of the Eastern Mediterranean 94
6.5. Evaluation on the 16th of February 2021 of L_{BUQ} 100
6.6. Evaluation on the 19th of February 2021 of L_{BUQ} 102
6.7. Evaluation L_{BUQ} on the Israel and Gaza coast for the close targets using the global and the Mediterranean data 103

7.1. Bathymetry of the Rafina area 113
7.2. Vertical discretization of the grid 115
7.3. Wind speed intensity at 10 meters in WRF domain 118
7.4. Sentinel 2 images in the Rafina Port 123
7.5. Sentinel 3A and B images in the Rafina Port area 124
7.6. Evaluation of M^b on the BS model for $\tau = 3$ days 127
7.7. Evaluation of M^b on several models for $\tau = 3$ days in November 133
7.8. Evaluation of M^b on several models for $\tau = 3$ days in December 134

List of Tables

6.1. Averages of L_{BUQ} 104

7.1. Parameters for the generic length scale turbulence closure model 110
7.2. Setup parameters of the ocean model 121
7.3. Base solution setup parameters 126
7.4. Parameters for defining categories and experiments 129
7.5. Results obtained for the sensitivity experiments 131
7.6. Averages results for the first and second periods 131

List of acronyms

ADCIRC	ADvanced CIRCulation model
ADCP	Acoustic Doppler Current Profiler
ADIOS2	The Adaptable Input/Output System version 2
AMOC	Atlantic Meridional Overturning Circulation
ARGO	Array of Profiling Floats Observing the Ocean in Real-Time
AVISO	Archiving, Validation, and Interpretation of Satellite Oceanographic data
BBL	Bottom Boundary Layer
BS	Base Solution
BLUQ	Backward Lagrangian Uncertainty Quantification
CIAMI	Comisión Permanente de Investigación de Accidentes e Incidentes Marítimos
CMEMS	Copernicus Marine Environmental Monitoring Service
CST	PdE Coastal model
DHT	Distinguished Hyperbolic Trajectory
ECMWF	European Centre for Medium-Range Weather Forecast
EMODNET	European Marine Observation and Data Network
EMSA	European Maritime Safety Agency
EO	Earth Observation
ECCO	Estimating the Circulation and Climate of the Ocean

EEZ	Exclusive Economic Zones
ERA5	fifth generation ECMWF atmospheric reanalysis of the global climate
ESA	European Space Agency
ESL	Extreme Sea Level
ETM+	Enhaced Thematic Mapper Plus
EU	European Union
DAC	Dynamic Atmospheric Correction
FNU	Formazin Nephelometric Units
FSLE	Finite-Size Lyapunov Exponents
FTLE	Finite-Time Lyapunov Exponents
GEBCO	General Bathymetric Chart of the Oceans
GFS	Global Forecast System
GNOME	General NOAA Operational Modeling Environment
GLS	Generic Length Scale
GODAE	Global Ocean Data Assimilation Experiment
GPT	Graphics Processing Tool
HF	High Frecuency
H2020	Horizon 2020
HYCOM	HYbrid Coordinate Ocean Model
IBI	Iberian Biscay Ireland model
ICON	Icosahedral Nonhydrostatic Weather and Climate Model
IHO	International Hydrographic Organization
IMPRESSIVE	Integrated Marine Pollution Risk assessment and Emergency management Support Service In ports and coastal enVironmEnts

IOC	Intergovernmental Oceanographic Commission
IW GRDH	Interformetric Wide Swatch Ground Range Detected
JRC	Joint Research Centre
LD	Lagrangian Descriptors
LCS	Lagrangian Coherent Structures
MCMC	Markov Chain Monte Carlo
MLE	Maximum Likelihood Estimation
MPI	Message Passing Interface
MOTHY	French operational oil spill drift forecast system
MSI	MultiSpectral Instrument
NARVAL	North Atlantic Regional VALidation
NCAR	National Center for Atmospheric Research
NE	Northeastern
NCOM	Navy Coastal Ocean Model
NEMO	Nucleus for European Modelling of the Ocean
NOAA	National Oceanic and Atmospheric Administration
NOPP	National Oceanographic Partnership Program
OBC	Open Boundary Condition
OLCI	Ocean and Land Colour Instrument
OLI	Operational Land Imager
OSCAR	Oil Spill Contingency and Response
OSIS	Oil Spill Information System
PDF	Probability Density Function
PdE	Puertos del Estado

PLOCAN	Plataforma Oceánica de Canarias
POLCOMS	Proudman Oceanographic Laboratory Coastal Ocean Modelling System
POM	Princeton Ocean Model
PRT	PdE Port model
ROMS	Regional Ocean Modeling System
RMSE	Root Mean Square Error
SAR	Synthetic Aperture Radar
SASEMAR	Sociedad de Salvamento y Seguridad Marítima
SAM2	Second Generation of MERCATOR Assimilation System
SAMOA	Sistema de Apoyo Meteorológico y Oceanográfico de la Autoridad Portuaria
SCHISM	Semi-implicit Cross-scale Hydroscience Integrated System Model
SELFE	Semi-implicit Eulerian-Lagrangian Finite-Element model
SLA	Sea Level Anomalies
SHYFEM	Shallow water HYdrodynamic Finite Element Model
SLIM	Second-generation Louvain-la-Neuve Ice-ocean Model
SNAP	Sentinel Application Platform
SST	Sea Surface Temperature
SSH	Sea Surface Height
UQ	Uncertainty Quantification
WPS	WRF Preprocessing System
WRF	Weather Research and Forecasting model

Chapter 1

Introduction

1.1. Motivation

The ocean, functioning as an intricate circulatory system of our planet, sustains a diverse array of marine life and plays a critical role in regulating Earth's climate. Ocean currents, apart from their involvement in global heat distribution, are complex systems that impact various physical and biological phenomena. Ocean transport, which includes turbulence and mixing processes, exerts influence over these phenomena. Turbulence, a key characteristic of ocean currents, emerges from the confluence of wind, tides, and varying water densities. It generates chaotic, swirling motions that lead to a mixing of water layers, effectively integrating cold, dense water from oceanic depths with lighter, warmer water from the surface strata. However, the same turbulent and mixing dynamics that support marine life pose considerable obstacles to mitigating marine pollution. Turbulence facilitates unpredictable dispersion of pollutants, rapidly extending their reach and making cleanup operations challenging. Small particles of plastics, oil spills, and chemical contaminants can be dispersed over vast distances, deeply infiltrating marine ecosystems, and proving difficult to track and remove. Therefore, understanding and accurately predicting the behavior of oceanic currents is crucial to safeguarding our marine ecosystems and addressing marine pollution effectively.

Although the discipline of oceanography is very old, modern oceanography initially emerged in the 1960s with the introduction of the first ocean climate models (Adcroft, 1995). Significant advances in technology and observation during the latter part of the 20th century greatly accelerated the progress of this field. The development of satellite Earth observation provided an unprecedented global perspective that complemented and far exceeded the scope of previous in situ measurements. Additionally, the significant increase in computational power has allowed the execution of advanced 3D simulations, providing new insights into the complex physical nature and behavior of the ocean. On the other hand, technological

advances have enabled the proliferation of on-site sensors, which in turn have increased the volume and coverage of on-site information. This data enables powerful synergy with satellite data through data assimilation (Copernicus Marine Service, 2023).

Only in recent decades operational oceanic models have achieved remarkable reliability that allows the scientific community to formulate novel methodologies to tackle pressing environmental issues such as oil spills (García-Garrido et al., 2016; García-Sánchez et al., 2022, 2021; Olascoaga and Haller, 2012), marine litter (Van Sebille et al., 2020), algae blooms (Olascoaga et al., 2008; Ramos et al., 2005), and to improve the efficiency of search and rescue operations (Serra et al., 2020).

Despite these advances, the nature of oceanic transport processes still presents significant challenges. Effectively addressing these issues requires a thorough understanding of these intricate processes, which is crucial for monitoring and mitigating environmental disasters and protecting natural marine resources. Hence, the objective of this thesis is to investigate and tackle various mathematical and computational aspects that are fundamental to understanding and representing transport phenomena in the ocean, as well as exploring their applications in real cases. By doing so, our goal is to significantly enhance our ability to predict and control these processes, opening the door to more informed environmental decision making and efficient management strategies.

1.2. State of the art

In order to understand transport in the ocean, it is crucial that the used ocean data velocity is accurate and representative. Indeed, this data plays a critical role in depicting the motion of fluid particles, including substances such as oil spills. In the following sections, we present an up-to-date summary of the latest progress in the topics and tools of interest for current work.

1.2.1. Ocean Modelling

Numerical methods are used in ocean modelling as tools to advance our understanding of both large-scale circulation and small-scale processes. Large-scale circulation is closely linked to processes on smaller scales. These processes must be resolved or precisely characterized if we want to draw an accurate image of the ocean. The scale of the geostrophic turbulence in the ocean is of the order of 30 to 100 km, which is very much smaller than the typical scale of 1000 km in the atmosphere. The limitations on the spatial resolution of numerical models imposed by computer technology are therefore more severe for marine

modelling than for meteorology (Adcroft, 1995). In the 1960s, the first attempts to simulate the global-scale ocean circulation were unable to capture the mesoscale features and had to be parametrized (Bryan, 1963). Despite the tremendous advances in computing power, with computers becoming faster and having more storage capacity, this is still the standard approach for regional and global models.

Traditional ocean models are typically based on finite differential schemes implemented on the Cartesian grid (Griffies et al., 2000). Recent advances have enabled the use of structured and unstructured mesh methods in ocean and coastal modelling, including discretization techniques for finite elements and finite volumes (Casulli and Walters, 2000; Danilov et al., 2004; Fringer et al., 2006; Walters, 2005). Examples of structured grid oceanic models include, Nucleus for European Modelling of the Ocean (NEMO), Navy Coastal Ocean Model (NCOM), Proudman Oceanographic Laboratory Coastal Ocean Modelling System (POLCOMS), HYbrid Coordinate Ocean Model (HYCOM), Princeton Ocean Model (POM), and Regional Ocean Modeling System (ROMS) that were originally designed for shelf seas and open regions (mesoscale) and later adapted to handle nearshore and coastal scales (Bolaños et al., 2011; Chassignet et al., 2007; Hedström, 1994a; Martin et al., 2009; O'Connor, 1991). On the other hand, for unstructured grid oceanic models, there are Shallow water HYdrodynamic Finite Element Model (SHYFEM), Semi-implicit Cross-scale Hydroscience Integrated System Model (SCHISM), Semi-implicit Eulerian-Lagrangian Finite-Element model (SELFE), Second-generation Louvain-la-Neuve Ice-ocean Model (SLIM), and ADvanced CIRCulation model (ADCIRC) (Consel, 1990; Delandmeter et al., 2018; Muhammad, 2015; Umgiesser et al., 2004; Westerink et al., 1994). These models are mainly employed in shallow-sea applications.

In recent decades, there have been significant advances in operational oceanic models, leading to improved reliability and applicability for addressing various environmental issues. A notable example is the Copernicus Marine Environmental Monitoring Service (CMEMS), which reached full operational status in May 2015 and offers a wide range of ocean data and models. As an initiative of the European Union, CMEMS focuses on providing information about the physical and biogeochemical characteristics of the ocean and sea ice. It collaborates with multiple data providers who develop ocean models and offer observations for both the global ocean and European seas. The data provided by CMEMS are classified into three categories: reanalysis, near-real-time, and forecasts. It offers over 200 ocean products, including Ocean Monitoring Indicators and expert insights. CMEMS aims to support decision makers, comply with EU policies, fulfill international legal commitments related to Ocean Governance, and address societal knowledge needs while promoting the Blue Economy (Fernandes-Salvador et al., 2021; García-Garrido et al., 2015; Le Traon et al., 2019; Pisano

et al., 2020). In addition to CMEMS, The US National Oceanographic Partnership Program (NOPP) from the USA facilitates partnerships between Federal agencies, academia, and industry to advance ocean science research and education, and provides ocean data through the portal hycom.org (Decker and Reed, 2009). Also, services such as Archiving, Validation, and Interpretation of Satellite Oceanographic data (AVISO) have proven to be valuable tools for obtaining ocean data (Liu et al., 2014). In particular, AVISO satellites measure sea surface height, allowing the analysis of geostrophic ocean currents and their variations over time. Complementing these, institutions like National Oceanic and Atmospheric Administration (NOAA) (Hu et al., 2022) and European Space Agency (ESA) (Malenovskỳ et al., 2012) have consistently launched different marine products using satellite observations.

The use of nested models has become more common in operational applications due to the availability of large-scale high-quality ocean models, which have improved our understanding of submesoscale processes and the precision of forecasts near coastlines and allowed port authorities to create tailored oceanographic consultation systems (Federico et al., 2017). Downscaling is a common practice in ocean modelling to transfer open-ocean dynamics into higher-resolution nested models via initial and boundary conditions (Kourafalou et al., 2015). Nested models rely on model software packages to solve hydrodynamic equations in various complex domains and bathymetry.

In Spain, Puertos del Estado (PdE), a public body dependent on the Ministry of Transport, Mobility and Urban Agenda, has developed downscaled high-resolution ocean models in domains of interest to our country, exemplified by their SAMOA project (‘Sistema de Apoyo Meteorológico y Oceanográfico de la Autoridad Portuaria’ or Meteorological and Oceanographic Support System of the Port Authority). This ongoing initiative aims to provide high-resolution operational met-ocean data for Decision Support Systems utilized by Spanish Harbor Authorities. The SAMOA project integrates observation, modeling, and end-user service tools, with a specific focus on designing and implementing a high-resolution ocean circulation forecast system capable of resolving coastal and local scales within ports. PdE has successfully developed a total of 20 high-resolution operational forecast systems for Spanish ports as part of the SAMOA initiative. Furthermore, there are plans to significantly expand SAMOA high-resolution operational forecast services. By 2021, a total of 22 Spanish ports were included in the SAMOA circulation forecast system (Sotillo et al., 2020a). Currently, the platform has expanded to include 33 ports. It is important to note that PdE is just one example of an organization that contributes to the development of very high-resolution ocean models. There exist other organizations that have made similar efforts in this field.

1.2.2. Oil Spill and Particle Drift Models

One of the substances transported by the ocean that is of significant interest for this thesis due to its environmental implications is oil. A first primitive approach to oil spill models consists of using a simplified linear superposition method to approximate the drift. In this strategy, the transport rate for a slick is represented as a vector sum of the transports induced by mean flow, tides, wind/waves, and turbulent dispersion. Mean flows and tidal currents are determined from observations or hydrodynamic models for the region of interest. The currents induced by winds and waves are generally combined and represented by an empirically-based drift factor and deflection angle that depend on the local wind speed and direction. In a typical application, the oil transport rate at a given location is calculated by vectorially adding the contributions of each component. Oil transport vectors are then numerically integrated in time to determine the new location of the spill (Stolzenbach et al., 1977).

Over the past 50 years, significant strides have been made in the development of oil spill models, evolving from this two-dimensional particle trajectory-type models to sophisticated three-dimensional models that incorporate transport and fate processes. These advanced models serve multiple objectives, including short-term tactical forecasting to assist in decision-making processes for containing, controlling, and cleaning up accidental spills, as well as long-term damage assessment. To achieve these goals, both probabilistic and deterministic models have been developed (Asce, 1996). Our study primarily focuses on deterministic models, which we outline next.

In general, oil spill models can be classified into two types: Eulerian and Lagrangian. The former utilizes mass and momentum conservation equations to describe the behaviour of the oil slick, while the latter represents the slick as a collection of discrete particles that are advected by wind, currents, and waves, and are transported through dispersion (Zodiatis et al., 2017). Eulerian models employ a convection-diffusion equation to describe the spreading of oil through diffusion and the advection of oil via wind and currents. However, researchers have shown that Lagrangian models are more appropriate for rapid simulations when oil spill accidents occur, and are easier, more efficient, and computationally less expensive than Eulerian approaches (Barker et al., 2020; Nagheeby and Kolahdoozan, 2010; Zafirakou, 2019). The accuracy of particle positions in Lagrangian models depends on the precision of the initial position, the reliability of the coupled met-ocean models used for forecasting, and the inclusion of suitable physical mechanisms that act on the tracked particles (Zodiatis et al., 2017).

Numerous software packages are available that are capable of tracking oil spills. Some examples of oil drift models include EUROSPILL, OILMAP, General NOAA Operational Mod-

eling Environment (GNOME), TRACMASS, French operational oil spill drift forecast system (MOTHY), Oil Spill Contingency and Response (OSCAR), The Adaptable Input/Output System version 2 (ADIOS2), Oil Spill Information System (OSIS), and Medslik-II. These models are designed to track individual fluid parcels and rely on a sufficient number of initial parcels to provide an accurate representation of the spill (Cheng et al., 2011; Dominicis et al., 2013; Xu et al., 2013).

The challenge faced by drifting models lies in the intricate and chaotic nature of fluid particle movement. Fluid parcels display complex paths, which can complicate the task of performing accurate analysis and predictions (Speetjens et al., 2004). To explore these aspects from an alternative standpoint, we will draw upon concepts from dynamical systems theory, which offers powerful tools for analyzing chaotic systems. Moreover, as it is necessary to effectively assess and compare the accuracy of different forecasts, we will also dive into methods for quantifying uncertainty.

1.2.3. Dynamical Systems

A tracer that moves passively with the ocean velocity field, without diffusion, follows the kinematic equation:

$$\frac{d\mathbf{x}}{dt} = \mathbf{v}(\mathbf{x},t), \mathbf{x} \in \mathbb{R}^n. \tag{1.1}$$

The equation in question is an ordinary differential equation, also known as a dynamical system, which states that the velocity of a fluid parcel at a particular point is equivalent to the velocity of the ocean current at that point. Following Hassen Aref seminal work on chaotic advection (Aref, 1984), dynamical systems theory provides the appropriate mathematical framework to describe the trajectories of fluid particles $x(t)$. This approach uses concepts from Poincare's work, originally developed in the context of celestial mechanics, searching for a geometrical partition of the phase space that supports a qualitative understanding of families of solutions of the dynamical system (1.1).

Applying these ideas to realistic geophysical flows poses challenges due to the finite-time nature and non-periodic characteristics of such flows. Poincaré's method still can be used to identify geometric flow structures that divide the ocean into distinct regions by finding distinguished material fluid structures, called Lagrangian Coherent Structures (LCS) that serve as transport barriers that fluid particles cannot cross. These structures mediate the transport and mixing processes between different flow regions. In this context, as explained by Mendoza and Mancho (2012), the approximation of LCS is achieved by computing ridges derived from fields, such as Finite-Size Lyapunov Exponents (FSLE) (Aurell et al., 1997) and Finite-Time Lyapunov Exponents (FTLE) (Nese, 1989). Studies have shown that, under

certain conditions, the FTLE ridges exhibit minimal flux (Shadden et al., 2005). Despite the progress made with these techniques, artifacts can arise in FTLE calculations (Branicki and Wiggins, 2010) due to unfulfilled assumptions. Additional approaches within the geometric framework have been explored, such as complexity measures of isolated trajectories (Rypina et al., 2011) and probabilistic descriptions (Froyland and Padberg-Gehle, 2014).

A different perspective within the geometrical approach, distinct from Lyapunov exponents, is offered by Distinguished Hyperbolic Trajectory (DHT). DHTs represent a revised concept of hyperbolic fixed points specifically designed for dynamical systems with general time dependence (Ide et al., 2002; Jiménez-Madrid and Mancho, 2009; Ju et al., 2003). Similarly to stationary points in autonomous systems, the detection of DHTs in a general time-dependent dynamical system is significant due to their ability to govern the long-term behavior of nearby trajectories. The stable and unstable manifolds of DHTs are composed of sets of trajectories that asymptotically approach the DHT in plus and minus infinite time, respectively (Mancho et al., 2006b). They act as barriers to transport that particles cannot cross. Insights into the computation of these invariant manifolds as material surfaces are available in studies such as (M. et al., 2004; Mancho et al., 2003).

A recent tool called M function has emerged among various Lagrangian techniques applied to geophysical systems. Initially introduced in a study by Jiménez-Madrid and Mancho (2009), the M function was used primarily to redefine DHT. Subsequently, it underwent further development in subsequent research by Mendoza et al. (2014); Mendoza and Mancho (2010), as well as by Mancho et al. (2013). This function serves as the foundation for a method known as Lagrangian Descriptors (LD) and has shown successful applications in describing transport processes within the atmosphere (as exemplified in studies by De la Cámara et al. (2013)), in the ocean (as shown by García-Garrido et al. (2015); García-Sánchez et al. (2022, 2021)), in chemistry (Agaoglou et al., 2019, 2020; Craven and Hernandez, 2016; Junginger et al., 2016; Katsanikas et al., 2022; Revuelta et al., 2019), cardiovascular flow (Darwish et al., 2021) and astrodynamics (Daquin et al., 2022). More recently, two articles by Lopesino et al. (2015, 2017) have proposed new versions of the Lagrangian descriptors method, specifically tailored for discrete time and continuous time dynamical systems, respectively. These updated approaches are accompanied by formal proofs that simplify the calculations required to obtain the explicit expression of the Lagrangian descriptor function. Importantly, they preserve the same key features displayed by the original method based on the M function. This thesis utilizes this method, which will be discussed in Chapter 2.

1.2.4. Uncertainty Quantification

Uncertainty Quantification (UQ) is a field dedicated to quantifying uncertainties in computational models applied to real-world scenarios. These uncertainties can stem from various sources, including noisy or incomplete data, numerical model errors, or gaps in our understanding of physical processes. Uncertainty is a highly relevant topic in geophysics, particularly in the context of equations governing fluid motion in the ocean and atmosphere. Ocean models typically solve the Navier-Stokes equations employing approximations such as hydrostatic and Boussinesq assumptions. Additionally, they utilize the Reynolds-averaged approach to address unresolved turbulent scales. However, due to the intrinsic constraints of these approximations, models that are imprecise or insufficient can lead to the introduction of structural uncertainty. Even if the underlying equations were perfectly accurate, the models incorporate parameters such as viscosity or diffusivity that are not precisely known, resulting in parameter uncertainty. Moreover, the boundary conditions applied to the input variables introduce parametric variability. For example, surface atmospheric winds impose forcings on ocean velocities, but these atmospheric forcings are subject to uncertainty in their precise estimation. Furthermore, the numerical solution of these models relies on discretization methods and numerical approximations, which introduce numerical errors and give rise to algorithmic uncertainty. Consequently, predicted ocean currents inherently contain uncertainties. This thesis specifically focuses on the uncertainty that arises from deterministic models, where uncertainties arise from unknown aspects of the model rather than from stochastic or noisy processes. For a comprehensive comparison between these two types of uncertainty, (Frenklach et al., 2016) provides valuable information.

A way to tackle uncertainty in deterministic models is to perform sensitivity analyzes, also known as *forward time propagation of uncertainty*. This approach examines how uncertainties in the input parameters of the model, usually expressed as partial differential equations, can lead to uncertainties in the model outputs. In cases where experimental data is available, it becomes possible to determine the parameter set that best aligns with the model output. This scenario can be precisely formulated as a Bayesian inverse problem, wherein the parameters most likely to have generated the observed data are inferred based on an assumed noise model. Bayesian analyses serve as a common framework for numerous applications in *backward time uncertainty quantification*, as highlighted in (Domitr et al., 2023; Wu et al., 2018). These methods leverage Bayesian inference theory and explore the posterior Probability Density Function (PDF) through Markov Chain Monte Carlo (MCMC) sampling. Additionally, statistical methods centered on Maximum Likelihood Estimation (MLE), as discussed by De Crècy (1996), and data assimilation methods, which combine experimental

observations with code predictions and associated errors, contribute to improved estimation of the state of the system and its associated uncertainty (Petruzzi, 2019).

Our focus lies on evaluating the reliability and assessing uncertainty of ocean currents data sets and their resulting transport. For more detailed information, refer to Chapters 4 and 6.

1.3. Objectives

The primary objective of this study is to develop and deploy mathematical tools specifically designed for environmental monitoring. According to the current state of the art described, the achievement of this objective involves pursuing the following specific goals:

- Analyzing the transport produced by CMEMS and high-resolution models like SAMOA, developed by PdE, to validate observations of marine pollution, such as oil spills. This analysis will involve the use of remote sensing techniques and dynamical system tools.
- Advancing the evaluation of ocean models by developing a quantifier of uncertainty. The focus will be on quantifying the uncertainty with respect to the transport produced by trajectories that are solutions of models generated from data sets.
- Enhancing the construction of appropriate high-resolution ocean models that accurately describe the transport process. This will involve using tools such as the Regional Ocean Modeling System (ROMS) and the Weather Research and Forecasting model (WRF) in the Rafina port area in Greece. The resulting model will be validated using remote sensing techniques and dynamical system tools. This approach explores the development of accurate models that can be validated in a cost-effective manner, without relying heavily on in situ measurements.

1.4. Thesis organization

In order to achieve the goals of this thesis it has been organized as follows. Chapter 2 provides an overview of the common methodology employed throughout the thesis. Chapter 3 explores the combined application of remote sensing images, very high-resolution models, and dynamical system tools, analyzing the evolution of a fuel oil spill at coastal scale. Specifically, it investigates the case of the 'Volcán de Tamasite' accident in Port of La Luz, Canary Islands, Spain in April 2017. Motivated by the need to evaluate the performance of different data sources in this event in Chapter 4, a novel method is presented to quantify

uncertainty in relation to the transport produced by the ocean model trajectories. Specifically, it focuses on forward-in-time uncertainty quantification, that is, when an event occurs, and it is required to evaluate uncertainty in the event's forward time evolution. Chapter 5 further explores the combined application of the same tools used in Chapter 3, but the analysis is focused on the event that occurred in the Eastern Mediterranean in February 2021, which in contrast to that of Chapter 3, involved very large scales and was of unknown source. Again, motivated by the need of evaluating the available model products, Chapter 6, presents a novel approach to uncertainty quantification called Backward Lagrangian Uncertainty Quantification (BLUQ), which is appropriate for the setting in which the origin of the contamination is unknown. This approach builds upon the ideas introduced in Chapter 4, but is specifically tailored for analyzing uncertainty in backward trajectories and the method is implemented to investigate the event discussed in Chapter 5. Finally, Chapter 7 outlines a methodology for evaluating and fine-tuning very high-resolution models using remote sensing images. The methodology is implemented in the Rafina Port in Greece, which was the one where a remote pilot was implemented within the framework of the European Union funded Innovation Action IMPRESSIVE project. The last chapter of this work, Chapter 8, presents the conclusions and potential avenues for further research.

Chapter 2

Methodology

This chapter provides a concise overview of the methodology employed in this thesis to investigate oceanic transport processes. In the forthcoming sections, we will delve into the specific details concerning the tools and techniques that have been utilized in the fields of ocean modelling and dynamical systems.

2.1. Ocean Modelling

The analysis we implement for selected environmental problems requires reliable ocean current data, which are increasingly available. For the applications reported in Chapters 3, 4, 5, and 6, we use the data supplied by the Copernicus Marine Environment Monitoring Service (CMEMS). CMEMS provides regular and systematic information about the physical state and dynamics of the ocean in regions of interest for this work. Additional oceanic services used in this thesis are high-resolution models from the SAMOA project developed by Puertos del Estado (PdE), in particular the one of the La Luz Port and the Gran Canaria region, which are used in Chapters 3, 4.

Many coastal applications require high-resolution data that are not available or produced by any institution. In this case, the data needs to be generated. The availability of products such as CMEMS can support the nesting and downscaling procedure towards high-resolution services. To implement this kind of output in Chapter 7, we use the ROMS software model. ROMS employs free-surface, terrain-following, primitive equations and has been extensively utilized by the scientific community for various applications. Some examples are (Budgell, 2005; Di Lorenzo et al., 2008a; Haidvogel et al., 2000; Marchesiello et al., 2001; Peliz et al., 2003; Warner et al., 2005; Wilkin et al., 2005). This study has employed the Regional Oceanic Model System (ROMS) version 3.7 to construct a high-resolution hydrodynamic model for the port of Rafina in Greece. Data from the Copernicus Marine

Environment Monitoring Service (CMEMS) and the European Centre for Medium-Range Weather Forecasts (ECMWF) were used to nest the model. ROMS, a FORTRAN-based framework, is used to simulate the dynamic evolution of marine currents in coastal areas. The C preprocessor was invoked during the compilation of ROMS to curate pertinent FORTRAN instructions for application-specific relevance. The preprocessor provides a range of toggles that can be enabled or disabled. The details of the adopted model are discussed in Chapter 7 and (Shchepetkin and McWilliams, 2003, 2005). ROMS has a great advantage in its modularity and its powerful parallelization strategy with Message Passing Interface (MPI). This allows the development of applications that have a very competitive computing time (Wang et al., 2005). After ROMS compilation, facilitated by the preprocessor directives, the code requires input parameters and datasets tailored to the Rafina coastal domain, such as bathymetry, lateral, and atmospheric forcings, among others. Chapter 7 examines how these parameters affect the solution.

In order to accurately simulate oceanic dynamics, it is fundamental to consider the influence of atmospheric forcings on the ocean. The interaction between air and water generates momentum transfer, leading to surface drift currents. In this thesis, we focus on wind stress as the principal forcing mechanism. Several atmospheric models are currently available, notably the Global Forecast System (GFS) (National Centers for Environmental Information, 2023), ICON (Max Planck Institute for Meteorology, 2023), and ERA5 (Copernicus Climate Change Service, 2023). For the purposes of our research, we have opted for the ERA5 model. However, its resolution of $0.25^\circ \times 0.25^\circ$, approximately equivalent to 30km $\times$ 30km, falls short of the demands of high-resolution oceanic modeling. To address this, we employed the Weather Research and Forecasting (WRF) model, downscaling the ERA5 data to achieve a resolution closer to 1km $\times$ 1km.

Computationally, the calculation times required to run wind computations using the Intel Xeon Gold 5218 CPU 2.30GHz up to 3.90 GHz (16 cores, 22 Mb L3 cache) [32 cores] with hyperthreading, utilizing a total of 64 cores, the computational time was $\sim$ 30 hours for a simulation span of 90 days. Additionally, for the execution of the ROMS model coupled with the wind forcing from the WRF model on the Intel Xeon Gold 5218 CPU 2.30GHz up to 3.90 GHz (16 cores, 22 Mb L3 cache) [32 cores], utilizing a total of 32 cores, the computational time was $\sim$ 7 hours for a 90-day simulation.

2.2. Dynamical Systems

The equation given in (1.1), as explained earlier, is a useful tool for studying how things move in geophysical flows. In this equation, n represents the number of directions in which

movement is happening, and for geophysical flows like in the ocean or atmosphere, n is usually 2 or 3. Typically such systems of ordinary differential equations can be autonomous or non-autonomous. An **autonomous system** is a system of ordinary differential equations of the form

$$\frac{d\mathbf{x}}{dt} = \mathbf{v}(\mathbf{x}),\ \mathbf{x} \in \mathbb{R}^n, \tag{2.1}$$

where the velocity field does not depend on time t, the independent variable. On the other hand, a **non-autonomous system** is defined as:

$$\frac{d\mathbf{x}}{dt} = \mathbf{v}(\mathbf{x},t),\ \mathbf{x} \in \mathbb{R}^n, \tag{2.2}$$

in which the velocity field, does depends on t. In our field, autonomous systems are found in the case of stationary flows.

For stationary flows, the concept of fixed point is essential for a geometrical description of the solutions. Fixed points (or stagnation points) are those that satisfy $\mathbf{v}(\mathbf{x}) = 0$. The fixed point of a stationary field is a trivial example of a fluid particle trajectory, i.e., it is a 'solution' (in this case a fixed point solution) of the equations for fluid particle motions defined by the velocity field. Fixed points might be classified as hyperbolic or non-hyperbolic, depending on their stability properties. Hyperbolic fixed points have stable and unstable manifolds that comprise, respectively, the trajectories that approach the fixed points as time tends to plus or minus infinity. With respect to the invariant manifolds, as they are formed of trajectories, they act as barriers to transport that particles cannot cross without violating the uniqueness of the solution. They are crucial since they allow qualitative predictions for the evolution of sets of initial conditions avoiding explicit integration on the whole domain. Hyperbolic fixed points and their stable and unstable manifolds are the basic notions used for the geometrical description of flows in autonomous dynamical systems. The concept of the stagnation point is extended to time-periodic flows by means of the Poincaré map, as periodic orbits with period T become fixed points of the Poincaré map. For hyperbolic periodic orbits, there also exist stable and unstable manifolds, which are geometric objects that organize the global dynamics. Again they are, respectively, the sets of orbits asymptotically approaching the periodic orbit as time tends to plus or minus infinity (Wiggins, 1992, 2003).

Realistic flows, such as those found in oceanography, are non-stationary and aperiodic, and in this context the Distinguished Hyperbolic Trajectory (DHT) (Ide et al., 2002; Jiménez-Madrid and Mancho, 2009; Ju et al., 2003) extends the saddle-type fixed points seen in steady flows to the time dependent case and therefore is that of a 'moving saddle point'. Hyperbolic trajectories, similar to those found in steady flows, possess stable and unstable manifolds that act as barriers to transport, dividing the flow into distinct regions with different types of

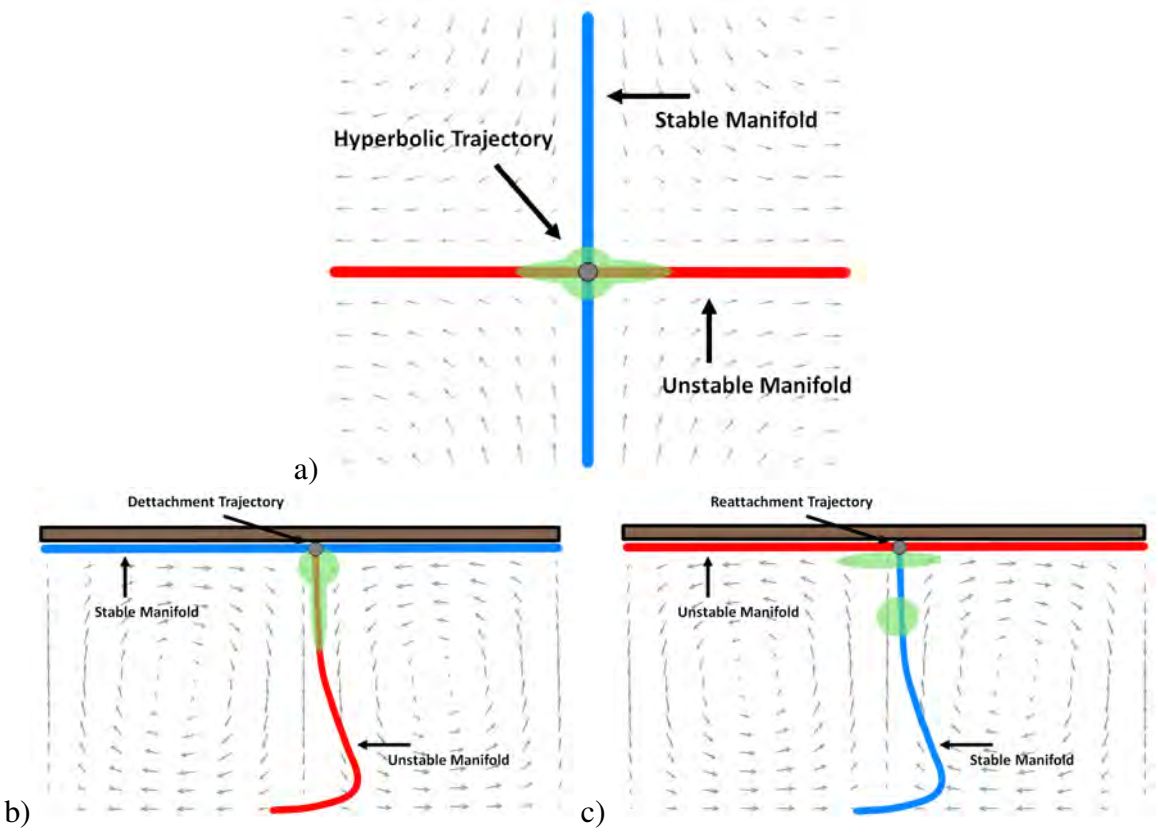
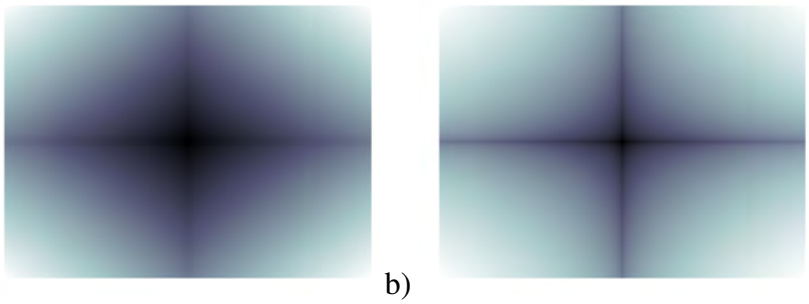


Figure 2.1 a) Unstable and stable manifolds of an hyperbolic trajectory in the interior of a flow, highlighted in red and blue, respectively. The light green blob demonstrates the material expansion and contraction along the unstable and stable directions; b) sketch of a hyperbolic trajectory and their stable and unstable manifolds in a detachment or separation configuration. Green blobs indicate the material evolution of fluid parcels in their neighbourhood; c) sketch of a hyperbolic trajectory and their stable and unstable manifolds in a reattachment configuration.

trajectories (Mancho et al., 2006b). Hyperbolic trajectories are characterized because in their neighborhood, the transported material in the purely advective approach, experiences high contraction and expansion rates. The directions of contraction and expansion are related, respectively, to the stable and unstable manifolds. Figure 2.1 a) illustrates a trajectory in the interior of a 2D flow and a time sequence showing the evolution of advected fluid parcels (green blob) placed at its neighbourhood. It may happen that hyperbolic trajectories are not in the interior of a flow, but attached at the boundaries. Dettachment are reattachment trajectories are special cases of this. In a detachment or separation configuration, matter near this hyperbolic trajectory at the coast is propelled into the ocean along the unstable manifold. On the other hand, the stable manifold of the reattachment trajectories pushes matter towards the coast, and then the unstable manifold of this trajectory, which is aligned with the boundary, controls the dispersion in this direction. Both trajectories are illustrated respectively in Figure 2.1 b) and c). In particular, the effect on an oil slick of a detachment trajectory present in the surface current is analysed in Chapter 3.



a) b)

Figure 2.2 a) M function for $\tau = 2$; b) M function for $\tau = 10$. When τ increases, the singular features becomes more visible.

Among the Lagrangian techniques suitable for uncovering phase space configurations of time-dependent dynamical systems, in this thesis we will use the Lagrangian Descriptors (LD) method based on the M function (Jiménez-Madrid and Mancho, 2009; Mendoza and Mancho, 2010) defined as follows:

$$M(\mathbf{x}_0, t_0, \tau) = \int_{t_0-\tau}^{t_0+\tau} \|\mathbf{v}(\mathbf{x}(t_0;\mathbf{x}_0), t)\| \, dt, \tag{2.3}$$

where $\|\cdot\|$ stands for the modulus of the velocity vector. At a given time t_0, $M(\mathbf{x}_0, t_0)$ function measures the arc length traced by the trajectory starting at $\mathbf{x}_0 = \mathbf{x}(t_0)$ as it evolves forward and backward in time for a time period τ. Forward integration provides information about the stable manifolds (repelling LCSs), while backward integration highlights the structure of unstable manifolds (attracting LCSs). Figure 2.2 b) illustrates the ability of the M function

to highlight, by means of 'singular features', the invariant stable and unstable manifolds represented in Figure 2.1. Lopesino et al. (2015, 2017) provide a precise definition of what is meant by 'singular feature'. It is related to the lack of regularity of the M function in a direction transversal to the invariant manifold. These articles also provide formal proofs in selected examples for the statement: invariant manifolds are aligned with singular features of this function. It is important to note that these singular features are visible for a sufficiently long integration period. Indeed, if this τ is too short, the pattern of M is smooth (see Figure 2.1 a)).

In the context of geophysical flows, there is sometimes interest in studying systems like Equation (2.2) under coordinate transformations. The behavior of the M function concerning Galilean transformations is discussed in (Lopesino et al., 2017; Mendoza and Mancho, 2012). These references provide details on the properties that are important to preserve under these transformations in order to reveal the phase space geometry.

Chapter 3

Volcán de Tamasite Oil Spill Accident

This chapter is based on the results described in the paper by García-Sánchez et al. (2021), which is the result of a collaborative effort in the framework of the European Union (EU) funded Innovation Action IMPRESSIVE. This project was focused on developing a universal-relocatable platform for real-time management of marine pollution events in the wider area of EU harbors and their vicinities, easy to manipulate and use from the harbor control post. For completeness and given the interdisciplinary character of the involved problems, this chapter includes the contribution made by different research groups. Also, for the sake of completeness and consistency, we will recall the methodology described in Chapter 2, to better explain its implementation in the specific problem.

On Friday 21 April 2017, the passenger ferry 'Volcán de Tamasite' collided with the 'Nelson Mandela' dike of the Port of La Luz (Las Palmas de Gran Canaria) at 7:00 p.m. As a consequence of the impact, two of the outermost fuel supply pipes along the dike were broken and diesel fuel poured into the sea. The national pollution alert was declared at 7:30 p.m. and the company responsible for the pipelines started working on emptying the damaged pipes. These works ended on April 24, 2017. Approximately 65 m^3 of diesel fuel was estimated to have been spilled along the Northeastern (NE) sector of Gran Canaria Island. The rate of evaporation/dispersion ranged from 80% by day. On April 23 at 7:00 a.m., satellite images reported the two major spill spots targeted near the coast. Both spots, of 0.9 km^2 and 2.4 km^2, respectively, were dispersed at ground level in the NE sector of the island, 12 km south of the port of La Luz, by the Maritime Security Service (SASEMAR) fleet. Continually, on this day, local newspapers reported a 13 km long fuel filament placed 1 km away, to the east of Gran Canaria (EFE, 2017). The national pollution alert ended on April 25, although monitoring and surveillance along the eastern sector of the island continued until May 5. On these days, some scarce and dispersed pollutant spots were reported and tracked by aerial and marine surveys some miles away from the coast until that date, when the event was officially declared

'finished' (Ciaim, 2018). Figure 3.1 shows the crash point of the ferry (in red) together with some specific coastal areas, where the arrival of pollution could have a very negative impact (in magenta, green, and blue). These vulnerable areas are: Las Canteras, a beach in the city of Las Palmas, along with a desalinization plant, a fish farm, and a thermoelectric plant, all on the eastern coast of the island.

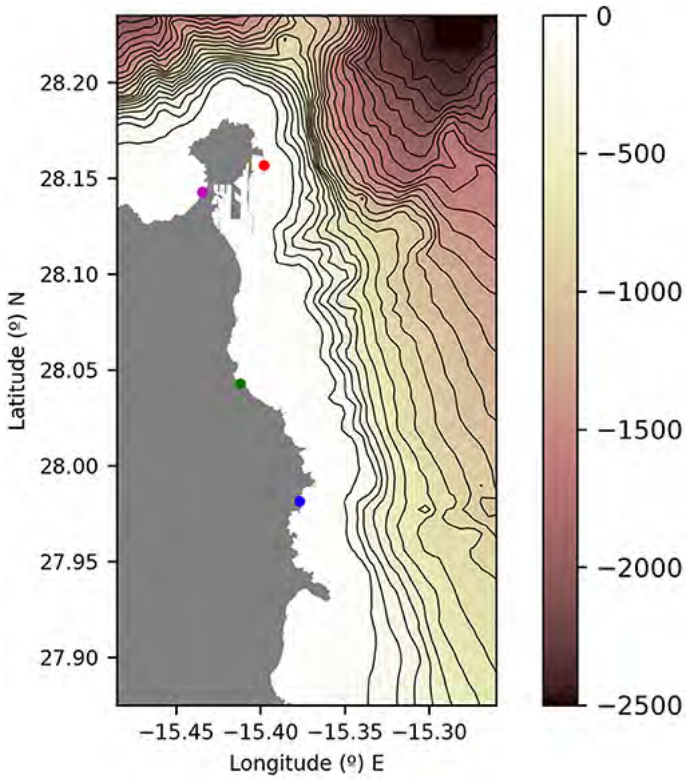


Figure 3.1 A map of the N-NE Gran Canaria Coast, displaying the ferry crash point (red) together with some highly vulnerable regions. These areas are: Las Canteras beach in the city of Las Palmas (magenta), a desalinisation/hydroelectric power plant (green) and the Port of Taliarte (fishing and aquaculture facilities) (blue). Contourlines represent the bathymetry in meters.

Pollutant transport monitoring in coastal areas is essential because of the many critical activities that occur in them. Recently, it has been reported that ocean current analysis, which is operated by ocean forecasting services (Dominicis et al., 2016), combined with the use of remote sensing techniques (Cheng et al., 2011; Martinho et al., 2013; Xu et al., 2013) and dynamical systems tools (García-Garrido et al., 2016; Olascoaga and Haller, 2012) is capable of providing important feedback to emergency services. Currently, synergies between these capabilities for coastal applications are flourishing due to the fact that remote sensing and modeling capabilities are reaching very resolved metric scales, thus providing the bedrock for future smart coasts.

Remote sensing capabilities allow for direct observation of extended areas. The limitations of these capabilities are due to the satellite swath, revisit time, atmospheric conditions and cloud coverage for optical sensors. Optical images from Sentinel-2 and Landsat 7 and 8 were available during the reported event and were analyzed by co-authors from the University of Las Palmas de Gran Canaria, as described below. These specific image products have been useful in the past for oil spill monitoring (García-Garrido et al., 2016; Pisano et al., 2015), and we explore their potential in this chapter. Furthermore, Synthetic Aperture Radar (SAR) images have been demonstrated to be a very adequate tool for remote detection of oil spills (Cheng et al., 2011; Pisano et al., 2015; Xu et al., 2013), especially due to their high spatial resolution and all-weather and all-day capabilities. During this case study, SAR images from Sentinel 1A and 1B were available. The spatial resolution of Sentinel 1 and 2 is very high (up to 10 m), while that of Landsat 7 and 8 is lower (up to 30 m).

Ocean model products also provide direct information on extensive areas. To perform this study, we have used two modelled data sources for ocean currents in the area of interest: (1) The regional forecast product for the Iberian Biscay Ireland model (IBI) area, operationally delivered by the CMEMS Service and (2) a very high-resolution coastal model system, specifically developed by Puertos del Estado (PdE) for the Port of La Luz. The IBI product shows a kilometric resolution (derived from the $1/36^{\circ}$ NEMO model application), too coarse for the coastal event under study. Nevertheless, we have applied the PdE ROMS model application that downscales the regional IBI solution for the Gran Canaria area by means of 2 nested grids (a coastal one, with $\sim$ 350 m horizontal resolution, which we refer to as the CST model, and a very high-resolution local domain, specifically focused on the Puerto de la Luz area with $\sim$ 40 m resolution, which we refer to as the PRT model). Transport processes associated with these currents are subject to uncertainties, such as those inherent in the modelled velocity fields, as they depend on assumptions taken in the modelling processes. Each result on the velocity fields produced by different model hypotheses may characterize pollutant dispersion differently, and thus we address the issue on how to compare outputs. This analysis goes beyond the tracking of individual pollutant trajectories by exploiting ideas from dynamical systems theory that involve the determination of geometrical structures in the ocean surface which define regions where fluid particle trajectories have qualitatively distinct dynamical behavior (Balibrea-Iniesta et al., 2019; García-Garrido et al., 2015, 2016; Mancho et al., 2006a; Wiggins, 2005). These geometrical structures provide a signature for a specific velocity field, highlighting the essential transport features associated to it.

This chapter is organized as follows. Section 3.1 describes the data sources used in this work: satellite data, ocean models, and the transport problem. Section 3.2 presents the results, a discussion on how the dynamical systems approach supports the interpretation of transport,

and a discussion on uncertainty quantification. Finally, Section 3.3 reports the conclusions of this work.

3.1. Data and Methodology

3.1.1. Satellite imagery and remote sensing

The following high-resolution satellite image data sources, corresponding to the dates for which the 'Volcán de Tamasite' ferry crash event took place, were downloaded (at no cost) and adequately processed:

- SAR data from Sentinel 1 (A,B), Level-1 Interformetric Wide Swatch Ground Range Detected (IW GRDH) with high-resolution were obtained from the Sentinel Data Hub (https://scihub.copernicus.eu/).
- Sentinel 2A MultiSpectral Instrument (MSI) Level 1C data was also downloaded from the Sentinel Data Hub.
- Landsat 7 Enhaced Thematic Mapper Plus (ETM+) and Landsat 8 Operational Land Imager (OLI) level 1C data was downloaded from the U.S. Geological Survey (https://earthexplorer.usgs.gov/).

The images were processed using the following tools. Sentinel 1 data was processed using SNAP
(https://step.esa.int/main/toolboxes/snap/) SAR tools. Sentinel 2 MSI, Landsat 7 ETM+ and Landsat 8 OLI were processed using the Acolite toolbox (Vanhellemont, 2019). The chronological sequence of satellite images available during the event is provided in the following list:

- 04/21/2017: Sentinel 1B, 7:04 p.m., a few minutes prior to the accident.
- 04/23/2017: Sentinel S1A 07:00 a.m., in situ confirmed spill patterns were weakly visible.
- 04/26/2017: Landsat 8 11:30 a.m., cloudless, no spill patterns identified.
- 04/27/2017: Sentinel 1A 7:00 p.m., no spill patterns identified.
- 04/29/2017: Sentinel 1B 07:00 a.m., no spill patterns identified.
- 05/01/2017: Sentinel 2A 11:50 a.m., cloudy.

- 05/03/2017: Sentinel 1B 7:00 p.m., no spill patterns identified.
- 05/04/2017: Landsat 7 11:30 a.m., no spill patterns identified.

With the purpose of identifying water discoloration due to the spill, the inspection of optical images was performed both through RGB composites and remote sensing reflectance spectra. However, this analysis did not provide insights for the event, and we do not report further about them. SAR images were also examined. Due to the spreading tasks done by the emergency services and the characteristics of the targeted oil spill, an intense signal was not expected. However, weak patterns (lately confirmed through in-situ observations) were identified on one Sentinel 1A image obtained on Sunday 23rd of April 2017 at 07:00 a.m. At that time, the Spanish coastguard fleet (SASEMAR) had already begun the daily operations (06:00 a.m.). Figure 3.2 displays this SAR Sentinel-1A image. Panels a), b) and c) show "low-roughness" spots around NE Gran Canarian waters, indicating potential positions for the diesel oil spill drift, after the ferry crash. The two "low-roughness" spots appearing in the image (marked with red circles in panels a), b), c) of Figure 3.2) were on ground confirmed spills (and dispersed) by three SASEMAR ships and one helicopter. Indeed, at the time of the Sentinel 1A passing over, two ships confirmed the spill spot at the North, in the vicinity of the Port. The spill spot located 12 km south from the Port, in the neighbourhood of the Marine Eolic Platform facility (www.plocan.eu) and 1 km far away from land, drifting southwards, was confirmed by a third ship and one helicopter (Ciaim, 2018).

3.1.2. Ocean Models

The ocean currents in the area of interest are supplied by two sources. One is the Copernicus Marine Service model for the Iberian-Biscay-Irish region (CMEMS IBI-PHY, IBI hereafter) available from http://marine.copernicus.eu/. The currents obtained from this product in the area of the accident are displayed in Figure 3.5a), where the accident location is marked with a red dot. IBI outputs have too coarse resolutions for the scale of the event we want to describe. For this reason, we used specific high-resolution modelled currents for the Port of La Luz, downscaling the IBI regional solution through two offline nested domains, with resolutions of 350 m in the intermediate coastal domain (the CST model) and 40 m in the local domain that covers the port waters (the PRT model). Details about the model product configurations and their quality are given next:

- **CMEMS IBI-PHY:** The CMEMS IBI provides operational regional short-term (5-days) hydrodynamic forecasts of a range of physical parameters (currents, temperature,

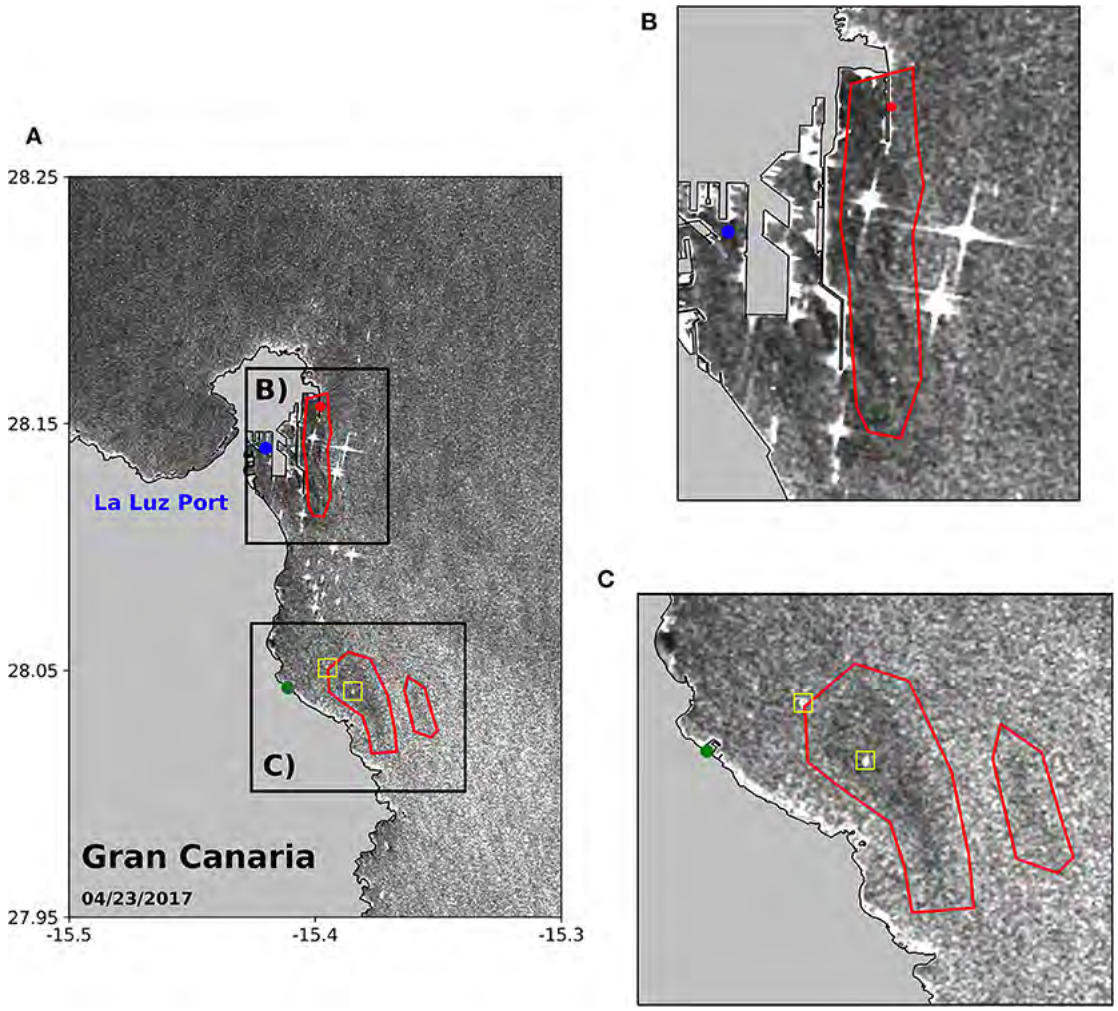


Figure 3.2 (a) SAR Sentinel-1A image obtained on Sunday 23rd of April 2017 at 07:00 a.m.. The image shows two areas with "low-roughness" spots that were ground confirmed spills by three ships and one helicopter of the Spanish Coastguard fleet (SASEMAR), who started to work on the affected areas on that day at 06:00 a.m.; (b) The Northern spilling area (red area) was dispersed in the neighborhood of the Port by two ships. The broken fuel lines were finally closed at 20:30 p.m., several hours after the Sentinel-1B passing over that region (07:00 a.m.); (c) The Southern spilled area reported by the SAR Sentinel-1B was located 12 km south from the Port, in the Marine Eolic Facility (www.plocan.eu) waters. This spill was validated by SASEMAR and coastguard helicopter flights (also reported in the SAR image). Both spots drifted southwards 1 km away from the coast, until the pollution alert ended on the 25th of April at 8:30 a.m.. SASEMAR's Airplane, however, continued surveying the whole Eastern coastline of the island until the 8th of May 2017 (Ciaim, 2018).

salinity, and sea level) since 2011 (Sotillo et al., 2015). IBI is based on an eddy-resolving NEMO model application (v3.6) that includes high-frequency processes required to characterize regional-scale marine processes. The model application runs at a $1/36° \sim 2.5\,\text{km}$ horizontal resolution and final products are routinely delivered in a service domain extending between 26–56°N and 19°W–5°E, see Figure 3.3. The NEMO model (Madec and the NEMO team, 2008) solves the three-dimensional finite-difference primitive equations in spherical coordinates discretized on an Arakawa C-grid and 50 geopotential vertical levels (z coordinate), assuming hydrostatic equilibrium and the Boussinesq approximation. Partial bottom cell representation of the bathymetry (a composite of ETOPO2 and GEBCO8) allows an accurate representation of the steep slopes characteristic of the IBI area. The IBI system is forced with up-to-date high-frequency $1/8° \sim 12.5\,\text{km}$ hourly meteorological forecasts provided by the ECMWF (European Centre for Medium-Range Weather Forecasts). Variables, such as 10 m wind, surface pressure, 2 m temperature, relative humidity, precipitation, shortwave and longwave radiative fluxes are used as forcing, being a CORE empirical bulk formulae (Large and Yeager, 2004) used to compute surface (latent and sensible) heat and freshwater (evaporation-precipitation) fluxes and surface stress.

The IBI regional system is nested into the CMEMS Global solution, using as open boundary conditions daily outputs from this CMEMS global eddy resolving system. Tidal solution is also added at the boundaries (at that time, IBI system was using 11 tidal harmonics). An atmospheric pressure component is also included assuming pure isostatic response at open boundaries (inverse barometer approximation). The CMEMS IBI system uses a SAM2-based data assimilation scheme to enhance its predictive skills by constraining the model in a multivariate way with a wealth of observations: Altimeter data (i.e, along-track sea level anomalies), in-situ temperature and salinity vertical profiles and satellite-derived sea surface temperature are regularly assimilated to estimate periodically initial conditions. Further details on the data assimilation scheme and on the analysis generated can be seen in the CMEMS IBI Product User Manual report (Amo et al., 2020), available at CMEMS, where more details of the operational suite can be found.

We used the data set IBI_ANALYSIS_FORECAST_PHYS_005_001 with horizontal resolution of $1/36° \sim 2.5\,\text{km}$ on a regular latitude/longitude equirectangular projection of the Northwest African waters domain. Daily 3D fields are available over 50 geopotential vertical levels, but in this chapter, the hourly fields provided for the upper layer are used (Aznar et al., 2016). The IBI ocean model forecasts are continuously monitored, using to this aim the NARVAL multi-parameter multi-platform validation

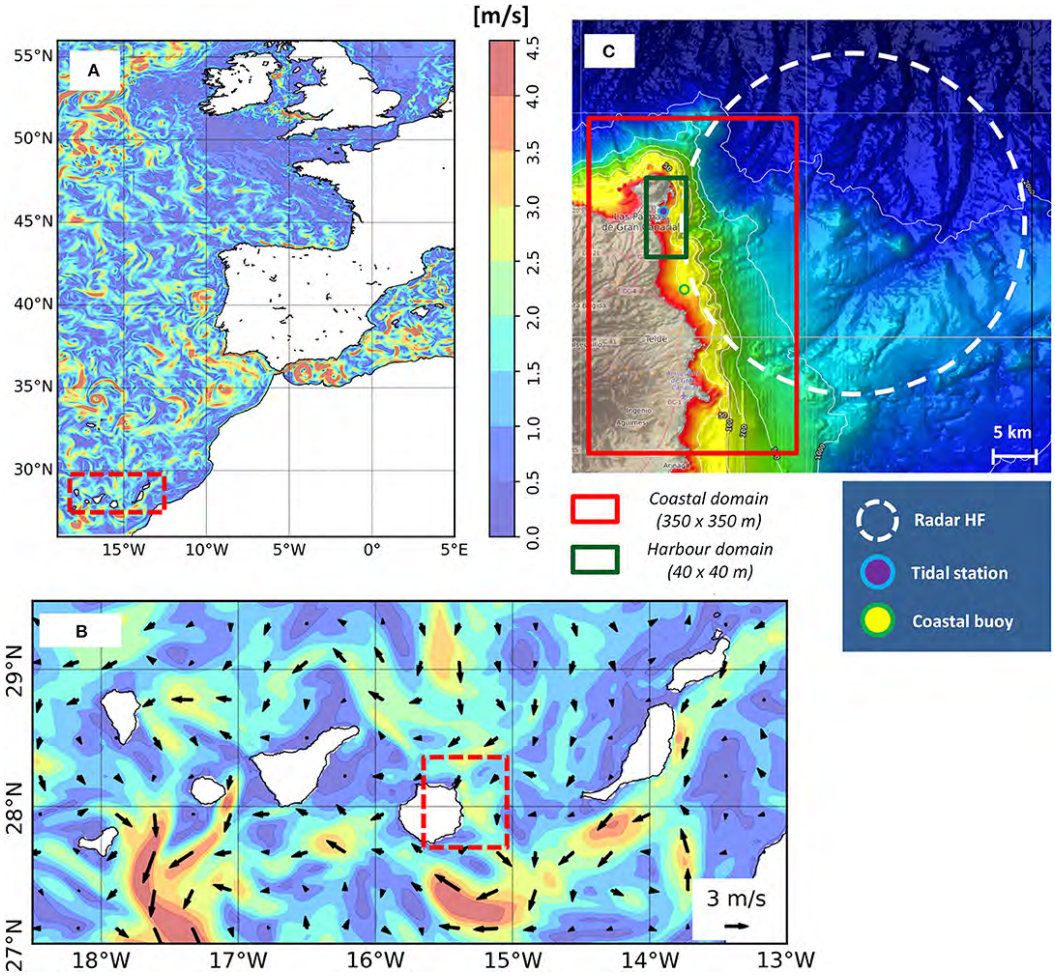


Figure 3.3 (a) Spatial domain of the IBI-PHY model. The colored areas denote the daily-averaged surface current speed on the 21st April 2017 in units of m/s. The dotted red rectangle encloses the Canary Islands (Spain). (b) Zoom of the Canary Islands for the same surface currents fields depicted in (a). The superposed black arrows represent the surface current field. (c) Nesting strategy for the Port of La Luz. The coastal domain area is enclosed in the red lined rectangle, whereas the local domain is enclosed in the green one. The colored areas show the bathymetry. The white dotted circle encloses the PLOCAN surface-current HF radar. The blue dot marks the tidal station within the harbour; whereas the yellow one marks the coastal buoy (Puertos del Estado monitoring network).

toolbox (Lorente et al., 2019). This multi-parametric ocean model skill assessment is performed by the IBI-MFC using all available operational observational sources in the IBI model domain. The list of observational data source used in the IBI validation includes remote sensed data (i.e. satellite L3 and L4 SST and sea level anomaly products, together with surface currents from coastal HF-Radars stations) and in-situ observations (from moorings and tide gauges and sea level essential variables such as surface temperature, salinity, currents and sea level; as well as from ARGO floats for 3D temperature and salinity). See further details in (Lorente et al., 2019) for a complete list of the observational products and platforms used, as well as the regions covered, to operationally validate the IBI ocean model product. Furthermore, the CMEMS IBI-MFC forecast model products are qualified before their entry into operational service. Main results from this scientific qualification of the IBI ocean model products can be seen in the comprehensive product quality document delivered together with the IBI product (the CMEMS IBI-MFC Quality Information Document, available online (Sotillo et al., 2020a)). This product quality report points out the good agreement on average between the model system and the available observations. Being particularly true for sea level when compared to along-track altimetry and tide gauge stations (in these coastal stations, model tidal and residual sea level measures are also close to the tide gauge observations used). The comparison with in-situ temperature-salinity profiles, all of them off-the-shelf, also shows good IBI model performances, especially below the thermocline. In the Canary Island region, model differences with observations are low (root mean square errors (RMSE) and biases of 0.45 and 0.07 °C and 0.15 and 0.01 psu, for temperature and salinity respectively; values obtained from the comparison of IBI with full ARGO profiles during the 2-year period 2013-2015). Concerning the Sea Surface Temperature (SST), the IBI system performs well in average, but can locally display high biases. Thus, RMSE computed over the whole IBI domain over a 6-year period is around 0.6 °C. This IBI referential product quality report shows also some IBI metrics for surface currents. However, it warns about the difficulty to assess such variable, mostly due to the very scarce availability of long time series of velocity measurements, and the very limited representativity of such measurements (there are only a few local measurements available, making it impossible to build regional metrics for surface currents, such as the ones provided for the SST and sea level fields or the 3D temperature and salinity).

- **PdE La Luz Port model:** CMEMS IBI provides a regional solution at kilometric scales. The IBI horizontal resolution in clearly not enough to characterize coastal events such as the one we discuss in this work. Therefore, a local high-resolution

dataset is needed to characterize circulation patterns in the Puerto de la Luz. In the framework of the H2020 IMPRESSIVE Project, PdE has developed a new model setup for this port, covering also nearby waters along the Eastern coast of Gran Canaria island. This newly developed model setup, with a very high-resolution, has been specifically designed for the Puerto de la Luz, and used by PdE to test some model updates that will be used in the future to upgrade the PdE SAMOA port forecast systems (Sotillo et al., 2020a), currently implemented and running operationally in different Spanish Port Authorities. The high-resolution hydrodynamic module is based on the ROMS (Shchepetkin and McWilliams, 2005) model (version 3.7). ROMS is a time split-explicit, free-surface, terrain-following-coordinate oceanic model that has been applied successfully for oceanographic forecasting at other Spanish harbors (M. et al., 2012). The proposed nesting strategy comprises two off-line nested domains: a coastal one nested with IBI with a horizontal resolution of 350 m and ranging from shallow waters to water depths around 2000 m (hereafter coastal model); and a local one (with a horizontal resolution of 40 m), nested in the previous one (hereafter local model). We illustrate it in Figure 3.3. Due to the sudden sharp slope gradients at the continental shelf, the vertical discretization has been setup at 30 sigma levels for the coastal model. At the local model, 15 sigma levels were found to be enough for handling the bathymetry. The vertical discretization follows the S-coordinate system described in (Song and Haidvogel, 1994). The bathymetry for both domains was built using a combination of bathymetric data from EMODNET (with an approximate resolution of 230 m) and from specific local high-resolution sources provided by the local Port Authority. Furthermore, within a transition region (2 km) along the open boundaries of the coastal model, the bathymetry from the CMEMS-IBI system is used to accommodate the high-resolution information and keep consistent the transports associated with IBI velocities imposed as open boundary conditions. In the local model, an updated and higher resolution bathymetry is also applied, adjusting the open boundary to the coastal bathymetries. The bathymetry information interpolated over the mesh is smoothed using a Shapiro filter (Shapiro, 1970) with an r-factor criterion below 0.25. The bottom boundary layer has been parameterized with a logarithmic profile using a characteristic bottom roughness height of 0.002 m. The turbulence closure scheme for the vertical mixing is the generic length scale (GLS) tuned to behave as k-ε (Warner et al., 2005). Horizontal harmonic mixing of momentum is defined with constant values of $5\,m^2/s$. Moreover, the atmospheric forcings come from the HARMONIE model (Bengtsson et al., 2017) with spatial resolution of 2.5 km. The following atmospheric variables are used: wind fields, sea-level pressure, temperature

at 2 m elevation, relative humidity at 2 m elevation, precipitation, long wave and solar radiation.

With respect to the quality assessment of very high-resolution coastal model systems, covering a very limited spatial domain such as the one we present here for La Luz Port, it is important to remark that one of the main bottlenecks identified is the lack of an adequate near-real-time delivery of operational observations. This lack of operational observations, specially on coastal areas, restricts the systematic production and exploitation of quality assessments of operational ocean model products such as the ones used here. Indeed, in a recent review performed by EuroGOOS for European coastal operational ocean model services (Capet et al., 2020), it is pointed out that only 20% of operational models currently available for European seas provide a dynamic uncertainty together with their forecast products. Unfortunately, this is the case in terms of validation of the Port of La Luz model currents for the dates (21-23 April 2017) of the event here studied. There is no option to analyze the quality of the surface current modelled fields for such specific dates due to the lack of in-situ or remote sensing observations in the area. Nevertheless, there is some information on the model dynamical performance derived from other validation exercise performed on different essential ocean variables and temporal periods that can illustrate the capability of the model setup proposed to reproduce the coastal dynamics in the area.

As previously mentioned, the Coastal and Port model systems implemented in La Luz Port are an evolution of the PdE operational SAMOA model setup, used for operational forecasting in the island of Gran Canaria (Sotillo et al., 2020a). In this study, the PdE coauthors evaluated the quality of the 1-year SAMOA ocean forecast products for nine Spanish Ports by comparing them to both in-situ mooring and remotely sensed data. It is important to highlight how the SAMOA model systems focused on the Canary Islands (4 out of 9 SAMOA system existing at that time) show the best agreement for SSH when compared to hourly sea level observations from tide gauges (with reported correlation coefficients around 0.98 and RMSE that ranges between 0.07-0.16 m). The performance of coastal SAMOA systems appears to be rather consistent in terms of SST, according to the skill metrics obtained (correlation values above 0.89 and RMSE usually in the range 0.2-0.4°C, considering more than 3200 hourly observations for each case). Indeed, the SAMOA system running in Gran Canaria shows the second best performance of a PdE SAMOA operational model when compared to hourly SST observations from a coastal buoy (in this case, moored close to the Port of La Luz).

3.1.3. The transport problem

The transport process of oil particles can be described by a concentration field $C(\mathbf{x},t)$ which depends on time t and the position $\mathbf{x}$. The position $\mathbf{x}$, has three components considering oil particles move on the ocean surface and may also sink. The evolution of the concentration $C(\mathbf{x},t)$ is affected by the flow, represented by the velocity field $\mathbf{v}(\mathbf{x},t)$, and molecular diffusion. It is described by the following advection-diffusion equation (Dominicis et al., 2013):

$$\frac{\partial C}{\partial t} + \mathbf{v} \cdot \nabla C = D\nabla^2 C\,, \tag{3.1}$$

Here D is the is the molecular diffusion coefficient. At the ocean scale, the diffusion transport is much smaller than the convective transport (Monroy, 2019) and hence the equation (3.1) reduces to:

$$\frac{dC}{dt} = 0\,, \tag{3.2}$$

where d/dt is the total time derivative. Equation (3.2) implies that the quantity C is conserved along fluid parcel trajectories and behaves as a passive tracer. Particles with a finite size and different density to that of water may not instantly follow fluid velocities. Other mechanisms besides passive advection contribute to their transport, such as gravity forces, their finite size, inertia and history dependence (Julyan et al., 2010; Maxey and Riley, 1983). Results in (Monroy et al., 2017) confirm, however, that for a wide range of particles that sediment in turbulent ocean flows, the description of passive tracers is appropriate, except for the addition of a constant vertical velocity arising from the particle weight. In particular, for the case of the diesel fuel under study, weight effects are negligible and therefore we considered that it follows fluid parcels. This approach is rather reasonable for diesel fuel since it is less dense than salty water and moves mainly horizontally, close to the surface, slightly below the waterline, and thus it is not subjected to direct wind sailing effects. Studies such as (García-Garrido et al., 2016; Lekien and Marsden, 2005; Olascoaga and Haller, 2012) confirm that considering advection as the dominant contribution to pollutant transport provides very good results.

Fluid parcels follow trajectories $\mathbf{x}(t)$ on the ocean surface that evolve according to the dynamical system:

$$\frac{d\mathbf{x}}{dt} = \mathbf{v}(\mathbf{x}(t),t)\,, \tag{3.3}$$

where the position is described in longitude (λ) and latitude (ϕ) coordinates, that is, $\mathbf{x} = (\lambda,\phi)$, and $\mathbf{v}$ represents the velocity field. In longitude/latitude coordinates, the dynamical

system in Equation (3.3) can be rewritten as:

$$\begin{cases} \dfrac{d\lambda}{dt} = \dfrac{u(\lambda,\phi,t)}{R\cos\phi} \\ \dfrac{d\phi}{dt} = \dfrac{v(\lambda,\phi,t)}{R} \end{cases}, \tag{3.4}$$

where R is the Earth's radius. This equation assumes that the vertical velocity component in the ocean is small compared to the horizontal ones and for that reason it has been disregarded. The two velocity components are determined by the zonal (u) and meridional (v) velocities, which are obtained from the different ocean models: IBI, CST and PRT. We have tracked fluid parcels that evolve according to velocities supplied by these three models. Due to the limitations of CST or PRT models in terms of spatial domain (the PRT domain is only focused on inner port waters and the nearby ones, and CST is focused on an area of the coast, see Figure 3.3) in order to be able to track fluid parcels outside their geographical coverage, the zonal and meridional velocity fields need to be composed with IBI fields. Figure 3.4a) illustrates a sketch of two grids corresponding to the IBI and CST models. Panel b) shows the structured grid resulting from the composition of grids in panel a). The grid is made up of cells with areas of different sizes. A linear interpolation is used within each cell to approximate the velocities within them. When the PRT model is used, its grid is nested within the CST grid, which in turn is nested with the IBI grid, i.e, a hierarchy of three nested data is required. The accuracy of this approach is supported, and justified, in the next section, by the agreement between the predictions made by the simulations, the oil sightings from satellite and in-situ observations.

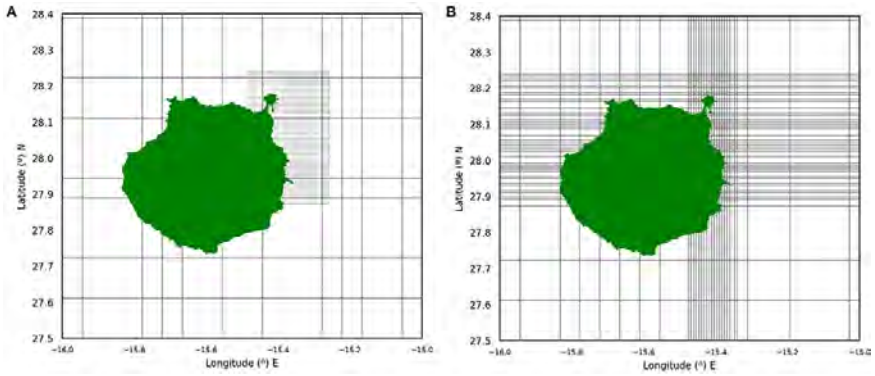


Figure 3.4 a) A sketch illustrating the two grids (IBI and CST) represented in the domains where the hydrodynamic models are solved; b) the composition of the two grids, which results in a structured, non uniform grid. Within each cell velocities are linearly interpolated.

There exist diverse software packages that are able to track oil spills. Among others, oil drift models include (Cheng et al., 2011; Xu et al., 2013) EUROSPILL, OILMAP (Oil Spill Model and Response System), GNOME (General NOAA Operational Modeling Environment), MOTHY (French operational oil spill drift forecast system), OSCAR (Oil Spill Contingency and Response), ADIOS2 (Automated Data Inquiry for Oil Spills), OSIS (Oil Spill Identification System) and Medslik-II (Dominicis et al., 2013). These models are focused on tracking individual fluid parcels, and they need to play with a sufficiently large number of initial parcels to maintain a good representation of the spill. Contrary to these oil spill approaches, in this work we track in time the whole area where the fuel is extended, and the algorithm self regulates the number of fluid parcels on the contour to ensure its accurate representation at all times. The area is tracked with contour advection algorithms developed in (Dritschel and Ambaum, 1997), including some modifications explained in (M. et al., 2004; Mancho et al., 2006b, 2003). More specifically, the spill is modelled by an initial contour surrounding an area, A_0, with a given thickness h_0. The product $V = A_0 \cdot h_0$ is the volume of the initial spill. While the contour is advected, the initial area, whose value is typically preserved for 2D incompressible flows, is distorted.

Transformation processes like evaporation, photo oxidation, etc., act on the slick while it drifts. Evaporation is an important process for most oil spills. Oils and fuels are slowly evaporating mixtures of compounds whose long-term behavior are not always well described by air-boundary layer interaction mechanisms, but through diffusion mechanisms (Fingas, 2015). However, the diesel under consideration has volatile components, that do evaporate via air boundary-layer-regulated mechanisms. Software packages quoted above include models to represent the weathering of the spills according to different oil properties. In our model, oil is presumed to consist of one component and its volume is assumed to decrease through evaporation by diminishing its thickness h_0. In this way spill contours are evolved uncoupled from degrading effects which are considered at representative levels as a change in the intensity color of the oil spill. The intensity will be adjusted depending on the degradation of the specific type of oil. According to (Giles, 1979; McIlroy et al., 2018), the fraction of the original diesel compound remaining after evaporation can be adjusted to a kinematic law:

$$\frac{V}{V_0} = e^{-Bt}, \tag{3.5}$$

where V_0 is the original volume, and V is the the volume at time t. According to in-situ reports, the spill reduced an 80% in approximately 72h (Montero, 2017), which give us an estimation of the evaporation rate $B = 0.02235\ \mathrm{h}^{-1}$.

3.2. Results and discussion

The passenger ferry crashed at the position marked by a red dot in Figure 3.1, located at 28°9.418′ N and 15°23.871′ W. Figure 3.5 shows a time frame that is representative of the surface current patterns during the event. Throughout the episode, surface currents were mainly driven by large-scale circulation patterns and tides. Current fields were southward, with a modelled daily-averaged current speed of 12-16 cm/s at the eastern shelf of Gran Canaria island. IBI-PHY and the high-resolution model presented similar current magnitudes. Note that only the semi-diurnal tidal current range was around 10 cm/s. Currents induced by residual tides can be considered as negligible: from the 21st to the 23rd of April, a negative surge was measured with an average value of 2 cm. At the end of the 23rd of April, though, the negative surge rose to 6 cm. Wind-induced currents had also a secondary role: measured surface wind at the tidal station was mainly from the N-NW sector, with a wind speed of 3.38 m/s (standard deviation of 0.88 m/s). There was no evidence of gustiness, either: average maximum wind speed was mild, with low variability (5.25 m/s with a std. deviation of 1.2 m/s). Finally, wave-induced currents may have had a secondary role: measured waves at the coastal buoy were moderate, with significant wave height of around 1.1 m and maximum wave heights of 1.5 m. The peak period was close to 8 seconds, exhibiting a young swell sea-state.

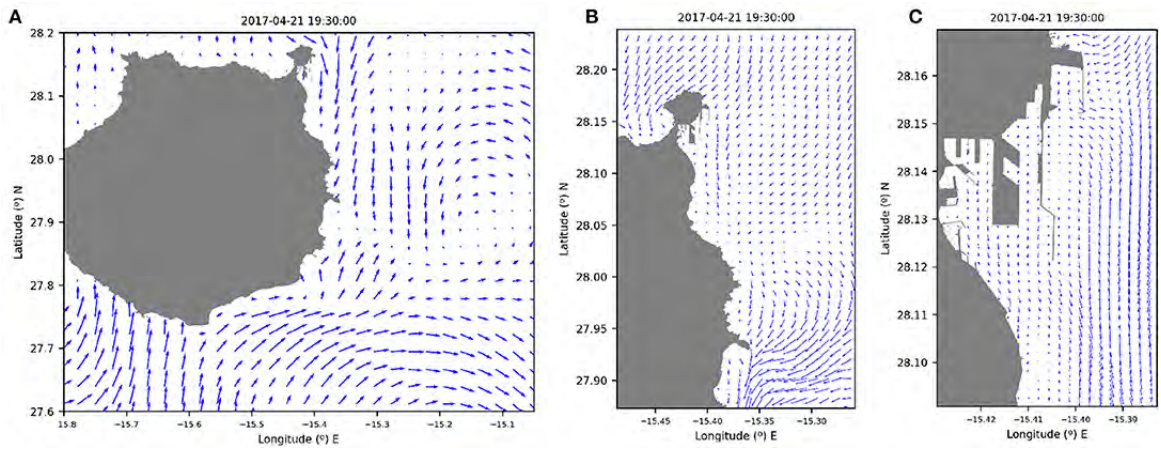


Figure 3.5 Currents in the Gran Canaria coast at different resolutions. a) currents by the IBI model; b) currents in the high-resolution CST model; c) currents in the very high-resolution PRT model.

On the 23rd of April 2017 at 7:00 a.m., remote sensing images confirmed the spreading of the diesel fuel southwards, (see Figure 3.2). This is consistent with the evolution of the spill, which is modelled as a blob at the accident location, according to the three models: IBI, CST and PRT. Figure 3.6 illustrates this point. Panel (a) shows how it evolves according

to IBI model, panel (b) illustrates the evolution according to the CST model nested in IBI data, and finally panel (c) displays the evolution according to the PRT model nested in CST and in IBI data. Arrows mark the position of the blob at successive times. The color degradation from black to white, in a gray scale represents the evaporation. All three models predict a southwards evolution, although IBI model drifts southwards faster than the others and at the observation time, i.e., 23rd of April 2017 at 7:00 a.m., the spill is outside the displayed domain. On the other hand, both CST and PRT models provide very similar outputs and predict a position for the spill at the observation time very close to the observed one. No significant differences are noticed between them, and this is somewhat expected given that the blob spends only a brief time within the very high-resolution PRT domain, and it rapidly evolves towards the high-resolution CST domain in the coastal area. The structure of the observed spill is not so filamentous as the simulated one, possibly because of the actions taken by the emergency services to dissolve it. However, it is clear that there is a significant intersection between both in space and time. The hypothesis of human interaction is consistent with the report by the ”Comisión Permanente de Investigación de Accidentes e Incidentes Marítimos" (CIAMI) (Ciaim, 2018) about the presence of many boats working to repel the diesel fuel, far from the desalinization plant. Results displayed in Figure 3.6, despite similarities among models, also present differences. A natural question that arises in this context is how we can compare them. The rest of this section is focused on providing a qualitative and quantitative comparison between the transport capacity associated to each model.

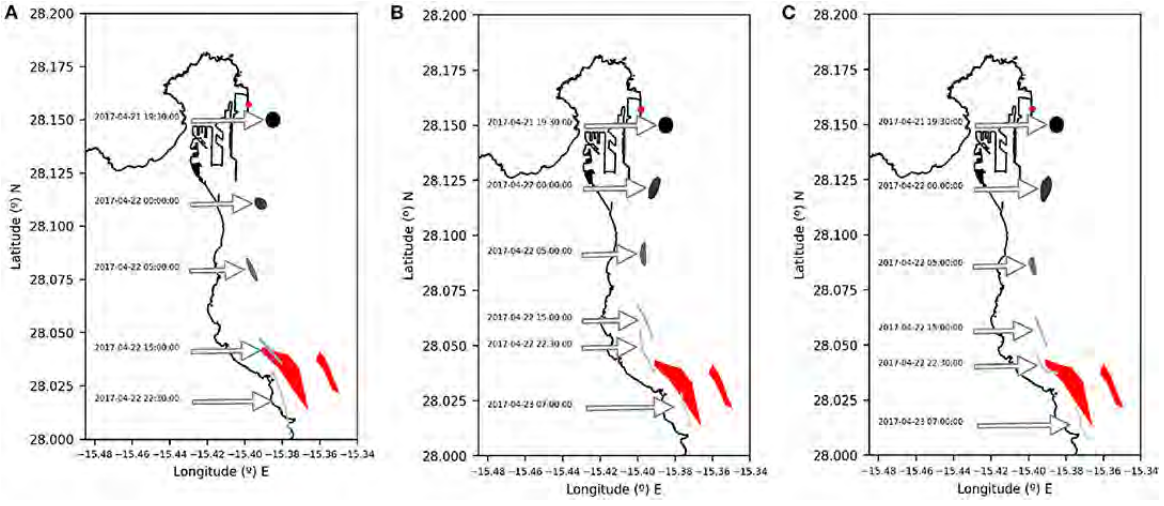


Figure 3.6 Simulations of the evolution of the spill in the neighborhood of the accident location, according to the three models. a) IBI; b) CST; c) PRT. Evaporation is represented by the degradation of the gray scale. The red color marks the position of accident and the observed spill on the 23rd April at 7:00 am.

3.2.1. The dynamical system perspective

A comparison of the transport processes induced by the different models requires a further step than just a contrast between individual trajectories. This can be carried out by means of applying Poincaré's idea of seeking geometrical structures in the phase space of the dynamical system described in Equation (3.3) that are responsible for schematically organizing particle trajectories into regions corresponding to qualitatively distinct dynamical behaviors. This approach brings an interesting new perspective into this problem. Thereby, the global behavior of particle trajectories on the ocean surface can be understood through a template (skeleton) formed by geometrical structures that organize flow trajectories into different ocean regions. These structures are known in the literature as Lagrangian Coherent Structures (LCS), which provide a robust way to compare transport features between velocity datasets. This is due to the fact that the geometry of LCS is preserved even for not so small velocity perturbations (Haller and Yuan, 2000). In this way, works such as (De la Cámara et al., 2010), compare transport across the stratospheric polar vortex in the atmosphere due to different models. It shows that the comparison of individual trajectories is not a robust test to quantify transport features in stratospheric datasets, while LCS are.

An essential ingredient of the geometrical structures associated with LCS are hyperbolic trajectories characterized by high contraction and expansion rates. Directions of contraction and expansion define, respectively, stable and unstable directions (Balibrea-Iniesta et al., 2019; García-Garrido et al., 2016). Of particular interest to our study are hyperbolic trajectories located on the coastline in what is known as a detachment configuration. Under this configuration, which is illustrated in Figure 3.7, material on the coast is ejected into the ocean as shown by the successive green blobs. This configuration is related to the phenomena of flow separation. The presence of these hyperbolic trajectories close to the 'Nelson Mandela' dike implies a higher risk of any spill event in such a location, because diesel fuel poured into the sea close to a detachment trajectory flows away, increasing the probability of affecting critical areas as those marked in Figure 3.1.

Computing the geometrical skeleton formed by the stable and unstable manifolds of hyperbolic trajectories in the described ocean models requires additional mathematical techniques that we discuss next. To this end, we use a tool known as Lagrangian descriptors (Lopesino et al., 2017; Mancho et al., 2013; Mendoza and Mancho, 2010) that has been successfully applied in similar studies (García-Garrido et al., 2015, 2016). This tool is based on the construction of a scalar function that we call M, which is defined as follows (Jiménez-Madrid and Mancho, 2009):

$$M(\mathbf{x}_0, t_0, \tau) = \int_{t_0-\tau}^{t_0+\tau} \|\mathbf{v}(\mathbf{x}(t), t)\| \, dt \,, \tag{3.6}$$

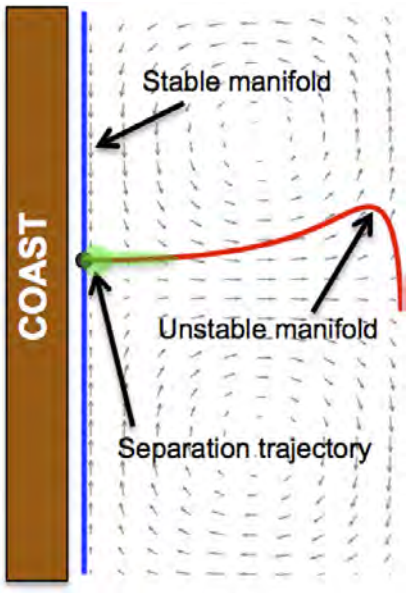


Figure 3.7 Sketch of a hyperbolic trajectory in a detachment or separation configuration. Successive green blobs separate from the coast flowing into the ocean.

where $\|\cdot\|$ stands for the modulus of the velocity vector. At a given time t_0, the function $M(\mathbf{x}_0, t_0, \tau)$ measures the arclength traced by the trajectory starting at $\mathbf{x}_0 = \mathbf{x}(t_0)$ as it evolves forward and backward in time for a time interval τ. Notice that we can split the computation of function M into its forward and backward contributions separately. This is important because forward integration provides information about the stable manifolds (repelling LCSs), while backward integration highlights the structure of unstable manifolds (attracting LCSs). Moreover, if we plot in the same figure the sum of both contributions, we can easily locate hyperbolic trajectories at the intersections of the stable and unstable manifolds. In fact, it can be shown that the scalar field provided by the computation of function M, when calculated over a grid of initial conditions, reveals the stable and unstable manifolds on the ocean surface at locations where the output values change abruptly, that is, at places where the gradient of the scalar field is very large. Figure 3.8 displays the calculation of M in the vicinity of the crash point using the CST model in the Port of La Luz coastal area. The pattern displayed by the function M has been computed for an integration period of $\tau = 3$ days. In Figure 3.8, stable and unstable manifolds are emphasized, respectively, by the red and blue tones that enhance the 'singular features' highlighted in the scalar field as a result of high gradient values. In this panel, a hyperbolic trajectory is visible as a point in a detachment configuration, similar to the one sketched in Figure 3.7. This trajectory is very close to the ferry crash point in the 'Nelson Mandela' dike, which increases the riskiness of the region due to the dispersion of the spilled diesel fuel.

Figure 3.9 displays the M function for $\tau = 5$ days. It highlights the LCSs for the three models at the time of the accident. This allows a straightforward qualitative comparison of the transport mechanisms produced by all models. The IBI and CST models present different patterns, however both show a detachment configuration as the one displayed in Figure 3.7. This confirms that both models will predict a southwards evolution of any spill in the neighborhood of the accident point. This is so because in both cases the unstable manifold follows that orientation. As expected, the PRT and CST models present very similar LCSs features. A comparison between figures 3.8 and 3.9b) show that as τ is increased in the computation of the M function, this produces a richer and more intricate LCS skeleton, since we are incorporating more information about the history of particle trajectories as they evolve in time for longer periods.

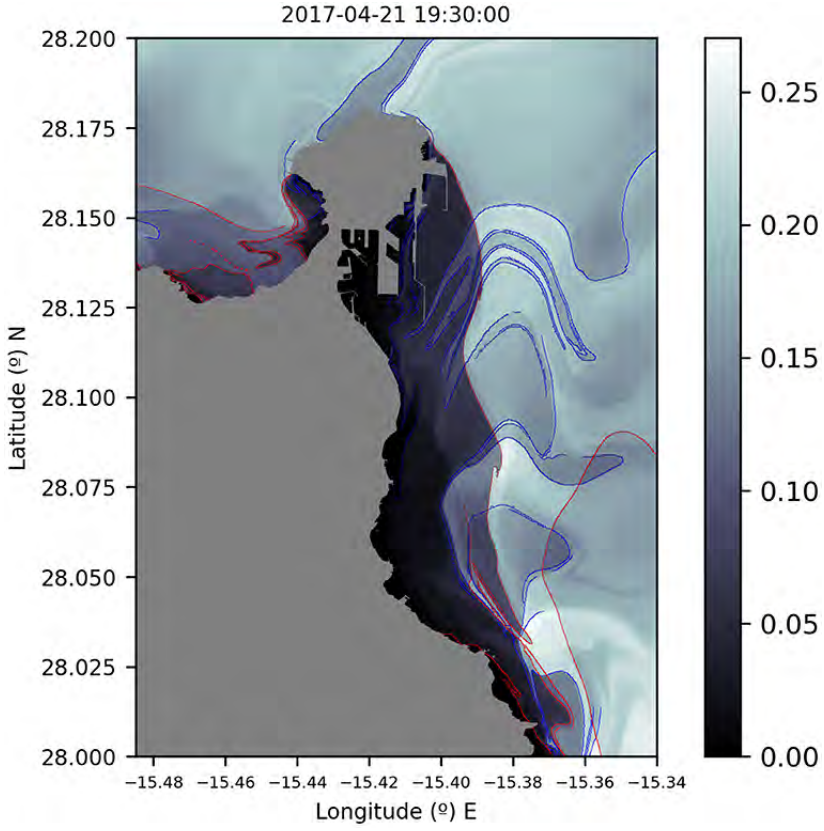


Figure 3.8 The Lagrangian skeleton of the CST model on the 21 April 2017 at 19:30h calculated with function M using $\tau = 3$ days. LCSs are highlighted by the intricate curves in gray at the background, where there is a sharp change in the scalar field values of the function. Red lines are marked to emphasize the locations of the unstable manifolds (attracting LCSs), while blue lines depict the stable manifolds (repelling LCSs).

The stable and unstable manifolds highlighted in Figure 3.9 are time dependent dynamical barriers that fluid parcels cannot cross. Fluid parcels tend to become aligned, for large enough

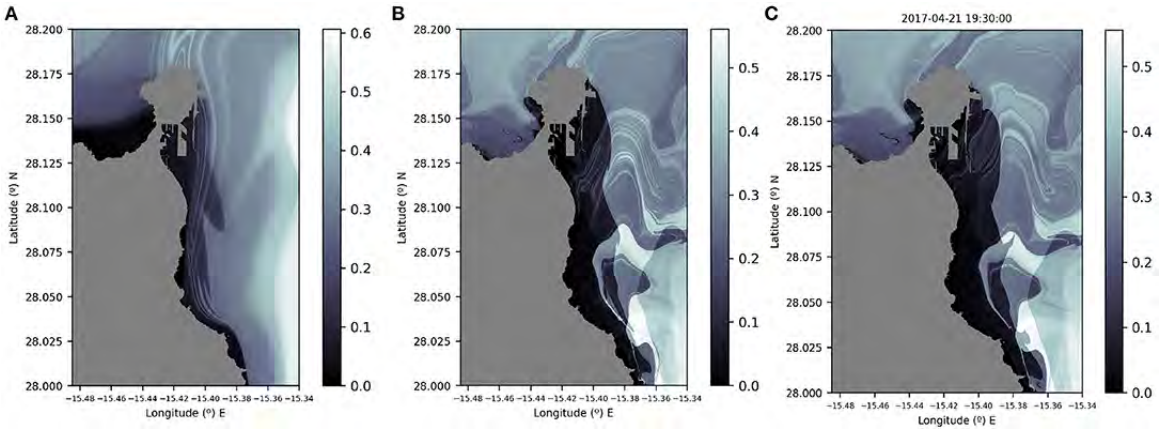


Figure 3.9 The Lagrangian skeleton as displayed by the function M computed for $\tau = 5$ days on the 21 April 2017 at 19:30h. LCSs are highlighted by the intricate curves in gray at the background, where there is a sharp change in the scalar field values of the function. a) Results for the IBI model; b) results for the CST model; c) results for the PRT model. All three models display a detachment configuration.

transition time intervals, with unstable manifolds, which are attracting material curves that adopt convoluted shapes. This is true no matter what the initial position of the spill is. Movies S1 and S2 [1] confirm this point. These movies show the evolution of several fluid blobs placed at different initial positions. At later times, all blobs are elongated and aligned with the unstable structures. This is the case, both for fluid parcels evolving according to the IBI model (movie S1) and to the CST model (movie S2). Similarly, but going backwards in time, blob particles align along repelling material curves, the stable manifolds, which also may be very intricate in shape. In forward time, stable manifolds represent the transition pathways towards the unstable manifolds.

3.2.2. Uncertainty quantification

The Lagrangian geometrical structures computed for the PRT, CST and IBI models allowed for a qualitative comparison among them, since they enhance similar features in what regards the presence of a separation or detachment trajectory on the coast close to the 'Nelson Mandela' dike. This is a particular hyperbolic configuration that pushes material out of the coast. The flow evolution in the neighbourhood of any hyperbolic trajectory is characterized by high expansion and contraction rates, which always are intrinsically related to uncertainties in the evolution. The outputs of the PRT and CST models, as already discussed, are barely distinguishable in the event scale. This is because the main differences

[1] These movies are available via the following hyperlink: https://shorturl.at/dnCFR

in the circulation patterns are within the harbour. The analyzed spill was rapidly advected outside the harbour, where the solutions of both models are identical. Consequently, the very high-resolution model would provide further insights only in those spills whose trajectories intersect the harbour waters.

In this section we quantify the differences between the transport outputs by the CST and IBI models with respect to the position of the observed purple spill, which is considered a target, a 'ground truth' that should be recovered by the model (see Figure 3.6). In order to achieve this, we have selected a number of positions in the neighborhood of the 'Nelson Mandela' dike, which are centered within each grid element displayed in Figure 3.10 a) and b). The evolution of blobs of identical initial radius (0.0035°) from all those positions is different due to the chaotic nature of transport in this setting. After a time interval from the initial time, these blobs evolve and distort while they approach the target observed spill. The calculation of uncertainties associated to each grid element, is based on an error metric that considers the distance between the centroid of the simulated slick ($\mathbf{c}_m$) at a given time t^* and the centroid of the ground value slick ($\mathbf{c}_g$), i.e,

$$e(t^*) = \|\mathbf{c}_m(t^*) - \mathbf{c}_g\|\,, \tag{3.7}$$

where $\|\cdot\|$ is the modulus of the vector. The centroid of a finite set of N points $\{\mathbf{x}_k\}_{k\in\mathbb{N}} \in \mathbb{R}^n$ ($n = 2$ in this setting) is defined as:

$$\mathbf{c} = \frac{1}{N}\sum_{k=1}^{N} \mathbf{x}_k\,, \tag{3.8}$$

where $\mathbf{x}_k$ are the (lon, lat) coordinates that define the contour of the slick in an equirectangular projection. Based on this error metric, the uncertainty of the model in a given grid element is computed starting on the 21st of April 2017, at time 7:30 pm, from a circular contour centred on the grid with a radius of 0.0035°. Then the set of errors e_i defined as in Equation (3.7) are considered for a sample of times t_i, where $i = 1\ldots 7$, within a three hour interval centred on the 23rd of April at 7:00 a.m., when the satellite image is taken. Finally, the minimum value of e_i in this set is taken as the representative error for each grid element. Results in a mesh next to the crash point are displayed in Figure 3.10. The error is given in degrees that can be easily transformed into kilometres. Grid elements of Figs. 3.10 a) and b) are colored in a different tone depending on this distance. The color scale is marked in the figure. It is evident that uncertainties, which are related to errors in the displacement, are greater for the IBI model than for the high-resolution CST model. Using the regional solution the average error obtained is 0.07° (around 8 km), whereas using the coastal model solution the error is

0.03° (around 3 km). La Luz CST model errors are a factor 2.5 lower than the IBI model errors in good agreement with grid sizes differences.

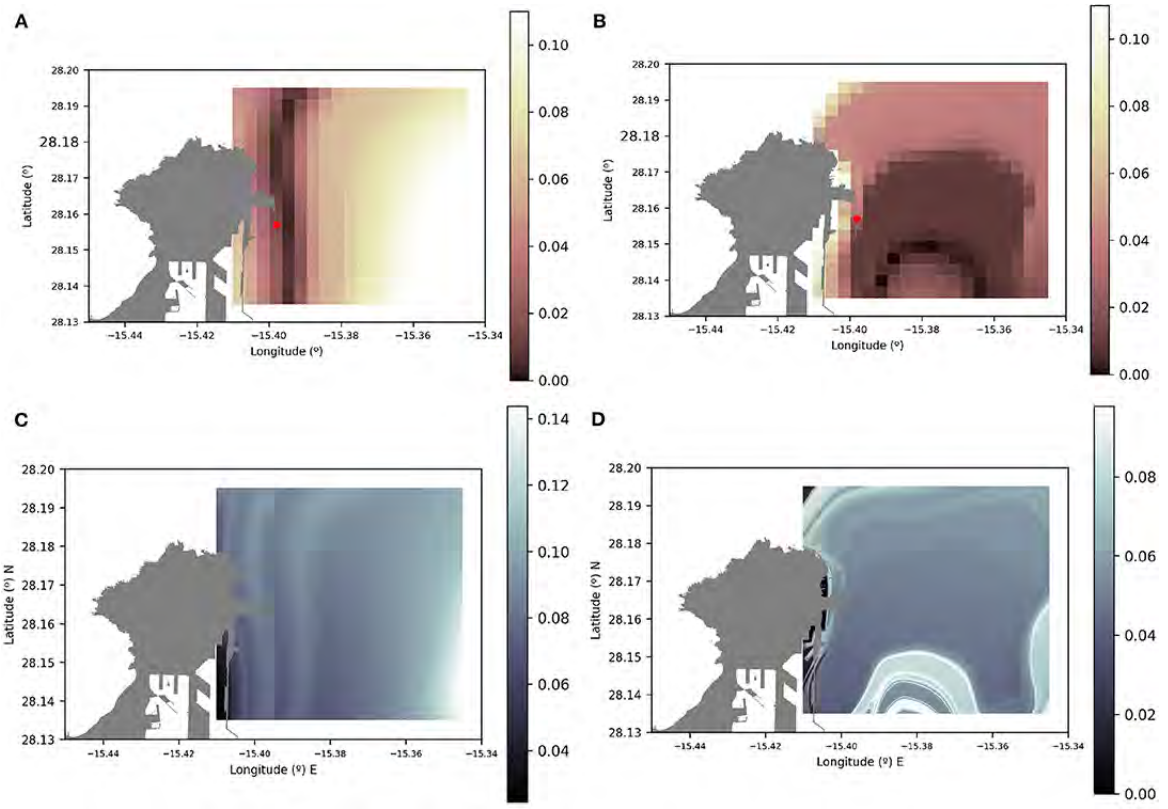


Figure 3.10 Panels a) and b): A quantitative measure of uncertainty based on blob initial positions and representative errors measured as distances to the target 'ground truth' spill. Higher colormap values correspond to larger errors or uncertainties. The accident location is marked with a red spot. a) Uncertainties associated to the IBI model; b) uncertainties associated to the high-resolution La Luz model. Panels c) and d): representation of the forward integrated M function for $\tau = 3$ days highlighting the stable manifolds. c) Stable manifolds associated to the IBI model; d) stable manifolds associated to the CST model.

Differences in the uncertainty distributions are visible from Figs. 3.10a) and b). IBI uncertainties are more significant in the right side of the mesh, while CST uncertainties are higher in the upper side. Panels c) and d), show for the IBI and CST models respectively, in the same area, the structure of the stable manifolds as highlighted by the M function. Indeed, stable manifolds are displayed by formula (3.6) when the integration interval is a forward time integration, i.e., $(t_0 - \tau, t_0 + \tau)$ is replaced by $(t_0, t_0 + \tau)$. Similarities between patterns in Figure 3.10a) and Figure 3.10c) and those in Figure 3.10b) and Figure 3.10d) are remarkable. Uncertainties seem to reach minimum values along the stable manifolds. Indeed, as explained before, and is visible from movies S1 and S2, blobs on the stable manifolds

rapidly travel towards the unstable manifolds, which in turn are the attracting material curves towards which all fluid parcels evolve. In this case both IBI and CST models have their unstable manifolds aligned with the observed spill, on the 23rd of April 2017.

3.3. Conclusions

In this chapter we have analyzed how emerging tools in coastal areas such as available very high-resolution hydrodynamic models and remote sensing images from satellite, are able to provide accurate responses to the management of pollution events in port areas. In particular, the collision event of the passenger ferry “Volcán de Tamasite" in La Luz Port on April 2017 is discussed.

Very good agreement is reported between Sentinel 1 radar images and spill evolution models based on velocity fields obtained from the CMEMS IBI regional product and from the two specific model solutions: the coastal one, CST, covering waters along the eastern coast of the Gran Canaria Island and; the highest resolution one, PRT, focused exclusively in the nearby waters of Puerto de la Luz. These downstream were developed by PdE, in the framework of the IMPRESSIVE project, to downscale the CMEMS regional solution.

The evolution of the spill is implemented with contour advection algorithms that are able to track very efficiently the whole area where the fuel is extended. This is so because the algorithm is capable of self-regulating the number of fluid parcels on the contour, to ensure an accurate representation of distortions at all times. Transformation process are caused by evaporation and are expressed by means of a degradation in the gray tone representing the spill.

Transport process describing the spill evolution under the IBI, CST and PRT models have been analyzed from the dynamical systems perspective. This perspective has allowed a qualitative comparison among them and has highlighted a similar transport scenario in the three models, in which the spreading of the fuel is controlled by the presence of a hyperbolic trajectory attached to the coast, close the ‘Nelson Mandela’ dike, in a detachment configuration. This configuration pushes waters along the coast out into the sea. In this framework, attracting material surfaces, also called invariant unstable manifolds, are identified. Passive scalars, and fuel behaves like them, become aligned along them.

A quantitative comparison of the transport outputs by the CST and IBI models has been implemented. For blobs in a neighbourhood of the accident point, an estimation of the uncertainty is provided by measuring errors or distances between simulated and observed spills. The average uncertainty is found to be lower for the CST than for the IBI model. Connections between stable manifolds and the uncertainty field have been discussed. It is

observed that for both models, minimum values of the uncertainty field are aligned along stable manifolds. This is congruent with the fact that stable manifolds are optimal transport routes towards the unstable manifolds and that all models consistently present unstable manifolds aligned with the observed spill.

Summarizing, counting with a coastal downstream service focused on downscaling the regional CMEMS solution by means of a higher resolution nested model is proved to be a positive approach. In particular, high-resolutions models decrease uncertainties in oil spill predictions. This confirms that high-resolutions tools have the potential to be effective contributors to the decision-making processes carried out by the emergency services in the real-time management of oil spills.

In this chapter, it has been shown the effectiveness of high-resolution nested models in reducing uncertainties in oil spill predictions. In the following chapter, we will explore further how to quantify the uncertainty of these models and create a new quantifier for forward time uncertainty in models generated from data sets. This approach is defined in the phase space in which trajectories evolve and is directly related to phase space structures from dynamical systems theory, such as stable and unstable manifolds. We apply this approach to an ocean data set and standard benchmark models from deterministic dynamical systems theory, allowing for a quantitative comparison of transport performance described from different data sets.

Chapter 4

Forward Time Lagrangian Uncertainty Quantification

This chapter is based on the results described in the paper by García-Sánchez et al. (2022), which is a continuation of the IMPRESSIVE collaborative effort. For the sake of completeness and consistency, we will recall methodological aspects described in Chapter 2, and results in Chapter 3 to show a more coherent description of our results.

Uncertainty Quantification (UQ) searches for a quantitative characterization of uncertainties in computational models of real-world applications. Uncertainties associated to these models have been studied for many years. Depending on the context uncertainties can arise as a result of noisy or incomplete data, errors introduced by numerical models, or by the lack of complete understanding of the governing physical processes. This work deals with uncertainty related to deterministic models, which occurs due to unknown aspects of the model, and not with that uncertainty derived from the presence of stochastic or noisy processes. A comparison between these two types of uncertainty may be found in (Frenklach et al., 2016).

In geophysical contexts uncertainty is a topic of much interest because it is inherent to the equations describing the motion of fluids, such as the ocean or the atmosphere. The motivation of this paper is to acquire a deeper understanding of uncertainty quantification that allows a better characterization of its presence in ocean models. Large amount of oceanic data are now becoming available. For example, the Copernicus Marine Environment Monitoring Service (CMEMS) provides regular and systematic information about the physical state and dynamics of the ocean for the global ocean and the European regional seas. The data cover the current and future state of variables and the provision of retrospective data records (re-analysis). Other oceanic services include ocean currents supplied by altimeter satellites, such as AVISO; the HYbrid Coordinate Ocean Model (HYCOM), a consortium, which is

a multi-institutional effort, sponsored by the National Ocean Partnership Program (NOPP), as part of the U. S. Global Ocean Data Assimilation Experiment (GODAE), to develop and evaluate a data-assimilative hybrid coordinate ocean models, etc. Validating data outputs from these models, or recognizing their suitability for operational purposes, is of paramount importance for providing valid solutions to real problems in our society. These problems may be related, for instance, to ocean transport phenomena, such as oil spills, chemical or plastic transportation. Uncertainty quantification in this context supports taking appropriate decisions about the use, or not, of a particular data source in these applications.

Ocean models are built on partial differential equations, which are only an approximation of reality. Indeed, typically ocean models approach ocean motion by the Reynolds-averaged Navier-Stokes equations using the hydrostatic and Boussinesq assumptions. In this context inaccurate or inadequate models lead to *structural uncertainty*. Even if these equations were perfectly accurate models, they contain parameters, such as viscosity or diffusivity, which are not known precisely and cause *parameter uncertainty*. Boundary conditions on input variables, lead to *parametric variability*. For instance input variables, such as velocities, experience at the surface atmospheric winds, which impose forcings on the velocities, and these atmospheric forcings are not precisely known. Eventually these models are not solved exactly, but numerically through discretization methods and numerical approximations which are subject to numerical errors, and results in *algorithmic uncertainty*. For all these reasons, the predicted ocean currents are also uncertain. Uncertainties in the system outputs determined from the solutions that result from uncertainties in the system inputs are referred to as *forward uncertainty* (Sullivan, 2015).

In this chapter, we are interested in evaluating the reliability of the outputs, i.e. the ocean currents, with respect to the transport that they produce. This is a perspective slightly different to the classical one now described in which ocean model adequacy is judged only against the velocity fields. Transport in the ocean surface is produced by fluid parcels that follow trajectories $\mathbf{x}(t)$ that evolve according to the dynamical system:

$$\frac{d\mathbf{x}}{dt} = \mathbf{v}(\mathbf{x}, t), \tag{4.1}$$

where the position is described in longitude (λ) and latitude (ϕ) coordinates, that is, $\mathbf{x} = (\lambda, \phi)$, and $\mathbf{v}$ represents the velocity field, which has two components determined by the zonal (u) and meridional (v) velocities. In longitude/latitude coordinates, the dynamical

system in Equation (4.1) can be rewritten as:

$$\begin{cases} \dfrac{d\lambda}{dt} = \dfrac{u(\lambda,\phi,t)}{R\cos\phi} \\ \dfrac{d\phi}{dt} = \dfrac{v(\lambda,\phi,t)}{R} \end{cases} \tag{4.2}$$

where R is the Earth's radius. The system (4.1), which is a general expression encompassing the specific problem dealt with in (4.2), is a nonlinear non-autonomous dynamical system in 2D. Uncertainties in the velocities $\mathbf{v}(\mathbf{x},t)$, or more generally in the vector field, produce uncertainties in the solutions $\mathbf{x}(t)$. In general, as illustrated in Figure 4.1, the exact model connecting two successive observations is not known. Only the initial observation, $\mathbf{x_0}$, and the final state, $\mathbf{x}^*$, are measurable. They are presented in the red color in the figure. The evolution of initial conditions, $\mathbf{X_0}$, in a neighbourhood close to the initial observation, $\mathbf{x_0}$, towards a final state, $\mathbf{X}^*$, predicted by a model is expressed with the pink color in the same figure. The uncertainty of the model in representing the observations can be expressed in a number of ways. It may be defined by an absolute error E, which measures distance, in a certain metrics, between the final observation $\mathbf{x}^*$, which is considered a target and the computed prediction $\mathbf{X}^*$. This study proposes measures for this error and links the proposed uncertainty quantifier with dynamical objects present in the model (4.1). This is done without making any mathematical assumption about the observations.

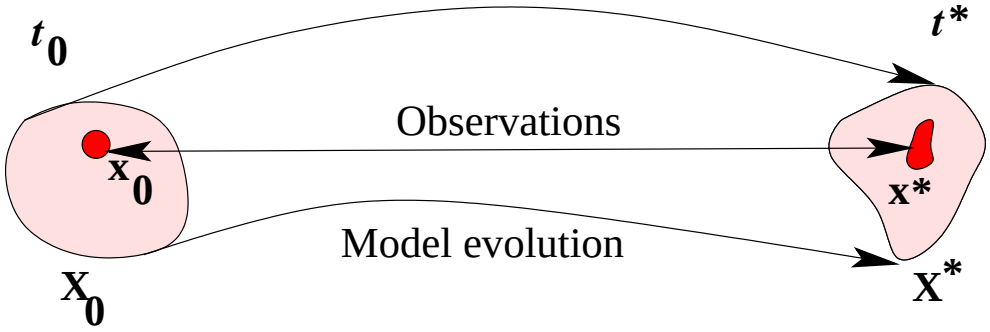


Figure 4.1 A graphical representation of two sequential observations and their evolution according to a mathematical model. The initial observation at time t_0 is expressed by the red initial condition $\mathbf{x_0}$. The final observed state $\mathbf{x}^*$ at time t^* is referred to as the "target". The evolution law for these observations is unknown, but is approximated by a model, which in our setting involves the velocities $\mathbf{v}(\mathbf{x},t)$ of the system (4.1). The evolution according to a model of a neighbourhood of points, $\mathbf{X_0}$, close to the initial observation, $\mathbf{x_0}$, is illustrated with the pink color.

This paper is structured as follows. In Section 4.1, we will discuss and develop an approach to uncertainty quantification recently taken for an ocean study case in Chapter 3. We will show evidence of connections between the introduced definitions and the dynamical objects of system (4.1). In Section 4.2, we will provide formal results to show how, for specific simple examples of the system (4.1), the definition of uncertainty quantification given in Section 4.1 is able to highlight these dynamical objects. These results support one of the main findings of this article, which is that stable invariant manifolds of hyperbolic trajectories provide a *structure* to forward uncertainty quantification. We will see in detail what is meant by this statement. Section 4.3 presents a discussion with further examples that illustrate the findings of this work and links uncertainty quantification to Lagrangian Descriptors and other Lagrangian indicators found in the literature. Finally, in Section 4.4, we discuss our conclusions.

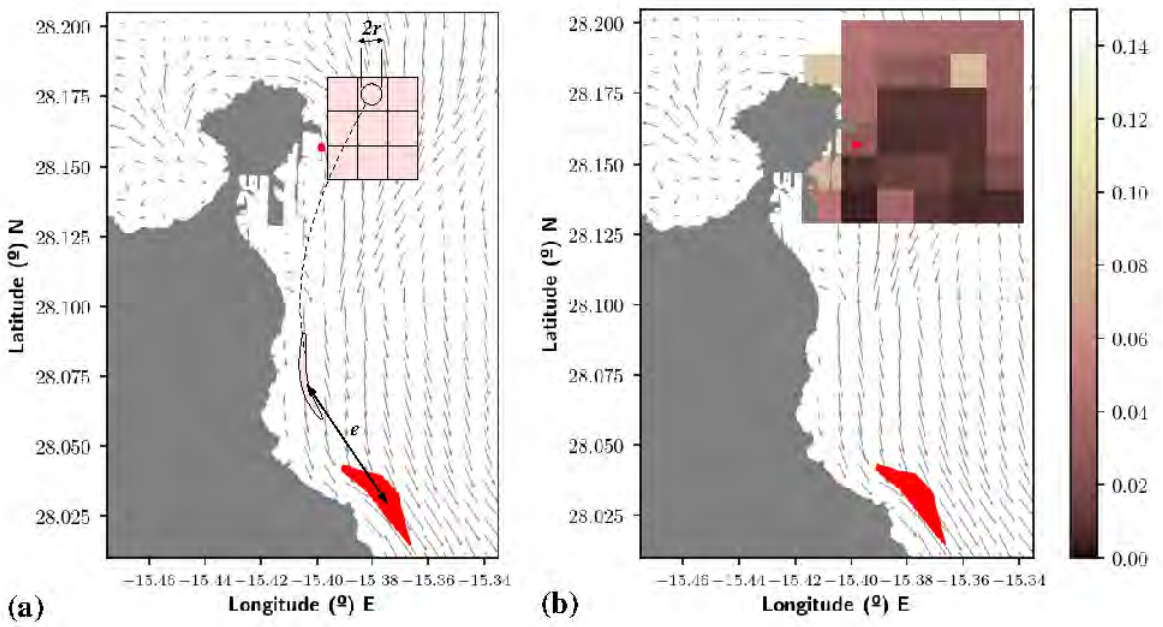


Figure 4.2 A graphical representation of the uncertainty quantification in a neighbourhood of the accident location (red dot) with respect to a target (the red blob). a) A schematic representation of Equation (4.3) computation for an initial pink blob with radius r and its evolution; b) results of the computation of Equation (4.3) for different initial blobs of radius $r = 3.5 \cdot 10^{-3}(^\circ)$ placed in the center of each cell in the meshgrid. The colormap is expressed in degree values for the final distances to the target.

4.1. Transport uncertainty quantification in ocean models

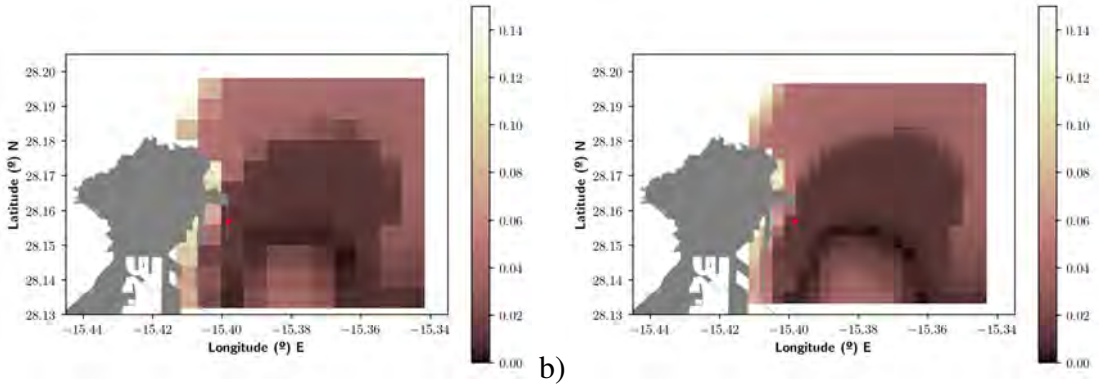
In this section we propose uncertainty quantification metrics. We work in the context of transport in ocean models, beginning the discussion from the results presented in Chapter 3, which considers the performance of very high-resolution tools for the monitoring and assessment of environmental hazards in coastal areas. In particular, this work, following the scheme presented in Figure 4.1, quantifies uncertainties of several high-resolution hydrodynamic models in the area of Gran Canaria by measuring an error between the observations and predictions for the evolution of a diesel fuel spill event, well documented by port authorities and tracked with very high-resolution remote sensing products. The pollution event was produced after the collision of the passenger ferry 'Volcán de Tamasite' with the Nelson Mandela dike in La Luz Port on April 2017. After the crash, supply pipes along the dike were broken and diesel fuel poured into the sea. SAR Sentinel 1 images were available in the area approximately one day and a half after the accident from which it was possible to identify the spill. For that period ocean currents in the area were available from two sources. One was the Copernicus Marine Service model for the Iberian-Biscay-Irish region (CMEMS IBI-PHY, IBI hereafter) and other was a very high-resolution model of Puerto de la Luz setup by Puertos del Estado currently implemented and running operationally in different Spanish Port Authorities within the SAMOA port forecast system (Sotillo et al., 2020a). In Chapter 3, for each model, uncertainties were quantified by measuring an error with respect to a target, a 'ground truth', which should be recovered by the model. In particular, following the scheme proposed in Figures 4.1, 4.2 illustrates how the uncertainty quantifier metrics is proposed. The ferry impact point, the Nelson Mandela dike, which is marked with the red dot, represents an initial observation. The currents represented in the background are the ones obtained from the model set by Puertos del Estado at day t_0. The elongated red blob represents the spill as identified from satellite images one day and a half after the accident. This is the target observation, the 'ground truth'. In panel (a) a set of initial conditions, $\mathbf{X_0}$, is selected in the neighbourhood of the initial observation and marked in a rectangular pink domain. This domain is divided into sub-domains and in each one a small circular blob with radius $r = 3.5 \cdot 10^{-3}(^\circ)$, is evolved in a time interval from the initial time t_0. This is represented just for one of the sub-domains. The blob distorts while it approaches the target observed spill. A way to measure the 'proximity' between the blob and the target spill at the final time, t^*, is to compute the distance between the centroid of the evolved blob, ($\mathbf{c}_m$), and that of the observed spill, ($\mathbf{c}_g^*$). Mathematically this can be expressed as:

$$e(t^*) = \|\mathbf{c}_m(t^*) - \mathbf{c}_g^*\|. \tag{4.3}$$

Here, $\|\cdot\|$ denotes the modulus of the vector. The position of the centroid of the evolved spill, $\mathbf{c}_m$, depends on time t, while the centroid of the ground value slick $\mathbf{c}_g^*$ does not, since it is an observation at a final time, t^*. The centroid of a finite set of N points $\{\mathbf{x}_k\}_{k\in\mathbb{N}} \in \mathbb{R}^n$ is defined as:

$$\mathbf{c} = \frac{1}{N}\sum_{k=1}^{N} \mathbf{x}_k\,, \tag{4.4}$$

where $\mathbf{x}_k$ are the (lon, lat) coordinates that define the contour of the slick in an equirectangular projection. The solid black line e in panel (a) is the distance between centroids of the modelled and observed blobs. This is the value taken by Equation (4.3). The procedure is repeated for additional circles centered in different positions of the sub-domains or cells, in the neighbourhood of the accident . The evolution of each of these circular blobs is different due to the chaotic nature of transport in this setting. Panel (b) in Figure 4.2 provides a visualization on how this calculation changes in each sub-domain. This panel represents a colormap which is placed in the port neighbourhood, at the same position than the pink domain in panel (a). It considers a 6×6 mesh-grid, and the colorcode within each cell represents the value of Equation (4.3) obtained for blobs with initial positions in the center of each cell and initial radius of $r = 3.5 \cdot 10^{-3}(^\circ)$. We observe a nonuniform distribution.



a) b)

Figure 4.3 A quantitative measure of uncertainty for the Puertos del Estado model for la Luz Port, based on errors measured as distances to the target 'ground truth' spill. Higher colourmap values correspond to larger errors or uncertainties. The accident location is marked with a red asterisk. a) Uncertainties computed on a 11×11 mesh considering initial blobs with radius $r = 3.5 \cdot 10^{-4}(^\circ)$; b) uncertainties associated with a 20×20 mesh considering initial blobs with radius $r = 3.5 \cdot 10^{-5}(^\circ)$.

Figure 4.3 expands results of Figure 4.2b) by increasing the number of cells in the neighborhood domain and decreasing the radius of each initial blob. In particular, Figure

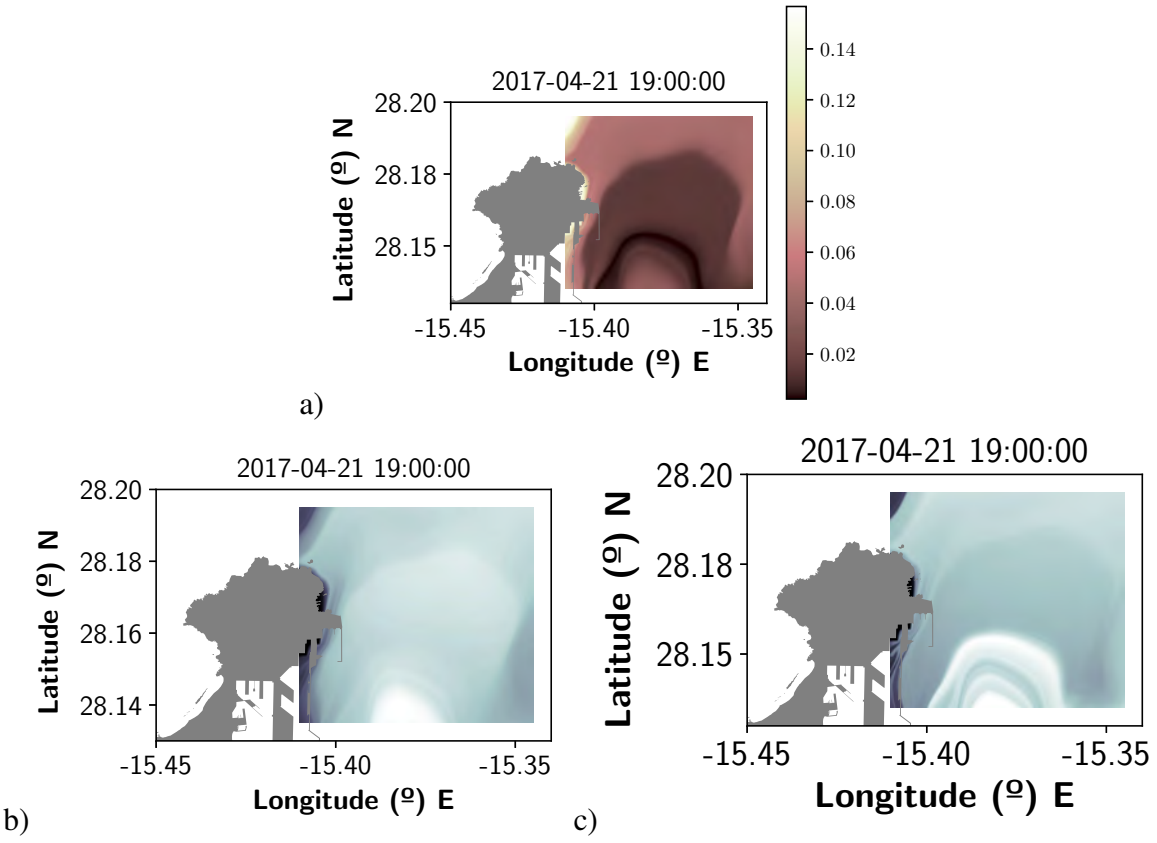


Figure 4.4 a) Evaluation of the Lagrangian uncertainty quantifier given in Equation (4.5); b) stable manifolds as revealed by the M function (4.7) using $\tau = 1.5$ days; c) stable manifolds as revealed by the M function using $\tau = 2$ days

4.3 a) considers a mesh 11×11 and initial blobs with radius $r = 3.5 \cdot 10^{-4}(^\circ)$. Figure 4.3 b) increases the number of cells to a 20×20 mesh-grid and decreases the radius of initial blobs to $3.5 \cdot 10^{-5}(^\circ)$. Figure 4.3b) makes visible an underlying structure which is directly related to the invariant dynamical structures, as we will shown later. In the limit $r \to 0$, expression (4.3) is rewritten as:

$$L_{UQ}(t^*) = \|\mathbf{x}(t^*) - \mathbf{c}_g^*\|. \tag{4.5}$$

where $\mathbf{x}(t)$ is a trajectory of a fluid parcel, a solution to the system (4.1), with initial position $\mathbf{x}_0$ at each cell in the grid. Figure 4.4a) illustrates the results of this calculation in a very fine grid. In a perfect model one would have expected that minimum uncertainty values would have been placed close to the point in which the accident occurred, however Figures 4.3 and 4.4a) do not show that, justifying that L_{UQ} is represented not just at the spill point, but in a domain close to it in order to gain insights into the quality of the model near the

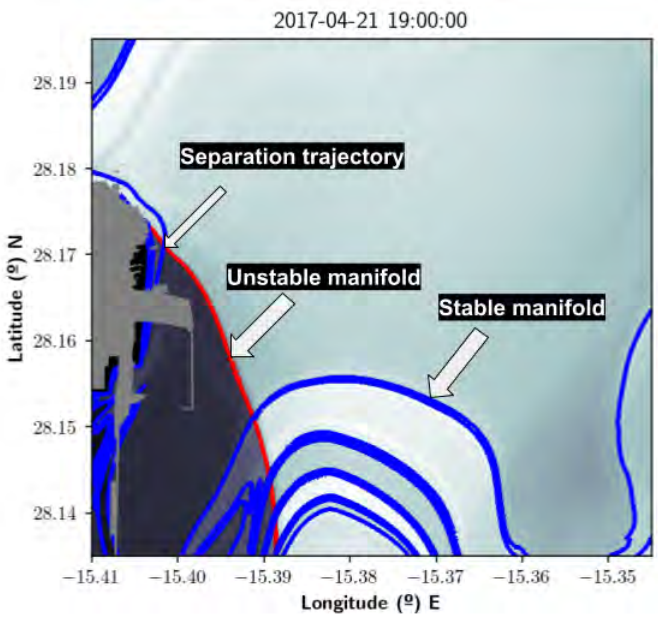


Figure 4.5 The Lagrangian skeleton of the ocean model on the accident day, the 21 April 2017 at 19:30h. LCSs are highlighted by the red and blue colors over the gray in the background.

initial observation. Next we discuss the distribution of minimum uncertainty values in this neighbourhood and its interpretation.

One of the goals of this paper is to establish connections between invariant dynamical objects that control transport in vector fields obtained from models and the uncertainty quantifier (4.5). The former are geometrical objects that organize the evolution of modelled particles schematically into regions corresponding to qualitatively distinct dynamical behaviors. In the context of fluid dynamics these objects are referred to as Lagrangian Coherent Structures (LCS). An essential ingredient of the LCS are hyperbolic trajectories characterized by high contraction and expansion rates. Directions of contraction and expansion define, respectively, stable and unstable directions, which are, respectively, related to the stable and unstable manifolds. In the context of the ocean model and the event described above, we have shown in Chapter 3 that there exists a hyperbolic trajectory located on the coastline very close to the accident point, in a detachment configuration, which is related to the phenomena of flow separation. Under this configuration, the stable manifold of the hyperbolic trajectory is aligned with the coast, and the unstable manifold is transversal to it. Figure 4.5 illustrates, respectively, in blue and red the stable and unstable manifolds of the separation trajectory for the studied case on the date the accident occurred. In the model any blob placed in the neighbourhood of the separation trajectory, eventually evolves to become aligned with the

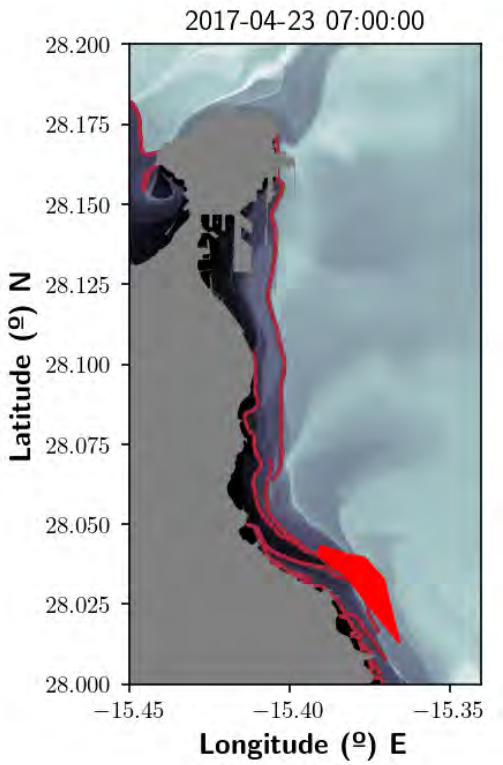


Figure 4.6 The Lagrangian skeleton of the ocean model on the 23rd April 2017 at 7:00 a.m, and the observed position of the spill according to satellite images (red blob). Unstable manifolds are highlighted by the red color over the gray in the background.

unstable manifold, which is an attracting material curve. Figure 4.6 shows the consistency between the model and observations. Indeed, the observed spill (in red) has evolved to become completely aligned with the unstable manifold. The technical justification underlying this behaviour would be the Inclination Lemma (also called the λ-Lemma) (Palis, 1969; Robbin et al., 1984) that roughly says that successive images of any disc transverse to the stable manifold of a hyperbolic fixed point eventually accumulate on the unstable manifold.

The invariant dynamical structures displayed in Figure 4.5 have been obtained by means of the Lagrangian Descriptor (Jiménez-Madrid and Mancho, 2009; Mancho et al., 2013; Mendoza and Mancho, 2010), which measures arc-length of trajectories:

$$M = \int_{t_0-\tau}^{t_0+\tau} \left\| \frac{d\mathbf{x}(t)}{dt} \right\| dt. \tag{4.6}$$

In Lopesino et al. (2017), for some generalizations of the expression (4.6), and for some specific vector fields, it is proved that stable and unstable manifolds are aligned with singular features of this function. The forward integration highlights the stable manifold, while

the backwards integration highlights the unstable manifold. In that work the notion of singular feature is related to an undefined directional derivative in a direction transverse to the manifold curve. In Figure 4.5, red and blue curves are placed on the singular features of M. These curves have been computed by processing the field provided by the Lagrangian Descriptor to extract its singular features. The processing is achieved by using the Canny algorithm implemented in the Python library opencv-python. Canny is an algorithm designed for edge detection. It is a basic algorithm for any line edge or contour detection that is accurate and easy to use. Although for the vector field under consideration there is not a formal proof that these lines correspond to stable and unstable manifolds, we refer to them like that because there exist results in the literature (De la Cámara et al., 2013; Mendoza and Mancho, 2010, 2012) in which, for vector fields coming from data sets like this one, it has been verified that stable and unstable manifolds are aligned with singular features of M. In those works this has been done by computing manifolds separately, with a high fidelity estimation method described in (M. et al., 2004; Mancho et al., 2006b, 2003), which has as its basis the local stable and unstable manifold theorem (Haller, 2001). Unstable manifolds displayed in Figure 4.6 are obtained similarly to those in Figure 4.5.

The metric given in (4.5) possess similarities with the forward definition of the function M:

$$M = \int_{t_0}^{t^*=t_0+\tau} \left\| \frac{d\mathbf{x}(t)}{dt} \right\| dt. \tag{4.7}$$

The analogy between structures obtained from expressions (4.5) and (4.7), is confirmed from Figure 4.4. Panel a) displays expression (4.5) results, while panels b) and c) display Equation (4.7) results for $\tau = 1.5$ and 2 days, respectively. Figure 4.4 highlights singularities both for the forward uncertainty quantifier and for the forward M function. From this figure it is clear that uncertainties displayed in panel a) reach minimum values along the stable manifold. In this case, since the observed evolution of the spill is aligned with the unstable manifold (see Figure 4.6), it is expected that minimum values of the uncertainty quantifier correspond to the stable manifold. Indeed, the stable manifold is an optimal pathway towards the unstable manifold (see the Inclination Lemma quoted above), which in turn is an attracting material curve towards which all modelled fluid parcels evolve after a transition time, and if the model is adequate also will behave this way for observed spills. On the other hand, indicators of *structural uncertainty* that show inadequacy of the model would correspond to situations in which these minimum values are not reached along the stable manifolds. For instance, this would have been the case if the observed spill in Figure 4.6 would have been found far from the unstable manifold.

4.2. Formal results

This section is focused on illustrating the analogies found in figure 4.4 between the pattern in panel a), which is related to uncertainty quantification, and those in panels b) and c), which are related to stable invariant manifolds. For the event described in the previous section computations in panel a) are performed with the measure proposed in Equation (4.5) to quantify uncertainty in a neighbourhood of the accident location. When the calculation is performed on a very fine grid it is found that the uncertainty L_{UQ} has a *structure* that is related to that of invariant stable manifolds. In order to find answers to the question of why there are singular structures obtained from the expression (4.5) that are aligned with invariant stable manifolds of hyperbolic trajectories, we need to assume an explicit expression for the vector field in Equation (4.1). Indeed in the example discussed in the previous section, velocities are given as data-sets and this makes difficult to proceed with exact calculations. In this way, in this section we perform an analysis in simplified planar vector fields with exact explicit expressions. Figure 4.7 displays such example. In panel a) an initial observation at time t_0 is marked with a red circle. At a later time, t^*, this observation is at the target position marked with a red asterisk. We model this evolution with the vector field at the background, which is represented at time t_0. In order to quantify the uncertainty in the neighbourhood of the initial observation, we display the evaluation of L_{UQ} around it. The colorbar placed at the bottom of the figure, measures the uncertainty in the domain units. This colorbar indicates that uncertainties in this neighbourhood are low. At least lower than those displayed for the experiment in panel b). In this case the initial observation is at a different position, although the target is kept at the same position than in a). In this case uncertainties are larger, indicating that the vector field in the background is not a good model to express the transition between these two observations. Finally panel c) displays L_{UQ} evaluated in the whole domain. This expresses the uncertainty associated to the planar flow, assuming that observations start in different points of the representation domain and that they evolve towards the assumed observed target position at the red asterisk. The panel confirms that model has a better performance for those initial observations placed at the diagonal. Results presented next in this section are displayed following this type of representation.

Our analysis in this section follows the spirit of the work by García-Garrido et al. (2018b); Lopesino et al. (2015, 2017); Mancho et al. (2013). We assume the definition of singular features given there, by considering that these are features of L_{UQ} on which the transversal derivative is not defined. We will prove, for simple selected examples, that stable manifolds are aligned with those singular features of L_{UQ}.

Finally, before beginning our discussion the definition (4.5) is generalized as follows:

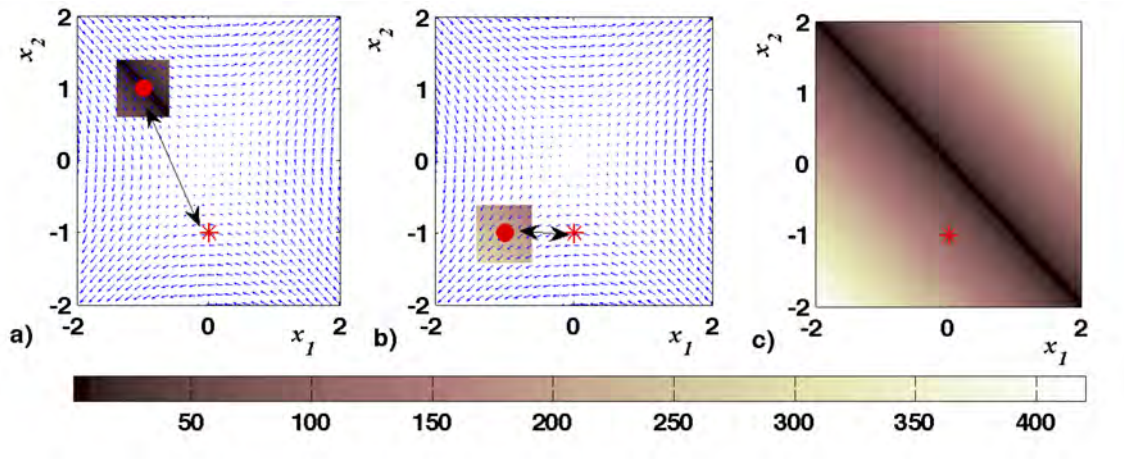


Figure 4.7 a) and b) two successive observations at time t_0 (red circle) and time t^* (red asterisk). The transition between them is modeled by the vector field at the background and L_{UQ} is represented in the neighbourhood of the initial observation. Uncertainties are lower for the case a) as confirmed by the colorbar; c) L_{UQ} evaluated in the whole domain. This expresses the uncertainty associated to the planar flow, assuming observations that start in different points of the representation domain and that evolve towards the red asterisk (target position).

$$L_{UQ}(\mathbf{x}_0,t,p,\delta) = \left[\sum_{i=1}^{n} |x_i(t) - x_i^*|^p\right]^{\frac{1}{p}},\ p > 1,\ \mathbf{x}_0 \in \mathbb{R}^n. \tag{4.8}$$

Here, $\mathbf{x}_0$ is the initial condition of the trajectory $(x_1(t),x_2(t),..,x_n(t))$. In the particular case described in the previous section $n = 2$, which corresponds to the ocean surface, and $p = 2$. The coordinates of the target $\mathbf{c}_g^*$ are (x_1^*,x_2^*) An alternative for this expression that we will use is the following:

$$L_{UQ}(\mathbf{x}_0,t,p) = \sum_{i=1}^{n} |x_i(t) - x_i^*|^p,\ p \leq 1,\ \mathbf{x}_0 \in \mathbb{R}^n. \tag{4.9}$$

4.2.1. The autonomous saddle point

The first example that we analyze is the vector field that corresponds to the Hamiltonian linear saddle case for which $\mathbf{x} \in \mathbb{R}^2$, satisfying $\mathbf{x} = (x,y)$ and the equations of motions are:

$$\begin{aligned} \frac{dx}{dt} &= \lambda x, \\ \frac{dy}{dt} &= -\lambda y, \end{aligned} \tag{4.10}$$

where $\lambda > 0$. For any initial observation (x_0, y_0), we consider the unique solution of this system passing through the condition (x_0, y_0), which is:

$$\begin{cases} x(t) = x_0 e^{\lambda t} \\ y(t) = y_0 e^{-\lambda t}, \end{cases} \qquad \lambda > 0 \tag{4.11}$$

For this example, the origin $(0,0)$ is a hyperbolic fixed point with stable and unstable manifolds:

$$W^s(0,0) = \{(x,y) \in \mathbb{R}^2 \colon x = 0, y \neq 0\}, \tag{4.12}$$

$$W^u(0,0) = \{(x,y) \in \mathbb{R}^2 \colon x \neq 0, y = 0\}, \tag{4.13}$$

For simplicity we assume, without loss of generality, that $t_0 = 0$ (this is possible for autonomous systems). We consider the target in the position (x^*, y^*) and apply (4.11) to (4.9) to obtain:

$$L_{UQ}(\mathbf{x}_0, t, p) = |x_0 e^{\lambda t} - x^*|^p + |y_0 e^{-\lambda t} - y^*|^p.$$

Regrouping terms, we get

$$L_{UQ}(\mathbf{x}_0, t, p) = |x_0|^p \omega^{-p} |1 - a\omega|^p + |y_0|^p |\omega - b|^p, \text{ where } a = \frac{x^*}{x_0}, b = \frac{y^*}{y_0}. \tag{4.14}$$

In this expression, $\omega = e^{-\lambda t}$, which always satisfies $\omega > 0$. We explore separately the first and second terms. For the factor $|1 - a\omega|^p$ there exists a t_L such that if $t > t_L$, then $a\omega << 1$ and $(1 - a\omega) > 0$. This is always the case for $a < 0$ and is a plausible assumption for $a > 0$, if $a << \omega^{-1}$. We recall that $a = x^*/x_0$ and that therefore such t_L exists if $x_0 \neq 0$. In this case positiveness is guaranteed for sufficiently large t, i.e, a Taylor series around $\omega = 0$, attained if $t \gg 1$ and $t > t_L$, is performed for the binomial:

$$(1 - a\omega)^p = 1 - ap\omega + \frac{1}{2}a^2(p-1)p\omega^2 - \frac{1}{6}\omega^3\left(a^3(p-2)(p-1)p\right) + O\left(\omega^4\right).$$

Therefore,

$$\frac{1}{\omega^p}(1 - a\omega)^p = \omega^{-p} + ap\omega^{(1-p)} + \frac{1}{2}a^2(p-1)p\omega^{(2-p)} + O\left(\omega^{(3-p)}\right).$$

We recall that $p \leq 1$ and $\omega = e^{-\lambda t}$. This yields,

$$|x_0|^p |e^{\lambda t} - a|^p = |x_0|^p e^{\lambda t p} + O\left(|x_0|^p a e^{-\lambda t(1-p)}\right).$$

We analyse next the second term in Equation (4.14). The sign of $(\omega - b)$ depends crucially on the sign of b given that for $t \gg 1$ the term ω can be as small as we like. Let us consider t_L such that if $t > t_L$ and $b < 0$, then $(e^{-\lambda t} - b) > 0$. The following is valid for t above this lower value:

$$|\omega - b|^p = (\omega - b)^p = (-b)^p + p\omega(-b)^{p-1} + \frac{1}{2}(p-1)p\omega^2(-b)^{p-2}$$

$$+\frac{1}{6}(p-2)(p-1)p\omega^3(-b)^{p-3} + O\left(\omega^4\right)$$

Therefore, when $t \gg 1$, $b < 0$ and $e^{-\lambda t} \ll 1$,

$$(\omega - b)^p = (-b)^p + O\left(e^{-\lambda t}\right), e^{-\lambda t} \ll 1 \tag{4.15}$$

Now, we consider $b > 0$ and $t > t_L$ satisfying $(\omega - b) < 0$. Therefore:

$$|\omega - b|^p = (-\omega + b)^p = b^p + p\omega b^{p-1} + \frac{1}{2}(p-1)p\omega^2 b^{p-2}$$

$$+\frac{1}{6}(p-2)(p-1)p\omega^3 b^{p-3} + O\left(\omega^4\right).$$

Therefore, when $t \gg 1$, $b > 0$ and $e^{-\lambda t} \ll 1$,

$$(-\omega + b)^p = b^p + O(\omega). \tag{4.16}$$

Finally, we conclude that

$$|\omega - b|^p = |b|^p + O\left(e^{-\lambda t}\right), \omega \ll 1. \tag{4.17}$$

Therefore, since $b = y^*/y_0$

$$|y_0|^p |e^{-\lambda t} - b|^p = |y^*|^p + O\left(|y_0|^p e^{-\lambda t}\right), e^{-\lambda t} \ll 1.$$

Thus, we can approximate L_{UQ} as

$$L_{UQ}(\mathbf{x}_0, t, p) \approx |x_0 e^{\lambda t}|^p + |y^*|^p = |x_0| e^{\lambda t p} + |y^*|^p \tag{4.18}$$

where the dominant term is $|x_0|^p e^{\lambda t p}$. Hence, to leading order, the stable manifold at $x = 0$ is aligned with a singular feature of L_{UQ} for 'sufficiently large' t. This statement however must

be considered in the sense that expression (4.18) expresses a good approximation for L_{UQ} as far as $x_0 \neq 0$, and that for any $|x_0| > 0$ is valid for a sufficient large t satisfying, $t > t_L$.

We have shown that Equation (4.9) is able to highlight the stable manifolds for the autonomous saddle point. Next, we analyse what happens when we consider Equation (4.8), and in which cases it provides information about the stable manifold of the autonomous saddle point. When we apply (4.11) to (4.8), it yields

$$L_{UQ}(\mathbf{x}_0,t,p) = \left[|x_0 e^{\lambda t} - x^*|^p + |y_0 e^{-\lambda t} - y^*|^p\right]^{1/p}.$$

We remark that our following calculations will be restricted to $p > 1$ and integer. Rewriting the expression for $\omega = e^{-\lambda t}$

$$L_{UQ}(\mathbf{x}_0,t,p) = \left[\left|\frac{x_0}{\omega}\right|^p |1 - a\omega|^p + |y_0|^p |\omega - b|^p\right]^{1/p} \tag{4.19}$$

$$= \left|\frac{x_0}{\omega}\right| \left[|1 - a\omega|^p + \left|\frac{y_0}{x_0}\right|^p \omega^p |\omega - b|^p\right]^{1/p} \tag{4.20}$$

Recalling that $p > 1$, $\omega > 0$ and that $(1 - a\omega) > 0$ for sufficiently small ω, i.e. sufficiently large t, and the case $b < 0$ and $(\omega - b) > 0$, a Taylor series around $\omega = 0$, for p integer number, for the second factor:

$$L_{UQ}(\mathbf{x}_0,t,p) = \left|\frac{x_0}{\omega}\right| \left[1 - a\omega + \left|\frac{y_0}{x_0}\right|^p (-b)^p \frac{\omega^p}{p} + O(\omega)^{p+1}\right] \tag{4.21}$$

Alternatively, considering the case $b > 0$ and $(\omega - b) < 0$, a Taylor series around $\omega = 0$ for the second factor is as follows:

$$L_{UQ}(\mathbf{x}_0,t,p) = \left|\frac{x_0}{\omega}\right| \left[1 - a\omega + \left|\frac{y_0}{x_0}\right|^p (b)^p \frac{\omega^p}{p} + O(\omega)^{p+1}\right] \tag{4.22}$$

Therefore in general:

$$L_{UQ}(\mathbf{x}_0,t,p) = \left|\frac{x_0}{\omega}\right| \left[1 - a\omega + \left|\frac{y_0}{x_0}\right|^p |b|^p \frac{\omega^p}{p} + O(\omega)^{p+1}\right]$$

$$= \left|\frac{x_0}{\omega}\right| - a|x_0| + |y_0|^p |x_0|^{1-p} \frac{|b|^p}{p} \omega^{p-1} + O(\omega)^p \tag{4.23}$$

We notice that since $p > 1$, the terms ω^{p-1}, ω^p have positive exponents and if $\omega \ll 1$ in principle are much smaller than the first term ω^{-1} and therefore:

$$L_{UQ}(\mathbf{x}_0, t, p) \sim \frac{1}{p}\left|\frac{x_0}{\omega}\right|, \ \omega \ll 1 \tag{4.24}$$

Hence, the stable manifold at $x = 0$ is aligned with a singular feature of this approximation to L_{UQ} for 'sufficiently large' t. This statement though, must be considered with care, because in Equation (4.23) the terms in ω^{p-1}, ω^p, are multiplied by $|x_0|^{1-p}$ which has a negative exponent, and therefore have a singularity at $x_0 = 0$. For this reason neglecting these terms versus the first one if we are very close to $x_0 = 0$ would require checking that the products, such as, $|x_0|^{1-p}\omega^{p-1}$ are really small. This implies that Equation (4.24) is correctly approximating L_{UQ} for $\omega \ll 1$ as far as we are sufficiently away from 0 in x_0, i.e. $|x_0|^{1-p}\omega^{p-1} \ll 1 \implies \omega^{p-1} \ll |x_0|^{p-1}$. In practice this condition is satisfied for any grid (x_0, y_0) used in later figures that exclude $x_0 = 0$. Also we can state that for sufficiently large t, L_{UQ} is very close in almost all the domain to the function given in Equation (4.24), which possess a "singular feature" aligned with the stable manifold. Figure 4.8 a) and b), illustrates how the stable manifold is aligned with singular features of the Lagrangian uncertainty quantifier defined either by Equation (4.8) or (4.9).

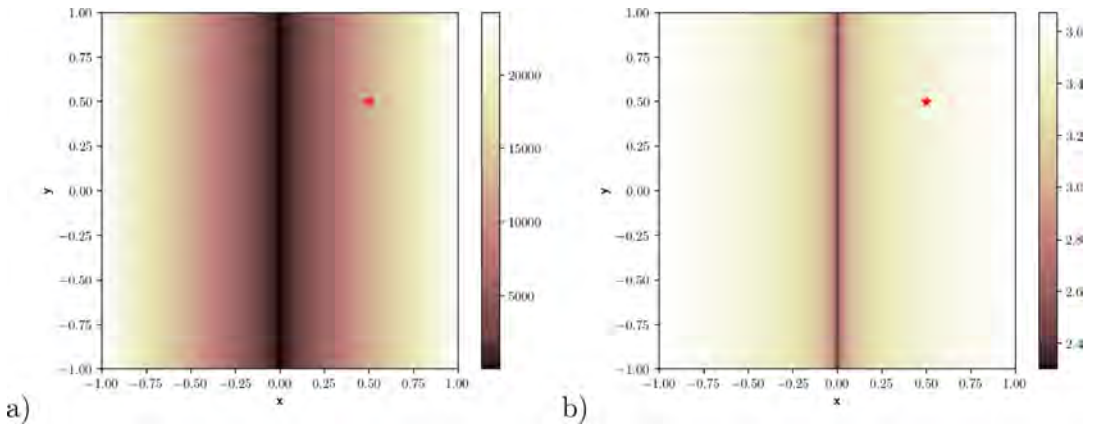


Figure 4.8 A representation of Equation (4.8) and Equation (4.9) for $t^* = 10$ and target $(x^*, y^*) = (0.5, 0.5)$ for the Hamiltonian linear saddle vector field. a) $p = 2$; b) $p = 0.1$. It can be appreciated how the stable manifold is aligned with a singular feature.

4.2.2. The autonomous rotated saddle point

This second case that we explore is the vector field of the rotated linear saddle for which the equations of motion are:

$$\begin{cases} \dot{x} = \lambda y \\ \dot{y} = \lambda x, \end{cases} \qquad \lambda > 0 \tag{4.25}$$

The general solution to this system is:

$$\begin{cases} x(t) = ae^{\lambda t} + be^{-\lambda t} \\ y(t) = ae^{\lambda t} - be^{-\lambda t}, \end{cases} \qquad \lambda > 0 \tag{4.26}$$

where a and b depend on the initial conditions x_0 and y_0 as follows:

$$a = \frac{x_0 + y_0}{2},\ b = \frac{x_0 - y_0}{2}.$$

Here, $a = 0$ corresponds to the stable manifold of the hyperbolic fixed point placed at the origin and $b = 0$ corresponds to its unstable manifold.

For any initial observation (x_0, y_0) and final target observation (x^*, y^*), we introduce the solution (4.26) into Equation (4.9) obtaining:

$$L_{UQ}(\mathbf{x}, t, p) = |ae^{\lambda t} + be^{-\lambda t} - x^*|^p + |ae^{\lambda t} - be^{-\lambda t} - y^*|^p \tag{4.27}$$

We expand next the first term in Equation (4.27). In particular, we consider the case in which $a > 0$ for which it is always possible to find a $t > t_L$ in which $(ae^{\lambda t} + be^{-\lambda t} - x^*) > 0$:

$$|ae^{\lambda t} + be^{-\lambda t} - x^*|^p = (ae^{\lambda t} + be^{-\lambda t} - x^*)^p = \left(\frac{a}{\omega} + b\omega - x^*\right)^p$$

$$= \omega^{-p}\left(a + b\omega^2 - x^*\omega\right)^p,$$

Here we have used $\omega = e^{-\lambda t}$. The Taylor expansion of the binomial when $\omega \ll 1$, i.e., when $t \gg 1$, is

$$\omega^{-p}\left(a + b\omega^2 - x^*\omega\right)^p = \omega^{-p}\left[a^p - p\omega x^* a^{p-1} + \omega^2\left(bpa^{p-1} + \frac{1}{2}(p-1)p(x^*)^2 a^{p-2}\right)\right.$$

$$\left. -\frac{1}{6}\omega^3\left((p-1)px^* a^{p-3}\left(6ab + p(x^*)^2 - 2(x^*)^2\right)\right) + O\left(\omega^4\right)\right].$$

Therefore,

$$\omega^{-p}\left(a+b\omega^2-x^*\omega\right)^p = a\omega^{-p} - p\omega x^* a^{p-1} + \omega^{(2-p)}\left(bpa^{p-1}+\frac{1}{2}(p-1)p(x^*)^2a^{p-2}\right)$$

$$-\frac{1}{6}\omega^{(3-p)}\left((p-1)px^*a^{p-3}\left(6ab+p(x^*)^2-2(x^*)^2\right)\right)+O\left(\omega^{(4-p)}\right)$$

Since $p<1$, $\omega^{(n-p)} \ll 1$ for $n>1$ when $t \gg 1$. Hence,

$$\omega^{-pt}\left(a+b\omega^{2t}-x^*\omega^t\right)^p = a^p\omega^{-pt}+O\left(\omega^{(1-p)t}\right).$$

By removing the change of variable, we obtain

$$\left(ae^{\lambda t}+be^{-\lambda t}-x^*\right)^p = a^p e^{\lambda pt}+O\left(e^{-(1-p)\lambda t}\right) \approx a^p e^{\lambda pt}, \text{ when, } t \gg 1. \tag{4.28}$$

We consider now the case $a<0$ that implies $\left(ae^{\lambda t}+be^{-\lambda t}-x^*\right)<0$ for some sufficiently large t. The Taylor series is the same, except for a minus sign. It yields,

$$\left(ae^{\lambda t}+be^{-\lambda t}-x^*\right)^p = -a^p e^{\lambda pt}-O\left(e^{-(1-p)\lambda t}\right) \approx -a^p e^{\lambda pt}, \text{ when, } t \gg 1. \tag{4.29}$$

Finally,

$$|ae^{\lambda t}+be^{-\lambda t}-x^*|^p = |a|^p e^{\lambda pt}+O\left(e^{-(1-p)\lambda t}\right) \approx |a|^p e^{\lambda pt}, \text{ when, } t \gg 1. \tag{4.30}$$

We analyse next the second term in Equation (4.27). As before, we start considering the case $a>0$ and $(ae^{\lambda t}-be^{-\lambda t}+y^*)>0$. After making the change of variable $\omega = e^{-\lambda t}$ we obtain:

$$\omega^{-p}\left(a-b\omega^2-y^*\omega^t\right)^p = \omega^{-p}\left[a^p - p\omega^t y^* a^{p-1} - \frac{1}{2}\omega^2\left(pa^{p-2}\left(2ab-p(y^*)^2+(y^*)^2\right)\right)\right.$$

$$\left.+\frac{1}{6}(p-1)p\omega^3 y^* a^{p-3}\left(6ab-p(y^*)^2+2(y^*)^2\right)+O\left(\omega^4\right)\right].$$

Since $p<1$, $\omega^{(n-p)} \ll 1$ for $n>1$ when $t \gg 1$. Hence,

$$\omega^{-p}\left(a-b\omega^2+y^*\omega\right)^p = a^p\omega^{-p}+O\left(\omega^{(1-p)}\right).$$

By removing the change of variable, we obtain:

$$\left(ae^{\lambda t} - be^{-\lambda t} - y^*\right)^p = a^p e^{\lambda pt} + O\left(e^{-(1-p)\lambda t}\right) \approx a^p e^{\lambda pt}, \text{ when, } t \gg 1. \tag{4.31}$$

We compute the same term but in the case $a < 0$ $\left(ae^{\lambda t} - be^{-\lambda t} - y^*\right) < 0$. The Taylor series is the same, except for a minus sign. It yields,

$$\left(ae^{\lambda t} - be^{-\lambda t} - y^*\right)^p = -a^p e^{\lambda pt} - O\left(e^{-(1-p)\lambda t}\right) \approx -a^p e^{\lambda pt}, \text{ when, } t \gg 1. \tag{4.32}$$

Finally,

$$|ae^{\lambda t} - be^{-\lambda t} - y^*|^p = |a|^p e^{\lambda pt} + O\left(e^{-(1-p)\lambda t}\right) \approx |a|^p e^{\lambda pt}, \text{ when, } t \gg 1. \tag{4.33}$$

Thus,

$$L_{UQ} = |ae^{\lambda t} + be^{-\lambda t} - x^*|^p + |ae^{\lambda t} - be^{-\lambda t} + y^*|^p \approx |a|^p e^{\lambda pt}, \text{ when, } t \gg 1. \tag{4.34}$$

The stable manifold at $a = 0$ is aligned with a singular feature also at $a = 0$.

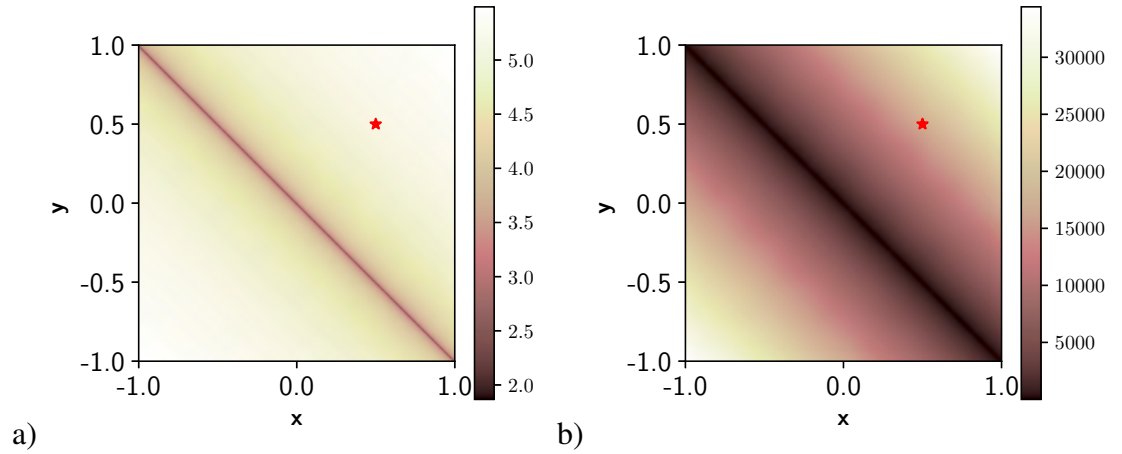
As for Equation (4.8) considering $p > 1$, $p = 1/\delta$ and $\omega = e^{-\lambda t}$ leads:

$$\begin{aligned} L_{UQ} &= \left[|ae^{\lambda t} + be^{-\lambda t} - x^*|^p + |ae^{\lambda t} - be^{-\lambda t} + y^*|^p\right]^{1/p} \\ &= \omega^{-1}\left[|a + b\omega^2 - x^*\omega|^p + |a - b\omega^2 + y^*\omega|^p\right]^{1/p} \\ &= 2^{\frac{1}{p}}|a|\omega^{-1} - 2^{-1+\frac{1}{p}}(2b + x^* - y^*) + 2^{-3+\frac{1}{p}}|a|^{-1} \cdot \\ &\quad (4ab + (-1+p)(-2b + x^* + y^*)^2)\omega + O(\omega)^2 \end{aligned} \tag{4.35}$$

As before the leading term in ω leads to:

$$L_{UQ} \sim 2^{\frac{1}{p}}|a|\omega^{-1} \tag{4.36}$$

and similar considerations apply in neglected terms to the ones made for Equation (4.23), but now regarding to singularities at $a = 0$. Figure 4.9 a) and b), illustrate how the stable manifold is aligned with singular features of the Lagrangian uncertainty quantifier defined either by Equation (4.8) or (4.9).



a) b)

Figure 4.9 A representation of Equation (4.8) and Equation (4.9) for $t^* = 10$ and target $(x^*, y^*) = (0.5, 0.5)$ for the rotated linear saddle vector field for a) $p = 2$; b) $p = 0.1$. It can be appreciated how the stable manifold is aligned with a singular feature.

4.2.3. Discrete maps

These findings in the previous two subsections can be easily extended to discrete time dynamical systems, which are also useful in applications. Discrete time dynamical systems are defined as maps.

The autonomous saddle point

Consider the following linear, area-preserving autonomous map:

$$\begin{cases} x_{n+1} = \lambda x_n \\ y_{n+1} = \frac{1}{\lambda} y_n, \end{cases} \qquad \lambda > 1. \tag{4.37}$$

For an initial condition (x_0, y_0), the unique solution of this system is:

$$\begin{cases} x_n = x_0 \lambda^n \\ y_n = y_0 \lambda^{-n}, \end{cases} \qquad \lambda > 1. \tag{4.38}$$

As for the continuous time case, the origin $(0,0)$ is a hyperbolic fixed point with stable and unstable manifolds:

$$W^s(0,0) = \{(x,y) \in \mathbb{R}^2 : x = 0, y \neq 0\}, \tag{4.39}$$

$$W^u(0,0) = \{(x,y) \in \mathbb{R}^2 : x \neq 0, y = 0\}, \tag{4.40}$$

We apply (4.38) to (4.9) to obtain:

$$L_{UQ}(\mathbf{x},n,p) = |x_0\lambda^n - x^*|^p + |y_0\lambda^{-n} - y^*|^p. \tag{4.41}$$

Regrouping terms, we get

$$L_{UQ}(\mathbf{x},n,p) = |x_0|^p|\lambda^n - a|^p + |y_0|^p|\lambda^{-n} - b|^p, \text{ where } a = \frac{x^*}{x_0}, b = \frac{y^*}{y_0}. \tag{4.42}$$

Considering that the transformation $e^{\lambda t} \to \lambda^n$ can be directly applied to all the calculations performed in the continuous time case, we recover from Equation (4.14):

$$L_{UQ} \approx |x_0|^p|\lambda^{np}| + O\left(|\lambda|^{-n(1-p)}\right), \text{ when, } n \gg 1. \tag{4.43}$$

When $p < 1$, the dominant term is $|x_0|^p\lambda^{np}$. Hence, the stable manifold at $x = 0$ is aligned with singular features of L_{UQ} for 'sufficiently large' iteration n.

The same is applicable to L_{UQ} (4.8). It yields,

$$L_{UQ} \approx |x_0||\lambda^n| + O(1), \text{ when, } n \gg 1 \text{ and } p\delta < 1. \tag{4.44}$$

We note that the stable manifold at $x = 0$ is aligned with singular features of L_{UQ} for a 'sufficiently large' iteration n. The same issues as before regarding singularities on the manifold position apply.

Figure 4.10 a) and b), illustrate how the stable manifold is aligned with singular features of the Lagrangian uncertainty quantifier defined either by Equation (4.8) or (4.9).

The autonomous rotated saddle point

We consider the following discrete dynamical system:

$$F(x,y) = A\begin{pmatrix} x \\ y \end{pmatrix}, \text{ where } A = \frac{1}{2\lambda}\begin{pmatrix} \lambda^2+1 & \lambda^2-1 \\ \lambda^2-1 & \lambda^2+1 \end{pmatrix}, \ \lambda > 1. \tag{4.45}$$

It is easy to see that the stable and the unstable manifolds are given by the vectors $(1,-1)$ and $(1,1)$ respectively. The solution of this system yields to,

$$\begin{cases} x_n = a\lambda^n + b\lambda^{-n} \\ y_n = a\lambda^n - b\lambda^{-n}, \end{cases} \qquad \lambda > 1 \tag{4.46}$$

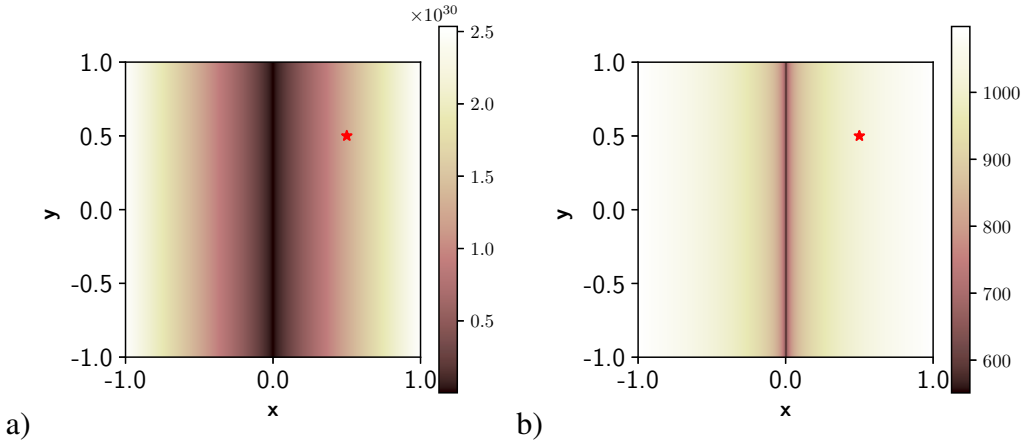


Figure 4.10 In Figure a) there is a representation for the autonomous saddle when we apply Equation (4.8) for $p = 2$. In b), we illustrate the same representation but for Equation (4.9) when $p = 0.1$. It can be appreciated how the stable manifold is aligned with the singular feature.

where

$$a = \frac{x_0 + y_0}{2},\ b = \frac{x_0 - y_0}{2}.$$

Again considering the transformation $e^{\lambda t} \to \lambda^n$ and the use of previous results for the continuous time case, we recover from Equation (4.34):

$$L_{UQ}(\mathbf{x}, n, p) = |a\lambda^n + b\lambda^{-n} - x^*|^p + |a\lambda^n - b\lambda^{-n} - y^*|^p.$$

Therefore, the dominant term is

$$L_{UQ}(\mathbf{x}, n, p) \sim |a|^p |\lambda|^{np}.$$

Since $a = \frac{x_0+y_0}{2}$, there is a singular feature at $x = -y$, i.e., in the subspace generated by $(1, -1)$. Hence, the stable manifold is aligned with a singular feature of L_{UQ}.

The same is applicable to L_{UQ} (4.8). It yields,

$$L_{UQ}(\mathbf{x}, n, p) \sim |a||\lambda|^n,$$

Hence, the stable manifold is aligned with a singular feature of L_{UQ}. Figure 4.11 a) and b), illustrates how the stable manifold is aligned with singular features of the Lagrangian uncertainty quantifier defined either by Equation (4.8) or (4.9).

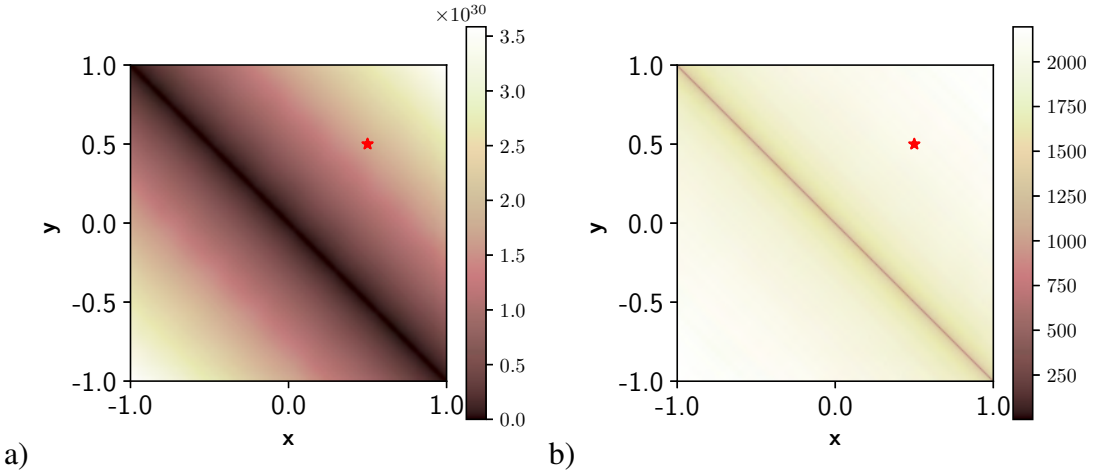


Figure 4.11 In Figure a) there is a representation for the rotated saddle when we apply Equation (4.8) for $p = 1/\delta = 2$. In b), we illustrate the same representation but for Equation (4.8) when $p = 1/\delta = 0.1$. It can be appreciate how the singular feature is aligned with stable manifold.

4.3. The Duffing equation

Results in the previous sections are generalized to the autonomous nonlinear case by means of the Moser's theorem (Moser, 1956). This theorem applies to analytic two-dimensional symplectic maps having a hyperbolic fixed point or, similarly, to two-dimensional time-periodic Hamiltonian vector fields having a hyperbolic periodic orbit (which can be reduced to the former case considering a Poincaré map). The case of a Hamiltonian nonlinear autonomous system is a one-parameter family of symplectic maps, and therefore Moser's theorem applies. Following proofs sketched by Lopesino et al. (2015, 2017) results may be extended to the case of non-autonomous nonlinear dynamical systems by utilizing results like the Hartman–Groβman theorem.

This section discusses further results on the Lagrangian Uncertainty Quantifier by considering the evaluation of (4.8) over a vector field obtained from the nonlinear periodically forced Duffing equation:

$$\begin{aligned} \dot{x} &= y \\ \dot{y} &= x - x^3 + \varepsilon \sin t \end{aligned} \tag{4.47}$$

Prior to discuss outputs of (4.8) into Equation (4.47), we discuss the structure of invariant manifolds of hyperbolic trajectories in Equation (4.47) for the case $\varepsilon = 0.1$ and the persistence versus this time dependent perturbation of tori present in the unforced version of Equation

(4.47), i. e, $\varepsilon = 0$. In the perturbed case, the hyperbolic fixed point placed at the origin, becomes a hyperbolic periodic trajectory (Jiménez-Madrid and Mancho, 2009), and their stable and unstable manifold can be highlighted by the Equation 4.6 appeared in Section 2 (Mancho et al., 2013). Additionally, as discussed in (Lopesino et al., 2017) a scale factor $1/(2\tau)$ applied to (4.6) converts the expression to an average, which in compact Hamiltonian systems like (4.47) converges for $\tau \to \infty$ and when this convergence is observed, level curves correspond to invariant structures of the dynamical system. Convergence of means are computationally verifiable on tori, however on hyperbolic sets as discussed in (García-Garrido et al., 2018a), rounding computational errors practically prevent convergence. Figure

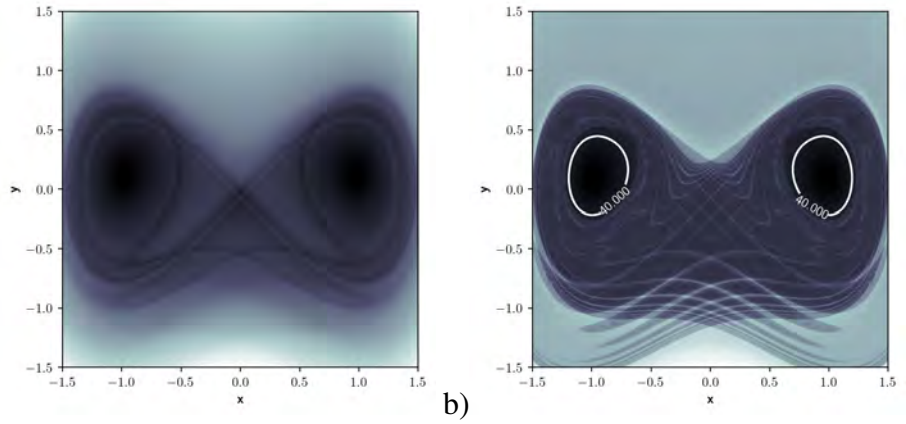


Figure 4.12 Evaluation of (4.6) for the Duffing equation (4.47) at $t_0 = 0$. a) $\tau = 10$; b) $\tau = 50$. At this τ the average of M in the smooth regions has converged and the level curve represent and invariant tori.

4.12 illustrates these points. Panel a) shows invariant manifolds related to the hyperbolic trajectory that are obtained from (4.6) for $\tau = 10$. These structures become much more rich for larger τ as panel b) confirms. In this panel since the average of M has converged in the smooth region, level curves in the area highlight tori. The outputs of Figure 4.12a) may be split into two figures, by separating the backwards and forwards integration of Equation (4.6), which displays, respectively, the unstable and stable manifolds. These outputs are depicted, respectively, in Figure 4.13a) and b).

Figure 4.14 shows the evaluation of L_{UQ} as in Equation (4.8) with $p = 2$ for $t_0 = 0$, $t = t_0 + \tau = 10$ and different targets. In panel a) the chosen target is $\mathbf{x}^* = (0.1, 0.1)$. This target is within the chaotic region displayed in Figure 4.12b), close to the unstable manifold of the Duffing equation. It is observed that minimum values are reached on the stable manifold and that the structure of L_{UQ} is correlated to it. This setting is similar to what was observed for the ocean case described in Section 2, in which the observed oil evolution is aligned

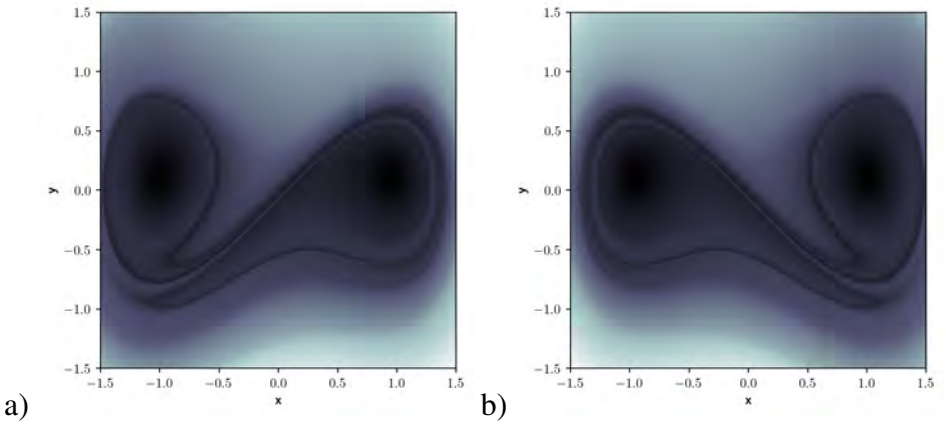


Figure 4.13 a) Evaluation of the backwards integration of (4.6) on the Duffing equation (4.47) at $t_0 = 0$ and $\tau = 10$. This represents the unstable manifold; b) Evaluation of the forwards integration of (4.6) on the Duffing equation (4.47) at $t_0 = 0$ and $\tau = 10$. This represents the stable manifold.

with the unstable manifold and minimum values of L_{UQ} are found on the stable manifold that are optimal pathways towards the unstable manifolds. In panel b) we show the results for the target $\mathbf{x}^* = (1,0)$ which is within the right tori like structure highlighted in Figure 4.12b). Accordingly, uncertainty values are very low for initial observations (x_0, y_0) in the corresponding tori region, but very high for the tori like region at the left side. Indeed initial observations in this region will never go near a final observation in the right tori like structure, and therefore this model is *structurally uncertain* for those observations, i.e. the model is inadequate to represent those. Panel c) shows the computation of the uncertainty for a target $\mathbf{x}^* = (0,1)$ outside the geometry of the unstable invariant manifold displayed in Figure 4.13a). It is remarkable the persistence in all these examples of an structure on the uncertainty field with singular features linked to the stable manifold independently of the target value $\mathbf{x}^*$.

Figure 4.15 shows the evaluation of Equation (4.9) with $p = 0.1$, and different targets or integration periods. Panels a) and b) have the same integration periods, but different targets. In them the black arrow points out different features that seem singular but *do not correspond to any invariant manifold* and in this sense they are spurious. This finding suggests that care must be taken in the invariant interpretation of singular features of Equation (4.8) and Equation (4.9), although these features truly represent the structure of uncertainty and in this sense they are not spurious. In the next section we will present results in the literature that have used an equation similar to (4.8) to highlight Lagrangian structures. Figure 4.15 c) shows the same than panel a) for an integration period of 50. The black arrow marks a region, which from the analysis of Figure 4.12, is known to be covered by tori, while the structure

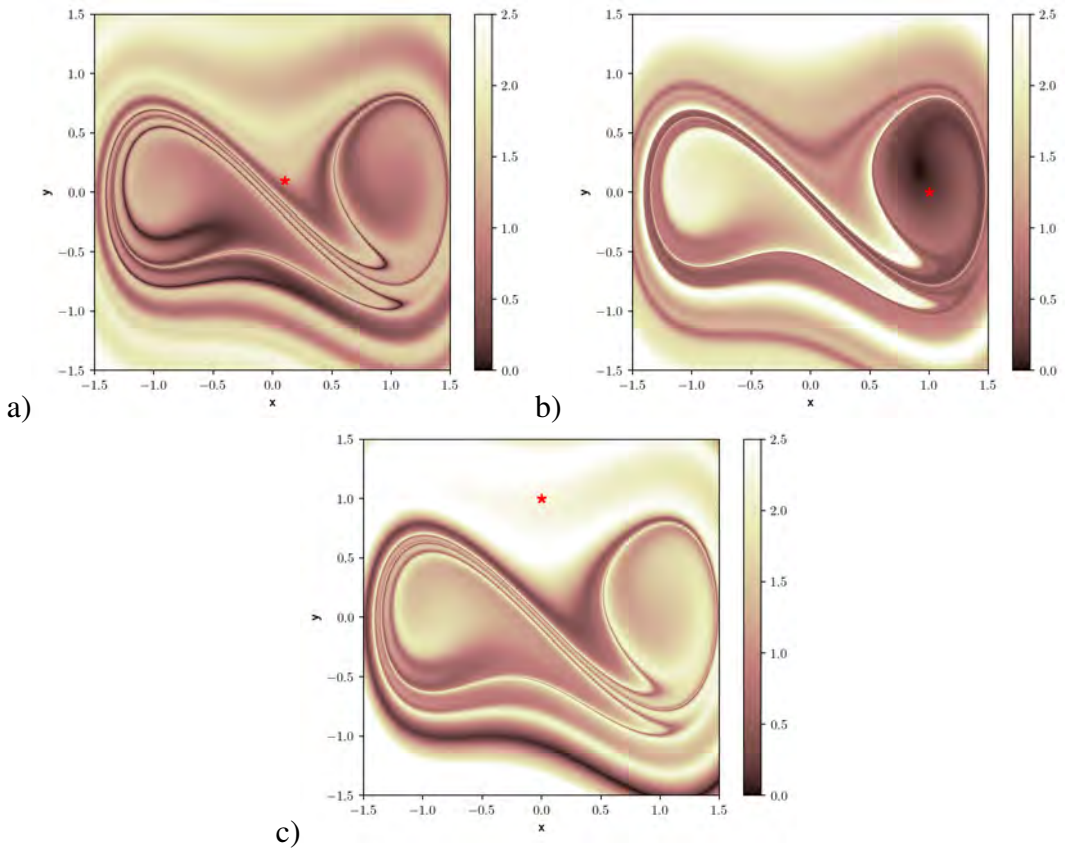


Figure 4.14 Evaluation of Equation (4.8) on the Duffing equation (4.47) at $t_0 = 0, t = t_0 + \tau = 10$ with different targets. a) Target $\mathbf{x}^* = (0.1, 0.1)$; b) target $\mathbf{x}^* = (1, 0)$; c) target $\mathbf{x}^* = (0, 1)$.

attained from Equation (4.9) does not highlight this, again showing the presence of patterns that do not have an invariant interpretation. Indeed, the ergodic partition theory discussed in (Mezić and Wiggins, 1999; Susuki and Mezić, 2009) and implemented in (Lopesino et al., 2017) for Lagrangian Descriptors such as that in Equation (4.6), shows that this ability to highlight tori, requires averaging along trajectories, while expressions Equation (4.8) or (4.9) *are not averages*, and therefore do not qualify for the application of ergodic principles. These expressions are not suitable for identifying this kind of invariant objects.

4.4. Discussion

Our formal results have shown that expressions for uncertainty quantification given in equations (4.8) and (4.9) provide singular features associated to the stable invariant manifolds of a hyperbolic trajectory. The numerical evidence found in the realistic ocean application that has motivated the current work indicates that more complex flows in which more hyperbolic

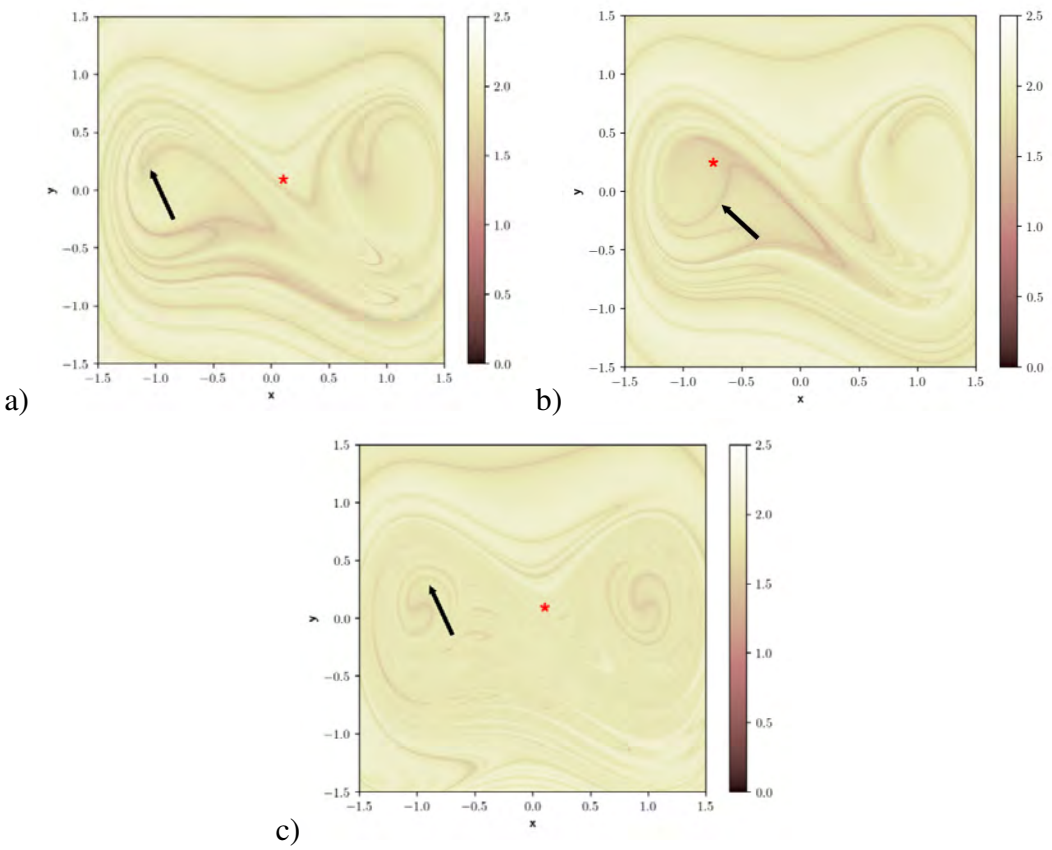


Figure 4.15 Evaluation of Equation (4.9) on the Duffing equation (4.47) at $t_0 = 0$, for $p = 0.1$ and different targets. Black arrows highlight features that for this system are known to be spurious. a) $t_0 = 0$, $t = t_0 + \tau = 10$ and target $\mathbf{x}^* = (0.1, 0.1)$; b) $t_0 = 0$, $t = t_0 + \tau = 10$ and target $\mathbf{x}^* = (-0.75, 0.25)$; c) $t_0 = 0$, $t = t_0 + \tau = 50$ and target $\mathbf{x}^* = (0.1, 0.1)$

trajectories are present will behave the same for each hyperbolic trajectory. The fact that L_{UQ} possess a structure associated with stable invariant manifolds, indicates that in time dependent flows its structure will become more and more complex in longer time intervals, as does the structure of stable manifolds (Mancho et al., 2013; Mendoza and Mancho, 2010). This reveals new hints about the behaviour of uncertainty measurements in long time intervals, which are missed by measures of uncertainty just focused on averages or statistical moments of distributions. However, these statistical measurements are still of much interest to quantify with just one representative number the performance of a data set in a specific application. For instance, if the average of L_{UQ} is considered to be a representative number for uncertainty, the associated uncertainty for the model discussed in the introduction for Figures 4.3a), 4.3b) and 4.4a) is respectively, $0.033°$, $0.031°$ or $0.030°$. A comparison of this number for different

models allows for determining which one is the most appropriate for describing a particular observation (see Chapter 3).

Recently, there has been much interest in uncertainty quantification involving trajectories in ocean data sets. Efforts in this direction are (Feng et al., 2019; Huntley et al., 2011; Kirwan et al., 2003; Vieira et al., 2020). Vieira et al. (Vieira et al., 2020) have developed a clustering method to partition the space of trajectory data sets into distinct flow regions. This method contains free parameters and they use uncertainty quantification to assess the parameter dependence on the partitions they obtain. The work (Feng et al., 2019) discusses approaches for uncertainty quantification from a geometrical perspective, and uncertainty quantifiers based on distances are proposed, but no connections are proposed with invariant dynamical structures. Similarly in (Huntley et al., 2011) uncertainty quantifiers based on a descriptive statistics of distances between modelled trajectories and observations are used, but no relations are presented between these and the invariant dynamical structures. Results appeared in (Kaszás and Haller, 2020) also discuss along these lines, but in the context of general models, not related to ocean data. In this work authors have established links between their measure of uncertainty, model sensitivity, and the FTLE field, which is related to invariant manifolds. Authors achieve these results under explicit mathematical assumptions for the "true" model, however results in our work do not require such assumptions for the ‘ground truth’. The FTLE field is constructed from derivatives along trajectories (the Cauchy-Green strain tensor), while the L_{UQ} field is not. It would be an interesting research direction to establish links between the FTLE and the L_{UQ} fields, but the authors have not pursued this.

Equations similar to (4.8) or (4.9) have been used in the literature to highlight Lagrangian structures in oceanic flows. For instance (Prants et al., 2014, 2011) have done so. Prants in (Prants et al., 2011) proposed to use the arc-length D to study the displacement of particles in the coasts of Japan.

$$D = \sqrt{(x_f - x_0)^2 + (y_f - y_0)^2}. \tag{4.48}$$

Here, D represents the relative displacement of a particle from its initial position (x_0, y_0) to certain final one (x_f, y_f). This expression is the analogue to Equation (4.8) with $p = 2$ and target adjusted to each initial condition. However, in this work no connections are established between Equation (4.48) and uncertainty quantification. On the other hand, our results in the previous section indicate that nonlinearities introduce features in the L_{UQ} pattern that do not have an invariant interpretation.

4.5. Conclusions

This chapter explores a definition for UQ recently proposed in oceanic contexts in Chapter 3. The findings described in this article are of particular interest for they have important environmental applications. Nowadays, multiple ocean data sources are available and in this context our results allow a quantitative comparison of the transport properties associated with them. In this way discriminating the level of performance of different data sources will help to gain precision in the description of dispersion of contaminants, determination of waste and plastic sources, etc.

We have also examined the implications of this definition. It is found that for this definition, which is associated to forward UQ, stable invariant manifolds of hyperbolic trajectories of the underlying flow, provide a structure for it. That is, we found that the proposed Uncertainty Quantifier is a function that contains a very rich structure, particularly for long time intervals, which is related to these well known structures from dynamical systems theory. For selected examples this statement has been proven. Also examples are discussed in which singular structures of the uncertainty quantifier highlights structures that are not aligned with invariant features of the dynamical system. Other invariant structures like tori, are not recovered by the uncertainty quantifier. Also, connections between UQ and invariant dynamical structures have been used to provide a framework for discussion on structural uncertainty, which is related to inadequate models. This vision enriches traditional descriptions of UQ on which structure is discussed just in terms of means and/or statistical moments of distributions.

In the upcoming chapter, we will investigate the use of LCS on a larger scale in the Eastern Mediterranean to gain insights into chaotic ocean events, such as oil spills. LCS can provide a way to find order in the seemingly random movement of ocean currents, allowing us to identify the source of oil spills and track their movement over time. We will apply this approach to a recent oil spill event in the Mediterranean Sea, showing the efficacy of our methodology in identifying the source and understanding the transport of oil and tar by ocean currents.

Chapter 5

Eastern Mediterranean Oil Spill Accident

This chapter is based on the results described in (García-Sánchez et al., 2022). To ensure that everything is complete and precise, the methodological aspects discussed in Chapter 2 and the results in Chapters 3, 4 used in this chapter are reviewed for better understanding.

At the beginning of 2021 the coastline of several Middle Eastern countries in the Eastern Mediterranean was affected by the presence of oil from unknown source(s). Figure 5.1 illustrates the affected geographical areas marked with pink and yellow bullets. A more detailed report on the impacted zones along the Israeli coast may be found in the interactive map whose link is provided in (Ben-Nun, 2021). Israeli authorities estimated that more than 1000 tons of tar (Rinat and Zikri, 2021) landed along 180 km of the israeli and lebanese shoreline (Joffre and Tercatin, 2021; Kaplan-Zantopp, 2021; News-Agencies, 2021; Polidura, 2021; Staff, 2021; Tercatin, 2021) in mid February. Gaza also reported that similar arrivals of tar reached their beaches days afterwards (Monitor, 2021). This sequence of events has caused one of the worst ecological disasters reported in decades in the affected countries, which will require years of cooperative action for the affected areas to be restored (Rinat and Zikri, 2021). Numerous photographs and visual material documented the nature of the oil and actions taken by governments to mitigate the disaster (Joffre and Tercatin, 2021; Kaplan-Zantopp, 2021; News-Agencies, 2021; Polidura, 2021; Staff, 2021; Tercatin, 2021; Wikimedia Foundation, 2021). The type of tar visible on the images is consistent with a degradation of the released oil for time periods of around a month.

What was the origin of these spills? Perhaps they could have been a ‘deliberate’ oil spills, in line with findings by Pavlakis et al. (1996) who report that such oils spills appear with considerably higher frequency than oil spills corresponding to ship accidents. Also these could have been caused by operative discharges from ships, since according to the ESA (1998) 45% of the oil pollution comes from these. There exist systematic efforts to prevent such events. Such as, for instance, the activities of the CleaSeaNet Service of the European

Maritime Safety Agency (EMSA), operating since 2007, to locate and identify polluters in areas under their jurisdiction. EMSA received a request from the Israeli authorities concerning this particular event (Joffre and Tercatin, 2021).

Is any attempt to reconstruct the sequence of events of this spill with the available information doomed to failure? Indeed, there exist recent examples in the literature that confirm that predictions on oil spill evolution still raise big questions. For instance, in 2015 the fishing ship Oleg Naydenov caught fire and sank in the south of Gran Canaria. There exist models for the spreading of the oil that however did not report neither the date or its arrival point to the coast of Gran Canaria (Ivorra et al., 2017); in 2018 the Iranian oil tanker Sanchi collided with a cargo ship, caught fire, and sank in the East China Sea. After the event, researchers tried to assess where pollutants from the Sanchi would travel, but there was no consensus between predictions from groups in China and the United Kingdom (Carswell, 2018); recently, on August 23rd, 2021 a spill from Syria's largest refinery spread across the Mediterranean. Predictions expected its arrival to Cyprus on the 31 August 2021 (CMCC et al., 2021), however by the 6th of September 2021 such a landing had not yet been reported (Kundu, 2021). Many other examples could have been added to this list. One aspect that makes the pollutant event addressed in this article particularly challenging is the fact that the date and geographical location where the spill, or the spills, were released are unknown. That is, if oil spills, such as those just quoted, are difficult to predict even if the time and position of the event that has produced them are known, the difficulty increases substantially if this information is not known.

The first models for oil spill spreading used simplified linear superposition techniques to model ocean currents that employed a vector sum of the mean flows, tides, wind/waves and turbulent dispersion (Asce, 1996; Stolzenbach et al., 1977). In contrast, nowadays there exist sophisticated models that integrate all these effects to predict ocean currents and all relevant ocean variables. These models are run operationally and provide unprecedented conditions to produce accurate oil spill predictions. One natural question in this context is if it is possible to provide answers for the event under consideration with currently available tools? Among these are those provided by Copernicus, one of the most ambitious programmes in Earth Observation (European Commission, 2014). Copernicus encompasses the Sentinel programme, which provides very high-resolution satellite images in radar and visible frequencies, and the CMEMS, which provides data on ocean currents on a daily basis. Despite the availability of these new products, oil spill forecasts are still uncertain since the underlying ocean flow, and the associated transport, is very chaotic. Importing into this setting dynamical systems concepts, which use concepts from chaos theory, may provide a wealth of new ideas that could assist in this struggle. One of these consist of

identifying geometrical features on the ocean surface that help to interpret colectively the behaviour of masses of fluid parcels, instead of considering individual fluid trajectories. The development of these geometrical ideas was begun by Poincaré in the context of his work on celestial mechanics. In the setting of geophysical flows these geometrical structures have been referred to as Lagrangian Coherent Structures (LCS). For oil spills this global vision has provided very satisfactory results. Using this perspective García-Garrido et al. (2016) were able to identify the date and arrival point of the oil to the coast of Gran Canaria after the Oleg Naydenov fishing ship accident; García-Sánchez et al. (2021) used this viewpoint to describe the Volcan Tamasite event and to compare the performance of different ocean models (García-Sánchez et al., 2022). It is important to remark that these episodes occurred in different space and time scales ranging from the mesoscale, to the submesoscale, and from hours to days. Above the mesoscale Olascoaga and Haller (2012) found that oil in the Gulf of Mexico, released after the Deepwater Horizon accident, was lined up with configurations obtained from LCS, which highlighted attracting material curves. Notably this approach has succeeded for events that involved different type of oils, from light fuel oil in (García-Sánchez et al., 2021), to denser IFO 380 oil (García-Garrido et al., 2016) and to a variety of crude elements (Olascoaga and Haller, 2012). Encouraged by these results we will address the description of the oil spill event described above. With the aid of LCS we identify attracting material curves along which oil spills tend to become aligned (see García-Sánchez et al. (2022); Olascoaga and Haller (2012)). Indeed, this article reports strong correlations between satellite observations and attracting material curves highlighted by LCS computed with the CMEMS data. These connections have been very valuable for identifying the sources of the contamination event. The agreement between satellite observations and modelling results supports the correctness of our approach. It is expected that these scientific and technological advances will be systematically implemented in the near future and will allow investigators to identify violators and take appropriate measures to protect the environment.

5.1. Satellite Data

During the time period and geographic region of interest a set of publicly available satellite data has been analyzed. The aim was to identify spills on the sea surface that could be linked to the reported spills along the coastline.

One source for these satellite images is the Synthetic Aperture Radar (SAR) high-resolution data from Sentinel 1 (A,B), Level-1 IW GRDH (Interferometric Wide Swath Ground Range Detected). SAR data were processed using the SNAP - ESA Sentinel Application Platform v8.0.3 Graphics Processing Tool (GPT) operators [https://step.esa.int/m

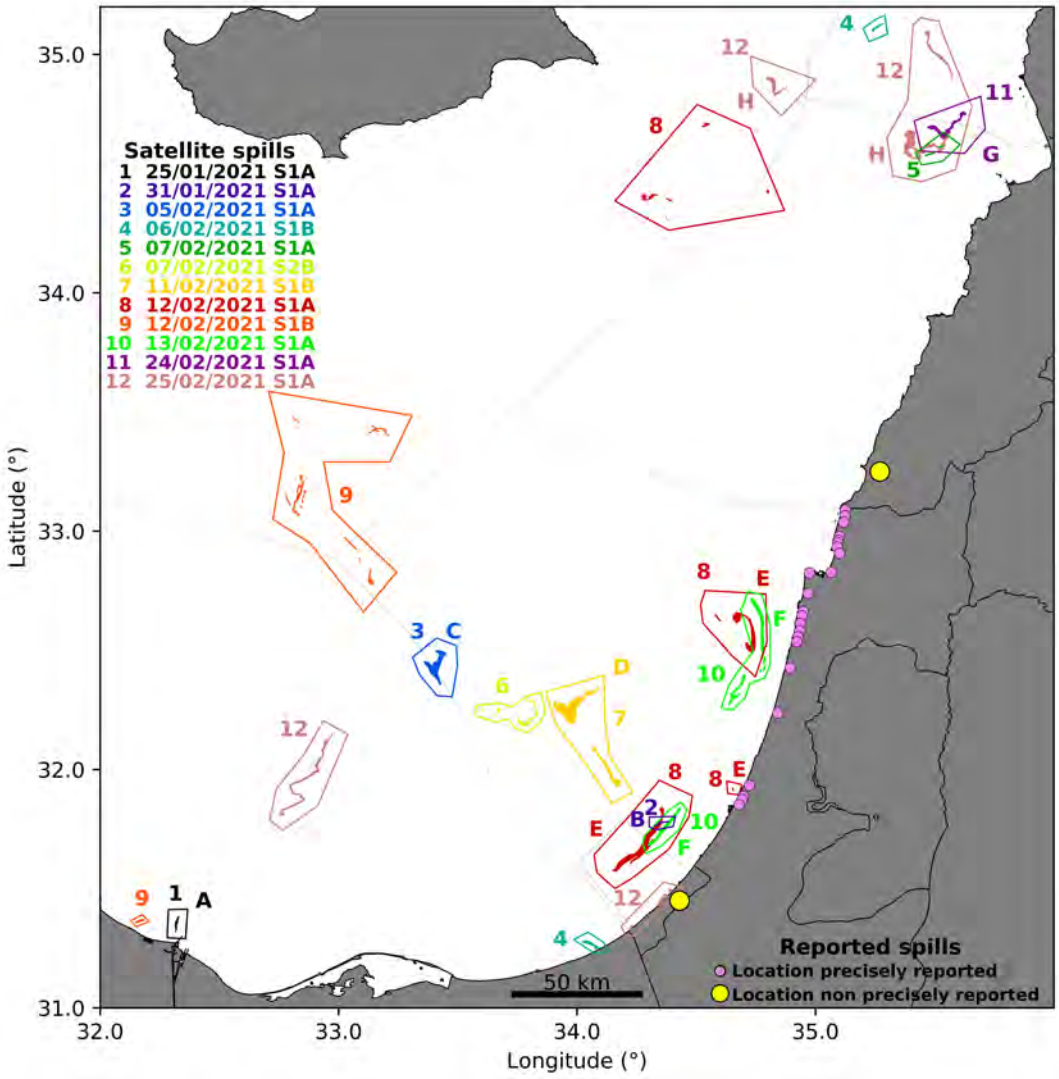


Figure 5.1 Scenario of affected areas. Exclusive Economic Zones (EEZ) are marked with a dotted line. Pink and yellow bullets mark coastal areas for which, according to mass media reports, there were in situ observations of oil or tar. Satellite observations are listed with numbers and colors according to the day in which they were detected. Some of them are double labelled with a letter since they are also reported in Figure 5.2. The figure has been created using python 3.8.10 and matplotlib module 3.1.2 (https://www.python.org/downloads/release/python-3810/). Coastlines and country boundaries have been obtained from GSHHG - A Global Self-consistent, Hierarchical, High-resolution Geography Database 2.3.7 version (https://www.ngdc.noaa.gov/mgg/shorelines/gshhs.html). EEZ have been obtained from https://www.marineregions.org/. The satellite observations vector representations have been created using QGIS software 3.10 version (https://qgis.org/) and the SAR processed images.

ain/toolboxes/snap/]. During the study period there were days around the third week of February in which, due to the atmospheric conditions, SAR images were not useful. The occurrence of storms, and their associated strong wind fields, produced atmospheric signals that were detected in SAR images. This prevented the information corresponding to surface sea phenomena from being showed. For this reason, SAR images interpretation require wind field data, and to support SAR image analysis, wind data with moderate resolution were obtained from Copernicus Marine Segment [https://marine.copernicus.eu/]. The selected product is identified with product code 012_004V6. This product corresponds to global near real time wind data every 6 hours with a spatial resolution of one-quarter degree. This product combines data from wind models of the ECMWF (European Centre for Medium-Range Weather Forecasts) with data from available wind scatterometers. Additionally, instantaneous wind fields were derived from SAR data using the corresponding GPT operator.

Both mineral oil and biogenic slicks are visible in SAR images at moderate wind speeds. The wind range for which both types of slicks are recognizable is not the same, although they overlap. In order to contradistinguish mineral oil slicks from natural origin surface films, the SAR images were analyzed not only with available wind fields but also with ocean colour data. To this end, Sentinel 2 (A, B) optical data from MultiSpectral Instrument (MSI) Level 1C and Sentinel 3 (A,B) Ocean and Land Colour Instrument (OLCI) Level 1B were downloaded from the Sentinel Data Hub [https://scihub.copernicus.eu/]. Sentinel 2 MSI data atmospheric correction was conducted using(Vanhellemont, 2019) the acolite toolbox [https://odnature.naturalsciences.be/remsem/software-and-data/acolite]. Sentinel 3 OLCI data were processed using SeaDAS 7.5.3 version [https://seadas.gsfc.nasa.gov/].

5.2. Satellite Results

Figure 5.2 displays a set of satellite images selected in the area and period of interest after performing the analysis described above. This selection is chosen also in the light of the numerical simulations reported next. Panel a) shows a spill detected close to the Suez Canal on the 25th of January 2021. As we will argue in the discussion, this spill has been detected shortly after its release and marks the origin of some of the spills that reached the coastline. Panel b) shows a second spill closer to the coast on the 31st of January 2021. As discussed later we conjecture that this observation is a second origin for those spills that reached the coastline. Panel c) displays one spill visible on the 5th of February 2021. Panel d) identifies spills on the 11th of February, not too far from the position in c). Panel e) shows spills very close to the Israeli coast on the 12th February 2021. Panel f) shows the evolution of these

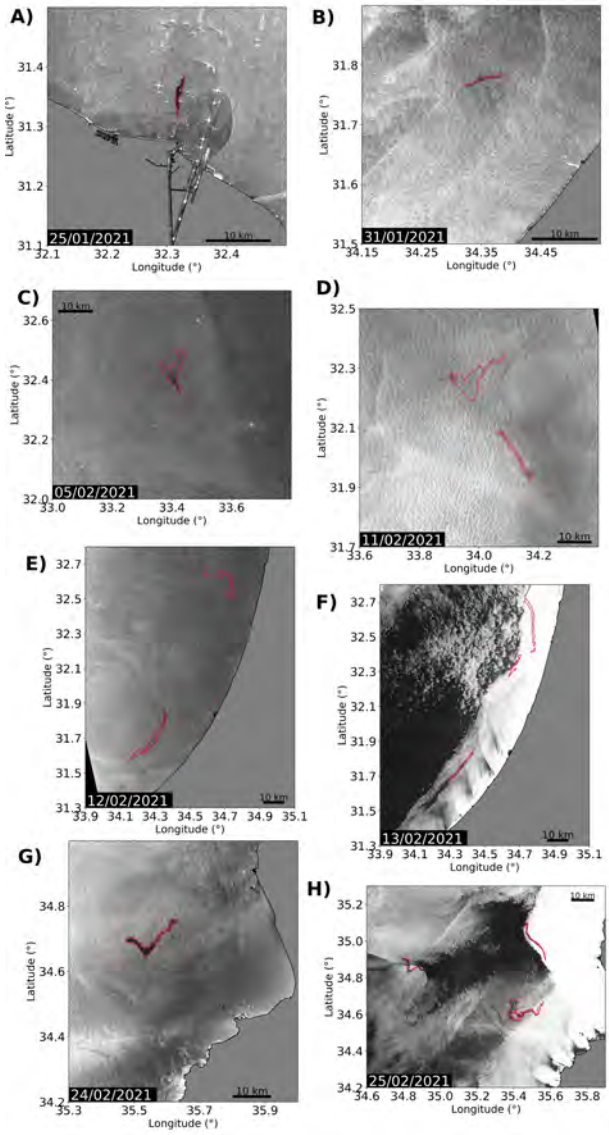


Figure 5.2 Satellite radar images. a) Sentinel 1A on the 25th January 2021; b) Sentinel 1A on the 31st January 2021; c) Sentinel 1A on the 5th February 2021; d) Sentinel 1B on the 11th February 2021; e) Sentinel 1A on the 12th February 2021; f) Sentinel 1A on the 13th February 2021 ; g) Sentinel 1A on the 24th February 2021; h) Sentinel 1A on the 25th February 2021. The figure has been created using python 3.8.10 and matplotlib module 3.1.2 (https://www.python.org/downloads/release/python-3810/). Coastlines have been obtained from https://osmdata.openstreetmap.de/data/land-polygons.html. The satellite observations vector representations have been created using QGIS software 3.10 version (https://qgis.org/) and the SAR processed images.

spills on the 13th February 2021. Panels g) and h) show a sequence of images detected close to the Syrian coast on the 24th February and 25th February 2021, respectively.

Spots in Figure 5.2 are displayed by zooming into smaller areas. In order to acquire a vision of their global distribution they are also represented in Figure 5.1. Figure 1 shows the position of all spills located from satellite images in the Eastern Mediterranean during the period of interest. Each shape appearing in Figure 5.2 is labelled in Figure 5.1 with the same letter. Figure 5.1 shows additional spills, some of them reported in the media (Surkes, 2021), for which we have not found relations to their arrival to the shoreline. These are labelled only with numbers, and their observation day is listed in the figure. Satellite images confirm that waters of the Exclusive Economic Zones (EEZ) of Egypt, Syria and Cyprus were also affected, and not only those of Israel, Gaza, and Lebanon. In this figure it is remarkable that spills in panels a) and b), which we have identified as the *sources*, are seen very small when compared to others. We remark that according to Schrope (Schrope, 2013) spills are often larger than detected, and their size very often is not correctly determined from remote sensing images. This is particularly true at the early stages when their spreading in the ocean surface has barely started. On the other hand, structures displayed in panels c), d), e), f), g) and h), which are more extended and present distorted shapes, suggest that they have been affected by the chaotic motion of ocean transport.

5.3. The transport problem

One natural question regarding those oil spills observed by satellite and at the coast is whether they are connected among themselves? Are they part of the same event? We provide answers to these questions in this section.

Oil transport can be described by a concentration field, C, whose evolution is affected by the flow, represented by the velocity field $\mathbf{v}(\mathbf{x}(\mathbf{t}),t)$, and molecular diffusion. At the ocean scales under consideration, the diffusion transport is much smaller than the convective transport (Monroy, 2019) and therefore it can be neglected. On the other hand, particles with a finite size and different density to that of water may not instantly follow fluid velocities: other mechanisms besides passive advection contribute to their transport, such as gravity forces, their finite size, inertia and history dependence, etc. Results in (Monroy et al., 2017) confirm, however, that for a wide range of particles, the description of passive tracers is appropriate, except for the addition of a constant vertical velocity arising from the particle weight. However, for the case under study, that correspond to oil that remains floating for a long time, weight effects should be negligible and therefore we considered that it closely follows the 2D horizontal motions of fluid parcels. This is a simplified approach, but studies such as (García-Garrido et al., 2016; García-Sánchez et al., 2021; Lekien and Marsden, 2005; Olascoaga and Haller, 2012) confirm that considering horizontal advection as the

dominant contribution to pollutant transport provides very good results. Similar approaches in other contexts of ocean transport confirm the same (García-Garrido et al., 2015). Finally, we will assume that the crude oil moves horizontally, close to the surface, but a bit below the waterline and therefore it is not subjected to direct wind sailing effects. Wind effects, jointly with tides, waves, etc., are included in the sophisticated ocean models that provide the velocity fields of the ocean currents, $\mathbf{v}(\mathbf{x}(\mathbf{t}),t)$, (see Section 5.4 below for more details) and we assume that oil parcels follow instantly water fluid velocities. The accuracy of this approach is supported, by the agreement between the predictions made by the simulations, the oil sightings from satellite and in situ observations. Under this approach oil parcels follow trajectories $\mathbf{x}(\mathbf{t})$ that evolve according to the dynamical system:

$$\frac{d\mathbf{x}}{dt} = \mathbf{v}(\mathbf{x},t) \tag{5.1}$$

In this equation the position $\mathbf{x}$ is described in longitude (λ) and latitude (ϕ) coordinates, that is, $\mathbf{x} = (\lambda,\phi)$, and $\mathbf{v}$ represents the velocity field. In longitude/latitude coordinates, the dynamical system (5.1) can be rewritten as:

$$\frac{d\lambda}{dt} = \frac{u(\lambda,\phi,t)}{R\cos(\phi)}, \quad \frac{d\phi}{dt} = \frac{v(\lambda,\phi,t)}{R}, \tag{5.2}$$

where R is the Earth's radius. This system assumes that the vertical velocity component in the ocean is small compared to the horizontal ones and for that reason it has been disregarded. The two velocity components are determined by the zonal (u) and meridional (v) velocities, which are obtained from the currents provided by CMEMS.

There exist diverse software packages that are able to track oil spills, of which for instance a list is found in (García-Sánchez et al., 2021). Most of these models are focused on tracking individual fluid parcels, and in order to maintain a good representation of the spill they play with a sufficiently large number of initial parcels. Contrary to these approaches, in the results reported in this work, we track in time the whole area where the fuel is extended, and the algorithm self regulates the number of fluid parcels on the contour to ensure its accurate representation at all times. At the beginning the area is a simple shape, but while it evolves, it becomes distorted and convoluted. The shape is tracked with contour advection algorithms developed by Dritschel and Ambaum (1997), including some modifications explained in (M. et al., 2004; Mancho et al., 2006b, 2003). Typical oil spill software packages include models to represent the weathering process according to different oil properties. In our approach we do not describe oil transformation. We consider that weathering does not affect to the transport process. Spill contours are evolved uncoupled from degrading effects. Degrading

effects could have been considered at representative levels *a posterior* (García-Sánchez et al., 2021) as a change in the color intensity of the oil spill. It could be that weathering implies oil evaporation, and in that case the evolved contour would be an upper bound to the oil evolution. Similarly would occur if oil forms clots that are denser and sink. In both cases the region of dispersion for the oil is a subset of our approach. Given that we do not have information on the type of floating oil and our focus is just on transport.

5.4. Ocean Data

The ocean velocity fields used in this work were obtained from the CMEMS [http://marine.copernicus.eu/]. In particular, we have used the datasets provided by the high-resolution Global Ocean Model (the global analysis and forecast product). The horizontal resolution of the model is 1/12° (approximately 8 km) with regular longitude/latitude equirrectangular projection and 50 vertical geopotential levels. Data are served on a daily and hourly basis. Hourly data rapidly fluctuate around daily data, which represent smooth averaged values. All the calculations reported in this article have been performed with the daily data, because they better match observations. Additionally, CMEMS provides a specific service with hourly and daily data for the Mediterranean area. The resolution of the Mediterranean Model is higher than that of the Global Model: on the horizontal plane it is 1/24° with regular longitude/latitude equirrectangular projection and along the vertical coordinate it has 141 depth levels. This resolution allows a representation of sub-mesoscale features, however calculations performed with the Mediterranean Model do not reproduce many of the transport features related to the oil spill event. Additionally we have found that small scale features from this Model do not accurately correspond to those observed from satellites.

5.5. The Dynamical Systems Perspective

A challenge to studying Equation (5.1) is that even flows with smooth velocity fields may exhibit complex particle trajectories. An approach taken from nonlinear dynamical systems theory, seeks to understand the behavior of large ensembles of particle trajectories by finding geometrical structures, known as Lagrangian Coherent Structures (LCS), that form time dependent material surfaces. This perspective has been successfully employed in pollution contexts (García-Garrido et al., 2016; García-Sánchez et al., 2021; Lekien and Marsden, 2005; Olascoaga and Haller, 2012). The LCS spatio-temporal template can be constructed with a recent technique referred to as Lagrangian Descriptors (LDs). The particular LD that we use is a function referred to as M (Jiménez-Madrid and Mancho, 2009; Mancho et al.,

2013; Mendoza and Mancho, 2010) which is defined as follows:

$$M(\mathbf{x}_0, t_0, \tau) = \int_{t_0-\tau}^{t_0+\tau} \|\mathbf{v}(\mathbf{x}(t), t)\| \, dt = \int_{t_0}^{t_0+\tau} \|\mathbf{v}(\mathbf{x}(t), t)\| \, dt + \int_{t_0-\tau}^{t_0} \|\mathbf{v}(\mathbf{x}(t), t)\| \, dt \,, \tag{5.3}$$

Singular features visible in this field represent attracting and repelling material surfaces. Of particular interest for our study are attracting material surfaces, visible from the backward integration (the second term) of Equation (5.3), along which oil blobs eventually tend to be elongated and aligned. More specifically, there exist regions in the ocean, characterized by high contraction and expansion rates, referred to as hyperbolic regions, such that blobs placed in the neighbourhood of trajectories in these regions (hyperbolic trajectories) evolve in time rapidly expanding and filamenting to become aligned with the attracting material curves. This effect has direct implications on our study since blobs that are originally located in small ocean regions, if they go close to these expansive/contractive regions, will spread in filaments affecting large sea areas. Alternatively, repelling material curves are obtained from the forward integration (the first term) of Equation (5.3). These curves describe how blobs placed in the neighbourhood of the hyperbolic region evolve in backward time. They also tend to form filaments, but as these are formed in reverse time, they are not observable and for this reason they are referred to as repelling material curves. A physical way to look into these curves is as follows: material spread on the ocean surface lined up with these filaments evolves in time contracting towards the neighbourhood of the hyperbolic trajectory.

The computation of fluid particle trajectories $\mathbf{x}(t)$ is necessary in order to evaluate the function M in Equation (5.3). For a given initial condition $\mathbf{x}_0(t)$ this function evaluates the arc length of trajectories when they are evolved forwards and backwards in time for a period τ. Trajectories are integrated with a 5^{th} order Runge-Kutta method, and arc length is computed by the addition of linear segments connecting successive steps of the Runge-Kutta method.

5.6. Transport Results

Figure 5.3 represents in gray tones the field M as evaluated from Equation (5.3) with $\tau =$ 15 days, which is a choice appropriate for the time scale of the described events (1 month). In maroon tones are highlighted the attracting material curves. Repelling material lines are also visible, but we do not highlight them as they are not of interest for our discussion at this moment. This figure represents the time evolution of orange and blue blobs that have

been released on the 25th and 31st of January, respectively, at the positions marked in panels a) and b), which are linked to spills detected in panels a) and b) of Figure 5.2. Initial blobs have a radius of 4 km, in agreement with the resolution of the CMEMS global model. It is clear from the evolution that blobs tend to end up elongated and aligned with the maroon features of the attracting material curves. Panel c) illustrates the evolution of these blobs on the 12th of February and the red shapes highlight satellite spills spotted on that day. The good agreement between parts of the evolved orange and blue blobs and these spills is remarkable. Panels d) and e) illustrate their evolution on the 16th and 17th of February and the arrival to the Israeli coast at points marked in pink and also reported in Figure 5.1. Panel f) illustrates the arrival at further points on the Israeli and Lebanon coasts on the 20th of February, in good agreement with reports marked in Figure 5.1.

Figure 5.4 is similar to Figure 5.3. It also represents in gray tones the field M and the attracting material curves highlighted in maroon. Panels a) and b) complete the description of Figure 5.3. Panel a) illustrates the blue and orange blobs on the 24th of February. Their structure is extremely filamented, closely following the attracting material curves. The red shape illustrates the spill visible in panel 5.2g) suggesting that this could have been related to the spill detected in panel 5.2b), associated with the blue blob. Panel 5.2h) confirms the connection between the "V" shaped spill in g) with the one observed in h) confirming the quality of the model (5.1) to provide a consistent connection of this spill with what is obtained from satellite observations. In this panel it is also remarkable the proximity between all satellite observations (in red), the blue blob and the attracting material curves. This suggests that these spots observed on the 25th of February close to the Syrian coast could also been related to the spill detected in Figure 5.2b). Finally on the Gaza coast are visible two red spots that highlight satellite observations of oil. There is a remarkable agreement between these observations and the spreading of the orange blob.

Panels c) and d) illustrate the position, respectively, of spills detected in panels c) and d) of Figure 5.2. The green blob in panel 5.3c) is released at the position of the spill of panel 5.2c) on the 5th of February and its evolution on the 11th of February according to the model (5.1) is illustrated in panel 5.3d). It is remarkable the connections established by the simulations between both satellite observations, suggesting that these spills correspond to the same event. Also we want to emphasize that these spills are not related to spills arriving to the coast. Arrivals to the coast are only achieved by the blue and orange blobs visible in Figure 5.3 and in panels a) and b) previously discussed. The movie supplied in the supplementary material completes the description given in Figures 5.2 and 5.3.

In all panels of figure 5.3 there exist V-shaped observed satellite spills. We conjecture that these shapes are again an effect of advection dominated transport. Indeed the convoluted

forms adopted by blobs while being transported, visible in Figures 5.2 and 5.3, present many corners with this kind of shape, at different orientations. Even the green blob in panels 5.3c) and d) is distorted into a V-shape. 'V' shapes are a footprint of typical stretching and folding mechanisms related to hyperbolicity and non-linearity present in equations like (5.1), adopted to describe oil transport (Ottino et al., 1994).

Finally, we discuss the perspective that searches for contamination sources by considering backwards integration of trajectories in the spirit of (Shu et al., 2018, 2014). Figure S1 [1] shows these results. Panel a) of this figure locates a blob in the neighbourhood of the Israeli coast on the date that tar was reported to reach the beach, the 16th February 2021. Panel b) in this figure, represents the backward evolution of this blob on the 31st January 2021. As anticipated, the backward evolution of the original blob becomes aligned with the repelling material curves that are highlighted in blue in the figure and spread over a large ocean region. This points out the difficulty in locating the spill point through this methodology.

5.7. Discussion and Conclusions

This paper discusses our findings concerning a recent oil spill event that we have studied by importing dynamical systems ideas. We have found evidence that our perspective recovers the essential features of the oil spill dispersion at large scale. Indeed oil spills form clots and its pieces tend to be aligned with segments of attracting material curves, Lagrangian Coherent Structures, confirming the assumptions. Indeed, the attracting material curves of the CMEMS Global model are closely related to SAR satellite spill observations for this Eastern Mediterranean event. Remarkably, several of these observed scattered spills emerge from two particular observations on the 25th and 31st January 2021 and are directly linked to the coastal spill arrivals. We also find that some observations of spills on the 5th and 11th of February 2021 visible from Sentinel SAR images are unrelated to spills observed at coastal points, however they seem to be connected between themselves. The entire description of the event, according to our findings, spans a period of almost one month and this is consistent with the fact that what has been reported to reach the coast is tar, a form of degraded oil after several weeks on the sea surface.

Connections and links between scattered pieces of oil observed from satellites and on coastal arrivals have been established for the CMEMS global model. However these types of connections are not found from other CMEMS models such as that in the Mediterranean sea domain. This suggest that CMEMS global model is particularly good for describing transport phenomena.

[1] This figure is available via the following hyperlink: https://shorturl.at/ruGK9

Dynamical system tools have provided concepts such as that of attracting material curves which have provided a simple global overview of the event and suggested connection routes for dispersed and scattered spills, helping to answer questions about where and when the spill originated. It is remarkable that these connections have been established for events that extend for a one month period, taking oil spill forecast capacities to their limit (Barker et al., 2020).

As a conclusion we have found that the synergistic combination of Copernicus services has provided a powerful technology that should be exploited in an operational manner to better predict and target the evolution at sea of spill events. These technologies will allow a better environmental protection of all seas and coasts, given that, as in this case, oil spills pay no attention to international borders.

In this chapter, we have presented our findings on the analysis of a recent oil spill event using dynamical systems concepts. In the next, we propose a new uncertainty measure to evaluate the performance of CMEMS Global and Mediterranean models in assessing the origin of observations. We call the proposed measure Backward Lagrangian Uncertainty Quantification (BLUQ) and is related to the invariant dynamical structures of the model in the neighborhood of the observation. We illustrate the implementation of this measure in the context of this oil spill event in the Eastern Mediterranean in 2021, providing a quantitative analysis of the performance of ocean data sets. Our approach provides a promising tool for evaluating the accuracy and reliability of models in predicting the origin of observed material transport events, and can contribute to better environmental protection of seas and coasts.

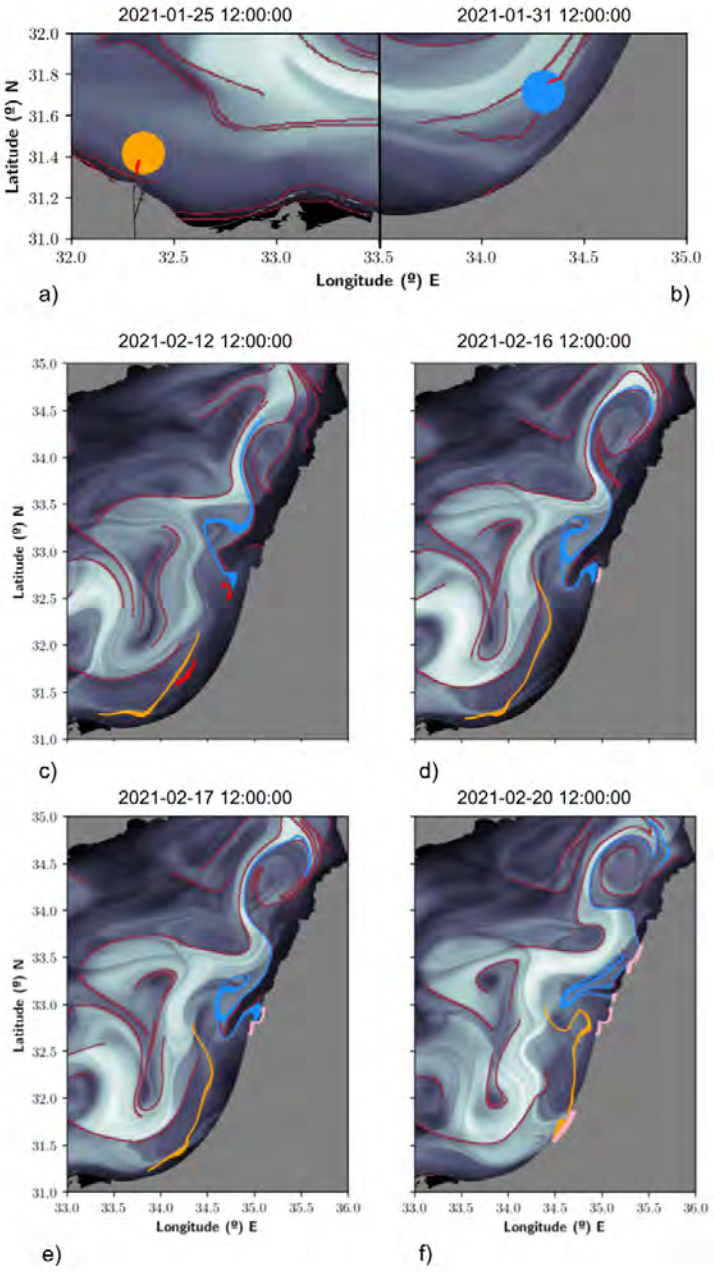


Figure 5.3 Simulations that reproduce the spreading on the sea and the arrival of the oil to the coast. The function M at the background is represented at t_0 equal to the corresponding date. a) 1st release on the 25th January 2021 and satellite observation; b) 2nd release on the 31st January 2021 and satellite observation; c) evolution on the 12th February 2021 and satellite observations; d) evolution on the 16th February 2021 and arrival to the coast; e) evolution on the 17th February 2021 and arrival to the coast; f) evolution on the 25th February 2021 and arrival to the coast. These masks indicate regions that correspond to the continental shelf. These figures have been created with Python 3.9.2 (https://www.python.org/downloads/release/python-392/). The maps shown have been generated with a mask provided by OpenStreetMaps (https://osmdata.openstreetmap.de/data/land-polygons.html).

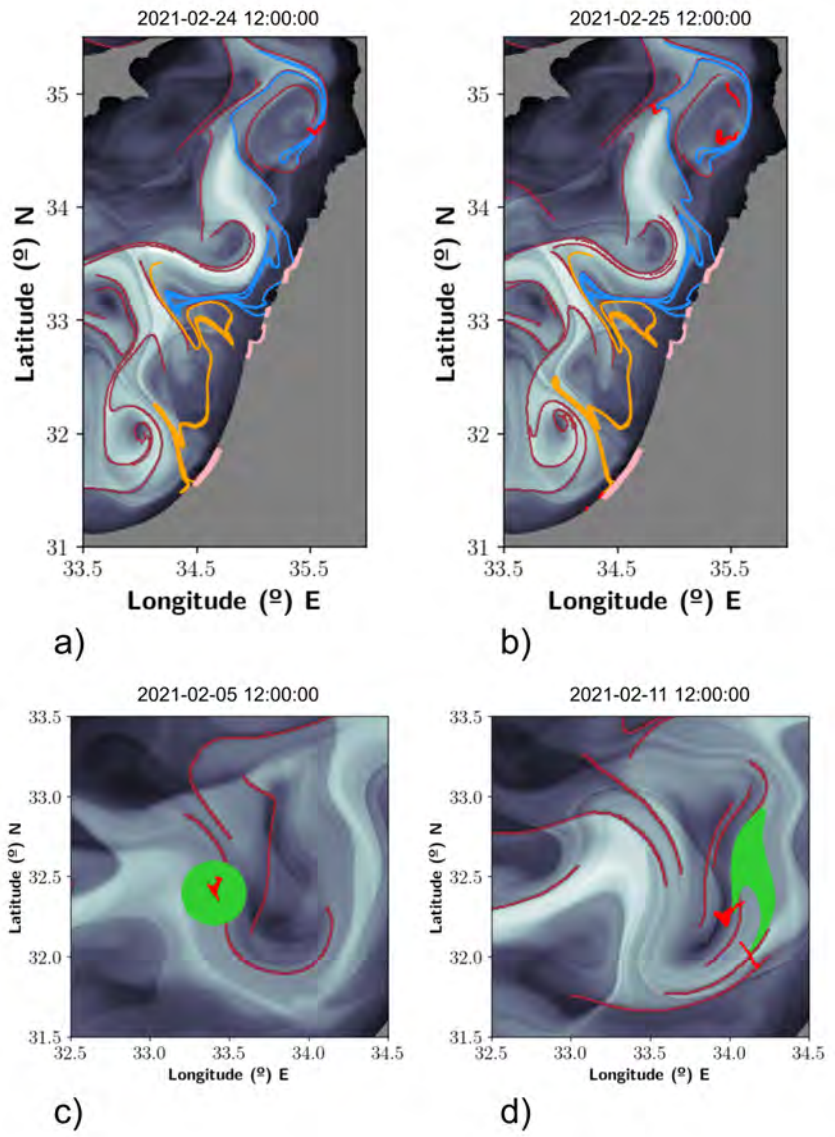


Figure 5.4 Simulations that connect successive oil spill observations. The function M at the background is represented at t_0 equal to the corresponding date. a) Evolution on the 24th February 2021 and satellite observations; b) evolution on the 25th February 2021 and satellite observations; c) satellite observation on the 5th February 2021 and a 1st release attached to the observation; d) evolution on the 11th February 2021 and satellite observations. These figures have been created with Python 3.9.2 (https://www.python.org/downloads/release/python-392/). The maps shown have been generated with a mask provided by OpenStreetMaps (https://osmdata.openstreetmap.de/data/land-polygons.html).

Chapter 6

Backward Time Lagrangian Uncertainty Quantification

This chapter is based on the results described in (García-Sánchez et al., 2023a). To ensure completeness and accuracy, methodological aspects discussed in Chapter 2 and the results in Chapters 4, 5 are recalled.

Models in real-world applications are subjected to uncertainty in their results, and this is particularly notorious in models that describe the ocean or the atmosphere state. In these geophysical contexts, the availability of tools that quantify the uncertainty of model outputs is very much desired as this allows the evaluation of their reliability and the assessment of their use in real applications. Uncertainty quantification is a very broad question and it has been addressed from different perspectives. One approach to this problem involves performing a sensitivity analysis, which determines what inputs in the model, which typically is a partial differential equation, affect the outputs the most. A related issue, referred to as forward propagation of uncertainty, consists of examining how uncertainty in the model parameter inputs affects uncertainty in the model outputs. In this framework it may happen that experimental data are available. In this case, it is possible to infer the set of parameters that better fit the outputs for the proposed model. This setting can be precisely formulated as a Bayesian inverse problem, which for a given observation, and an assumed noise model, determines the parameters that are most likely to have produced the data. Typically, Bayesian analyses provide the framework for many inverse uncertainty quantification applications (Domitr et al., 2023; Wu et al., 2018). These methods employ Bayesian inference theory along with exploring the posterior Probability Density Function (PDF) by Markov Chain Monte Carlo (MCMC) sampling. Other methods include statistical methods based on maximum likelihood estimation (MLE) (De Crècy, 1996) and data assimilation methods. Data assimilation methods combine experimental observations with code predictions and their

respective errors to provide an improved estimate of the system state and of the associated uncertainty (Petruzzi, 2019). All of these approaches assume that the model is known, with undetermined parameters, and perform adaptations on the model inputs. However, there is a different type of problem for which only an approximate model is available and its exact expression is unknown. We delve into an explanation of such problems.

Recently, García-Sánchez et al. (2022) have proposed to quantify uncertainty associated with transport by currents in settings in which the exact model connecting two successive observations (or the currents producing the observed transport) was not known. They have quantified uncertainty motivated by the need to judge the performance of ocean model outputs to describe oil spill events such as that described in (García-Sánchez et al., 2021). In this reported event an identified spill occurs at a certain time and it is required to describe its evolution to determine if it will affect critical areas, and there is a need to assess ocean models to this end. García-Sánchez et al. (2022) approach evaluates the reliability of the ocean currents with respect to the transport that they produce. Indeed, transport in the ocean surface is produced by fluid parcels that follow trajectories $\mathbf{x}(t)$ that evolve according to the dynamical system:

$$\frac{d\mathbf{x}}{dt} = \mathbf{v}(\mathbf{x},t), \tag{6.1}$$

This system is a nonlinear non-autonomous dynamical system in which there are uncertainties in the velocities $\mathbf{v}(\mathbf{x},t)$, because they are not exactly known given that they come from solving highly sensitive partial differential equations. This is what we mean by *not knowing* the exact problem: the right-hand side of Equation (6.1) is only an approximation. Typically, in other problems where uncertainty has been studied, the system obeys an explicitly known partial differential equation where the unknowns are not within the model itself but rather in adjustable parameters of the equation or in the observations. However, our case is of a different nature because the right-hand side of Equation (6.1) is a key part of the equation and not exactly known. The uncertainties in the velocities $\mathbf{v}(\mathbf{x},t)$ produce uncertainties in the solutions $\mathbf{x}(t)$. García-Sánchez et al. (2022) quantified this type of uncertainty by means of error measures in settings where the initial observation was known, $\mathbf{x_0}$, and a target state at a later final time, $\mathbf{x}^*$. This approach was adequate to quantify the suitability of the model given in Equation (6.1) to represent this sequence of observations in forward time. In doing so they found links between the uncertainty and the stable invariant manifolds of hyperbolic trajectories present in the system (6.1).

This chapter aims to complete the described picture as follows. While results in (García-Sánchez et al., 2022) consider the uncertainty of a model based on ocean currents in order to describe the final fate of an observation as it evolves *forward* in time, the new setting considers the uncertainty of a similar model in order to identify the original location of an

observation in a *past* time, once the position, $\mathbf{x_1}$, of this observation is known at the present time. In a nutshell, previous results were about: where do trajectories end up? How could it be measured if they are consistently described by a model constructed from approximate velocities? Now the results we desire are about: where do trajectories come from? how could it be measured if their origin is consistently described by a model that is constructed from approximate velocities? In this context, this chapter provides a new approach to measuring uncertainty using errors adequate for the backward time setting. We find that similar to what was found in García-Sánchez et al. (2022), this uncertainty has a *structure* in a neighborhood of the observation $\mathbf{x_1}$, and this structure is related to the unstable invariant manifolds of the hyperbolic trajectories present in the vector field of Equation (6.1).

Once this new type of uncertainty is introduced, we proceed to assess ocean data capabilities in real events that demand this type of perspective. In particular, a recent contamination event that occurred in 2021 in the Eastern Mediterranean is considered. Specifically in this event, thoroughly described in (García-Sánchez et al., 2022), several beaches were affected by a spill of unknown origin. In contrast to the results by García-Sánchez et al. (2022), now observations are done at the arrival point and the identification of their source is the goal. Equipped with the new tool we describe in detail its use to quantify the performance of different ocean data sets for describing observations adequately. There are other attempts to identify the best dataset for predicting the drift of oil spills (Brushett et al., 2011; Zhang et al., 2020). However, their approach consists of using uncertainty estimators in forward time.

In summary, the goal of this article is to propose a new uncertainty measure appropriate for quantifying the suitability of a model to describe the origin of trajectories. It is found that the considered uncertainty has a structure correlated with the unstable manifolds of the hyperbolic trajectories of the model. The capacity of this new measure is exploited for characterizing the performance of ocean data sets in real events. Accordingly, the structure of this article is as follows. Section 6.1 provides a new definition for uncertainty quantification suitable to describe the new setting and, in a simple example, discusses links with unstable manifolds of hyperbolic trajectories. In Section 6.2 a formal proof of this observation is given. Section 6.3 presents the application of this tool to the mentioned oil spill event that affected the Eastern Mediterranean, and shows how it helps to discriminate between two data sets, and supports the identification of the most suitable one for searching the spill source. In Section 6.4, the chapter concludes with a discussion of the implications and potential applications of this approach.

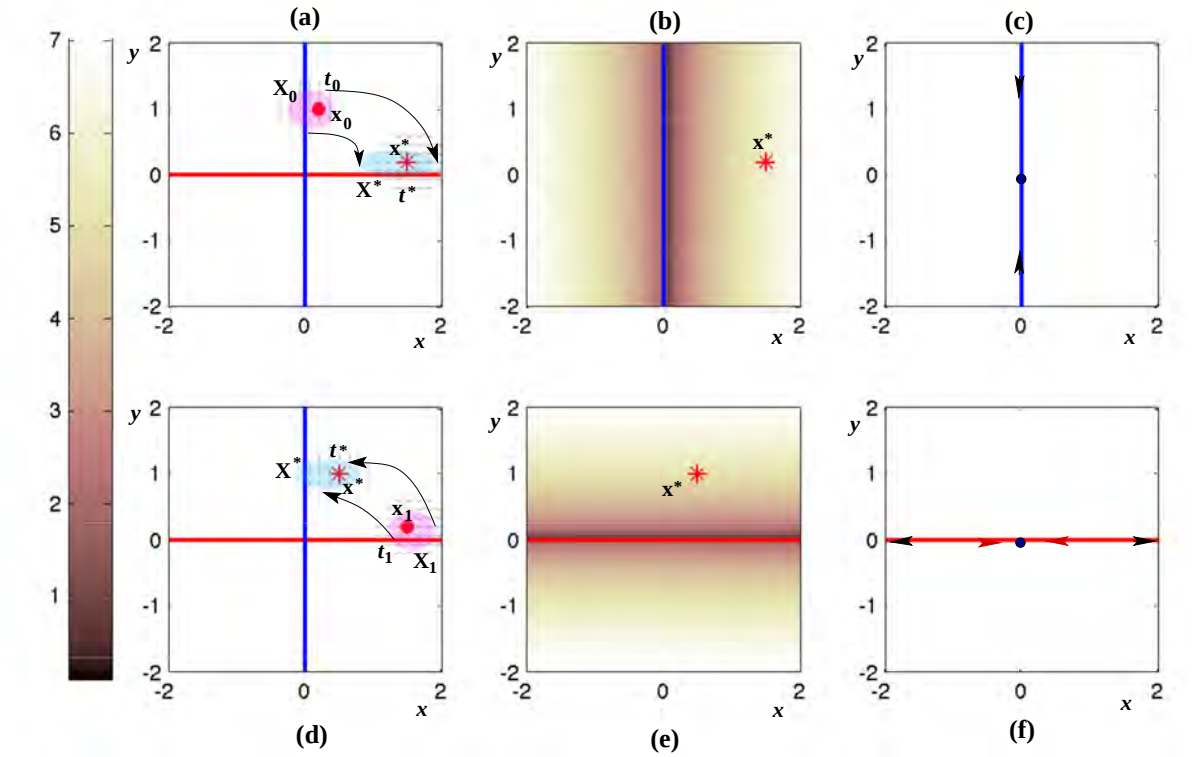


Figure 6.1 Panels a), b) and c) display a graphical representation of two sequential observations and their forward time evolution. a) The initial observation at time t_0 is expressed by the red circle with initial condition $\mathbf{x_0}$. The final observed state $\mathbf{x}^*$ at time t^* is referred to as the "target". In general, the evolution law linking these observations is unknown, but in our setting, it is approximated by Equation (6.2), a system with a hyperbolic fixed point at the origin with stable and unstable manifolds in blue and red, respectively. The forward evolution of $\mathbf{X_0}$ (the pink blob) to $\mathbf{X}^*$ (the light blue blob) according to this model is illustrated; b) a representation of L_{UQ}, in a domain beyond the neighbourhood X_0 for $\tau = 3$, where singular features are identified aligned with the stable manifold (in blue); c) a representation of the stable manifold. Black arrows point out the forward time evolution for initial condition on the stable manifold towards the fixed point at the origin; Panels d), e) and f) display a graphical representation of two sequential observations and their backward time evolution, d) the final observation at time t_1 is expressed with the red circle at the position $\mathbf{x_1}$. Although both the origin and the model of this observation are unknown, its evolution is approached by Equation (6.2), a system with a hyperbolic fixed point at the origin with stable and unstable manifolds in blue and red respectively. The backward evolution of $\mathbf{X_1}$ (the pink blob) to $\mathbf{X}^*$ (the light blue blob) according to this model is illustrated; e) a representation of L_{BUQ}, in a domain beyond the neighborhood X_1 for $\tau = 3$, where singular features are identified aligned with the unstable manifold (in red); f) a representation of the unstable manifold. Red arrows point out the evolution in backward time towards the fixed point for initial conditions on the unstable manifold. Black arrows point out the evolution forward time moving away from the fixed point. The color bar at the top indicates a color scale for L_{UQ} and L_{BUQ} in panels b) and e).

6.1. Uncertainty Quantification in Backward Time

This section is focused on proposing a new definition of uncertainty quantification to describe the uncertainty in the origin or source of certain observations based on predictions by a model constructed from velocities. This section is limited to present the definition and to discuss its implementation in one simple example. This simplified scenario enables us to establish connections between the new definition of uncertainty and the unstable manifolds of hyperbolic trajectories. The objective, however, is to apply this definition to distinguish the most appropriate velocity field among various options, the one that best matches the observations.

We start by recalling results reported in (García-Sánchez et al., 2022) in the context of the simple example illustrated in Figure 6.1. Panel a) within this figure shows an initial observation, $\mathbf{x}_0$, at time t_0 marked with a red circle. At a later time, t^*, this observation is at a target position, $\mathbf{x}^*$, marked with a red asterisk. This evolution is assumed to be following the model provided by Equation (6.2), with a vector field in the background, which is represented at time t_0, in the neighborhood of $\mathbf{x}_0$ and at time t^* in the neighborhood of $\mathbf{x}^*$. This vector field is chosen to be stationary, therefore its representation at later times, t^*, is the same as at t_0. However, in general, this vector field will be time-dependent and therefore its representation at t^* is different from that at t_0. The explicit expression for this vector field is:

$$\begin{cases} \frac{dx}{dt} = x, \\ \frac{dy}{dt} = -y, \end{cases} \tag{6.2}$$

This system has a stable manifold aligned with the vertical axis at $x = 0$ (blue line in Figure 6.1) and an unstable manifold aligned with the horizontal axis at $y = 0$ (red line in Figure 6.1).

García-Sánchez et al. (2022) proposed several expressions to measure the error in a neighborhood $\mathbf{X}_0$ of $\mathbf{x}_0$. Among those we consider this one:

$$L_{UQ}(\mathbf{X}_0, t_0, \tau, p) = \sum_{i=1}^{n} |x_i(t_o + \tau) - x_i^*|^p \,,\ p \leq 1,\ \mathbf{X}_0 \in \mathbb{R}^n, \tau > 0. \tag{6.3}$$

Here, $\mathbf{X}_0$ represents a set of initial conditions whose coordinates $(x_1, x_2, .., x_n)$, belong to a n dimensional system (6.1) and are in the neighbourhood of the observation $\mathbf{x}_0$. The coordinates of the target, towards which the system is assumed to evolve in a time interval τ, are $(x_1^*, x_2^*, .., x_n^*)$. Panel a) in Figure 6.1 illustrates the evolution from the set $\mathbf{X}_0$ (the pink blob) to $\mathbf{X}^*$ (the light blue blob). Panel b) displays L_{UQ} evaluated in the whole domain. This

representation expresses how much uncertainty would be associated with the system (6.2) beyond the neighborhood $\mathbf{X}_0$, assuming that initial observations start at different points of the representation domain and that they evolve towards the assumed observed target position at the red asterisk in $\tau = 3$. It is clear from the representation, that L_{UQ} presents a structure that consists of singular features aligned with the stable manifold of the hyperbolic fixed point present in the vector field, as discussed and proven in (García-Sánchez et al., 2022).

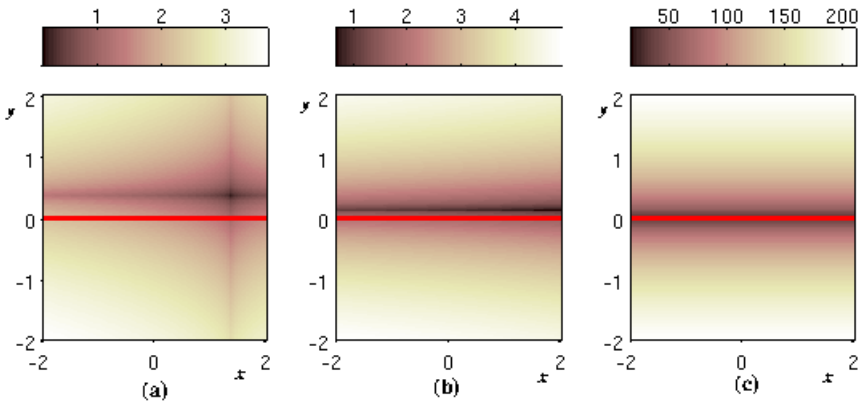


Figure 6.2 A representation in the plane of L_{BUQ} for the dynamical system (6.2) with target $x^* = (0.5, 1)$. a) $\tau = 1$; b) $\tau = 2$; c) $\tau = 15$. The red line represents the position of the unstable manifold.

In this chapter, our interest is in quantifying the uncertainty of a model for identifying a target source $\mathbf{x}^*$, which is consistent with a later observation $\mathbf{x}_1$ at time t_1. In this way, the target source, $\mathbf{x}^*$, is located at an earlier time $t^* = t_1 - \tau$. Similarly to the previous definition, for this setting, we propose the uncertainty to be:

$$L_{BUQ}(\mathbf{X}_1, t_1, \tau, p) = \sum_{i=1}^{n} |x_i(t_1 - \tau) - x_i^*|^p, \; p \leq 1, \; \mathbf{X}_0 \in \mathbb{R}^n, \tau > 0. \tag{6.4}$$

where now $\mathbf{X}_1$ represents a neighbourhood around the observation $\mathbf{x}_1 = (x_1, x_2, .., x_n)$ at time t_1 being n the dimension of the system (6.1), which in our specific examples is $n = 2$. The coordinates of the target are (x_1^*, x_2^*), and uncertainty is provided in terms of a distance metric between the target and the *backward* evolution of points near to $\mathbf{x}_1$ for a period τ.

Panel d) in Figure 6.1 illustrates the backward in time evolution of $\mathbf{X}_1$ (the pink blob) to $\mathbf{X}^*$ (the light blue blob) In the background, the panel also illustrates the vector field in a neighborhood of $\mathbf{x}_1$ at time t_1, and in the neighborhood of $\mathbf{x}^*$ at time t^*. Given that this vector field is stationary, its representation at an earlier time, $t^* = t_1 - \tau$, will be the same as at t_1, although in general this vector field is time-dependent and therefore its representation at t^* is different from that at t_1.

Panel e) displays in the whole domain, that is beyond the neighborhood $\mathbf{X}_1$, L_{BUQ} evaluated for $p = 0.5$, assuming $\tau = 3$. This representation expresses how much uncertainty is associated to the system (6.2), assuming that observations $\mathbf{x}_1$ could be anywhere in the domain and that they have evolved there from the target position $\mathbf{x}^*$ at $t^* = t_1 - \tau$. It is clear from the representation that L_{BUQ} presents a structure that consists of singular features aligned with the unstable manifold of the hyperbolic fixed point present in the vector field. A formal proof of this observation is given in the Section 6.2. In the proof it is shown how a sufficiently large τ is required for the singular structures obtained from Equation (6.4) to become aligned with the unstable manifolds. This is more clearly visualized in Figure 6.2. Panel a) shows the evaluation of L_{BUQ} for $\tau = 1$, where clearly the alignment with the unstable manifold is not yet achieved. Panels b) and c) confirm the convergence of the alignment towards the unstable manifold for, respectively, $\tau = 2$ and $\tau = 15$. This result completes the link between invariant dynamical structures and uncertainty quantification.

Panels c) and f) in Figure 6.1 graphically illustrate why the forward time uncertainty for system (6.2) is related to the stable manifold of the hyperbolic fixed point, while the backward time uncertainty is linked to the unstable manifold of that fixed point. Indeed, the forward time integration for initial conditions that stay on the stable manifold, for a sufficiently large τ, approach the fixed point at the origin, maintaining a fixed distance to the target, while all other initial conditions in the plane will increase their distance to the target for increasing τ. This is the origin of the singular features aligned with the stable manifold in forward time. Analogously, the backward time integration of initial conditions that stay on the unstable manifold, for a sufficiently large τ, approaches the fixed point at the origin, maintaining a fixed distance to the target. All other initial conditions in the plane will increase their distance to the target for increasing backward integration. This is the origin of the singular features aligned with the unstable manifold in backward time. Analogously this explanation also illustrates why both L_{UQ} and L_{BUQ} take minimum values along the unstable manifold. Indeed, they express the finite distance between the fixed point and the target, while the value of L_{UQ} and L_{BUQ} diverge for growing τ for all other points in the plane.

Figure 6.3 illustrates further these ideas. Panel a) represents the evolution versus τ of L_{UQ} at points: (0,2) in red – which is on the stable manifold– and (0,0) in black –the hyperbolic fixed point– as a function of τ, both with a target $\mathbf{x}^* = (1.5, 0.2)$ and $p = 0.5$. There is a transient behavior in τ for the point on the stable manifold, while in the limit of large τ both values converge to $|1.5|^{0.5} + |0.2|^{0.5} \sim 1.672$, which is the distance, in the defined metric, between the fixed point and the target. Similarly, panel b) represents the evolution of L_{BUQ} at points: (2, 0) in red –which is on the unstable manifold– and (0,0) in black –the hyperbolic

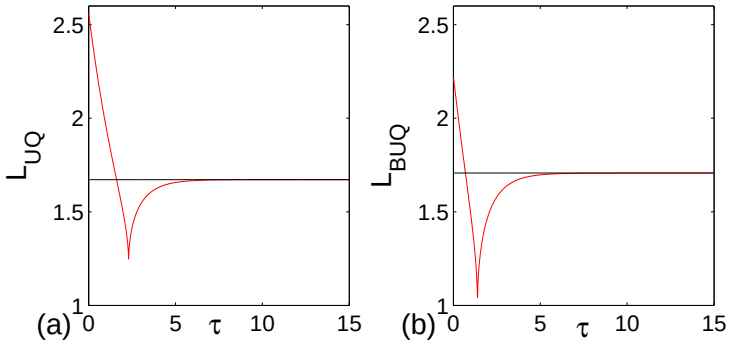


Figure 6.3 For the system given by Equation (6.2), a) evolution of L_{UQ} versus τ on the fixed point (black line) and on a point on the stable manifold (red line) with target $\mathbf{x}^* = (1.5, 0.2)$; b) evolution of L_{BUQ} versus τ on the fixed point (black line) and on a point on the unstable manifold (red line) with target $\mathbf{x}^* = (0.5, 1)$.

fixed point– as a function of τ, both with a target $\mathbf{x}^* = (0.5, 1)$ and $p = 0.5$. In the limit of large τ, both converge to the constant ~ 1.71.

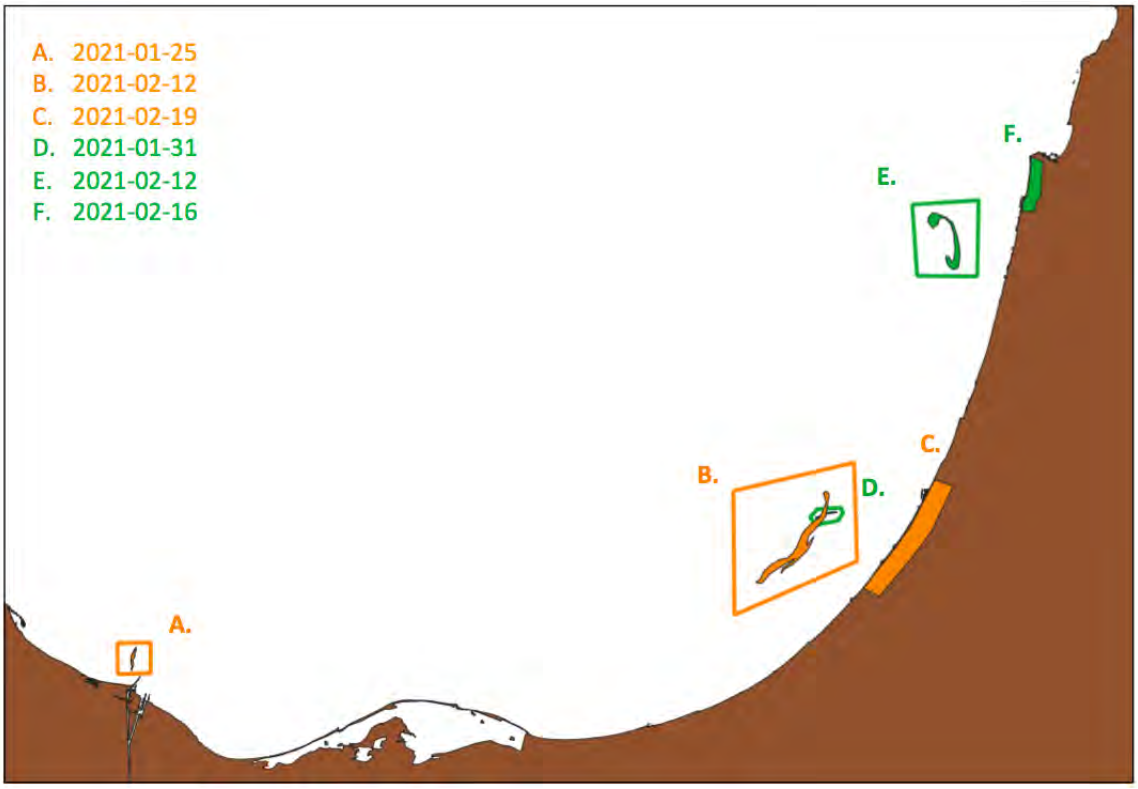


Figure 6.4 A graphical representation of the spills observed along the coastline of the Eastern Mediterranean and satellite observations matching the sources.

6.2. A proof for singularites in L_{BUQ}

Our proof follows the spirit of the work in Chapter 4 and by García-Garrido et al. (2018b); Lopesino et al. (2015, 2017). We assume the definition of singular features given there, by considering that these are features of L_{BUQ} (we consider for simplicity the expression for L_{BUQ} given in Equation 6.4) on which the transversal derivative is not defined. We prove that, for the simple case of the linear saddle, the unstable manifold of the hyperbolic fixed point is aligned with singular features of L_{BUQ}.

We study the vector field of the autonomous saddle case, where the equations of motion are the following:

$$\begin{cases} \frac{dx}{dt} = \lambda x, \\ \frac{dy}{dt} = -\lambda y, \end{cases} \qquad \lambda > 0 \tag{6.5}$$

The system has a unique solution for a given condition (x_1, y_1) at time $t = t_1$:

$$\begin{cases} x(t) = x_1 e^{\lambda(t-t_1)} \\ y(t) = y_1 e^{-\lambda(t-t_1)}, \end{cases} \qquad \lambda > 0 \tag{6.6}$$

Notice that the origin $(0,0)$ is a hyperbolic fixed point with stable and unstable manifolds which are the following:

$$W^s(0,0) = \{(x,y) \in \mathbb{R}^2 \colon x = 0, y \neq 0\}, \tag{6.7}$$

$$W^u(0,0) = \{(x,y) \in \mathbb{R}^2 \colon x \neq 0, y = 0\}, \tag{6.8}$$

Since in this chapter we study the backwards uncertainty quantification method we will consider according to (6.4):

$$\begin{aligned} L_{BUQ}(\mathbf{X}_1, t_1, \tau, p) &= \sum_{i=1}^{n} |x_i(t_1 - \tau) - x_i^*|^p \\ &= |x_1 e^{\lambda \tilde{t}} - x^*|^p + |y_1 e^{-\lambda \tilde{t}} - y^*|^p \\ &= |x_1|^p |\omega - a|^p + |y_1|^p \omega^{-p} |1 - b\omega|^p \end{aligned} \tag{6.9}$$

where $\tilde{t} = t_1 - \tau - t_1 = -\tau < 0$, $a = \frac{x^*}{x_1}, b = \frac{y^*}{y_1}$ and $\omega = e^{\lambda \tilde{t}} = e^{-\lambda \tau}$, $p \leq 1$. In order to compute equation (6.9) we will calculate, for simplicity, each of the terms separately. In the first term we notice that the sign of the expression $(\omega - a)$, for $\tau \gg 1$, will be positive when $a < 0$ and could be negative when $a > 0$.

- For $a < 0$:

$$|\omega - a|^p = (\omega - a)^p \tag{6.10}$$
$$= (-a)^p + p\omega(-a)^{p-1} + \frac{1}{2}(p-1)p\omega^2(-a)^{p-2} \tag{6.11}$$
$$+ \frac{1}{6}(p-2)(p-1)p\omega^3(-a)^{p-3} + O\left(\omega^4\right) \tag{6.12}$$
$$= (-a)^p + O\left(e^{-\lambda\tau}\right), e^{-\lambda\tau} \ll 1 \tag{6.13}$$

- For $a > 0$ let be t_L such that for $\tau > t_L$, we get that $(\omega - a) < 0$:

$$|\omega - a|^p = (-\omega + a)^p = a^p + p\omega a^{p-1} + \frac{1}{2}(p-1)p\omega^2 a^{p-2} + \tag{6.14}$$
$$\frac{1}{6}(p-2)(p-1)p\omega^3 a^{p-3} + O\left(\omega^4\right) \tag{6.15}$$
$$= a^p + O(\omega) \tag{6.16}$$

Therefore

$$|\omega - a|^p = |a|^p + O\left(e^{-\lambda\tau}\right), \omega \ll 1. \tag{6.17}$$

Note that $a = x^*/x_1$. Thus

$$|x_1|^p|\omega - a|^p = |x_1|^p|e^{-\lambda\tau} - a|^p = |x^*|^p + O\left(|x_1|^p e^{-\lambda\tau}\right), e^{-\lambda\tau} \ll 1.$$

For the factor $|1 - b\omega|^p$ of the second term there exists a t_L such that if $\tau > t_L$, then $b\omega << 1$ and $(1 - b\omega) > 0$. This is always the case for $b < 0$ and is a plausible assumption for $b > 0$, if $b << \omega^{-1}$. We recall that $b = y^*/y_1$ and that therefore such t_L exists if $y_1 \neq 0$. In this case positiveness is guaranteed for sufficiently large τ, i.e, a Taylor series around $\omega = 0$, attained if $\tau \gg 1$ and $\tau > t_L$, is performed for the binomial:

$$(1 - b\omega)^p = 1 - bp\omega + \frac{1}{2}b^2(p-1)p\omega^2 - \frac{1}{6}\omega^3\left(b^3(p-2)(p-1)p\right) + O\left(\omega^4\right).$$

Therefore,

$$\frac{1}{\omega^p}(1 - b\omega)^p = \omega^{-p} - bp\omega^{(1-p)} + \frac{1}{2}b^2(p-1)p\omega^{(2-p)} - O\left(\omega^{(3-p)}\right).$$

Finally we get:

$$|y_1|^p\omega^{-p}|1-b\omega|^p = |y_1|^p|\omega^{-p}-b|^p \tag{6.18}$$
$$= |y_1|^p|e^{\lambda\tau p}-b|^p \tag{6.19}$$
$$= |y_1|^p e^{\lambda\tau p} + O\left(|y_1|^p be^{-\lambda\tau(1-p)}\right) \tag{6.20}$$

Thus, we can approximate L_{BUQ} as

$$L_{BUQ}(\mathbf{X}_1,t_1,\tau,p) \approx |x^*|^p + |y_1 e^{\lambda\tau}|^p = |x^*|^p + |y_1|^p e^{\lambda\tau p} \tag{6.21}$$

the dominant term is the term $|y_1|^p e^{\lambda\tau p}$. Therefore the unstable manifold at $y=0$, for 'sufficiently large' τ, is aligned with a singular feature of L_{BUQ}, as long as $y_1 \neq 0$, and for any $|y_1| > 0$ for a sufficient large τ satisfying, $\tau > t_L$.

6.3. Results

The backward-time uncertainty definition provided in Equation (6.4), or its analog for the Euclidean distance given by:

$$L_{BUQ}(\mathbf{X}_1,t_1,\tau) = \left[\sum_{i=1}^{n} |x_i(t_1-\tau)-x_i^*|^2\right]^{\frac{1}{2}},\ \mathbf{X}_1 \in \mathbb{R}^n, \tau > 0 \tag{6.22}$$

are very suitable for assessing the performance of ocean models for describing events where the source of a certain observable, for instance, a contaminant, is unknown. This section describes how to implement the use of the definitions given in (6.4) or (6.22) to assess and determine the model that better achieves the observations in a recent oil spill of this type. This event is of a different nature to those described in (García-Sánchez et al., 2021), where after a reported oil spill accident the interest was in describing and controlling its evolution in order to minimize its impact. In contrast, now we are interested in assessing models that provide information about when and where did the spill originate. Good models in the setting described in Figure 6.1d) are expected to have small distances between $\mathbf{X}^*$ (the blue domain) and $\mathbf{x}^*$ (the target) and we will exploit this idea to measure the quality of available ocean data sets.

We describe next the specific event to be considered under this perspective. At the beginning of 2021, the coastline of several Middle Eastern countries in the Eastern Mediterranean

was affected by the presence of oil from an unknown source(s) (Wikimedia Foundation, 2021). No accidents were reported for these spills previous to their arrival at the coast, and therefore there was no hint of their origin. Israeli authorities estimated that more than 1000 tons of tar (Rinat and Zikri, 2021) landed along 180 km of the Israeli and Lebanese shoreline (Joffre and Tercatin, 2021; Kaplan-Zantopp, 2021; News-Agencies, 2021; Polidura, 2021; Staff, 2021; Tercatin, 2021) in mid-February. They combined the use of satellite images with simulations by Garcia-Sánchez et al. (García-Sánchez et al., 2022), which provided possible sources for this spill. Their work studied this event both from the remote sensing and modeling perspectives. Figure 6.4 illustrates some affected geographical areas. In this figure, orange and green colors along the coastline mark the oil arrivals. The systematic search of satellite images identified potential sources of these observations and a careful examination concluded that those sources surrounded by green and orange polygons, which correspond to satellite observations, were located in position and time in a manner consistent with the position and dates of the oil that subsequently arrived at the coast. According to (García-Sánchez et al., 2022), orange polygons labeled as A and B, are successive earlier locations to the orange arrival labeled as C. Analogously green polygons labeled as D and E, correspond to the green arrival labeled as F. The successive dates for each observation are given in the figure.

Simulations in (García-Sánchez et al., 2022) demonstrated that the spill was closely following fluid parcel trajectories $\mathbf{x}(t)$ that obeyed the equation:

$$\begin{cases} \dfrac{d\lambda}{dt} = \dfrac{u(\lambda,\phi,t)}{R\cos\phi} \\ \dfrac{d\phi}{dt} = \dfrac{v(\lambda,\phi,t)}{R} \end{cases} \tag{6.23}$$

where the position of the fluid parcel at the ocean surface is given in longitude (λ) and latitude (ϕ), and R is the Earth's radius. The system (6.23) is the particular form for our study of the general expression given by Equation (6.1), where $\mathbf{x} = (\lambda, \phi)$ and its right-hand side represent the two components of the vector field $\mathbf{v}$, which are determined by the zonal (u) and meridional (v) velocities. These velocity components are obtained as data sets from the Copernicus Marine Monitoring Environmental Service (CMEMS).

Equation (6.23) is a nonlinear non-autonomous dynamical system in 2D and it is required for implementing the backward evolution of fluid parcels in expression (6.22). L_{BUQ} in Equation (6.22) will have different evaluations for different CMEMS data sets. The goal of this section is to use these outputs to discriminate models. CMEMS provides two data sets describing currents in the Mediterranean Sea. One is the operational Mercator global ocean

analysis and forecast system that provides 10 days of 3D global ocean forecasts updated daily. This product includes daily and monthly mean fields of variables such as temperature, salinity, currents, sea level, mixed layer depth, and ice parameters from the top to the bottom of the global ocean. It also includes hourly mean surface fields for sea level height, temperature, and currents. The global ocean output files are displayed with a 1/12 degree horizontal resolution with an equirectangular longitude/latitude projection and 50 vertical levels ranging from 0 to 5500 meters.

The second data set is the physical component of the Mediterranean Forecasting System (Med-Currents), which is a coupled hydrodynamic-wave model, including tides, implemented over the whole Mediterranean Basin, with a higher resolution than the global model. Indeed, its horizontal grid resolution is 1/24 degree with 141 unevenly spaced vertical levels. The model solutions are corrected with a variational data assimilation scheme (3DVAR) of vertical profiles of temperature and salinity along the satellite track that provides observations of sea level anomalies (SLA).

Given that both models provide information for the same area, a natural question is to determine whether one is more suitable than the other for describing transport in the type of event described above. Models such as that given in Equation (6.23), possess a transport signature based on invariant manifolds associated with hyperbolic trajectories, which following Poincaré's idea, constitute geometrical structures on the ocean surface that organize particles schematically by regions corresponding to qualitatively different types of trajectories. These geometrical features allow a more robust analysis of the transport capacity of ocean currents than that based on individual trajectories. Indeed, there exist mathematical results that discuss the persistence of these geometrical structures in the presence of small perturbations, while individual trajectories may be affected much more drastically by perturbations (García-Garrido et al., 2018b; Haller, 2002). In the past these features have been used to assess the transport performance of data sets (García-Garrido et al., 2015; Haza et al., 2007, 2010; Kuznetsov et al., 2002; Mendoza et al., 2014; Shadden et al., 2009). In the context of geophysical flows, these geometrical structures are referred to as Lagrangian Coherent Structures (LCSs). The use of LCS allows a *qualitative* assessment of the performance of data sets, however, definitions such as that given in Equation (6.22) allow a *quantitative* analysis that we will implement next in the context of the oil spill event described in (García-Sánchez et al., 2022).

In this work, we compute LCS using Lagrangian Descriptors (Mancho et al., 2013; Mendoza and Mancho, 2010), a method based on computing the function defined as:

$$M(\mathbf{x}_0, t_0, \tau) = \int_{t_0-\tau}^{t_0+\tau} ||\mathbf{v}(\mathbf{x}(\mathbf{x}_0, t), t)||\, dt, \tag{6.24}$$

where the Euclidean norm, $||.||$, of the vector field $\mathbf{v}$ is evaluated along fluid parcel trajectories $\mathbf{x}(\mathbf{x}_0,t)$ of Equation (6.23), and therefore the integral in Equation (6.24) evaluates the arclength of this trajectory on the latitude-longitude plane at the ocean surface. In expression (6.24), the forward integration from t_0 reveals by means of singular features the stable manifolds associated to hyperbolic trajectories, whereas the backward integration highlights their unstable manifolds. This is explicitly expressed by splitting the integral (6.24) into two terms as follows:

$$\begin{aligned} M(\mathbf{x}_0,t_0,\tau) &= \int_{t_0-\tau}^{t_0} \mathbf{v}(\mathbf{x}(\mathbf{x}_0,t),t)\,dt + \int_{t_0}^{t_0+\tau} \mathbf{v}(\mathbf{x}(\mathbf{x}_0,t),t)\,dt \\ &= M^{(b)}(\mathbf{x}_0,t_0,\tau) + M^{(f)}(\mathbf{x}_0,t_0,\tau) \end{aligned} \tag{6.25}$$

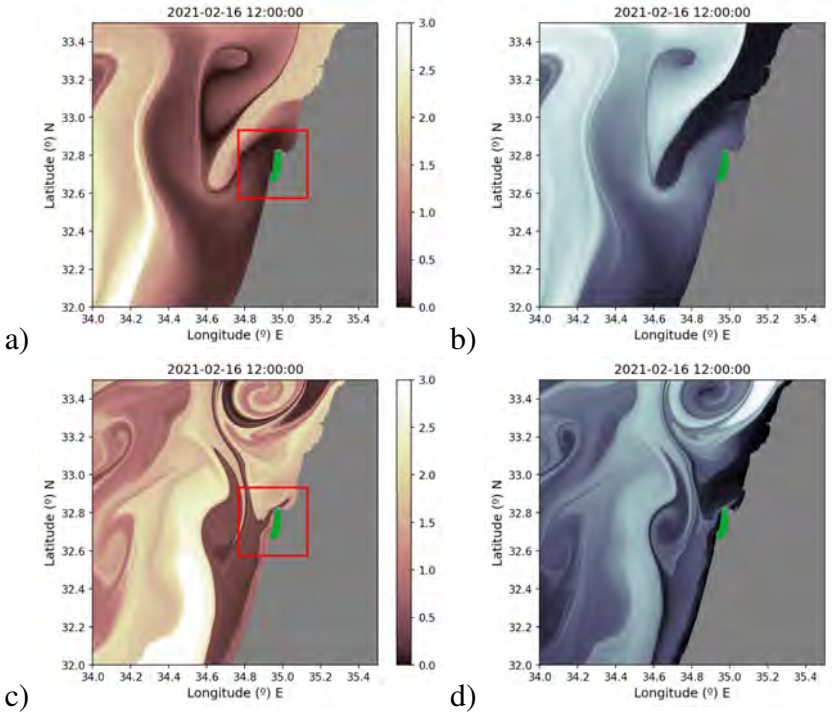


Figure 6.5 Evaluation on the 16th of February 2021 of L_{BUQ} using the target, $\mathbf{x}^* = (34.36°\text{E}, 31.78°\text{N})$ and of $M^{(b)}$ using $\tau = 16$ days; a) L_{BUQ} with the CMEMS global product; b) $M^{(b)}$ with the CMEMS global product; c) L_{BUQ} with the CMEMS Mediterranean product; d) $M^{(b)}$ with the CMEMS Mediterranean product.

We explore next the implementation of the ideas discussed in the previous section, to evaluate the performance of the two CMEMS products in the context of this environmental damage and their links to the unstable manifolds of hyperbolic trajectories present in the system Equation (6.23). Following oil detections displayed in Figure 6.4, we start the

discussion considering the first arrival to the coast on the 16th of February 2021, which is the green mark at the Israeli coast (F) and is considered to be the observation $\mathbf{x_1}$. For it, we consider that the position (D) on the 31st of January 2021 is its backward time target $\mathbf{x}^* = (34.355734°\text{E}, 31.777414°\text{N})$. Figure 6.5a) shows the evaluation of L_{BUQ} according to Equation (6.22) in a large area, considering that the eastward (u) and northward (v) velocity components are provided by the CMEMS global model. It is remarkable that its structure presents important analogies with the $M^{(b)}$, visible in panel b), which has been computed for $\tau = 16$ days. This image highlights, by means of singular features, the unstable manifolds of hyperbolic trajectories present in the vector field supplied by Equation (6.23). This result confirms that the uncertainty associated with the model has a structure closely related to invariant dynamical structures. The red square in panel a) highlights a neighborhood of the observation whose origin is conjectured to be at target $\mathbf{x}^*$. This domain $\mathbf{X_1}$ is used to characterize the performance of the model with respect to the hypothesis, assuming that the model is good if the target is consistent with arrivals in all this domain $\mathbf{X_1}$. The model is characterized through mean values of L_{BUQ} in this box. Panels c) and d) reproduce results for the CMEMS Mediterranean product. It is again clear the close relationship between the structure of L_{BUQ} and the unstable manifolds of hyperbolic trajectories present in Equation (6.23).

We continue the discussion considering that the observation $\mathbf{x_1}$ is the orange mark at the Gaza coast (C) on the 19th of February 2021. For it, we consider that the position (A) on the 25th of January 2021 is its backward time target: $\mathbf{x}^* = (32.319813°\text{E}, 31.350392°\text{N})$. Figure 6.6 displays the results both for CMEMS global and Mediterranean products. Panels a) and c) display the outputs of L_{BUQ}, and the red box highlights the neighborhood $\mathbf{X_1}$ used to characterize the performance of the model. Panels b) and d) again confirm the similarities between the unstable manifolds of hyperbolic trajectories in Equation (6.23) and the structure of L_{BUQ}.

It is remarkable that for both cases examined in figures 6.5 and 6.6, L_{BUQ} takes, in the neighborhood $\mathbf{X_1}$, considerably larger values for the CMEMS Mediterranean product than for the global one. Table 6.1 confirms this point by providing the averages in both domains in the column labeled as “Remote Targets", suggesting the better performance of the global model for these cases.

Figure 6.4 shows that related to the oil arrivals marked in green (F) and orange (C), there exist additional targets $\mathbf{x}^*$ nearer and closer to the observation $\mathbf{x_1}$, than those previously discussed. These backward-in-time targets, labeled (B) and (E), were identified from satellite imagery between the dates of the original sources and the dates of arrival on shore. These spills, after several days have elapsed since their leak, spread out on the ocean surface due

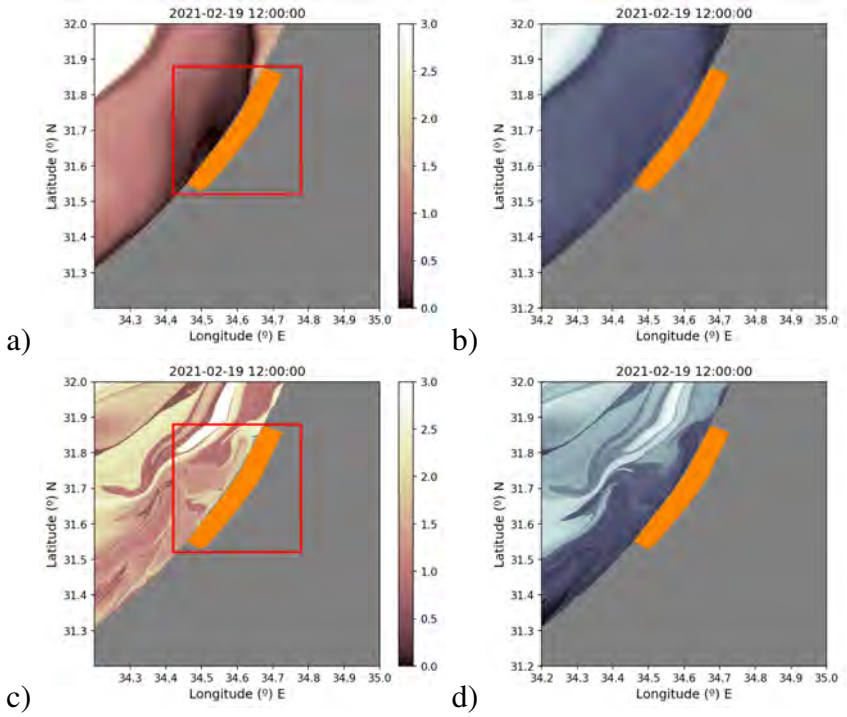


Figure 6.6 Evaluation on the 19th of February 2021 of L_{BUQ} using the target, $\mathbf{x}^* = (34.32°\text{E}, 31.35°\text{N})$ and of $M^{(b)}$ using $\tau = 25$ days; a) L_{BUQ} with the CMEMS global product; b) $M^{(b)}$ with the CMEMS global product; c) L_{BUQ} with the CMEMS Mediterranean product; d) M^b with the CMEMS Mediterranean product.

to the ocean movement, which stretches and folds them in a chaotic dynamic. Indeed, this description matches well the appearance of targets (B) and (E), as discussed in (García-Sánchez et al., 2022). Now we consider the evaluation of L_{BUQ} using these new $\mathbf{x}^*$ to assess both models. We start considering the green observation (F) ($\mathbf{x_1}$) on the Israeli coast. For it, central coordinates of the spill contour on the 12th of February 2021 are $\mathbf{x}^* = (34.72008°\text{E}, 32.59311°\text{N})$. Other target positions within the extended spill could have been considered, but they do not lead to substantial changes either in the results or in the discussions. Panels a) and b) in Figure 6.7 display the evaluation L_{BUQ} for this target, considering the CMEMS global and Mediterranean products respectively. Regarding the orange observation (C) coordinates that correspond to its backward-in-time target on the 12th of February 2021 are $\mathbf{x}^* = (34.2891°\text{E}, 32.59311°\text{N})$. As before, given that this is a rather spread contour, other target positions could have been considered, but we do not discuss them as they provide no changes in the conclusions. For these assumptions panels c) and d) of Figure 6.7 display L_{BUQ} considering the CMEMS global and Mediterranean products respectively. In these pictures, the red box delimits the boundaries of the neighborhood $\mathbf{X_1}$

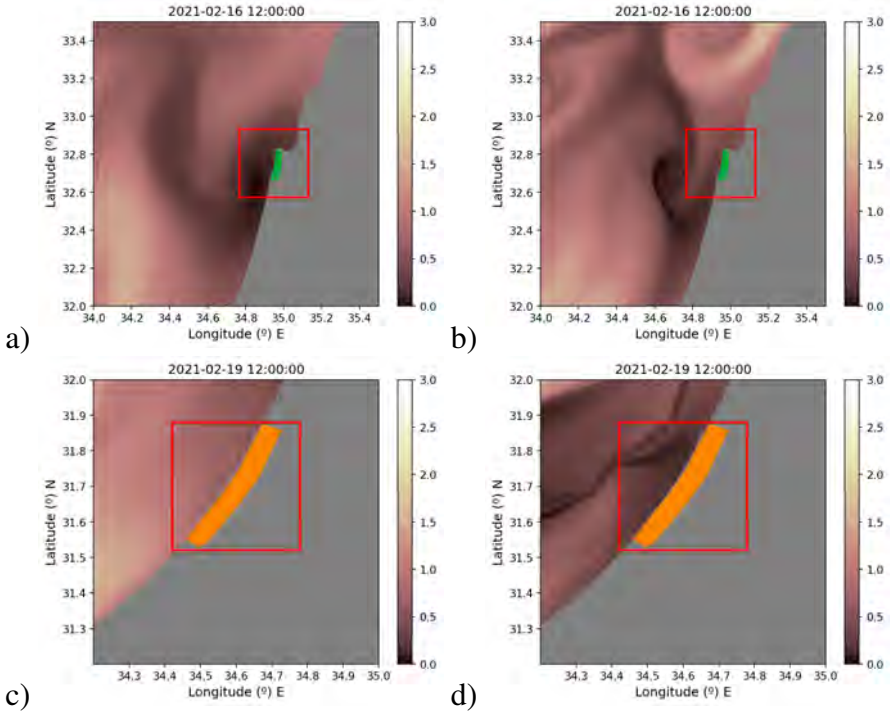


Figure 6.7 Evaluation L_{BUQ} on the Israel and Gaza coast for the close targets using the global and the Mediterranean data. L_{BUQ} on 16th of February 2021 using the target, $\mathbf{x}^* = (34.72°\text{E}, 32.59°\text{N})$; a) L_{BUQ} on the Israel coast with the CMEMS global product; b) $M^{(b)}$ on the Israel coast with the CMEMS Mediterranean product. L_{BUQ} on 19th of February 2021 using the target, $\mathbf{x}^* = (34.28°\text{E}, 32.59°\text{N})$; c) L_{BUQ} on the Gaza coast with the CMEMS Global product; d) $M^{(b)}$ on the Gaza coast with the CMEMS Mediterranean product.

used to evaluate the model performance. In this case the column “Close Targets" in Table 6.1 shows the results for both models.

A discussion of these results requires highlighting the sizes involved in the different settings. The distance between the remote targets and the Gaza (orange) and Israeli (green) shore impact points are, respectively, $\sim$ 215 km and 127 km. These size ranges involve ocean mesoscale structures, which seem to be better represented in the global model. The close targets are at distances $\sim$ 28 km and 33 km respectively of the Gaza and Israel arrival points (C) and (F). These sizes involve ocean submesoscale structures, which should be better represented by the higher resolution model, which is the CMEMS Mediterranean product. Indeed, this is the one that on average performs better for the closer targets, although the global model shows a good performance as well for the Israel case, despite its lower resolution.

	Remote Targets		Close Targets	
Case	Global	Mediterranean	Global	Mediterranean
Israel	0.2989	0.9434	0.1642	0.3375
Gaza	0.34074	1.5426	0.7810	0.24666

Table 6.1 Averages of L_{BUQ} within the $\mathbf{X_1}$ domains highlighted with red boxes.

6.4. Conclusions

This article proposes a new definition for uncertainty quantification that extends those recently proposed in oceanic contexts in (García-Sánchez et al., 2022, 2021). The new definition is referred to as Lagrangian Uncertainty Quantification in Backward time (L_{BUQ}), and it is suited to measure if a given transport model consistently describes the source of an observation whose origin is unknown.

We have found that the defined quantity L_{BUQ}, when evaluated in the neighborhood of an observation with respect to its backward-in-time target, has a *structure* which has been linked to the unstable invariant manifolds of the hyperbolic trajectories present in the model vector field. This link has been rigorously proven in a simple example, and numerically verified in a real inspired case: the oil spill accident that affected the Eastern Mediterranean in 2021, which was studied in (García-Sánchez et al., 2022).

The new definition, L_{BUQ}, has been exploited to quantify the performance of different CMEMS products to describe the sequence of events reported in (García-Sánchez et al., 2022) regarding the oil spill accident in the Eastern Mediterranean in 2021. In this event, some of the backward-in-time targets are very far from the impact point, and their evolution involves mesoscale structures, which our analysis shows are better represented in the CMEMS global model. On the contrary for targets that are close, involving submesoscale structures, on average the CMEMS Mediterranean product performs better, although in some cases CMEMS global product also performs well.

Our results are set within a different framework compared to other inverse uncertainty studies. In those studies, the model typically consists of a dissipative partial differential equation with adjustable parameters, and the uncertainty analysis aims to determine the best-fitting parameters based on observations. However, in our framework, the model comprises a two-dimensional set of volume-preserving (non-dissipative) non-autonomous differential equations, and their exact form is unknown as they rely on approximated velocity fields. Many classical inverse problems, such as the inverse heat equation, are ill-posed, meaning that inferring a previous temperature distribution from final data is highly sensitive to changes in the final data. Although our framework differs from such cases, we still observe a high

sensitivity to the uncertainty measured around a final observation, as demonstrated in Figures 6.5, 6.6, 6.7. In the neighborhood surrounding the final observation, the uncertainty exhibits a complex structure with high oscillations, and we have established a connection with the unstable manifolds of hyperbolic trajectories. Thus, we illustrate how concepts from dynamical systems are linked to uncertainty quantification, whereas a statistical perspective has traditionally been the main focus in this context. Finally, we have shown how to implement these concepts for the practical purpose of discriminating the best data set performer on specific environmental applications.

Chapter 7

Dynamical Systems and Satellite Imagery for Hydrodynamic Models

This chapter is based on the results described in the paper by García-Sánchez et al. (2023b), which is a continuation of the IMPRESSIVE collaborative effort. For the sake of completeness and consistency, we will recall the methodological aspects described in Chapter 2.

Ocean numerical models help to understand and predict the ocean variables that have an impact on the environment, climate, and human activities. Oceanic data produced by models are increasingly becoming available, with various services providing valuable information on the ocean's physical state and dynamics. For instance, the Copernicus Marine Environment Monitoring Service (CMEMS) offers regular and systematic data on current and future variables, as well as retrospective data records (reanalysis) of the global and European regional seas. Alternatively, the HYbrid Coordinate Ocean Model (HYCOM), a multi-institutional effort sponsored by the National Ocean Partnership Program (NOPP) as part of the US Global Ocean Data Assimilation Experiment (GODAE), is dedicated to developing and evaluating data-assimilative hybrid coordinate ocean models. The products offered by these services typically have resolutions of the order of 2.5-8 km and have been successful in describing events above those scales (García-Garrido et al., 2015, 2016; García-Sánchez et al., 2022). More recently, it has been pointed out (García-Sánchez et al., 2021) the necessity of using products with much higher resolution to address management needs at the coastal level. These needs may include navigation, harmful algae blooms, effluent dispersion, search and rescue operations, oil spill response, etc. In these cases, models are particularly valuable for understanding and predicting ocean currents for the management of aspects that affect life in these areas, including beach conditions and near-shore environments.

In situ measurements are incorporated into ocean models through different methodologies to achieve outputs that are accurate and consistent with the real ocean state. Among the instruments employed for in situ measurements are moored current meters, drifters, shipboard current profilers that measure sea surface velocity, etc. The deployment and maintenance of this equipment is expensive and, in general, its spatial coverage is limited to hotspot areas where the investment in these measurements is worth it. There exist however wide coastal and marine protected areas, where high-resolution models can be very valuable for management purposes, but for which in situ measurements are not available and therefore their validation is challenging. However, observations in these areas are possible through satellites that today are equipped with multiple remote sensing systems capable of providing valuable information on the dynamic properties of extensive oceanic coastal areas. In this work, we will explore the use of methodologies based on dynamical systems and satellite imagery for feedback and adjustment of ocean model outputs and as a validation method.

More specifically, this chapter starts with the creation of a very high-resolution hydrodynamic model in an area for which no in situ measurements were available. This is the area of the Rafina port in Greece, which was taken as a study case in the framework of the IMPRESSIVE project. Sentinel 2 and Sentinel 3 images near the coast provide images in the optical band that after being processed are able to identify turbidity caused by suspended particles, including particulate and dissolved organic and inorganic matter. These materials may derive from sources such as primary production blooms and wastewater. The spread of these compounds makes visible convoluted shapes, which are linked to invariant dynamical objects, called Lagrangian Coherent Structures (LCS), obtained from the currents. Thus, patterns visible in remote sensing images can be correlated to patterns obtained from the hydrodynamic model. We will utilize this idea to explore an effective methodology for validating the transport capacity of the model outputs. This approach differs from classical validations that compare in situ measurements of currents, sea level, etc. with those obtained from the models. Our comparison is systematically implemented by adjusting the parameters and parameterizations required by the model, which include closure relationships for unresolved turbulent scales, lateral boundary conditions for the nested model, and the coupling of surface ocean motion with atmospheric winds, among others. In addition, an index is defined to quantify the degree of fitting of each parameter set to the satellite observations.

The manuscript is structured as follows. Section 7.1 provides a description of the equations and software utilized to set up the hydrodynamical model for the Rafina Port. It also discusses the boundary conditions and settings specific to the temporal window of October-December 2019. In Section 7.2, the available remote sensing products for that temporal window are described. Section 7.3 delves into the dynamical systems concepts

used to establish the connection between the hydrodynamical model outputs and the satellite imagery. Section 7.4 outlines the various settings for the experiments conducted and details the procedure used to quantify their performance. The results are presented in Section 7.5, and finally, the conclusions are explained in Section 7.6.

7.1. The hydrodynamic model

7.1.1. The oceanic regional model

To set up the hydrodynamic model we have used the Regional Oceanic Modeling System (see details on (Hedström, 1994b)). ROMS numerically solves the Navier–Stokes equations while considering the hydrostatic and Boussinesq assumptions (Haidvogel et al., 2000; Shchepetkin and McWilliams, 2005). However, ROMS does not solve these 3D equations exactly in a turbulent regime; instead, it utilizes the unsteady Reynolds-Averaged Navier–Stokes (RANS) equations. These are derived from the Navier-Stokes equations by applying Reynolds decomposition, which decomposes the instantaneous velocity field ($\mathbf{v}_T$) into a time-averaged ($\overline{\mathbf{v}}_T$) and a fluctuating component ($\mathbf{v}'_T$). In this work, the mean velocity is the velocity field solved in equations (7.1)-(7.3), which is referred to as $\mathbf{v} = (u, v, w)$ there. The fluctuating component $\mathbf{v}'_T = (u', v', w')$ is solved using turbulent closure relations, which are detailed later in this section. ROMS has been employed in numerous operational oceanography systems on regional scales. Examples include the NOAA operational forecast systems for locations such as Tampa Bay, Chesapeake Bay, and the Gulf of Maine, and the SAMOA system, which the Spanish Public State Port Agency developed to offer tailored operational meteorological and oceanographic data (Sotillo et al., 2020b). ROMS has also been utilized in diverse applications like estuarine modeling (Cerralbo et al., 2015), sediment transport (Grifoll et al., 2014), oceanic basin modeling (Malanotte-Rizzoli et al., 2000), climate research (Di Lorenzo et al., 2008b), and the study of atmosphere-wave-current interactions (Warner et al., 2010). A key advantage of ROMS is its modular structure and efficient parallelization using the Message Passing Interface (MPI), enabling rapid computational performance (Wang et al., 2005).

ROMS solves the governing dynamical equations in flux form. The vertical takes terrain-following coordinates that are named sigma vertical coordinates. We have used Cartesian coordinates in the horizontal, although other choices are available. These equations take the form (Haidvogel et al., 2008):

$$\frac{\partial u}{\partial t} + \mathbf{v} \cdot \nabla u - fv = -\frac{\partial \phi}{\partial x} - \frac{\partial}{\partial z}\left(\overline{u'w'} - \nu \frac{\partial u}{\partial z}\right) + \mathscr{F}_u + \mathscr{D}_u, \tag{7.1}$$

Parameters	p	m	n	σ_k	σ_ψ	c_μ^0	c_1	c_2	c_3^+	c_3^-	$k_{\min}$	$\psi_{\min}$	F_{wall}	c	ν	ν_θ
Values for $k-\varepsilon$ model	3	1.5	-1	1.0	1.3	0.5544	1.44	1.92	1.0	-0.518	$7.6\cdot10^{-6}$	$1.0\cdot10^{-12}$	1.0	1	$5.0\cdot10^{-6}$	$5.0\cdot10^{-6}$

Table 7.1 Parameters for the generic length scale turbulence- $k-\varepsilon$ model and Kantha-Clayson stability functions (see (Warner et al., 2005)).

$$\frac{\partial v}{\partial t}+\mathbf{v}\cdot\nabla v+fu=-\frac{\partial \phi}{\partial y}-\frac{\partial}{\partial z}\left(\overline{v'w'}-\nu\frac{\partial v}{\partial z}\right)+\mathscr{F}_v+\mathscr{D}_v, \tag{7.2}$$

In the Boussinesq approximation, changes in density are disregarded in the momentum equations, except for their influence on the buoyancy force within the vertical momentum equation. When the hydrostatic approximation is employed, it is additionally presumed that the buoyancy force is counterbalanced by the vertical pressure gradient:

$$\frac{\partial \phi}{\partial z}=-\frac{\rho g}{\rho_0} \tag{7.3}$$

where $\phi = p/\rho_0$ and $p \approx -\rho_0 g z$ is the total pressure. The continuity equation for an incompressible fluid:

$$\frac{\partial u}{\partial x}+\frac{\partial v}{\partial y}+\frac{\partial \omega}{\partial z}=0 \tag{7.4}$$

Here $\mathbf{v}=(u,v,\omega)$ and u, v, and ω are the components of velocity in the horizontal (x and y) and vertical (scaled sigma coordinate, s) directions respectively; and f is the Coriolis parameter. An over-bar represents a time average, and a prime ($'$) represents turbulent fluctuations. ρ and ρ_0 are total and reference densities; g is the acceleration due to gravity; ν is the molecular viscosity. Here all $\mathscr{F}$ are forcing terms and $\mathscr{D}$ are horizontal diffusive terms.

Temperature (T) and salinity (S) scalar tracers, generically denoted as C, are coupled to the momentum equations, and their transport equation is given by:

$$\frac{\partial C}{\partial t}+\mathbf{v}\cdot\nabla C=-\frac{\partial}{\partial z}\left(\overline{c'w'}-\nu_\theta\frac{\partial C}{\partial z}\right)+C_{\text{source}}+\mathscr{F}_C+\mathscr{D}_C \tag{7.5}$$

Here C_{source} represents scalar source/sink terms; ν_θ is the molecular diffusivity. Again $\mathscr{F}$ are forcing terms and $\mathscr{D}$ are horizontal diffusive terms. A function $\rho=\rho(T,S,p)$ is required to specify the equation of state. We have selected the option of the nonlinear equation of state introduced by Jackett and Mcdougall (1995).

Equations (7.1)-(7.2) and (7.5) are closed by parameterizing the Reynolds stresses and turbulent tracer fluxes as:

$$\overline{u'w'}=-K_M\frac{\partial u}{\partial z};\quad \overline{v'w'}=-K_M\frac{\partial v}{\partial z};\quad \overline{c'w'}=-K_H\frac{\partial \rho}{\partial z} \tag{7.6}$$

with

$$K_M = c\sqrt{2k}lS_M + \nu \qquad K_H = c\sqrt{2k}lS_H + \nu_\theta \tag{7.7}$$

In these equations, K_M represents the eddy viscosity for momentum and K_H represents the eddy diffusivity for tracers. S_M and S_H are stability functions that describe the effects of shear and stratification. From the several possibilities available in ROMS, we have chosen the Kantha-Clayson stability functions (see (Warner et al., 2005)). The replacement of Eqs. (7.6) into Eqs.(7.1)-(7.2) and (7.5) leads to the standard harmonic form for vertical viscous/diffusive terms. The turbulent quantities k (turbulence kinetic energy) and l (turbulent length scale) must be determined in order to close the set of equations. ROMS contains a variety of methods to do this. In this work, we considered the generic lengthscale (GLS), proposed by Umlauf and Burchard (2003) and implemented in ROMS by Warner et al. (2005). This is a generic two-equation turbulence closure scheme. The first equation represents the conventional transport equation for the turbulent kinetic energy (k),

$$\frac{\partial k}{\partial t} + \mathbf{v}\cdot\nabla k = \frac{\partial}{\partial z}\left(\frac{K_M}{\sigma_k}\frac{\partial k}{\partial z}\right) + P + B - \varepsilon, \tag{7.8}$$

where σ_k is the turbulence Schmidt number for k. P and B represent production sources by shear and buoyancy, and ε is the dissipation. They are given by:

$$P = K_M\left[\left(\frac{\partial u}{\partial z}\right)^2 + \left(\frac{\partial v}{\partial z}\right)^2\right],\ B = K_H\left(\frac{g}{\rho_0}\frac{\partial \rho}{\partial z}\right),\ \varepsilon = (c_\mu^0)^{3+p/n}k^{3/2+m/n}\psi^{-1/n}, \tag{7.9}$$

here the stability coefficient c_μ^0 is determined based on experimental data for the unstratified channel flow with a log-layer solution. The second equation of the GLS model describes the evolution of ψ, a generic parameter used to establish the turbulence length scale:

$$\frac{\partial \psi}{\partial t} + \mathbf{v}\cdot\nabla\psi = \frac{\partial}{\partial z}\left(\frac{K_M}{\sigma_\psi}\frac{\partial \psi}{\partial z}\right) + \frac{\psi}{k}(c_1 P + c_3 B - c_2\varepsilon F_{\text{wall}}), \tag{7.10}$$

The parameter σ_ψ represents the turbulence Schmidt number for ψ, indicating the ratio of momentum diffusivity to the diffusivity of ψ. Coefficients c_1 and c_2 are chosen to be consistent with experimental observations of decaying homogeneous, isotropic turbulence (Wilcox et al., 1998). The parameter c_3 assumes different values for stable (c_3^+) or unstable (c_3^-) stratification. Also,

$$\psi = (c_\mu^0)^p k^m l^n. \tag{7.11}$$

The parameters in expressions (11)-(13) for the $k-\varepsilon$ model, which is considered in our simulations, take values summarized in Table 7.1 (see (Warner et al., 2005)).

We further explain the sigma vertical coordinates used in ROMS. The variables related to this coordinate are ζ, representing the wave-averaged free-surface elevation, and h, denoting the depth of the sea floor relative to the mean sea level. In a topography-following vertical coordinate system, there is a transformation,

$$z = z(x, y, \sigma), \tag{7.12}$$

where z is the Cartesian height and σ is the vertical distance from the surface measured as the fraction of the local water column thickness; i.e, $-1 \leq \sigma \leq 0$, where $\sigma = 0$ correspond to the free surface, $z = \zeta$, and $\sigma = -1$ corresponds to the oceanic bottom or bathymetry, $z = h(x, y)$. In the case of the classical σ-coordinate, (7.12) reduces to

$$z = \sigma \cdot h(x, y) \tag{7.13}$$

This may be combined with nonlinear stretching, $S(\sigma)$,

$$z(x, y, \sigma) = S(\sigma) \cdot h(x, y). \tag{7.14}$$

ROMS allows to use a general vertical coordinate system *S*-coordinate (Song and Haidvogel, 1994):

$$z(x, y, \sigma) = \zeta(x, y, t) + [\zeta(x, y, t) + h(x, y)]\, S(x, y, \sigma) \tag{7.15}$$

$$S(x, y, \sigma) = \frac{h_c \sigma + h(x, y) C(\sigma)}{h_c + h(x, y)} \tag{7.16}$$

where $h_c \leq h_{min}$ is a free parameter that must be adjusted for each application. h_c is a depth above which the vertical grid spacing of the sigma layers becomes (a) nearly uniform and (b) nearly independent of local depth, h, as long as $h \gg h_c$. In our case h_c = 84 m and $C(\sigma)$ can take different forms. In our application, we are assuming that

$$S(x, y, \sigma) = \begin{cases} 0 & \text{if } \sigma = 0,\ C(\sigma) = 0, \text{ at the free-surface,} \\ -1 & \text{if } \sigma = -1,\ C(\sigma) = -1, \text{ at the ocean-bottom,} \end{cases} \tag{7.17}$$

and $C(\sigma)$ is defined as a continuous, double-stretching function controlled at the surface by θ_s and at the bottom layer by θ_b. In our particular case, we have selected $\theta_S = 5$ and $\theta_B = 0.4$. The refinement function is then defined in two steps. First, we consider for the surface:

$$C_s(\sigma) = \frac{1 - \cosh(\theta_S \sigma)}{\cosh(\theta_S) - 1}, \quad \text{for } \theta_S > 1 \tag{7.18}$$

Then we consider the bottom refinement function:

$$C(\sigma) = \frac{\exp(\theta_B C_s(\sigma)) - 1}{1 - \exp(-\theta_B)}, \quad \text{for } \theta_B > 0. \tag{7.19}$$

7.1.2. The geographical domain

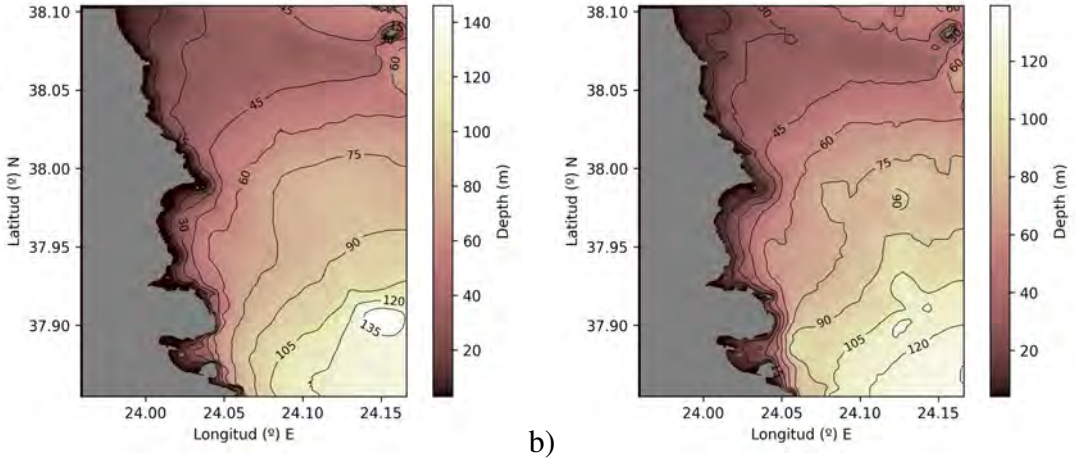


Figure 7.1 Bathymetry of the Rafina area in the domain L_0. The color intensity corresponds to the depth of the sea floor, with brighter colors indicating greater depths. a) NAVIONICS source data; b) GEBCO source data.

Our study sets up a hydrodynamic model in the neighborhood of Rafina Port. The area lies on the Aegean Sea coast, east of the Penteli mountains and northeast of the Mesogaia plain. It is 5 km (3 mi) north of Artemida, 7 km (4 mi) south of Nea Makri, and 25 km (16 mi) east of Athens city center. Specifically, the selected domain L_0 is between latitudes 37.8541-38.1042 degrees North and longitudes 23.9583-24.1667 degrees East.

Figure 7.1 illustrates the domain where equations are solved with two different choices for the function $h(x,y)$ representing the sea bed. Panel a) shows a bathymetry in the area obtained from contour levels that follow a NAVIONICS chart, which we have computed with a resolution of up to 10×10 meters. Panel b) displays the sea floor offered by GEBCO. This is a publicly-available bathymetry of the world's oceans. It operates under the joint auspices of the International Hydrographic Organization (IHO) and the Intergovernmental Oceanographic Commission (IOC) (of UNESCO). Its resolution is about 15 arc seconds. Sigma-coordinates employed by ROMS require that topographic steepness is limited to prevent pressure gradient errors. For this reason, topographies in Figure 7.1 are smoothed by selectively applying a local filter to reduce the r-factor below 0.2. The r-factor is a measure of the sharpness of the variations in the bathymetry. It is defined as the ratio of the maximum

height difference between adjacent points (Δh) to the average height of those points ($2h$); see, for example, (Haidvogel and Beckmann, 1999). Additionally, all depths in L_0 shallower than 0.5 m are reset to 0.5 m.

Although the appearance of both bathymetries is very similar we will explore their influence on the model outputs in section 7.5. Indeed, the sea floor has a number of impacts on ocean circulation. It helps steer large-scale circulation, and small gaps in the ocean floor can even influence the direction of dominant currents. In addition, small-scale bathymetric features can also affect ocean circulation. When ocean currents flow over the rough sea floor, energy is converted from horizontal flow into vertically propagating waves, leading to increased vertical mixing over rough topography (Gille and Smith, 2003).

7.1.3. Discretization and numerical algorithms

Regarding the spatial resolution implemented in the domain of interest, we have adopted a horizontal resolution of $80\times$ 80 meters, which is achieved with the grid of dimensions $Lm \times Mm$ reported in Table 7.2. The horizontal discretization implemented by ROMS is on an Arakawa 'C' grid and spatial derivatives are computed with a centered, second-order finite difference approximation.

Discretization of the vertical coordinate introduces a set of coordinate surfaces,

$$\{z_{k+\frac{1}{2}} = z_{k+\frac{1}{2}}(x,y), k = 0,1,\cdots N\} \tag{7.20}$$

In particular, for our application we have considered $N = 10$, that is 10 sigma levels. Figure 7.2 illustrates the $\sigma-$levels used at longitude 24.15 °E.

The stability of numerical models are affected by the numerical time-integration method, the spatial discretization, and the permitted modes in the equations. Advection is characterized by a velocity scale, U. The shortest advective timescale in a numerical model is Δ/U, where Δ is the spatial grid scale and U is a measure of the maximum characteristic velocity. The CFL number is the ratio of this characteristic timescale to the model time step:

$$CFL = \frac{U\Delta t}{\Delta}. \tag{7.21}$$

In the case of ROMS' time scheme, CFL must be less than a number on the order of unity. Then, the largest time step that can support numerical stability for a given flow and grid spacing scales is

$$\Delta t^u_{\max} \propto \frac{\Delta}{U}. \tag{7.22}$$

As we said before, $\Delta = 80$ meters so we consider $\Delta t = 10$ seconds.

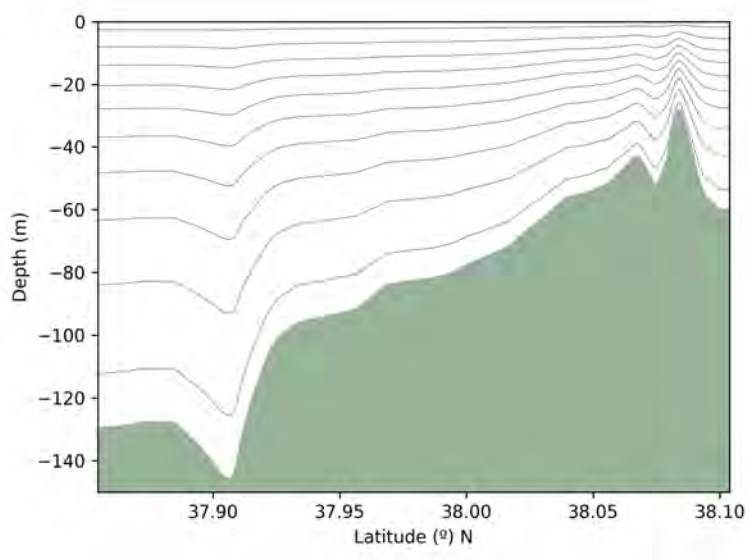


Figure 7.2 Vertical discretization at longitude 24.15 °E. The green color represents the bathymetry, while the lines indicate the different $\sigma-$levels based on the stretching function utilized.

The horizontal viscous and diffusivity terms $\mathscr{D}$ are given by the harmonic expressions:

$$\mathscr{D}_X = A_X \nabla^2 X, \quad \text{for } X = \{u, v, T, S\}, \tag{7.23}$$

where $A_{u,v}$ is the horizontal viscosity coefficient for u, v and A_T and A_S are the horizontal diffusivity coefficients for T, S. In our application, we will explore optimal settings of A_X for $X = \{u, v, T, S\}$ according to values given in Table 7.4.

ROMS uses a computational kernel that combines temporal averaging of the barotropic mode with modified pressure-gradient terms to accurately resolve barotropic processes and reduce errors in the density field, while maintaining the efficiency of the split-explicit formulation. In this process, two time steps are used to advance 3D momentum and tracer variables in the numerical model to effectively capture the complex interactions between the barotropic and baroclinic modes in the ocean. The first time step (Δ_t) is used to compute the right side of the 3D momentum equations, while the second time step (Δ_{tt}) is used for updating the barotropic mode. Vertical interpolation is carried out using either fourth-order centered schemes or conservative parabolic splines. The combination of moderate-order spatial approximations, quasi-monotone advection operators, and enhanced conservation properties leads to more robust, accurate, and less diffusive solutions than those produced by earlier terrain-following ocean models (Haidvogel et al., 2008). More details on the numerical

methods used in ROMS can be found in the literature (Shchepetkin and Mcwilliams, 1998; Shchepetkin and McWilliams, 2003, 2005).

7.1.4. Boundary Conditions

The ocean near coastlines experiences dynamic interactions at various scales. Coastal currents are influenced by local wind forcing, tides, and remote factors transmitted offshore and along the coastal waveguide. Offshore currents may be generated as part of the large-scale circulation or emerge from near-shore regions. However, it is impractical to accurately resolve all types of currents. Instead, regional models can be used to calculate local currents under the influence of local forcing and the larger-scale circulation, given a suitable prescription for lateral boundary forcing (Marchesiello et al., 2001). We detail next how boundary conditions are chosen in order to implement an appropriate downscaled high-resolution model.

Bottom boundary layer (BBL)

The dynamics of the Bottom Boundary Layer (BBL) affect the stress on the flow exerted by the bottom, which is incorporated into the Reynolds-averaged Navier–Stokes equations as boundary conditions for momentum. ROMS can use either of two sub-models to represent BBL processes: (i) simple drag-coefficient expressions, or (ii) more complex formulations that consider the interactions of waves and currents over a moveable bed. In our application, we use the former.

$$K_M \frac{\partial u}{\partial z} = \tau_b^x(x,y,t); \quad K_M \frac{\partial v}{\partial z} = \tau_b^y(x,y,t); \quad K_H \frac{\partial T}{\partial z} = 0; \quad K_H \frac{\partial S}{\partial z} = 0 \tag{7.24}$$

The drag-coefficient methods implement formulae for linear bottom friction, quadratic bottom friction, or a logarithmic profile. For our application, we have considered the quadratic bottom friction:

$$\tau_b^x(x,y,t) = C_d^b \cdot u\sqrt{u^2+v^2}; \quad \tau_b^y(x,y,t) = C_d^b \cdot v\sqrt{u^2+v^2} \tag{7.25}$$

$$\tau_b^x(x,y,t) = C_d^b \cdot (u-u_b)\|\mathbf{u}-\mathbf{u}_b\|, \quad \tau_b^y(x,y,t) = C_d^s \cdot (v-v_b)\|\mathbf{u}-\mathbf{u}_b\|, \tag{7.26}$$

where u_b, v_b refers to the eastward and northward bottom speed components and $\mathbf{u} = (u,v)$. We consider that $u_b, v_b = 0$. The values we will explore of C_d^b are given in Tables 7.3 and 7.4.

We also examined the effect of the oceanic topography's bottom drag in two different scenarios: free-slip and no-slip. In the no-slip scenario, the normal and tangential components of the fluid velocity field are both equal to zero at the interface between a moving fluid and a stationary wall. In the free-slip scenario, the normal component of the fluid velocity field is equal to zero at the interface, but the tangential component is unrestricted. This condition is also known as the no-penetration condition.

Atmospheric forcing

The surface conditions, evaluated at $z = \zeta$ are

$$K_M \frac{\partial u}{\partial z} = \tau_s^x(x,y,t); \quad K_M \frac{\partial v}{\partial z} = \tau_s^y(x,y,t); \quad K_H \frac{\partial T}{\partial z} = 0; \quad K_H \frac{\partial S}{\partial z} = 0 \tag{7.27}$$

Where τ_s^x and τ_s^y are the components of the wind stress acting on the free surface in the x and y directions, respectively. We have assumed there is no exchange of heat and salinity with the atmosphere. Moreover, we have chosen a simple wind stress given by

$$\tau_s^x(x,y,t) = C_d^s \cdot (u - u_w)\|\mathbf{u} - \mathbf{u}_w\|, \quad \tau_s^y(x,y,t) = C_d^s \cdot (v - v_w)\|\mathbf{u} - \mathbf{u}_w\|, \tag{7.28}$$

where u_w, v_w refers to the eastward and northward wind speed components and $\mathbf{u} = (u,v)$. The C_d^s values we have explored are given in Tables 7.3 and 7.4.

The winds were computed using the NCAR Weather Research Forecasting (WRF) model version 4.0. which is a fully compressible, Eulerian non-hydrostatic equations model (with a run-time hydrostatic option) that uses Arakawa-C grid staggering for horizontal discretization and the time-split 3rd ordered Runge Kutta integration scheme. It includes various parameterizations and schemes for microphysical processes, cumulus parameterization, land-surface modeling, boundary layer parameterization, long-wave and short-wave radiation interactions in the atmosphere. For this study, the parameterizations and schemes used were as follows: surface layer based on the Monin-Obukhov Similarity scheme, incorporating a Carlson-Boland viscous sub-layer and standard similarity functions (Beljaars, 1995); land-surface parametrization from the Thermal Diffusion scheme, using a soil temperature-only scheme with five layers; boundary-layer YSU scheme (Hong et al., 2006); and the Noah land-surface model. The model domain encompasses the geographical region of the Greek territory, ranging from 23.64 °N to 24.36 °N in latitude and from 33.7 °E to 34.35 °E in longitude. The horizontal grid spacing is set at 800 meters, and there are 34 vertical levels within the model.

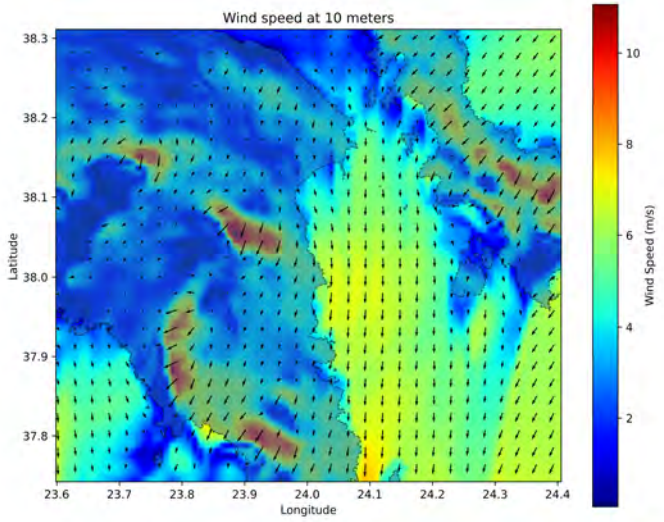


Figure 7.3 The figure depicts the WRF domain, with the wind speed intensity at 10 meters above the ground visualized in the background. The visualization corresponds to the specific date and time of November 2, 2019, at 12:00:00. Arrows are employed to indicate the direction of the wind.

The model assimilates the ERA5 data, obtained from both single and pressure levels, as a data source (Hersbach et al., 2020). Figure 7.3 displays the plotted wind speed at a height of 10 meters.

Open boundary conditions

In this study, we have set up a model that aspires to provide realistic and informative high-resolution fields in the sense of operational oceanography. This requires careful nesting on the boundaries and in our setting, we have considered that the CMEMS product in the Mediterranean Sea offers good estimations for the required external fields on the described boundaries below. The Mediterranean Forecasting System's physical component (Med-Physics) consists of a combined hydrodynamic-wave model that covers the entire Mediterranean Basin, including tides. The model has a horizontal grid resolution of about 4 km (1/24°) and features 141 unevenly spaced vertical levels. The hydrodynamics are derived from the Nucleus for European Modelling of the Ocean (NEMO v3.6) and incorporate tidal representation, while the wave component comes from Wave Watch-III. Model solutions are adjusted using a 3DVAR assimilation scheme (OceanVar) that incorporates temperature and

salinity vertical profiles, as well as satellite Sea Level Anomaly observations along the track (Clementi et al., 2019).

We define next conditions at the lateral boundaries. First, we take into consideration tides that constrain sea surface height and barotropic velocities at the boundaries. ROMS adjusts tides through the Chapman and Flather boundary conditions, which we detail next.

Chapman boundary condition. This condition for surface elevation was investigated by Chapman (Chapman, 1985). It assumes that ζ, the sea surface elevation at an open boundary, satisfies the wave equation:

$$\frac{\partial \zeta}{\partial t} = \pm\sqrt{gh}\frac{\partial \zeta}{\partial x} \tag{7.29}$$

where $\sqrt{gh}$ is shallow-water wave speed.

Flather boundary condition. For the normal component of the barotropic velocity, $\overline{u}_n$, it is used the radiation condition proposed by (Flather, 1976):

$$\overline{u}_n = \overline{u}_n^{\text{ext}} - \sqrt{\frac{g}{h}}\left(\zeta - \zeta^{\text{ext}}\right) \tag{7.30}$$

where $\overline{u}_{\text{ext}}$ represents the external barotropic velocity and h is the local water depth. In this equation, the differences between the external data and the model predictions are permitted to propagate beyond the domain at the speed of the external gravity waves.

The exterior values are used to provide tidal boundary conditions to the barotropic mode. In limited area coastal domains -as it is our case- the tides can be treated as being entirely remotely forced, i.e., the influence of the gravitational tide generating forces within the domain is negligible. The principal challenge to modeling tides accurately is the proper representation of tidal elevation and velocity boundary conditions around the entire model perimeter (He and Wilkin, 2006), but as explained those values are taken from CMEMS products.

For the rest of the fields, that is baroclinic velocities, salinity, and temperature, which we refer to generically as ϕ, ROMS has various types of boundary conditions including open, closed, and periodic. See (Marchesiello et al., 2001) for a more thorough exploration of the options. We examined the effects of several of those conditions: mixed radiation-nudging open boundary conditions, clamped boundary conditions, and the use of a sponge layer.

Clamped boundary condition. This is a Dirichlet type of boundary condition. It consists in setting the boundary value to a known exterior value:

$$\phi = \phi_{\text{ext}} \tag{7.31}$$

Here ϕ_{ext} represents the exterior value of the field ϕ, provided in our case by the CMEMS Med-Physics data.

Mixed radiation-nudging boundary condition. Open boundary conditions in coastal ocean modeling can be challenging to implement due to the possibility of incoming and outgoing flow at the same boundary or at different depths at the same horizontal location. A mixed boundary condition combining radiation and nudging, first introduced in (Marchesiello et al., 2001), has been proposed as a solution. This boundary condition uses the radiation condition to determine whether the boundary is passive (outward propagation) or active (inward propagation). In the passive case, the solution is allowed to pass through the boundary using radiation extrapolation to prevent excessive reflection. In the active case, the solution is nudged towards external data sources, such as observed climatologies or large-domain model outputs, to provide the necessary information for the dynamical equations without over-specifying the solution. One-way nesting can also be used when the external data is taken from time-evolving large-domain model solutions.

The radiation condition for a prognostic model variable ϕ is:

$$\frac{\partial \phi}{\partial t} = -\left(c_x \frac{\partial \phi}{\partial t} + c_y \frac{\partial \phi}{\partial t}\right) \tag{7.32}$$

where (x,y) are respectively, the normal and tangential directions to the boundary in local Cartesian coordinates. The phase speeds (c_x, c_y) are projections of the oblique radiation, calculated from the ϕ field surrounding the boundary point as follows:

$$c_x = -\frac{\partial \phi}{\partial t} \frac{\partial \phi / \partial x}{\left(\frac{\partial \phi}{\partial x}\right)^2 + \left(\frac{\partial \phi}{\partial y}\right)^2} \tag{7.33}$$

and

$$c_y = -\frac{\partial \phi}{\partial t} \frac{\partial \phi / \partial y}{\left(\frac{\partial \phi}{\partial x}\right)^2 + \left(\frac{\partial \phi}{\partial y}\right)^2}. \tag{7.34}$$

In the active boundary, we apply the nudge equation. The nudging layer is a region where model data is relaxed towards external data. For this region, a nudging term is added to the equations of tracers and surface elevation. Its mathematical form is added to the right-hand side of the prognostic equations as follows:

$$\frac{\partial \phi}{\partial t} = \text{r.h.s} - \frac{1}{\tau_{\text{nud}}}(\phi - \phi^{\text{ext}}). \tag{7.35}$$

Parameter	Value	Description
Lm	344	number of points in longitude direction
Mm	228	number of points in latitude direction
N	10	number of vertical (sigma) levels
$h_{\max}$	146	maximum depth of the domain (metres)
$h_{\min}$	0.29	minimum depth of the domain (metres)
θ_s	5.0	sigma coordinate surface stretching factor
θ_b	0.4	sigma coordinate bottom stretching factor
Δ_t	10	baroclinic time-step (seconds)
Δ_{tt}	7	barotropic time-step (seconds)

Table 7.2 Numerical values for the parameters associated with the setup of the ocean model.

In our work, when mixed radiation-nudging boundary condition is used, $\tau_{\text{nud}} = 10$ days. The selected value was determined based on a typical advective timescale: Given our grid size of 80 m and maximum velocities of 0.01 m/s, we derive a timescale of 80/0.01 = 8000 seconds, which equates to approximately 10 days for the inflow.

Sponge layer. It is typically used to dump noisy effects at the boundaries due to discrepancies between the evolving model solution in the domain and the external data in which it is nested. This is implemented by increasing there the coefficients that enhance the horizontal mixing. Both a factor that multiplies the horizontal mixing and its width are indicated (see Table 7.4).

7.2. Remote sensing

The waters surrounding the Rafina Port and its vicinity are oligotrophic-like (clear and transparent), which limited the number of available turbidity images that could contribute to the qualification of the Rafina Port hydrodynamic model. To qualify the hydrodynamic model, data from the Sentinel 2A and 2B Multi-Spectral Instrument (MSI) were examined for the period ranging from November 1st, 2019 to January 31st, 2020.

Sentinel 2A and 2B had a revisiting cycle of 5 days. Level 1C Top of Atmosphere reflectance products from Sentinel 2 were downloaded from the Sentinel Data Hub. The standard SEN2COR library of atmospheric correction algorithms, provided by Scihub Copernicus, for the Sentinel 2 MSI sensor was initially designed for land applications. However, for the purpose of reporting ocean color-derived products and qualifying the hydrodynamic model outputs, Level 2 data required an atmospheric correction algorithm specifically designed to handle the radiometric constraints of water pixels data. As a result, the ACOLITE toolbox (Vanhellemont and Ruddick, 2018) was selected. ACOLITE enabled easy and

efficient processing to correct Sentinel-2 Level 1C data and generate value-added derived products for both coastal and inland waters through the use of a dark spectrum algorithm for atmospheric correction (Vanhellemont, 2019).

The ACOLITE atmospheric correction generates Level 2 images that include biogeochemical-derived products such as turbidity (Nechad et al., 2009) and suspended matter (Nechad et al., 2010), among others. Additionally, the ACOLITE toolbox includes sunglint correction developed by Harmel et al. (2018). These images are useful for model qualification as ACOLITE produces both well-corrected and water discoloration products, including phytoplankton blooms, turbidity, and suspended matter. The spread of these compounds, as evidenced by water discoloration, makes visible the convoluted shapes of the dynamical objects that we will explain in detail in the next section. As a result, the patterns shown in remote sensing images can be correlated with patterns obtained from the hydrodynamic model. Conversely, in the absence of these compounds, the use of very high-resolution images for this purpose is limited. Figure 7.4 shows patterns visible on the sea surface in the Rafina Port area on November 22, 2019, as captured by Sentinel 2 satellite images. Figure 7.4a) depicts a quasi-true color image in RGB (using band 4, band 3, and band 2 of the MSI sensor), while Figure 7.4b) shows a pseudocolor turbidity image in Formazin Nephelometric Units (FNU).

Ocean and Land Colour Instrument (OLCI) Level 1B data, covering the study area, were acquired from Sentinel 3A and 3B via the Sentinel Data Hub. These data underwent processing using SeaDAS version 8.2 to produce the required outputs. Ancillary files needed for atmospheric correction were obtained using the "getanc.py" routine. The l2gen SeaDAS binary was utilized to derive geophysical variables, resulting in Level 2 files. These files include remote sensing reflectances and [Chlorophyll-a], among other ocean color products. To produce projected images onto a geographical Lat/Lon WGS84 GeoTIFF, Sentinel 3 Level 2 files were mosaicked by satellite and day using the Graphic Processing Tool (gpt.sh) Mosaic operator. Figure 7.5 displays the sea surface patterns captured by Sentinel 3 A and B in the same area. Despite the lower resolution, higher frequency passes enabled the identification of a longer series during the study period. This series also includes an image taken on November 22nd, where Sentinel 2 provided a higher resolution.

7.3. Transport and dynamical systems

Images displayed in section 7.2 show patterns that correspond to Particulate or Dissolved, Organic or Inorganic Matter (POM, DOM, PIM, DIM), Chlorophyll, Turbidity, etc., with different origins (primary production blooms, sediments, wastewater plumes). These light passive particles, suspended in the ocean, are described by a concentration field, C, whose

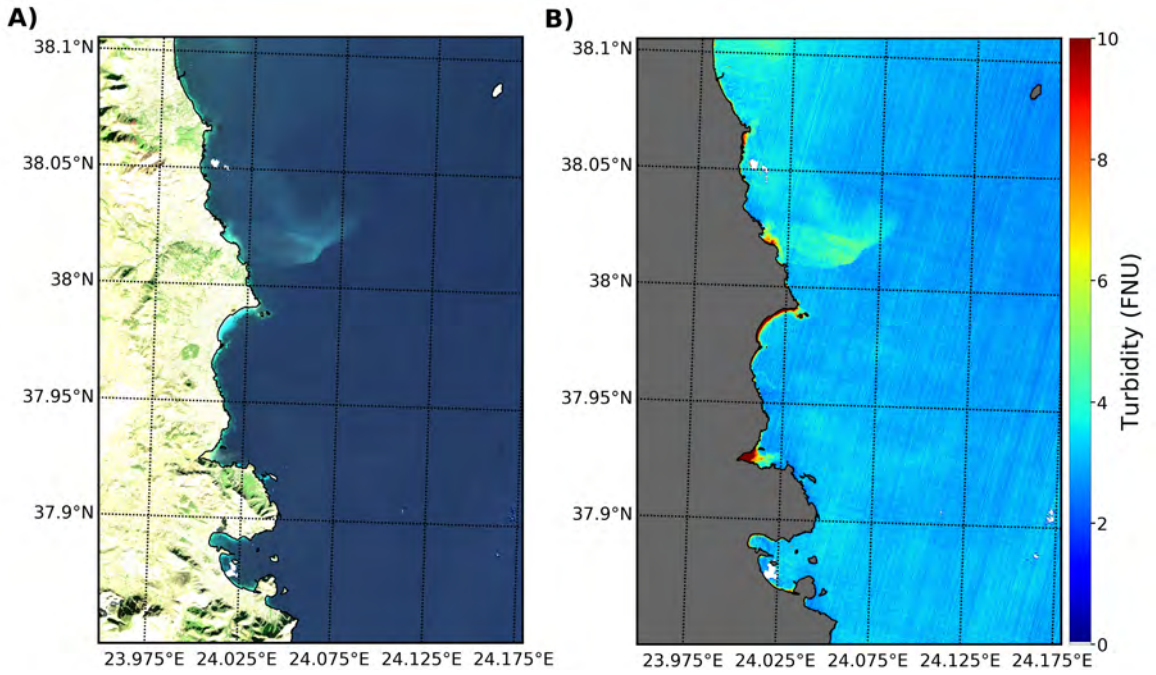


Figure 7.4 Sentinel 2 images on the 22nd of November 2019 in the Rafina Port area showing convoluted shapes. (a) Quasi-true RGB color image;(b) turbidity image obtained from ACOLITE algorithms.

general evolution is given by equation (7.5). Assuming that at the surface motion is mainly horizontal, equation (7.5) can be reduced to the following advection-diffusion equation:

$$\frac{\partial C}{\partial t} + \mathbf{v}_h \cdot \nabla C = \mu \nabla^2 C, \tag{7.36}$$

where μ is the horizontal molecular diffusion and $\mathbf{v}_h$ is the vector with the horizontal velocity components of the ocean model. Assuming that at our scales advection is the dominant factor in transport (see (García-Garrido et al., 2015; García-Sánchez et al., 2022, 2021; Lekien and Marsden, 2005; Olascoaga and Haller, 2012)) then $\mu \sim 0$ and equation (7.36) reduces to:

$$\frac{\partial C}{\partial t} + \mathbf{v}_h \cdot \nabla C = \frac{dC}{dt} = 0. \tag{7.37}$$

This equation assumes that C is conserved along the fluid parcel trajectories. Fluid parcels on the ocean surface follow trajectories in longitude/latitude coordinates $\vec{x}(t) = (\lambda(t), \phi(t))$

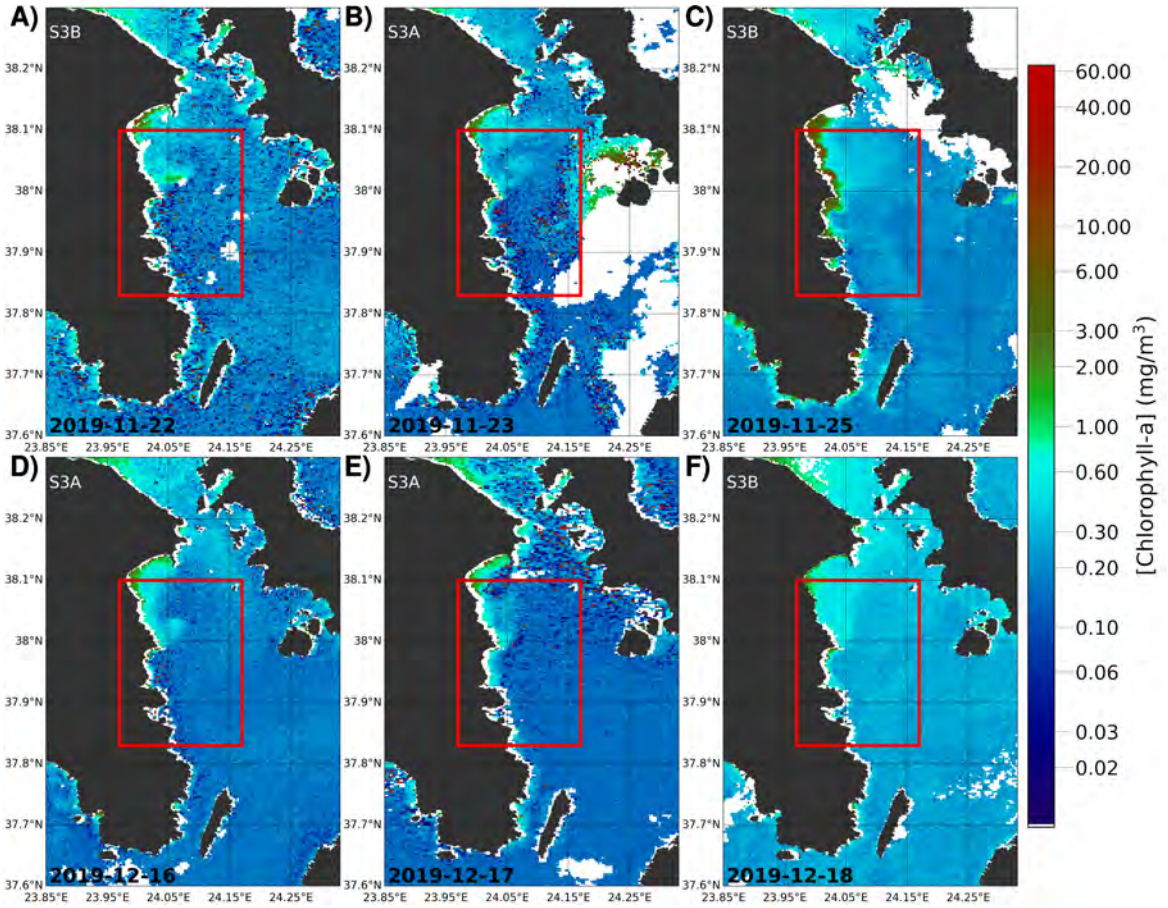


Figure 7.5 Sentinel 3A and B images in the Rafina Port area showing convoluted shapes of chlorophyll. (a) on the 22th of November 2019, (b) on the 23th of November 2019, (c) on the 25th of November, (d) on the 16th of December, (e) on the 17th of December, and (f) on the 18th of December. Red rectangles mark the region where very high-resolution simulations have been performed.

that evolve according to the dynamical system:

$$\begin{aligned} \frac{d\lambda}{dt} &= \frac{u(\lambda,\phi,t)}{R\cos\phi}, \\ \frac{d\phi}{dt} &= \frac{v(\lambda,\phi,t)}{R}. \end{aligned} \tag{7.38}$$

where R is the Earth's radius and u and v are the eastwards and northwards velocity components provided by the hydrodynamical model at the surface layer.

In order to characterize the performance of u and v to consistently describe patterns observed in satellite images in Figures 7.4 and 7.5, we are going to extract geometrical structures from Equation (7.38) using specific velocity fields obtained under different settings of the hydrodynamical model. The geometrical structures that we will use, the Lagrangian Coherent Structures (LCS), provide a signature for a specific velocity field that highlights the essential transport features associated with it. LCS form time-dependent material surfaces that separate fluid paths that behave differently. An important mathematical result is that these Lagrangian patterns are robust against velocity field perturbations, whereas the comparison of two individual trajectories is not. This allows a better characterization of the velocity fields produced by the model, by allowing to establish as different outputs those that have a different Lagrangian signature, while those that present a similar Lagrangian pattern, can be characterized as similar. This approach has found successful application in the context of pollution (García-Sánchez et al., 2022).

We compute the LCS with the method known as Lagrangian Descriptors (LDs). The particular LD that we use is a function referred to as M (Jiménez-Madrid and Mancho, 2009; Mancho et al., 2003, 2013) which is defined as follows:

$$M(\vec{x}_0,t_0,\tau) = \int_{t_0-\tau}^{t_0+\tau} \|\mathbf{v}_h(\vec{x}(t),t)\| = \int_{t_0}^{t_0+\tau} \|\mathbf{v}_h(\vec{x}(t),t)\| + \int_{t_0-\tau}^{t_0} \|\mathbf{v}_h(\vec{x}(t),t)\|. \tag{7.39}$$

where $\|\cdot\|$ stands for the modulus of the velocity vector. In this expression, the computation of the function M is split into its forward time (M^f) and backward time (M^b) contributions. At a given time t_0, the function $M(\vec{x}_0,t_0,\tau)$ measures the arc length traced by the trajectory starting at $\vec{x}_0 = \vec{x}(t_0)$ as it evolves forward and backward in time for a time interval τ. For a sufficiently large τ, the function M exhibits a distinct structure that reveals singular features emphasizing the Lagrangian Coherent Structures (LCS). Figure 7.6 displays the calculation of M^b in the vicinity of Rafina port for $\tau = 3$ days on selected dates consistent with those of Figure 7.5. To compute Figure 7.6, we perform trajectory calculations in accordance with Equation (7.39) by integrating them using a 5^{th} order Runge-Kutta method. The arc length is

Parameter	Value
Horizontal Viscosity $A_{u,v}$	2
Horizontal Diffusivity $A_{T,S}$	2
Bottom Drag factor C_d^b	0.003
Sponge factor	1
Wind drag factor C_d^s	$6.0 \cdot 10^{-5}$
Bathymetry	NAVIONICS
Boundary conditions	Clamped

Table 7.3 This table presents the numerical values associated with each parameter utilized in the base solution

then determined by summing the lengths of linear segments connecting consecutive steps in the Runge-Kutta method.

In Equation (7.39) the backward integration (M^b) highlights the structure of attracting LCS and we expect that suspended material will eventually, after a transient time, be aligned with these features. Patterns visible from satellite imagery correspond to suspended material that could decay towards these features (García-Sánchez et al., 2022; García-Sánchez et al., 2022, 2021). Additionally dynamical barriers on the sea surface could also be made visible by the suspended matter, as barriers would keep the suspended material on both sides unmixed as far as the original distribution of the suspended material was only on one side of the barrier.

7.4. Numerical experiment setups and performance quantification

The hydrodynamical model can be set up with different parameters and boundary conditions, which can lead to different outputs, particularly in the currents. Typically, these free parameters are adjusted by benchmarking ocean model outputs against in situ Eulerian metrics obtained from Acoustic Doppler Current Profiler (ADCP), mooring data, and other sources. In this work, we aim to evaluate the performance of these models from a Lagrangian perspective by using satellite imagery, as described in the previous section.

We begin by establishing a configuration for a Base Solution (BS) with parameters provided in Table 7.3, which complement those shown in Table 7.2 and are kept constant. We execute this configuration during the timeframe for which reference images are accessible. These consist of two consecutive periods in 2019 (refer to Figures 7.4 and 7.5), with a total of six images. The first period ranges from 2019-11-22 to 2019-11-25, while the second period

spans from 2019-12-15 to 2019-12-18. To ensure that these outputs are not dependent on the initial conditions used, the system is initialized prior to the period of interest and run for a sufficient period of time to converge to the global attractor. Given that our system is subject to time-dependent boundary conditions (such as winds and open lateral boundary conditions), the type of attractor involved is called a pullback attractor (Medjo, 2018). When LCS are computed using velocity fields from different initial conditions, there are no discrepancies observed once the solutions have converged to the pullback attractor.

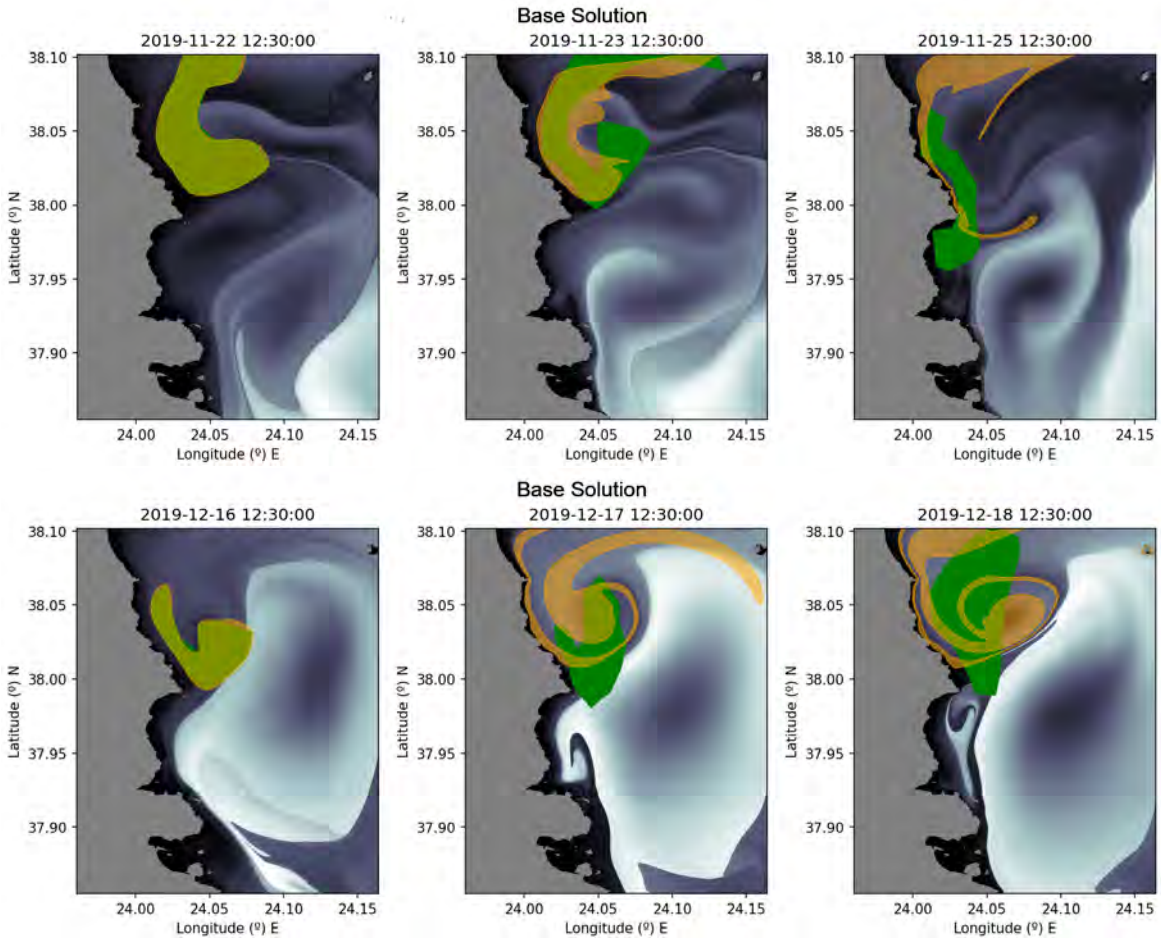


Figure 7.6 Evaluation of M^b on the BS model for $\tau = 3$ days. Patterns are displayed in a gray tone. Panels a), b), and c) show the results on the time series correlated to the satellite imagery displayed in panels a), b), and c) of Figure 7.5. Panels d), e), and f) show the results on the time series correlated to the satellite imagery displayed in panels d), e), and f) of the same figure. The green blobs show the contours of an estimation of the evolution of chlorophyll from the satellite images. The brown blobs show the evolution according to the model of the green blob at the initial date of each time series.

Defining a metric that provides a quantification to compare the sequence of satellite observations with the performance of the hydrodynamic model outputs is not an easy task. The reason for this difficulty is that it involves comparing complicated and subtle dynamical objects. To accomplish this, we have proposed a methodology that makes assumptions about both the observations and the models. Regarding observations, we have extracted polygons from the satellite imagery that represent zones where the chlorophyll is homogeneously distributed. Figure 7.6 shows a sequence of green polygons for the two periods. Assuming that these structures are formed by suspended particles and are purely advected by the currents, they provide a ground truth or benchmark to be recovered by the model. This figure also shows, in brown, the evolution of the chlorophyll blobs that were initialized on the first day of the sequence by using the velocity fields from the base solution set. In the background, for interpretation purposes, we have represented the evaluation of M^b for $\tau = 3$ days, which highlights, through singular features, the attracting material curves of the flow. There is a nice consistency between these features and the evolution of the brown blob. Ideally, if the model is good we would expect a lot of overlap between the green and brown blobs. Certainly, for the suspended particulate matter there may be sinks and/or sources and this is reflected in the fact that the sequence of green blobs does not preserve the area. Additionally, diffusion adds to spreading on the ocean surface. These phenomena are not described by pure advection, but still, the overlap is an intuitive measure to consider. For each sequence, in the days after the first one, we establish as a measure the area fraction of the green blob that is covered with the brown blob. This will be a number $\mathscr{A}$ satisfying $0 \leq \mathscr{A} \leq 1$ that we interpret as follows, close to 1 means good performance while close to 0 implies poor performance. We will comment further on these images in the results section.

We complete this section by describing a series of free parameter configurations in the hydrodynamic model. These are defined from variations of the parameters taken for the base solution and define a series of experiments. Our study aims to qualify the results of all these experiments, using the newly defined metric. The experiments are divided into six categories:

- C1: Varying horizontal mixing coefficients (viscosity and diffusivity) in two experiments compared to the Base Solution (BS).
- C2: Investigating two different bottom drag coefficients in comparison to the BS.
- C3: Assessing two distinct surface forcing wind stress fields relative to the BS.
- C4: Conducting a single experiment with bathymetry replaced by GEBCO data.
- C5: Implementing a sponge layer with six times the base horizontal viscosity and diffusivity in one experiment.

- C6: Executing two experiments where the Open Boundary Condition (OBC) was replaced by the mixed radiation-nudging boundary condition, modifying the factor between passive (outflow) and active (inflow).

Details of the parameters taken for each experiment can be found in Table 7.4.

Summary of experiments

Category	**Experiment**	**Parameters**
C1: Horizontal Mixing Coefficient	Exp 1	$A_{u,v} = A_{T,S} = 0.2m^2/s$
	Exp 2	$A_{u,v} = A_{T,S} = 5m^2/s$
C2: Bottom Drag Coefficient	Exp 1	$C_d^b = 0.03$ (non-dimensional)
	Exp 2	$C_d^b = 3 \cdot 10^{-5}$ (non-dimensional)
C3: Wind stress	Exp 1	$C_d^s = 6 \cdot 10^{-4}$
	Exp 2	$C_d^s = 6 \cdot 10^{-7}$
C4: Modified Bathymetry	Exp 1	GEBCO data (Fig. 7.1 b))
C5: Sponge at Boundary	Exp 1	$6 \cdot A_{u,v,T,S}$
C6: Mixed Radiation-Nudging BC	Exp 1	No sponge, $\tau_{\text{nud}} = 10$ days,
	Exp 2	Sponge, $\tau_{\text{nud}} = 10$ days

Table 7.4 Setting the varying parameters for defining categories and experiments to conduct sensitivity tests.

7.5. Results

First, we comment on the results displayed in Figure 7.6. The upper row shows a sequence of satellite imagery captured between November 22nd and 25th, 2019, where chlorophyll is visible. On November 23rd, the tracer appears to swirl, while on November 25th, the chlorophyll in the upper half of the domain has diffused, weakening all features except for a large concentration aligned with the coast. A material barrier transverse to the coast at around 38 degrees North appears to persist in all these upper panels. The dynamical structure of the currents of the BS model is obtained from M^b, whose pattern is displayed in the gray tones in the background. The attracting material curves are visible through the singular features and consistently show the transverse barrier to the coast present in the observations. The evolution of the blob according to the BS model is depicted in brown, which also exhibits swirling (panel b) and contraction towards the coast (panel c). The bottom row displays satellite imagery where chlorophyll is visible between December 16th and 18th, 2019. On December 16th, the chlorophyll tracer has a swirling shape. The boundary of this shape progressively weakens on December 17th and 18th. A pronounced transverse barrier to the coast in a northeasterly direction evolves progressively, bringing its alignment closer

to the north. The M^b pattern is shown in the gray tones in the background of the image. It confirms the presence of a barrier in a northeasterly direction, although with a slightly different inclination than that of the satellite images. According to the BS model, the brown blobs swirl counterclockwise as they evolve. The first row of Table 7.5 provides values of the computed $\mathscr{A}$ for the first chlorophyll series on November 23rd and 25th, 2019, and for the second chlorophyll series on December 17th and 18th, 2019, quantifying the performance of the BS model. In addition to this data, Table 7.6 shows the averages of these quantities for the first and second periods as well as for the total period.

Tables 7.5 and 7.6 also provide quantification of the performance of all experiments. Results for $\mathscr{A}$ fluctuate between 0 and 0.75 for individual experiments, and between 0.2 and 0.65 for averaged values. Averaged values of $\mathscr{A} \sim 0.2$ or individual values of $\mathscr{A} \sim 0.1$ indicate poor performance. During the first period, extremely low performances on individual days are obtained for instance on 25, November 2019 for the category 4 model that uses the GEBCO bathymetry (C4, exp1) and for the sponge layer experiment (C5,exp1) that introduces high diffusivity and viscosity on the boundaries of the domain. Explicit representations for selected poor-performing cases are provided in Figure 7.7, where the top two rows are represented the cases (C4,exp1) and (C5,exp1). The highest-performing model for the first period corresponds to the (C6, exp2) experiment that implements a mixed sponge and radiation-nudging condition. The last row in Figure 7.7 provides a visualization of the performance of this model. Remarkably, its dynamical structure allows the blob to be maintained elongated along the coast, although the model also shows incursions towards the interior of the sea.

Regarding the second period, the top two rows of Figure 7.8 represent simulations performed with the (C1, exp1) model, which decreased the horizontal viscosity and diffusivity coefficients, and the (C6, exp1) model, which considers only a radiation-nudging condition. Both simulations perform poorly. The (C1, exp1) model presents invariant dynamical structures that are very rich and involve very small scales. Some of these structures remain within the observed green blob. The (C6, exp1) model performs poorly. The absence of a sponge effect at the boundary in the (C6, exp1) model influences the solution compared to what is obtained by considering it in the (C6, exp2) model. The latter is illustrated in the bottom row, the (C6, exp2) model. According to the values given in Table 7.5, the performance is rather good on the 17th but decays on December 18th, 2019.

The effects of different models performing differently on different days and periods can be clearly observed in Table 7.5 and Table 7.6. For example, model (C6, exp2) obtained with the mixed sponge radiation-nudging condition performs rather consistently in the first period, but worse in the second period. The same occurs for the experiment that considers only the

radiation-nudging condition (C6, exp1). On the contrary, the model (C1, exp2) obtained by increasing horizontal viscosity and diffusivity performs more consistently in the second period, than in the first period. Similarly occurs for the model (C2, exp1) which increases the bottom drag coefficient. All in all, the total average column in Table 7.6 confirms that (C6, exp2), with the mixed radiation-nudge condition, has the best performance and the initial BS choice has moderate performance.

Experiments	**2019-11-23**	**2019-11-25**	**2019-12-17**	**2019-12-18**
B.S	0.49919	0.085	0.3669	0.2720
C1. Horizontal mixing exp 1	0.3953	0.1185	0.2065	0.2802
C1. Horizontal mixing exp 2	0.4654	0.3188	0.4875	0.3815
C2. Bottom drag exp 1	0.4224	0.1096	0.3618	0.4835
C2. Bottom drag exp 2	0.4375	0.3165	0.2282	0.3676
C3. Wind stress exp 1	0.4462	0.4343	0.3164	0.3224
C3. Wind stress exp 2	0.4883	0.087	0.3793	0.2848
C4. Modified bathymetry exp 1	0.4491	0.005	0.1305	0.2363
C5. Sponge exp 1	0.3778	0.0278	0.29965	0.2528
C6. Mixed radiation-nudging exp 1	0.5315	0.3682	0.2337	0.1660
C6. Mixed radiation-nudging exp 2	0.5555	0.7476	0.5192	0.2551

Table 7.5 Results of measured index $\mathscr{A}$ obtained for the sensitivity experiments. they include the first period (2019-11-23 and 2019-11-25), and the second period (2019-12-17 and 2019-12-18).

Experiments	**Avg First Period**	**Avg Second Period**	**Total Avg**
B.S.	0.2922	0.3195	0.3058
C1. Horizontal mixing exp 1	0.2569	0.2433	0.2501
C1. Horizontal mixing exp 2	0.3921	0.4345	0.4133
C2. Bottom drag exp 1	0.2660	0.4226	0.3443
C2. Bottom drag exp 2	0.3770	0.2980	0.3375
C3. Wind stress exp 1	0.4402	0.3194	0.3798
C3. Wind stress exp 2	0.2876	0.3321	0.3099
C4. Modified bathymetry exp 1	0.2273	0.1834	0.2054
C5. Sponge exp 1	0.2028	0.2762	0.2395
C6. Mixed radiation-nudging exp 1	0.4498	0.1998	0.3249
C6. Mixed radiation-nudging exp 2	0.6515	0.3871	0.5194

Table 7.6 Averages of measured index $\mathscr{A}$ for the first and second periods.

7.6. Conclusions

In this paper, we explore a methodology based on the use of dynamical systems ideas to assess the quality of results from different configurations of a high-resolution coastal ocean model. Our aim is to leverage satellite imagery, which provides observations at a lower cost than in situ observations, and to propose a strategy for quantifying the quality of model results using an $\mathscr{A}$ index. The models are defined by specifying parameters or boundary conditions of the system with various options that are not known beforehand.

We have found that many model configurations produce reasonable results and that the choice of boundary conditions for nesting has a significant impact. Among these, radiation-nudging lateral boundary conditions appear to be particularly suitable. The coupling with the wind at the surface, the adherence at the bottom, and parameters related to the horizontal mixing can all cause distortions in the solutions, leading to deviations from observations.

We expect that this methodology will be useful for adjusting high-resolution coastal models in regions where in situ observations are scarce, and it also opens up new avenues for the application and exploitation of satellite imagery.

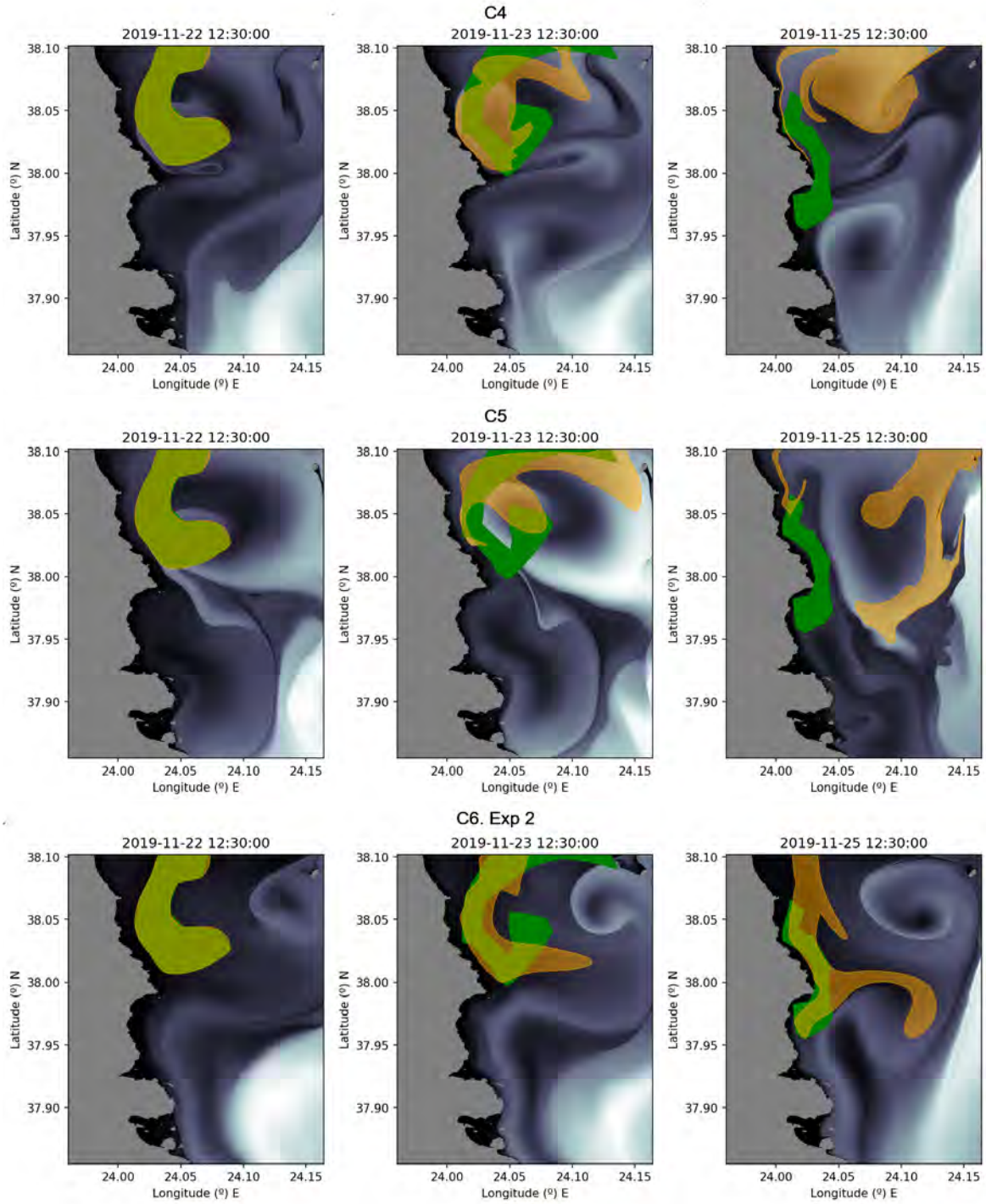


Figure 7.7 Evaluation of M^b on several models for $\tau = 3$ days. Patterns are displayed in a gray tone. The first, second, and third columns show the results on the time series correlated to the satellite imagery displayed in panels a), b), and c) of Figure 7.5. The first row shows the results for Category 2, experiment 2, on the bottom drag condition. The second row shows the results for Category 5, experiment 1, on the sponge conditions. The third row shows the results for Category 6, experiment 2, on the mixed radiation-nudging conditions. The green blobs show the contours of an estimation of the evolution of chlorophyll from satellite images. The brown blobs show the evolution according to each model of the green blob at the initial date of each time series.

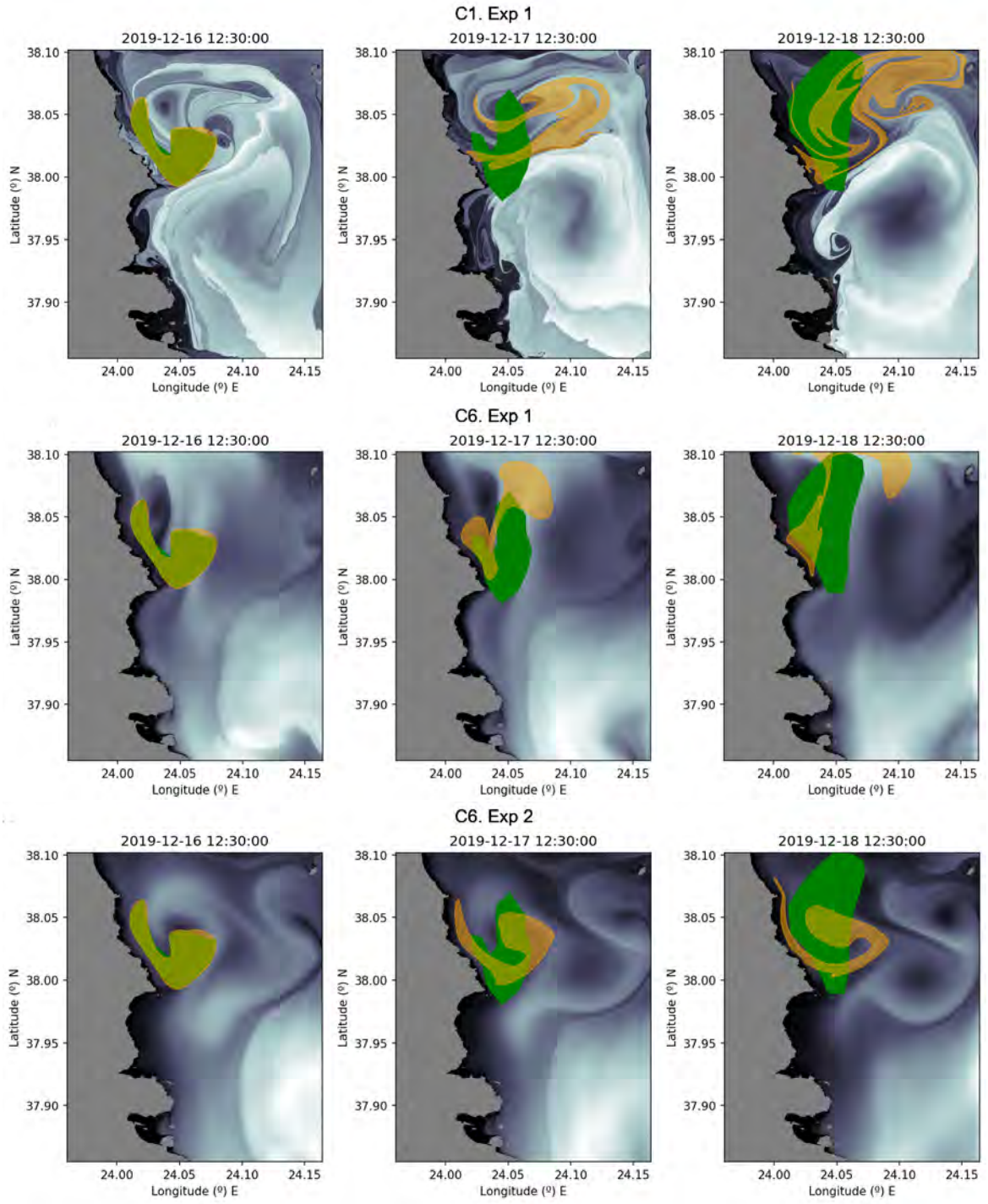


Figure 7.8 Evaluation of M^b on several models for $\tau = 3$ days. Patterns are displayed in a gray tone. The first, second, and third columns show the results on the time series correlated to the satellite imagery displayed in panels d), e), and f) of Figure 7.5. The first row shows the results for Category 1, experiment 1, on the horizontal diffusion and viscosity coefficients. The second row shows the results for Category 3, experiment 1, on the wind stress conditions. The third row shows the results for Category 6, experiment 2, on the mixed radiation-nudging conditions. The green blobs show the contours of an estimation of the evolution of chlorophyll from satellite images. The brown blobs show the evolution according to each model of the green blob at the initial date of each time series.

Chapter 8

Conclusions and Outlook

The results of the research conducted in this PhD thesis have been discussed in the conclusion sections of Chapters 3, 4, 5, 6, 7. To facilitate the readers, this final chapter provides a compilation of these conclusions. Additionally, a brief discussion on potential avenues for future research is presented.

8.1. Research conclusions

In conclusion, the chapters presented in this thesis highlight the advancements and insights gained through the application of emerging tools, which involve high-resolution models, remote sensing techniques, and dynamical systems approaches in coastal and oceanic contexts. These findings have important implications for the management of pollution, the quantification of uncertainties, the assessment of models, and environmental protection.

Chapter 3 demonstrates the effectiveness of using high-resolution hydrodynamic models, remote sensing satellite images and dynamical systems tools to manage a specific pollution event. The use of such tools provides accurate responses and reduces uncertainties in the prediction of oil spills, thus supporting real-time decision-making by emergency services. In particular, the use of LCS on different data sets provided by various services, emphasize their role in understanding the transport in the analysed data and capturing essential features that control dispersion. A consistent geometric pattern has been identified, particularly a hyperbolic trajectory in a detachment configuration and its unstable and stable manifolds. Although both elements are present in the data, the high-resolution models provide superior quantitative results.

The introduction of a new definition for UQ in Chapter 4 expands the traditional understanding of UQ in oceanic contexts. This definition enables quantitative comparisons of transport properties associated with different ocean data sources. The rich structure revealed

by this definition, incorporating dynamical systems theory, relates uncertainty with the stable invariant manifolds of hyperbolic trajectories and goes beyond statistical moments usually used on the field of UQ. This brings new perspectives to our understanding of uncertainty in oceanic processes.

The application of dynamical systems ideas in Chapter 5 provides essential insights into an oil spill dispersion at a large scale in the Eastern Mediterranean. This spill is different from the one discussed in Chapter 3 not only because of the scale involved, but also because the source of the spill is unknown. The observed alignment of oil spills with the attracting material curves (which are related to the unstable LCS) confirms the assumptions made and underscores the potential of the combined technologies based on Copernicus services and dynamical systems in predicting and managing oil spills, thus enhancing environmental protection.

Chapter 6 introduces a novel definition, Backward Lagrangian Uncertainty Quantification (BLUQ), which quantifies the consistency of transport models in describing the source of observations with unknown origins. This definition exhibits a structural link to unstable invariant manifolds of hyperbolic trajectories, and its application to an oil spill accident in the Eastern Mediterranean highlights the performance of different CMEMS products in representing mesoscale and submesoscale structures.

In Chapter 7, a methodology based on ideas of dynamical systems is proposed to assess, using remote observations, the quality of the results of a high-resolution coastal ocean models. The findings emphasize the significant impact of boundary conditions on model performance and identify radiation-nudging lateral boundary conditions as particularly suitable. This methodology enables model adjustment and enhances, to this end, the utilization of satellite imagery in regions with limited in situ observations.

In conclusion, this research has demonstrated the potential of combining advanced simulation techniques, satellite-based observations, and dynamical system theories to improve our approach to marine and coastal issues. This convergence of methodologies provides a new perspective to understand oceanic processes, as well as the tools to proactively address environmental threats, improve the accuracy of our models, and promote a more sustainable relationship with our oceans and coastlines.

8.2. Outlook

The results obtained in this thesis, except for those in Chapter 7, are mainly focused on transport processes at the ocean surface. In this context, several opportunities emerge to expand these results and to explore further applications of the implemented methodologies.

3D Oceanic Transport

Comprehending the complexities of oceanic phenomena requires a transition to a three-dimensional perspective. This is of particular relevance to improve our understanding of significant environmental issues such as the spread and deposition of microplastics in marine ecosystems, which has been widely discussed in (Cai et al., 2023; Sutherland et al., 2023). In order to implement dynamical system concepts in this context, it is essential to incorporate the key concepts outlined in (Branicki and Wiggins, 2009). Recognizing this, we have taken steps in this direction, although referred to other phenomena involving 3D transport in fluids. In (Bruera et al., 2023), we have explored transport across the fully 3D Atlantic Meridional Overturning Circulation (AMOC) and (Amahjour et al., 2023) the dissemination of infectious organisms in a 3D turbulent environment. Studies in high-dimensional systems in which I have been involved, in the context of Celestial Mechanics, is for instance (Daquin et al., 2022).

Advancing Oceanic Models

Emergency services face a major challenge in selecting the most suitable dataset from the large amount of data available (Futch and Allen, 2019). Our research, discussed in Chapters 4 and 6, introduces a novel index for dataset comparison. This approach is further explored by the findings in our preprint (García-Sánchez et al., 2023), emphasizing the importance of robust dataset evaluation methods. Furthermore, the UQ metrics we developed, both forward and backward, have the potential to improve the methodology described in Chapter 7. In this context, our main objective was to acquire reliable oceanic data for the analysis of transport in coastal zones, typically characterized by data scarcity. Such advances offer the potential for the development of high-resolution models in regions with limited available data, addressing a critical concern for emergency services.

As we advance our models, understanding waves and storm surges becomes increasingly crucial, particularly in the context of rising sea levels and concerns about climate change (Vousdoukas et al., 2018). Despite the progress in current large-scale coastal models, there remains a significant gap in representing near-shore dynamics, attributable mainly to their coarse resolutions. These omissions could lead to potential inaccuracies in risk assessments. To address this, we highlight the importance of high-resolution models that intricately detail near-shore processes of waves and storm surges, as reinforced by the collaboration with the Joint Research Centre (JRC) (Mentaschi et al., 2023).

Bibliography

Adcroft, A. J. (1995). *Numerical algorithms for use in a dynamical model of the ocean*. PhD thesis, University of London 1995.

Agaoglou, M., Aguilar-Sanjuan, B., García-Garrido, V. J., et al. (2019). *Chemical Reactions: A Journey into Phase Space*. zenodo:10.5281/zenodo.3568210.

Agaoglou, M., Aguilar-Sanjuan, B., García-Garrido, V. J., et al. (2020). *Lagrangian Descriptors: Discovery and Quantification of Phase Space Structure and Transport*. zenodo: 10.5281/zenodo.3958985.

Amahjour, N., García-Sánchez, G., Agaoglou, M., and Mancho, A. M. (2023). Analysis of the spread of SARS-CoV-2 in a hospital isolation room using CFD and Lagrangian Coherent Structures. *Physica D: Nonlinear Phenomena*, page 133825.

Amo, A., Reffray, G., Sotillo, M. G., et al. (2020). *Product User Manual Atlantic -Iberian Biscay Irish- Ocean Physics Analysis and Forecast Product: IBI_ANALYSIS_FORECAST_PHYS_005_001*. https://resources.marine.copernicus.eu/documents/PUM/CMEMS-IBI-PUM-005-001.pdf.

Aref, H. (1984). Stirring by chaotic advection. *Journal of Fluid Mechanics*, 143:1–21.

Asce (1996). State-of-the-art review of modeling transport and fate of oil spills. Committee on Modeling Oil Spills.Water Resources Engineering Division. *Journal of Hydraulic Engineering*, 122.

Aurell, E., Boffetta, G., Crisanti, A., Paladin, G., and Vulpiani, A. (1997). Predictability in the large: an extension of the concept of Lyapunov exponent. *Journal of Physics A: Mathematical and General*, 30(1):1.

Aznar, R., Sotillo, M. G., Cailleau, S., et al. (2016). Strengths and weaknesses of the CMEMS forecasted and reanalyzed solutions for the Iberia-Biscay-Ireland (IBI) waters. *Journal of Marine Systems*, 159:1–14.

Balibrea-Iniesta, F., Xie, J., García-Garrido, V. J., et al. (2019). Lagrangian transport across the upper Arctic waters in the Canada Basin. *Quarterly Journal of the Royal Meteorological Society*, 145.

Barker, C. H., Kourafalou, V. H., Beegle-Krause, C. J., et al. (2020). Progress in operational modeling in support of oil spill response. *Journal of Marine Science and Engineering*, 8.

Beljaars, A. (1995). The parametrization of surface fluxes in large-scale models under free convection. *Quarterly Journal of the Royal Meteorological Society*, 121(522):255–270.

Ben-Nun, S. (2021). *Israel's beaches see more tar as oil spill consequences continue*. Jerusalem Post, https://www.jpost.com/breaking-news/israels-beaches-see-more-tar-as-oil-spill-consequences-continue-661788.

Bengtsson, L., Andrae, U., Aspelien, T., et al. (2017). The HARMONIE-AROME model configuration in the ALADIN-HIRLAM NWP system. *Monthly Weather Review*, 145.

Bolaños, R., Osuna, P., Wolf, J., Monbaliu, J., and Sánchez-Arcilla, A. (2011). Development of the POLCOMS–WAM current–wave model. *Ocean Modelling*, 36(1-2):102–115.

Branicki, M. and Wiggins, S. (2009). An adaptive method for computing invariant manifolds in non-autonomous, three-dimensional dynamical systems. *Physica D: Nonlinear Phenomena*, 238.

Branicki, M. and Wiggins, S. (2010). Finite-time Lagrangian transport analysis: Stable and unstable manifolds of hyperbolic trajectories and finite-time Lyapunov exponents. *Nonlinear Processes in Geophysics*, 17.

Bruera, R., Curbelo, J., García-Sánchez, G., and Mancho, A. M. (2023). Mixing and geometry in the North Atlantic Meridional Circulation. *Geophysical Research Letters*, 50(7):e2022GL102244.

Brushett, B. A., King, B. A., and Lemckert, C. J. (2011). Evaluation of met-ocean forecast data effectiveness for tracking drifters deployed during operational oil spill response in Australian waters. *Journal of Coastal Research*, pages 991–994.

Bryan, K. (1963). A Numerical Investigation of a Nonlinear Model of a Wind-Driven Ocean. *Journal of the Atmospheric Sciences*, 20.

Budgell, W. P. (2005). Numerical simulation of ice-ocean variability in the Barents Sea region. *Ocean Dynamics*, 55.

Cai, C., Zhu, L., and Hong, B. (2023). A review of methods for modeling microplastic transport in the marine environments. *Marine Pollution Bulletin*, 193:115136.

Capet, A., Fernández, V., Shen, J., et al. (2020). Operational Modeling Capacity in European Seas–An EuroGOOS Perspective and Recommendations for Improvement. *Frontiers in Marine Science*, 7.

Carswell, C. (2018). Unique oil spill in East China Sea frustrates scientists. *Nature*, 554:17–18.

Casulli, V. and Walters, R. A. (2000). An unstructured grid, three-dimensional model based on the shallow water equations. *International Journal for Numerical Methods in Fluids*, 32.

Cerralbo, P., Grifoll, M., and Espino, M. (2015). Hydrodynamic response in a microtidal and shallow bay under energetic wind and seiche episodes. *Journal of Marine Systems*, 149:1–13.

Chapman, D. C. (1985). Numerical treatment of cross-shelf open boundaries in a barotropic coastal ocean model . *Journal of Physical oceanography*, 15(8):1060–1075.

Chassignet, E. P., Hurlburt, H. E., Smedstad, O. E., Halliwell, G. R., Hogan, P. J., Wallcraft, A. J., Baraille, R., and Bleck, R. (2007). The HYCOM (HYbrid Coordinate Ocean Model) data assimilative system. *Journal of Marine Systems*, 65(1):60–83. Marine Environmental Monitoring and Prediction.

Cheng, Y., Li, X., Xu, Q., et al. (2011). SAR observation and model tracking of an oil spill event in coastal waters. *Marine Pollution Bulletin*, 62.

Ciaim (2018). Informe de colisión del buque RO/PAX VOLCÁN DE TAMASITE contra el dique Nelson Mandela del puerto de Las Palmas de Gran Canaria, el 21 de abril de 2017. CIAIM-05/2018. Ministerio de Fomento. Gobierno de España. 27pp.

Clementi, E., Pistoia, J., Escudier, R., et al. (2019). Mediterranean sea analysis and forecast (CMEMS MED-currents 2016-2019). *Copernicus Monitoring Environment Marine Service (CMEMS)*.

CMCC, EOS, O., and ORION (2021). *MEDSLIK-II simulations of transport and fate of a massive oil spill from the Banias electrical plant in the coastal area of Syria*. CMCC, https://www.cmcc.it/wp-content/uploads/2021/08/CMCC_ORION_ORBITALEOS_Report_n5_V1.pdf.

Consel, C. (1990). The Schism Manual. *Yale University, New Haven, Connecticut*.

Copernicus Climate Change Service (2023). *ERA5 Single Levels Reanalysis Dataset*. https://cds.climate.copernicus.eu/cdsapp#!/dataset/reanalysis-era5-single-levels.

Copernicus Marine Service (2023). *Operational Oceanography: History*. https://marine.copernicus.eu/explainers/operational-oceanography/history.

Craven, G. T. and Hernandez, R. (2016). Deconstructing field-induced ketene isomerization through Lagrangian descriptors. . *Phys. Chem. Chem. Phys*, 18:4008.

Danilov, S., Kivman, G., and Schröter, J. (2004). A finite-element ocean model: Principles and evaluation. *Ocean Modelling*, 6.

Daquin, J., Pédenon-Orlanducci, R., Agaoglou, M., García-Sánchez, G., and Mancho, A. M. (2022). Global dynamics visualisation from Lagrangian Descriptors. Applications to discrete and continuous systems. *Physica D: Nonlinear Phenomena*, 442:133520.

Darwish, A., Norouzi, S., Di Labbio, G., and Kadem, L. (2021). Extracting Lagrangian coherent structures in cardiovascular flows using Lagrangian descriptors. *Physics of Fluids*, 33(11).

De Crècy, A. (1996). Determination of the uncertainties of the constitutive relationships in the CALTHARE 2 code. Technical report, American Society of Mechanical Engineers, New York, NY (United States).

De la Cámara, A., Mechoso, C. R., Ide, K., et al. (2010). Polar night vortex breakdown and large-scale stirring in the southern stratosphere. *Climate Dynamics*, 35.

De la Cámara, A., Mechoso, C. R., Mancho, A. M., et al. (2013). Isentropic Transport within the Antarctic Polar-Night Vortex: Rossby Wave Breaking Evidence and Lagrangian Structures. *Journal of the Atmospheric Sciences*, 70.

Decker, C. J. and Reed, C. (2009). The National Oceanographic Partnership Program: a decade of impacts on oceanography. *Oceanography*, 22(2):208–227.

Delandmeter, P., Lambrechts, J., Legat, V., et al. (2018). A fully consistent and conservative vertically adaptive coordinate system for SLIM 3D v0.4 with an application to the thermocline oscillations of Lake Tanganyika. *Geoscientific Model Development*, 11(3):1161–1179.

Di Lorenzo, E., Schneider, N., Cobb, K. M., et al. (2008a). North Pacific Gyre Oscillation links ocean climate and ecosystem change. *Geophysical Research Letters*, 35.

Di Lorenzo, E., Schneider, N., Cobb, K. M., et al. (2008b). North Pacific Gyre Oscillation links ocean climate and ecosystem change. *Geophysical Research Letters*, 35(8).

Dominicis, M. D., Bruciaferri, D., Gerin, R., et al. (2016). A multi-model assessment of the impact of currents, waves and wind in modelling surface drifters and oil spill. *Deep-Sea Research Part II: Topical Studies in Oceanography*, 133.

Dominicis, M. D., Pinardi, N., Zodiatis, G., et al. (2013). MEDSLIK-II, a Lagrangian marine surface oil spill model for short-term forecasting-Part 1: Theory. *Geoscientific Model Development*, 6.

Domitr, P., Włostowski, M., Laskowski, R., and Jurkowski, R. (2023). Comparison of inverse uncertainty quantification methods for critical flow test. *Energy*, 263:125640.

Dritschel, D. G. and Ambaum, M. H. (1997). A contour-advective semi-Lagrangian numerical algorithm for simulating fine-scale conservative dynamical fields. *Quarterly Journal of the Royal Meteorological Society*, 123.

EFE (2017). *La punta de la mancha, de 13 km. de largo, ya está a la altura de La Garita pero a 1.000 metros de la costa.* Telde Actualidad, https://www.teldeactualidad.com/hemeroteca/noticia/medioambiente/2017/04/23/2402.html.

ESA (1998). *Oil pollution monitoring.* ESA brochure: ERS and its applications–Marine, BR-128, 1, https://earth.esa.int/web/guest/-/ers-and-its-applications-marine-4680.

European Commission (2014). *About Copernicus*. European Space Agency, https://www.copernicus.eu/en/about-copernicus.

Federico, I., Pinardi, N., Coppini, G., et al. (2017). Coastal ocean forecasting with an unstructured grid model in the southern Adriatic and northern Ionian seas. *Natural Hazards and Earth System Sciences*, 17.

Feng, D., Passalacqua, P., and Hodges, B. R. (2019). Innovative approaches for geometric uncertainty quantification in an operational oil spill modeling system. *Journal of Marine Science and Engineering*, 7.

Fernandes-Salvador, J. A., Davidson, K., Sourisseau, M., Revilla, M., Schmidt, W., Clarke, D., Miller, P. I., Arce, P., Fernández, R., Maman, L., et al. (2021). Current status of forecasting toxic harmful algae for the North-East Atlantic shellfish aquaculture industry. *Frontiers in Marine Science*, 8:666583.

Fingas, M. (2015). *Handbook of Oil Spill Science and Technology*.

Flather, R. A. (1976). A tidal model of the north-west European continental shelf. *Mem. Soc. Roy. Sci. Liege*, 10:141–164.

Frenklach, M., Packard, A., García-Donato, A., et al. (2016). Comparison of statistical and deterministic frameworks of uncertainty quantification. *SIAM-ASA Journal on Uncertainty Quantification*, 4.

Fringer, O. B., Gerritsen, M., and Street, R. L. (2006). An unstructured-grid, finite-volume, nonhydrostatic, parallel coastal ocean simulator. *Ocean Modelling*, 14.

Froyland, G. and Padberg-Gehle, K. (2014). Almost-invariant and finite-time coherent sets: Directionality, duration, and diffusion. *Springer Proceedings in Mathematics and Statistics*, 70.

Futch, V. and Allen, A. (2019). Search and Rescue Applications: On the Need to Improve Ocean Observing Data Systems in Offshore or Remote Locations. *Frontiers in Marine Science*, 6.

García-Sánchez, G., Agaoglou, M., Smith, E. M. C., and Mancho, A. M. (2023). Validation of the transport capacity of ocean models: a Lagrangian uncertainty quantification approach. Preprint.

García-Garrido, V. J., Balibrea-Iniesta, F., Wiggins, S., Mancho, A. M., and Lopesino, C. (2018a). Detection of phase space structures of the cat map with Lagrangian descriptors. *Regular and Chaotic Dynamics*, 23:751–766.

García-Garrido, V. J., Curbelo, J., Mancho, A. M., et al. (2018b). The Application of Lagrangian Descriptors to 3D Vector Fields. *Regular and Chaotic Dynamics*, 23(5):551–568.

García-Garrido, V. J., Mancho, A. M., Wiggins, S., et al. (2015). A dynamical systems approach to the surface search for debris associated with the disappearance of flight MH370. *Nonlinear Processes in Geophysics*, 22.

García-Garrido, V. J., Ramos, A. G., Mancho, A. M., et al. (2016). A dynamical systems perspective for a real-time response to a marine oil spill. *Marine Pollution Bulletin*, 112:1–10.

García-Sánchez, G., Mancho, A. M., and Wiggins, S. (2022). A bridge between invariant dynamical structures and uncertainty quantification. *Communications in Nonlinear Science and Numerical Simulation*, 104:106016.

García-Sánchez, G., Mancho, A. M., Agaoglou, M., and Wiggins, S. (2023a). New links between invariant dynamical structures and uncertainty quantification. *Physica D: Nonlinear Phenomena*, 453:133826.

García-Sánchez, G., Mancho, A. M., Ramos, A. G., Coca, J., and Jimenez-Madrid, J. J. (2023b). Dynamical systems for remote validation of very high-resolution ocean models. Preprint.

García-Sánchez, G., Mancho, A. M., Ramos, A. G., et al. (2022). Structured pathways in the turbulence organizing recent oil spill events in the Eastern Mediterranean. *Scientific Reports*, 12:3662.

García-Sánchez, G., Mancho, A. M., Ramos, A. G., J., C., Pérez-Gómez, B., Álvarez Fanjul, E., Sotillo, M. G., García-León, M., García-Garrido, V. J., and Wiggins, S. (2021). Very High Resolution Tools for the Monitoring and Assessment of Environmental Hazards in Coastal Areas. *Frontiers in Marine Science*, 7.

Giles, M. A. (1979). Marine Pollutant Transfer. *Journal of the Fisheries Research Board of Canada*, 36.

Gille, S. and Smith, L. (2003). Bathymetry and Ocean Circulation. *Charting the Secret World of the Ocean Floor. The GEBCO Project 1903-2003*.

Griffies, S. M., Böning, C., Bryan, F. O., et al. (2000). Developments in ocean climate modelling. *Ocean Modelling*, 2.

Grifoll, M., Gracia, V., Aretxabaleta, A., et al. (2014). Formation of fine sediment deposit from a flash flood river in the Mediterranean Sea. *Journal of Geophysical Research: Oceans*, 119(9):5837–5853.

Haidvogel, D. B., Arango, H., Budgell, W. P., et al. (2008). Ocean forecasting in terrain-following coordinates: Formulation and skill assessment of the Regional Ocean Modeling System. *Journal of Computational Physics*, 227:3595–3624.

Haidvogel, D. B., Arango, H. G., Hedstrom, K., et al. (2000). Model evaluation experiments in the North Atlantic Basin: Simulations in nonlinear terrain-following coordinates. *Dynamics of Atmospheres and Oceans*, 32.

Haidvogel, D. B. and Beckmann, A. (1999). *Numerical Ocean Circulation Modeling* . Imperial College Press.

Haller, G. (2001). Distinguished material surfaces and coherent structures in three-dimensional fluid flows. *Physica D: Nonlinear Phenomena*, 149.

Haller, G. (2002). Lagrangian coherent structures from approximate velocity data. *Phys. Fluids*, 14:1851–1861.

Haller, G. and Yuan, G. (2000). Lagrangian coherent structures and mixing in two-dimensional turbulence. *Physica D: Nonlinear Phenomena*, 147:352–370.

Harmel, T., Chami, M., Tormos, T., et al. (2018). Sunglint correction of the Multi-Spectral Instrument (MSI)-SENTINEL-2 imagery over inland and sea waters from SWIR bands . *Remote Sensing of Environment*, 204:308–321.

Haza, A. C., Griffa, A., Martin, P., et al. (2007). Model-based directed drifter launches in the Adriatic Sea: Results from the DART experiment. *Geophys. Res. Lett*, 34:L10605.

Haza, A. C., Özgökmen, T., Griffa, A., et al. (2010). Transport properties in small-scale coastal flows: relative dispersion from VHF radar measurements in the Gulf of La Spezia. *Ocean Dynam.*, 60:861–882.

He, R. and Wilkin, J. L. (2006). Barotropic tides on the southeast New England shelf: A view from a hybrid data assimilative modeling approach . *Journal of Geophysical Research: Oceans*, 111.

Hedström, K. S. (1994a). *Technical manual for a coupled sea-ice/ocean circulation model (version 1)*. Minerals Management Service, Alaska OCS Region.

Hedström, K. S. (1994b). *Technical manual for a coupled sea-ice/ocean circulation model (version 1)*. Minerals Management Service, Alaska OCS Region.

Hersbach, H., Bell, P. B., et al. (2020). The ERA5 global reanalysis. *Quarterly Journal of the Royal Meteorological Society*, 146(730):1999–2049.

Hong, S., Noh, Y., and Dudhia, J. (2006). A new vertical diffusion package with an explicit treatment of entrainment processes. *Monthly weather review*, 134(9):2318–2341.

Hu, Z., Xue, Y., Huang, B., Kumar, A., Wen, C., Xie, P., Zhu, J., Pegion, P. J., Ren, L., and Wang, W. (2022). Global Ocean Monitoring and Prediction at NOAA Climate Prediction Center: 15 Years of Operations. *Bulletin of the American Meteorological Society*, 103(12):E2701–E2718.

Huntley, H. S., Lipphardt, B. L., and Kirwan, A. D. (2011). Lagrangian predictability assessed in the East China Sea. *Ocean Modelling*, 36.

Ide, K., Small, D., and Wiggins, S. (2002). Distinguished hyperbolic trajectories in time-dependent fluid flows: Analytical and computational approach for velocity fields defined as data sets. *Nonlinear Processes in Geophysics*, 9.

Ivorra, B., Gomez, S., Glowinski, R., et al. (2017). Nonlinear Advection–Diffusion–Reaction Phenomena Involved in the Evolution and Pumping of Oil in Open Sea: Modeling, Numerical Simulation and Validation Considering the Prestige and Oleg Naydenov Oil Spill Cases. *Journal of Scientific Computing*, 70.

Jackett, D. R. and Mcdougall, T. J. (1995). Minimal Adjustment of Hydrographic Profiles to Achieve Static Stability. *Journal of Atmospheric and Oceanic Technology*, 12(2):381–389.

Jiménez-Madrid, J. A. and Mancho, A. M. (2009). Distinguished trajectories in time dependent vector fields. *Chaos*, 19:013111.

Joffre, T. and Tercatin, R. (2021). *Israel investigates tar spill calamity, places inquiry under gag order*. Jerusalem Post, https://www.jpost.com/israel-news/israel-oil-spill-disaster-investigation-details-placed-under-censor-659765.

Ju, N., Small, D., and Wiggins, S. (2003). Existence and computation of hyperbolic trajectories of aperiodically time dependent vector fields and their approximations. *International Journal of Bifurcation and Chaos in Applied Sciences and Engineering*, 13.

Julyan, H. E., Ulrike, F., Károlyi, G., et al. (2010). Dynamics of Finite-Size Particles in Chaotic Fluid Flows. *Understanding Complex Systems*, 2010.

Junginger, A., Craven, G. T., Bartsch, T., et al. (2016). Transition state geometry of driven chemical reactions on time-dependent double-well potentials. *Phys. Chem. Chem. Phys*, 18:30270.

Kaplan-Zantopp, M. (2021). *Israel oil spill: How did it happen and what will we do going forward?* Jerusalem Post, https://www.jpost.com/israel-news/israel-oil-spill-how-did-it-happen-and-what-will-we-do-going-forward-660242.

Kaszás, B. and Haller, G. (2020). Universal upper estimate for prediction errors under moderate model uncertainty. *Chaos: An Interdisciplinary Journal of Nonlinear Science*, 30(11).

Katsanikas, M., Agaoglou, M., and Montoya, F. (2022). Introduction to special issue: Chaos Indicators, Phase Space and Chemical Reaction Dynamics. *Physica D: Nonlinear Phenomena*, 439:133385.

Kirwan, A. D., Toner, M., and Kantha, L. (2003). Predictability, uncertainty, and hyperbolicity in the ocean. *International Journal of Engineering Science*, 41(3):249–258.

Kourafalou, V. H., De Mey, P., Le Hénaff, M., et al. (2015). Coastal ocean forecasting: System integration and evaluation. *Journal of Operational Oceanography*, 8.

Kundu, A. (2021). *Syrian Oil Spill Spreads Across The Mediterranean, Endangers Northern Cyprus Coast*. FleetMon, https://www.fleetmon.com/maritime-news/2021/35177/syrian-oil-spill-spreads-across-mediterranean-enda/.

Kuznetsov, L., Toner, M., Kirwan, A. D., et al. (2002). The Loop Current and adjacent rings delineated by Lagrangian analysis of the near-surface flow. *J. Mar. Res.*, 60:405–429.

Large, W. G. and Yeager, S. (2004). *Diurnal to decadal global forcing for ocean and sea-ice models: The data sets and flux climatologies*. University Corporation for Atmospheric Research., http://www.doi.org/10.5065/D6KK98Q6.

Le Traon, P. Y., Reppucci, A., Alvarez-Fanjul, E., Aouf, L., Behrens, A., Belmonte, M., Bentamy, A., Bertino, L., Brando, V. E., Kreiner, M. B., et al. (2019). From observation to information and users: The Copernicus Marine Service perspective. *Frontiers in Marine Science*, 6:234.

Lekien, F. and Marsden, J. (2005). Tricubic interpolation in three dimensions. *International Journal for Numerical Methods in Engineering*, 63.

Liu, Y., Weisberg, R. H., Vignudelli, S., et al. (2014). Evaluation of altimetry-derived surface current products using Lagrangian drifter trajectories in the eastern Gulf of Mexico. *Journal of Geophysical Research: Oceans*, 119.

Lopesino, C., Balibrea, F., and Wiggins, S. o. (2015). Lagrangian descriptors for two dimensional, area preserving, autonomous and nonautonomous maps. *Communications in Nonlinear Science and Numerical Simulation*, 27(1–3):40–51.

Lopesino, C., Balibrea-Iniesta, F., García-Garrido, V. J., et al. (2017). A theoretical framework for lagrangian descriptors. *International Journal of Bifurcation and Chaos*, 27:1730001.

Lorente, P., Sotillo, M. G., Amo-Baladrón, A., et al. (June 12–14, 2019). *Proceedings of the 19th International Conference on Computational Science*, volume Part IV, chapter The NARVAL Software Toolbox in Support of Ocean Models Skill Assessment at Regional and Coastal Scales., pages Doi: 10.1007/978–3–030–22747–0_25. ICCS 2019, Faro, Portugal.

M., G., G., J., G., S. M., et al. (2012). Water circulation forecasting in Spanish harbours. *Scientia Marina*, 76.

M., M. A., D., S., and S., W. (2004). Computation of hyperbolic trajectories and their stable and unstable manifolds for oceanographic flows represented as data sets. *Nonlinear Processes in Geophysics*, 11.

Madec, G. and the NEMO team (2008). *NEMO ocean engine*. Institut Pierre-Simon Laplace (IPSL), France, No 27, ISSN No 1288-1619., https://zenodo.org/record/3248739#.X0UXgpNLgSQ.

Malanotte-Rizzoli, P., Hedstrom, K., Arango, H., and Haidvogel, D. B. (2000). Water mass pathways between the subtropical and tropical ocean in a climatological simulation of the North Atlantic ocean circulation. *Dynamics of Atmospheres and Oceans*, 32(3-4):331–371.

Malenovskỳ, Z., Rott, H., Cihlar, J., Schaepman, M. E., García-Santos, G., Fernandes, R., and Berger, M. (2012). Sentinels for science: Potential of Sentinel-1,-2, and-3 missions for scientific observations of ocean, cryosphere, and land. *Remote Sensing of environment*, 120:91–101.

Mancho, A. M., Small, D., and Wiggins, S. (2006a). A tutorial on dynamical systems concepts applied to Lagrangian transport in oceanic flows defined as finite time data sets: theoretical and computational issues. *Physics Reports*, 437(3–4):55–124.

Mancho, A. M., Small, D., and Wiggins, S. (2006b). A tutorial on dynamical systems concepts applied to Lagrangian transport in oceanic flows defined as finite time data sets: Theoretical and computational issues. *Physics Reports*, 437.

Mancho, A. M., Small, D., Wiggins, S., et al. (2003). Computation of stable and unstable manifolds of hyperbolic trajectories in two-dimensional, aperiodically time-dependent vector fields. *Physica D: Nonlinear Phenomena*, 182.

Mancho, A. M., Wiggins, S., Curbelo, J., et al. (2013). Lagrangian descriptors: A method for revealing phase space structures of general time dependent dynamical systems. *Communications in Nonlinear Science and Numerical Simulation*, 18(12):3530–3557.

Marchesiello, P., McWilliams, J. C., and Shchepetkin, A. (2001). Open boundary conditions for long-term integration of regional oceanic models. *Ocean Modelling*, 3.

Martin, P. J., Barron, C. N., Smedstad, L. F., Campbell, T. J., Wallcraft, A. J., Rhodes, R. C., Rowley, C., Townsend, T. L., and Carroll, S. N. (2009). User's manual for the Navy Coastal Ocean Model (NCOM) version 4.0. Technical report, Naval Research Lab Stennis Space Center MS Ocean Dynamics and Prediction Branch.

Martinho, M. A., Ruiz-Villarreal, M., Pereira, J., et al. (2013). Efficient tools for marine operational forecast and oil spill tracking. *Marine Pollution Bulletin*, 71.

Max Planck Institute for Meteorology (2023). *ICON Public*. https://code.mpimet.mpg.de/projects/iconpublic.

Maxey, M. R. and Riley, J. J. (1983). Equation of motion for a small rigid sphere in a nonuniform flow. *Physics of Fluids*, 26.

McIlroy, J. W., Smith, R. W., and McGuffin, V. L. (2018). Fixed- and variable-temperature kinetic models to predict evaporation of petroleum distillates for fire debris applications. *Separations*, 5.

Medjo, T. T. (2018). Pullback attractors for the multi-layer quasi-geostrophic equations of the ocean . *Nonlinear Analysis: Real World Applications*, 17:365–382.

Mendoza, C., Mancho, A., and Wiggins, S. (2014). Lagrangian descriptors and the assessment of the predictive capacity of oceanic data sets. *Nonlinear Processes in Geophysics*, 21(3):677–689.

Mendoza, C. and Mancho, A. M. (2010). Hidden geometry of ocean flows. *Physical Review Letters*, 105(3):038501.

Mendoza, C. and Mancho, A. M. (2012). Review Article: "The Lagrangian description of aperiodic flows: A case study of the Kuroshio Current". *Nonlinear Processes in Geophysics*, 19.

Mentaschi, L., Vousdoukas, M. I., García-Sánchez, G., Fernández-Montblanc, T., Roland, A., Voukouvalas, E., Federico, I., Abdolali, A., Zhang, Y. J., and Feyen, L. (2023). A global unstructured, coupled, high-resolution hindcast of waves and storm surge. *Frontiers in Marine Science*, 10.

Mezić, I. and Wiggins, S. (1999). A method for visualization of invariant sets of dynamical systems based on the ergodic partition. *Chaos*, 9.

Monitor, A. (2021). *Oil spill in Mediterranean reaches besieged Gaza Strip*. Al-Monitor, https://www.al-monitor.com/originals/2021/03/gaza-beach-oil-spill-israel-environment-pollution.html.

Monroy, P. (2019). *Doctoral Thesis: Lagrangian Studies of Sedimentation and Transport. Impact on marine ecosystems.* Universitat de les Illes Balears, https://ifisc.uib-csic.es/es/publications/lagrangian-studies-of-sedimentation-and-transport/.

Monroy, P., E., H.-G., Rossi, V., et al. (2017). Modeling the dynamical sinking of biogenic particles in oceanic flow. *Nonlinear Processes in Geophysics*, 24.

Montero, A. R. (2017). La reducción de la mancha de gasoil un 80% permite abrir las ocho playas. *La Provincia*.

Moser, J. (1956). The analytic invariants of an area-preserving mapping near a hyperbolic fixed point. *Communications on pure and applied mathematics*, 9:673–692.

Muhammad, A. (2015). Exploring Salinity Issues in the Texas Coast using SELFE: Semi-Implicit Finite-Element/Volume Eulerian-Lagrangian algorithm. Technical report.

Nagheeby, M. and Kolahdoozan, M. (2010). Numerical modeling of two-phase fluid flow and oil slick transport in estuarine water. *International Journal of Environmental Science and Technology*, 7.

National Centers for Environmental Information (2023). *Global Forecast System*. https://www.ncei.noaa.gov/products/weather-climate-models/global-forecast.

Nechad, B., Ruddick, K., and Neukermans, G. (2009). Calibration and validation of a generic multisensor algorithm for mapping of turbidity in coastal waters . *SPIE Europe Remote Sensing. International Society for Optics and Photonics*, page 74730H–74730H.

Nechad, B., Ruddick, K., and Neukermans, G. (2010). Calibration and validation of a generic multisensor algorithm for mapping of total suspended matter in turbid waters . *Remote Sensing of Environment*, 114(4):854–866.

Nese, J. M. (1989). Quantifying local predictability in phase space. *Physica D: Nonlinear Phenomena*, 35.

News-Agencies (2021). *Aljazeera*. Aljazeera, https://www.aljazeera.com/news/2021/2/27/lebanon-begins-cleaning-beaches-after-oil-spill.

O'Connor, W. P. (1991). A user's manual for the Princeton numerical ocean model. Technical report, Institute for Naval Oceanography Stennis Space Center MS.

Olascoaga, M. J., Beron-Vera, F. J., Brand, L. E., and Kocak, H. (2008). Tracing the early development of harmful algal blooms on the West Florida Shelf with the aid of Lagrangian coherent structures. *Journal of Geophysical Research: Oceans*, 113(C12).

Olascoaga, M. J. and Haller, G. (2012). Forecasting sudden changes in environmental pollution patterns. *Proceedings of the National Academy of Sciences of the United States of America*, 109.

Ottino, J. M., Jana, S. C., and Chakravarthy, V. S. (1994). From Reynolds's stretching and folding to mixing studies using horseshoe maps. *Physics of Fluids*, 6.

Palis, J. (1969). On Morse-Smale dynamical systems. *Topology*, 8.

Pavlakis, P., Sieber, A., and Alexandry, S. (1996). Monitoring oil-spill pollution in the Mediterranean with ERS SAR. *Earth Observation Quarterly*, 52.

Peliz, A., Dubert, J., Haidvogel, D. B., et al. (2003). Generation and unstable evolution of a density-driven Eastern Poleward Current: The Iberian Poleward Current. *Journal of Geophysical Research: Oceans*, 108.

Petruzzi, A. (2019). The casualidad method for uncertainty evaluation of best-estimate system thermal-hydraulic calculations. *Nuclear Technology*, 205(12):1554–1566.

Pisano, A., Bignami, F., and Santoleri, R. (2015). Oil spill detection in glint-contaminated near-infrared MODIS imagery. *Remote Sensing*, 7.

Pisano, A., Marullo, S., Artale, V., Falcini, F., Yang, X., Leonelli, F. E., Santoleri, R., and Buongiorno Nardelli, B. (2020). New evidence of Mediterranean climate change and variability from sea surface temperature observations. *Remote Sensing*, 12(1):132.

Polidura, A. (2021). *Israel's oil spill now affects entire Lebanese coastline*. Atalayar, https://atalayar.com/en/content/israels-oil-spill-now-affects-entire-lebanese-coastline.

Prants, S. V., Budyansky, M. V., and Uleysky, M. Y. (2014). Lagrangian study of surface transport in the Kuroshio Extension area based on simulation of propagation of Fukushima-derived radionuclides. *Nonlinear Processes in Geophysics*, 21.

Prants, S. V., Uleysky, M. Y., and Budyansky, M. V. (2011). Numerical simulation of propagation of radioactive pollution in the ocean from the Fukushima Dai-ichi nuclear power plant. *Doklady Earth Sciences*, 439.

Ramos, A. G., Martel, A., Codd, G. A., Soler, E., Coca, J., Redondo, A., Morrison, L. F., Metcalf, J. S., Ojeda, A., Suárez, S., et al. (2005). Bloom of the marine diazotrophic cyanobacterium Trichodesmium erythraeum in the Northwest African Upwelling. *Marine Ecology Progress Series*, 301:303–305.

Revuelta, F., Benito, R. M., and Borondo, F. (2019). Unveiling the chaotic structure in phase space of molecular systems using Lagrangian descriptors. *Physical Review E*, 99:032221.

Rinat, Z. and Zikri, A. B. (2021). *Oil Spill Off Israel's Coast Is Its Worst Maritime Pollution in Decades, and Cleanup 'Could Take Years'*. Haaretz, https://www.haaretz.com/israel-news/.premium-oil-spill-off-israel-s-coast-is-its-worst-maritime-pollution-in-decades-1.9553528.

Robbin, J., Palis, J., and De Melo, W. (1984). Geometric Theory of Dynamical Systems: An Introduction. *The American Mathematical Monthly*, 91.

Rypina, I. I., Scott, S. E., Pratt, L. J., et al. (2011). Investigating the connection between complexity of isolated trajectories and Lagrangian coherent structures. *Nonlinear Processes in Geophysics*, 18.

Schrope, M. (2013). Minor oil spills are often bigger than reported. *Nature*, 10.1038/nature.2013.12307.

Serra, M., Sathe, P., Rypina, I., Kirincich, A., Ross, S. D., Lermusiaux, P., Allen, A. A., Peacock, T., and Haller, G. (2020). Search and rescue at sea aided by hidden flow structures. *Nature communications*, 11(1):2525.

Shadden, S. C., Lekien, F., and Marsden, J. E. (2005). Definition and properties of Lagrangian coherent structures from finite-time Lyapunov exponents in two-dimensional aperiodic flows. *Physica D: Nonlinear Phenomena*, 212.

Shadden, S. C., Lekien, F., Paduan, J. D., et al. (2009). The correlation between surface drifters and coherent structures based on high-frequency radar data in Monterey Bay. *Deep Sea Res. II*, 56:161–172.

Shapiro, R. (1970). Smoothing, filtering, and boundary effects. *Reviews of Geophysics*, 8.

Shchepetkin, A. F. and Mcwilliams, J. C. (1998). Quasi-monotone advection schemes based on explicit locally adaptive dissipation. *Monthly Weather Review*, 126.

Shchepetkin, A. F. and McWilliams, J. C. (2003). A method for computing horizontal pressure-gradient force in an oceanic model with a nonaligned vertical coordinate. *Journal of Geophysical Research: Oceans*, 108.

Shchepetkin, A. F. and McWilliams, J. C. (2005). The regional oceanic modeling system (ROMS): A split-explicit, free-surface, topography-following-coordinate oceanic model. *Ocean Modelling*, 9.

Shu, Y., Wang, D., Feng, M., et al. (2018). The Contribution of Local Wind and Ocean Circulation to the Interannual Variability in Coastal Upwelling Intensity in the Northern South China Sea. *Journal of Geophysical Research: Oceans*, 123.

Shu, Y., Xue, H., Wang, D., et al. (2014). Meridional overturning circulation in the South China Sea envisioned from the high-resolution global reanalysis data GLBa0.08. *Journal of Geophysical Research: Oceans*, 119.

Song, Y. and Haidvogel, D. (1994). A semi-implicit ocean circulation model using a generalized topography-following coordinate system. *Journal of Computational Physics*, 115.

Sotillo, M. G., Cailleau, S., Lorente, P., et al. (2015). The myocean IBI ocean forecast and reanalysis systems: Operational products and roadmap to the future copernicus service. *Journal of Operational Oceanography*, 8(1):63–79.

Sotillo, M. G., Cerralbo, P., Lorente, P., et al. (2020a). Coastal ocean forecasting in Spanish ports: the SAMOA operational service . *Journal of Operational Oceanography*, 13(1):37–54.

Sotillo, M. G., Cerralbo, P., Lorente, P., et al. (2020b). Coastal ocean forecasting in Spanish ports: the SAMOA operational service. *Journal of Operational Oceanography*, 13(1):37–54.

Speetjens, M. F., Clercx, H. J., and van Heijst, G. J. (2004). A numerical and experimental study on advection in three-dimensional Stokes flows. *Journal of Fluid Mechanics*, 514:77–105.

Staff, R. (2021). *Oil spill off Israel reaches south Lebanese beaches*. Rutgers, https://www.reuters.com/article/us-israel-environment-oil-spill-lebanon-idUSKBN2AM19V.

Stolzenbach, K. D., Madsen, O. S., Adams, E. E., et al. (1977). Review And Evaluation Of Basic Techniques For Predicting The Behavior Of Surface Oil Slicks. *MIT Dep Civ Eng Ralph M. Parsons Lab Water Resour Hydrodyn Rep*.

Sullivan, T. J. (2015). *Introduction to Uncertainty Quantification*. Springer.

Surkes, S. (2021). *Satellite images of oil slicks off coast show recent spill far from a one-off*. Times of Israel, https://www.timesofisrael.com/satellite-images-of-oil-slicks-off-coast-show-recent-spill-far-from-a-one-off/.

Susuki, Y. and Mezić, I. (2009). Ergodic partition of phase space in continuous dynamical systems. *Proceedings of the IEEE Conference on Decision and Control*.

Sutherland, B. R., DiBenedetto, M., Kaminski, A., and Van Den Bremer, T. (2023). Fluid dynamics challenges in predicting plastic pollution transport in the ocean: A perspective. *Physical Review Fluids*, 8(7):070701.

Tercatin, R. (2021). *Damage to Israeli marine environment from tar spill extreme, experts say*. Jerusalem Post, https://www.jpost.com/israel-news/damage-to-israeli-marine-environment-from-tar-spill-extreme-experts-say-659716.

Umgiesser, G., Canu, D. M., Cucco, A., et al. (2004). A finite element model for the Venice Lagoon. Development, set up, calibration and validation. *Journal of Marine Systems*, 51.

Umlauf, L. and Burchard, H. (2003). A generic length-scale equation for geophysical turbulence models. *Journal of Marine Research*, 61(2):235–265.

Van Sebille, E., Aliani, S., Law, K. L., Maximenko, N., Alsina, J. M., Bagaev, A., Bergmann, M., Chapron, B., Chubarenko, I., Cózar, A., et al. (2020). The physical oceanography of the transport of floating marine debris. *Environmental Research Letters*, 15(2):023003.

Vanhellemont, Q. (2019). Adaptation of the dark spectrum fitting atmospheric correction for aquatic applications of the Landsat and Sentinel-2 archives. *Remote Sensing of Environment*, 225:175–192.

Vanhellemont, Q. and Ruddick, K. (2018). Atmospheric correction of metre-scale optical satellite data for inland and coastal water applications . *Remote Sensing of Environment*, 216:586–597.

Vieira, G. S., Rypina, I. I., and Allshouse, M. R. (2020). Uncertainty quantification of trajectory clustering applied to ocean ensemble forecasts. *Fluids*, 5.

Vousdoukas, M. I., Mentaschi, L., Voukouvalas, E., et al. (2018). Global probabilistic projections of extreme sea levels show intensification of coastal flood hazard. *Nature Communications*, 9.

Walters, R. A. (2005). Coastal ocean models: Two useful finite element methods. *Continental Shelf Research*, 25.

Wang, P., Song, Y. T., Chao, Y., and Zhang, H. (2005). Parallel computation of the regional ocean modeling system. *The International Journal of High Performance Computing Applications*, 19(4):375–385.

Warner, J. C., Armstrong, B., He, R., and Zambon, J. B. (2010). Development of a coupled ocean–atmosphere–wave–sediment transport (COAWST) modeling system. *Ocean modelling*, 35(3):230–244.

Warner, J. C., Sherwood, C. R., Arango, H. G., et al. (2005). Performance of four turbulence closure models implemented using a generic length scale method. *Ocean Modelling*, 8.

Westerink, J. J., Luettich Jr, R., Blain, C., and Scheffner, N. W. (1994). Adcirc: an advanced three-dimensional circulation model for shelves, coasts, and estuaries. report 2. user's manual for adcirc-2ddi. Technical report, Army engineer waterways experiment stations Vicksburg MS.

Wiggins, S. (1992). *Chaotic Transport in Dynamical Systems*. Springer-Verlag, New York.

Wiggins, S. (2003). *Introduction to applied nonlinear dynamical systems and applications*. Springer-Verlag Heidelberg.

Wiggins, S. (2005). The dynamical systems approach to Lagrangian transport in oceanic flows. *Annu. Rev. Fluid Mech.*, 37:295–328.

Wikimedia Foundation (2021). *2021 Mediterranean Oil Spill.* Wikipedia, https://en.wikipedia.org/wiki/2021_Mediterranean_oil_spill.

Wilcox, D. C. et al. (1998). *Turbulence modeling for CFD*, volume 2. DCW industries La Canada, CA.

Wilkin, J. L., Arango, H. G., Haidvogel, D. B., et al. (2005). A regional ocean modeling system for the Long-term Ecosystem Observatory. *Journal of Geophysical Research: Oceans*, 110.

Wu, X., Kozlowski, T., Meidani, H., and Shirvan, K. (2018). Inverse uncertainty quantification using the modular Bayesian approach based on Gaussian Process, Part 2: Application to TRACE. *Nuclear Engineering and Design*, 335:417–431.

Xu, Q., Li, X., Wei, Y., et al. (2013). Satellite observations and modeling of oil spill trajectories in the Bohai Sea. *Marine Pollution Bulletin*, 71.

Zafirakou, A. (2019). *Oil Spill Dispersion Forecasting Models*. Monitoring of Marine Pollution.

Zhang, X., Cheng, L., Zhang, G., Wu, J., Li, S., Liu, J., Chu, S., Xia, N., Min, K., Zuo, X., et al. (2020). Evaluation of multi-source forcing datasets for drift trajectory prediction using Lagrangian models in the South China Sea. *Applied Ocean Research*, 104:102395.

Zodiatis, G., Lardner, R., Alves, T. M., et al. (2017). Oil spill forecasting (prediction). *Journal of Marine Research*, 75.